TU Delft

Delft University of Technology

A discontinuity-enriched finite element method for the computational design of phononic crystals

van den Boom, S.J.

DOI
10.4233/uuid:9b3a8dff-40ca-4b95-ae73-9a568302d1e5

Publication date
2022

Document Version
Final published version

Citation (APA)
van den Boom, S. J. (2022). *A discontinuity-enriched finite element method for the computational design of phononic crystals*. [Dissertation (TU Delft), Delft University of Technology]. https://doi.org/10.4233/uuid:9b3a8dff-40ca-4b95-ae73-9a568302d1e5

Important note
To cite this publication, please use the final published version (if applicable).
Please check the document version above.

Copyright
Other than for strictly personal use, it is not permitted to download, forward or distribute the text or part of it, without the consent of the author(s) and/or copyright holder(s), unless the work is under an open content license such as Creative Commons.

Takedown policy
Please contact us and provide details if you believe this document breaches copyrights.
We will remove access to the work immediately and investigate your claim.

This work is downloaded from Delft University of Technology.
For technical reasons the number of authors shown on this cover page is limited to a maximum of 10.

A discontinuity-enriched finite element method for the computational design of phononic crystals

S.J. van den Boom

A discontinuity-enriched finite element method for the computational design of phononic crystals S.J. van den Boom

A DISCONTINUITY-ENRICHED FINITE ELEMENT METHOD FOR THE COMPUTATIONAL DESIGN OF PHONONIC CRYSTALS

A DISCONTINUITY-ENRICHED FINITE ELEMENT METHOD FOR THE COMPUTATIONAL DESIGN OF PHONONIC CRYSTALS

Proefschrift

ter verkrijging van de graad van doctor
aan de Technische Universiteit Delft,
op gezag van de Rector Magnificus Prof. dr. ir. T.H.J.J. van der Hagen,
voorzitter van het College voor Promoties,
in het openbaar te verdedigen op
woensdag 6 april 2022 om 15:00 uur

door

Sanne Jolene VAN DEN BOOM

werktuigkundig ingenieur,
Technische Universiteit Delft, Nederland
geboren te Bergen op Zoom, Nederland.

Dit proefschrift is goedgekeurd door de promotoren.

Samenstelling promotiecommissie:

Rector Magnificus,	voorzitter
Prof. dr. ir. A. van Keulen,	Technische Universiteit Delft, promotor
Dr. A.M. Aragón,	Technische Universiteit Delft, copromotor
Onafhankelijke leden:	
Prof. dr. H.A. Kim	University of California San Diego, USA
Prof. dr. P.H. Geubelle	University of Illinois at Urbana-Champaign, USA
Prof. dr. A. Simone	University of Padova, Italy
Prof. dr. ir. L.J. Sluijs	Technische Universiteit Delft
Dr. ir. V.G. Kouznetsova	Technische Universiteit Eindhoven
Prof. dr. U. Staufer	Technische Universiteit Delft, reservelid



Keywords: Phononic crystals, Enriched finite element methods, Topology optimization

Printed by: Gildeprint

Front & Back: Crystel van Bruggen & Sanne van den Boom

Copyright © 2022 by S.J. van den Boom

ISBN 978-94-6384-315-7

An electronic version of this dissertation is available at
http://repository.tudelft.nl/.

SUMMARY

Phononic crystals can be designed to have bandgaps—ranges of frequencies whose propagation through the material is prevented. They are therefore attractive for vibration isolation applications in different industries, where unwanted vibrations reduce performance. Yet, important steps are still to be made for the integration of phononic crystals into engineering practice. For instance, methods for large scale production are still in development. Furthermore, it is essential that design methods are established to enable the design of phononic crystals that meet all of the, often conflicting, requirements for practical applications. This thesis focuses on the latter challenge by proposing a computational design method for phononic crystals based on the combination of an advanced finite element method and level set-based topology optimization.

The working principle of phononic crystals is based on destructive interference of waves reflecting from the periodic arrangement of material interfaces (Bragg scattering). Consequently, it is essential that a numerical design tool accurately captures the mechanical behavior at material interfaces. Generally, in finite element analyses, this is ensured by creating a *matching* mesh: a discretization that conforms to the material interfaces. However, during computational *design*, the locations and geometry of these material interfaces change in every design iteration. One solution to this would be to create a new matching mesh for every iteration during the computational design. Nevertheless, creating new matching meshes for every design iteration is a challenging and error-prone procedure. In standard topology optimization methods this problem is commonly avoided altogether by using a density-based representation. In this approach, the discretization does not conform to the material interfaces. Instead, the interfaces are resolved by assigning a (pseudo-) density to each mesh element. As a result, these material boundaries are diffused and staircased, which is detrimental for obtaining the dynamic response of phononic crystals. The extremely fine finite element meshes required to compensate for this boundary description result in exceedingly large and expensive optimization problems.

A possible solution is to decouple the boundary description from the discretization using a level set method. Level sets have been widely used in topology optimization as an alternative design parametrization that offers more defined material boundaries. However, in most cases the level set is mapped to element densities using an Ersatz method for the analysis. Although gray values are limited to the elements that are intersected by the level set boundary, even during the optimization, the method still suffers from staircasing and diffuse boundaries. This problem can be solved using enriched or immersed finite element methods. In these methods, standard finite element procedures are enhanced or modified to resolve material interfaces inside elements. Many such enriched and immersed methods exist, each having their own advantages and disadvantages. This thesis focuses on the Interface-enriched Generalized Finite Element Method (IGFEM), and its extensions: the Hierarchical Interface-enriched

Finite Element Method (HIFEM) and the Discontinuity-Enriched Finite Element Method (DE-FEM). As DE-FEM is a generalization of IGFEM/HIFEM, collectively they are also referred to as discontinuity-enriched finite element methods. An important advantage of discontinuity-enriched FEMs is the fact that, using a new method that is introduced in Chapter 2, *strong* enforcement of essential (Dirichlet) boundary conditions is possible on boundaries that are non-matching to the discretization mesh. Because of this strong enforcement of boundary conditions, smooth reaction fields are recovered along these non-matching boundaries. In Chapter 3 it is demonstrated that this method can also be extended to the strong enforcement of Bloch-Floquet periodic boundary conditions, which are required for the immersed analysis of phononic crystals. These two chapters together show that IGFEM is suitable for PnC design, as it can be used to modify both the phononic crystal geometry and periodicity without changing the underlying discretization, and without loss of accuracy.

By creating a framework for topology optimization using IGFEM and level set functions parametrized by radial basis function, in Chapter 4 a computational design procedure is established that inherits the benefits of discontinuity-enriched methods as well as level set methods. The sensitivities required for design updates for compliance problems are derived analytically. Combining aforementioned procedures, in Chapter 5, phononic crystals are optimized using the previously introduced topology optimization procedure. To this end, the sensitivities for bandgap maximization are also derived analytically. This chapter also highlights the importance of accurately capturing the mechanical behavior near material interfaces for phononic crystal design. The methods introduced in this thesis can not only be employed for the topology optimization of phononic crystals, but may also be advantageous for other optimization problems such as fluid-structure interaction or contact.

SAMENVATTING

Phononische kristallen kunnen zodanig ontworpen worden dat ze een gewenste *bandgap* vertonen—een bereik van frequenties die verhinderd wordt zich voort te planten door het materiaal. Dit maakt ze onder andere een aantrekkelijke kandidaat voor het gebruik in vibratie-isolatie in verschillende industrieën, waar ongewenste vibraties het behalen van strikte toleranties belemmeren. Toch moeten er nog belangrijke stappen worden gezet voordat phononische kristallen naadloos geïntegreerd kunnen worden in de technische praktijk. Zo zijn er bijvoorbeeld productiemethoden nodig om phononische kristallen op grote schaal te kunnen produceren. Ook is het essentieel dat er ontwerp-methodieken worden ontwikkeld waarmee phononische kristallen kunnen worden ontworpen die voldoen aan alle, vaak conflicterende, eisen. Dit proefschrift richt zich op deze laatstgenoemde uitdaging door toe te werken naar een numerieke ontwerpmethode die gebruikt maakt van een geavanceerde eindige elementen methode en topologie optimalisatie.

De werking van phononische kristallen is gebaseerd op destructieve interferentie van mechanische golven die weerkaatsen van periodieke materiaalgrenzen (Bragg-reflectie). In een numeriek model is het daarom van groot belang om het mechanische gedrag dicht bij deze materiaalovergangen goed te omschrijven. In het algemeen wordt hier in eindige elementen analyses voor gezorgd door het creëren van een conformerend rekenrooster; een discretisatie die de lokatie van materiaalgrenzen in acht neemt. Echter veranderen tijdens een numerieke *ontwerp*procedure de locaties en geometrie van de materiaalgrenzen in iedere ontwerp-iteratie. Een mogelijke oplossing hiervoor zou zijn om een nieuw rekenrooster te creëren voor iedere iteratie in het ontwerpproces. Niettemin is het maken van een nieuw conformerend rekenrooster voor iedere ontwerp-iteratie een uitdagend en foutgevoelig proces. In standaard topologie optimalisatie wordt dit probleem gewoonlijk helemaal ontweken door het gebruik van methodes gebaseerd op een pseudo-dichtheid. In deze aanpak neemt de discretisatie de materiaalgrenzen niet in acht. In plaats daarvan worden de materiaalgrenzen gerepresenteerd door middel van een pseudo-dichtheid in ieder element van het rekenrooster. Dit heeft tot resultaat dat de materiaalgrenzen diffuus en getrapt zijn, wat nadelig is voor de nauwkeurigheid waarmee het gedrag van phononische kristallen wordt beschreven. De extreem verfijnde rekenroosters die nodig zijn om te compenseren voor de getrapte materiaalgrensdefinities resulteren in buitengewoon grote optimalisatieproblemen.

Een mogelijke oplossing is om de materiaalgrensdefinitie los te koppelen van het rekenrooster door gebruik te maken van een level set methode. Level sets worden veel toegepast als alternatieve parametrisering die zorgt voor een beter gedefinieerde materiaalgrenzen. Echter wordt de level set in de meeste gevallen voor de analyse gerepresenteerd met elementdichtheden doormiddel van een Ersatz methode. Hoewel grijswaarden dan beperkt worden tot elementen die worden doorkruist door een materiaalgrens, ook tijdens de optimalisatie, lijdt deze methode nog steeds aan grijze en getrapte materi-

aalgrenzen. Dit kan worden opgelost door middel van verbeterde of aangepaste eindige elementen methodes. In deze methodes wordt de standaard eindige elementen formulering uitgebreid en aangepast om materiaalgrenzen door elementen heen te accommoderen. Er bestaan verschillende van dit soort methodes, die elk hun eigen voor- en nadelen hebben. Dit proefschrift richt zich op de Interface-enriched Generalized Finite Element Method (IGFEM), en de uitbreidingen: de Hierarchical Interface-enriched Finite Element Method (HIFEM) en de Discontinuity-Enriched Finite Element Method (DE-FEM). Omdat DE-FEM een generalisatie van IGFEM/HIFEM wordt als verzamelnaam voor deze methodes *discontinuity-enriched* eindige elementen methodes gebruikt. Een belangrijk voordeel van discontinuity-enriched eindige elementen methodes is het feit dat essentiële (Dirichlet) randvoorwaarden, gebruikmakend van een nieuwe methode die in Hoofdstuk 2 wordt geïntroduceerd, *sterk* kunnen worden voorgeschreven op randen en oppervlaktes die niet conformeren aan het rekenrooster. Hierdoor is het ook mogelijk gladde reactievelden te verkrijgen op niet-conformerende randen. In Hoofdstuk 3 wordt gedemonstreerd dat dit ook geldt voor het sterk voorschrijven van de Bloch-Floquet periodieke randvoorwaarden die nodig zijn voor het analyseren van phononische kristallen. Deze hoofdstukken samen tonen dat IGFEM geschikt is voor het ontwerp van phononische kristallen, omdat het gebruikt kan worden om zowel de geometrie als periodiciteit van phononische kristallen aan te passen zonder daarbij de onderliggende discretisatie te hoeven veranderen, en zonder verlies van nauwkeurigheid.

Door een werkwijze te ontwikkelen voor topologie optimalisatie die gebruikt maakt van IGFEM en *level set*-functies die worden geparametriseerd met behulp van radiale basisfuncties, wordt in Hoofdstuk 4 een ontwerpmethode ontwikkeld met de voordelen van zowel discontinuity-enriched methodes als level set methodes. De afgeleiden die nodig zijn voor het doen van ontwerpstappen in stijfheidsmaximalisatieproblemen worden analytisch afgeleid. Door eerdergenoemde procedures te combineren worden in Hoofdstuk 5 phononische kristallen geoptimaliseerd. De hiervoor benodigde ontwerpafgeleiden worden analytisch afgeleid. Dit hoofdstuk benadrukt ook het belang van het nauwkeurig beschrijven van het mechanisch gedrag in de buurt van materiaalgrenzen in phononische kristallen. Deze topologie optimalisatie methode kan niet alleen gebruikt worden voor het ontwerpen van phononische kristallen, maar kan ook aantrekkelijk zijn voor andere optimalisatieproblemen zoals vloeistof-structuur interacties of contact.

INHOUDSOPGAVE

Summary v

Samenvatting vii

1 Introduction 1
1.1 Phononic crystals . . . 1
1.2 Decoupling the design from the analysis mesh . . . 2
1.3 Research aim and scope . . . 3
1.4 Main contributions of this thesis . . . 4
1.5 Thesis outline . . . 4

2 An Interface-enriched Finite Element Method for Immersed Problems 7
Abstract . . . 8
2.1 Introduction . . . 8
2.2 DE-FEM as an immersed method . . . 11
2.2.1 Discretization . . . 11
2.2.2 Treatment of boundary conditions . . . 17
2.3 Numerical examples . . . 20
2.3.1 The "Ultimate" discontinuity patch test . . . 20
2.3.2 Convergence: immersed Eshelby inclusion problem . . . 22
2.3.3 Stability: slightly rotated mesh . . . 27
2.3.4 A 3-D immersed thermo-mechanical "popcorn" . . . 28
2.4 Summary and conclusions . . . 30
Appendix: Pseudo code for hierarchical implementation . . . 31

3 Immersed Analysis of Phononic Crystals using IGFEM 35
Abstract . . . 36
3.1 Introduction . . . 36
3.2 Problem formulation . . . 39
3.2.1 Bloch-Floquet periodicity on enriched nodes . . . 42
3.3 Numerical results . . . 44
3.3.1 1-D phononic crystal . . . 44
3.3.2 2-D uniform material . . . 46
3.3.3 2-D phononic crystal with a circular inclusion . . . 48
3.3.4 2-D phononic crystal with a varying lattice . . . 51
3.3.5 3-D phononic crystal . . . 52
3.4 Summary and Conclusions . . . 54
Appendix: Constructing a transformation matrix for a simple 1-D PUC . . . 57

4 Level set-based topology optimization using IGFEM **59**
Abstract . . . 60
4.1 Introduction . . . 60
4.2 Formulation . . . 63
4.2.1 IGFEM-based analysis . . . 63
4.2.2 Radial basis functions . . . 69
4.2.3 Optimization . . . 70
4.3 Numerical examples . . . 72
4.3.1 Numerical verification of the sensitivities . . . 73
4.3.2 Cantilever beam . . . 73
4.3.3 MBB beam . . . 76
4.3.4 3-D cantilever beam . . . 78
4.3.5 Heat sink . . . 80
4.4 Discussion . . . 83
4.4.1 Oscillations: the level set discretization . . . 83
4.4.2 Zigzagging: approximation error . . . 83
4.5 Summary and Conclusions . . . 85
4.6 Replication of results . . . 87
Appendix A: Derivation of IGFEM from X/GFEM . . . 87
Appendix B: Isoparametric mapping of integration elements . . . 88
Appendix C: Derivatives of the Jacobian inverse and determinant . . . 90

5 Topology Optimization of Phononic Crystals **93**
Abstract . . . 94
5.1 Introduction . . . 94
5.2 Computational analysis of phononic crystals . . . 96
5.2.1 Governing equation and formulation . . . 97
5.2.2 Boundary representations . . . 98
5.2.3 Enriched band structure analysis . . . 98
5.3 Comparison of boundary representations . . . 99
5.4 Optimization problem . . . 100
5.4.1 Sensitivity analysis . . . 102
5.5 Optimized phononic crystal designs . . . 103
5.5.1 Bandgap maximization in 2-D PnCs . . . 103
5.5.2 Bandgap maximization in 3-D PnCs . . . 106
5.6 Discussion and conclusions . . . 108
Appendix A: Objective scaling . . . 110
Appendix B: Sensitivity analysis . . . 111

6 Discussion and conclusions **113**
6.1 Smooth boundaries in phononic crystal design . . . 113
6.2 Boundary conditions in enriched formulations . . . 114
6.3 Topology optimization using IGFEM . . . 114
6.4 Related research . . . 116
6.5 Recommendations for future work . . . 116

References 119

Curriculum Vitæ 135

List of Publications 137

Acknowledgements 139

1

INTRODUCTION

1.1. PHONONIC CRYSTALS

Mechanical waves and vibrations play a significant role in many aspects of both everyday life and industries. From an environmental point of view, unwanted noise and vibrations have negative effects on human health and wildlife well-being. For instance, long-term exposure to whole-body vibration and hand-transmitted vibration gives rise to a range of disorders in humans (European Parliament Council of the European Union, 2002). Human-induced noise in the sea, such as noise induced by ships, drilling, and pile driving, has been found to affect the behavior of ocean life (Peng *et al.*, 2015). In industries, unwanted vibrations impair mechanical performance and precision, where the trend for miniaturization of features calls for ever-increasing demands on tolerances. Conversely, mechanical waves and vibration can be harnessed for many applications, for example, energy harvesting (Wei and Jing, 2017).

Consequently, the ability to block or otherwise influence these waves is of great importance. Phononic crystals (PnCs) provide such control by a periodic arrangement of materials; they may exhibit *bandgaps*, *i.e.*, ranges of frequencies which are attenuated due to Bragg scattering. The existence of bandgaps can occur on any length scale, and therefore, applications are found in thermal control (Davis and Hussein, 2014) by operating on extremely small wave lengths, using unit cells on the nanometer scale, all the way to seismic engineering (Witarto *et al.*, 2019; Yan *et al.*, 2015), where the unit cells are in the order of a meter. Other applications include, for instance, low vibration environments (Hussein *et al.*, 2014), and new sensing schemes for the characterization of sensitive chemicals and biological samples, where the liquid sample becomes part of a solid-liquid PnC (Lucklum *et al.*, 2021).

To achieve full command over the travelling waves, intuitive or trial-and-error-based approaches to design do not suffice. Instead, systematic design tools such as topology optimization (TO) (Bendsøe and Kikuchi, 1988) have been used to design periodic arrangements of materials for specific wave propagation properties. At the base of systematic design procedures is the numerical analysis method. For wave propagation through

periodic materials, a variety of modeling techniques is available (Yi and Youn, 2016), including the Boundary Element Method (BEM) (Isakari *et al.*, 2016; Li *et al.*, 2013a,b), Finite Differences - Time Domain (FDTD) (Su *et al.*, 2010; Tanaka *et al.*, 2000), Plane Wave Expansion (PWE) (Economou and Sigalas, 1993; Kushwaha *et al.*, 1994) and the Finite Element Method (FEM) (Veres *et al.*, 2013). Although all of these methods have their own advantages and disadvantages, FEM (see Section 1.2) is found to be advantageous for cases with complex geometries because irregular meshes may be used, and is often used in TO. Sigmund and Jensen (Sigmund and Jensen, 2003) were the first to use TO for the design of phononic crystals. Many works on the topology optimization of PnCs have been published since, the majority of which focus on the maximization of the absolute or relative bandgaps, exploiting symmetry of the periodic unit cells. However, in some works, improvements in the band gap width could be achieved by relaxing the symmetry conditions (Dong *et al.*, 2014; Gazonas *et al.*, 2006). Other objective functions, such as maximizing the spatial decay of evanescent waves (Chen *et al.*, 2017a), maximizing the wave attenuation in viscoelastic materials (Chen *et al.*, 2018), and self-collimation of elastic waves (Park *et al.*, 2015), have also been demonstrated. Reviews on the developments of TO of PnCs were written by Yi and Youn (2016) and by Li *et al.* (2019b).

1.2. DECOUPLING THE DESIGN FROM THE ANALYSIS MESH

The finite element method (FEM) has proven to be tremendously valuable for the numerical analysis of structural, thermal, electromagnetic, fluid and multi-physics problems. In FEM, the domain of interest is subdivided into smaller sections—finite elements—for which simple interpolation rules are used. The assembly of elements with simplified behavior can then accurately describe the behavior of the entire domain, provided a sufficiently large number of elements is used. Nevertheless, despite the many advantages of this method, there is a major drawback: a *discretization mesh* (*i.e.* the subdivision into elements) is needed that conforms to the problem's geometry. Creating such a *matching* (or *geometry-conforming*) mesh poses a challenge in optimization cases, where the location of the interface changes at every iteration, and consistent sensitivities should consider also the change in element shape.

In TO, this is commonly solved by creating a *structured* mesh and approximating the geometry by means of a density-based model. Each element in the discretization is assigned a density, which is used as a continuous design variable. This concept is illustrated in Figure 1.1a, where a circle is approximated by means of elemental densities (or gray values). These density values are used in TO as design variables, giving the optimizer the opportunity to distribute material freely in the design domain.

Despite the successful application of TO to PnCs and other problems, there are some downsides to the method. First of all, as the design variables are coupled directly to the mesh elements, the resulting designs are inevitably "staircased" or "pixelized", as is demonstrated in Figure 1.1. In this thesis it will be shown that this is detrimental for the accuracy of the analysis, especially for problems which are dominated by the boundaries, as is the case for Bragg scattering in PnCs. Refining the mesh partly alleviates the issue, but it increases computation time in both the analysis and the optimization, as the number of design variables is directly coupled to the number of elements in the mesh.

Furthermore, for PnCs, which are periodic, a periodic unit cell (PUC) is used. Such

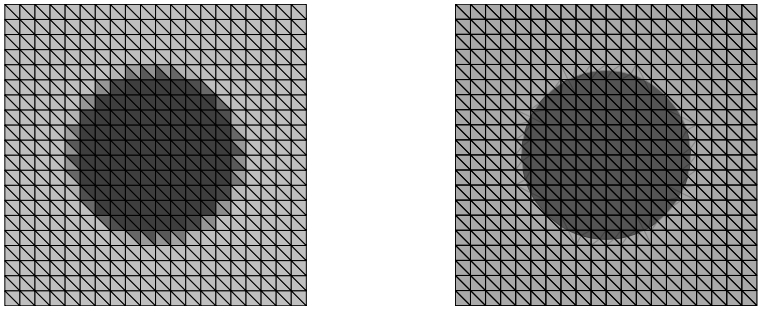

(a) (b)

Figuur 1.1: A density-based topology optimization representation of a circle, versus an enriched FEM representation. In (a), the geometry is approximated by a "staircased" description, where elements on the boundary of the circle are assigned an intermediate (gray) value that corresponds to the volume fraction of the element that lies within the circle; (b) uses an enriched finite element method to obtain a crisper representation of the circle, without intermediate material properties.

a PUC, describes a single geometry, that is tiled along its lattice vectors $\mathbf{a}_1$, $\mathbf{a}_2$ and $\mathbf{a}_3$ to create a periodic structure. Periodicity is then enforced by requiring the displacements at either side of the PUC to be equal, or, in cases with travelling waves, equal with a phase shift. The latter boundary conditions are known as Bloch-Floquet periodic boundary conditions. They determine that not only the geometry *within* the PUC is important, but also the shape of the PUC *itself*.

Enriched finite element methods can be used to mitigate these problems: through enrichment functions, they can model a *smooth* description of material interfaces, as shown in Figure 1.1. Boundaries may be defined explicitly as line sections, or implicitly using level sets. The latter are very suitable as an alternative design parametrization in TO. As such, they avoid problems with "staircased" or "pixelized" boundary representations. Furthermore, when used in an immersed setting, where the PUC is fully enclosed by the mesh, enriched FEM might be used to decouple the PUC shape from the discretization mesh. The Interface-enriched Generalized Finite Element Method (IGFEM) (Soghrati *et al.*, 2012a) is an enriched method that might be used to this extent. It differs from the more known the eXtended/Generalized Finite Element Method (X/GFEM) (Duarte *et al.*, 2001; Moës *et al.*, 1999) in that it places enrichments exclusively at locations on the discontinuity. This approach has many advantages, including the extension to an unified formulation for both weak and strong discontinuities—DE-FEM (Aragón and Simone, 2017), the possibility for hierarchical implementation HIFEM (Soghrati, 2014), and the use in an immersed setting (Cuba Ramos *et al.*, 2015). In this thesis, these methods will be referred to as discontinuity-enriched finite elements methods.

1.3. RESEARCH AIM AND SCOPE

The main research question in this work is formulated as:

How can a numerical analysis and design methodology be formulated
that provides accurate and computationally efficient results for phononic crystals?

In order to answer this question, in the subsequent chapters, the following questions will be answered:

- How can boundary conditions be prescribed on immersed edges using discontinuity-enriched analysis?
- How can this method be extended to Bloch-Floquet boundary conditions for the fully immersed analysis of phononic crystals?
- How can discontinuity-enriched analysis be used in a level set-based topology optimization setting?
- How can this optimization procedure be extended to the smooth design of phononic crystals?

1.4. MAIN CONTRIBUTIONS OF THIS THESIS

The main contributions of this thesis revolve around decoupling the design from the analysis mesh by means of the Interface-enriched Generalized Finite Element Method and Discontinuity-Enriched Finite Element method.

- **Immersed enriched finite element analysis:** This thesis demonstrates the use of discontinuity-enriched finite element methods as an immersed boundary method, where the physical domain is enclosed by a simple structured mesh. Material properties are only assigned to the physical parts of the domain, and elements that lie completely outside of the physical domain are removed from the analysis. It is shown that it is straightforward to impose boundary conditions in discontinuity-enriched finite element methods. To the best of the author's knowledge, the paper on which Chapter 2 is based was the first work where essential (Dirichlet) boundary conditions could be applied to non-matching edges in a strong manner. Not only does this significantly simplify the use of the method, it also ensures that reaction forces on non-matching edges can be recovered accurately. Furthermore, the Bloch-Floquet periodic boundary conditions, that are used for the analysis of phononic crystals in Chapter 3, can be applied in a similar manner.
- **Levelset-based topology optimization using IGFEM:** This thesis shows the first level set-based topology optimization using the Interface-enriched Generalized Finite Element Method for analysis. This combination required special treatment of sensitivities, which are required for updating the design. The computation of these sensitivities is first developed for compliance minimization problems. The formulation is then applied to phononic crystals.

1.5. THESIS OUTLINE

This thesis presents three research chapters that have been published as journal papers, one research chapter that will be submitted for publication, and one concluding chapter. The first two research chapters are about immersed *analysis*, and were a prerequisite for the two *optimization* chapters that follow. A visual overview of the thesis outline is found in Figure 1.2.

Chapter 2 presents an enriched formulation for immersed finite element analysis. This formulation allows for the *strong* enforcement of essential (Dirichlet) boundary conditions on edges that are non-matching to the discretization mesh. The method is demonstrated to be stable and optimally convergent, by means of a number of numerical examples. Moreover, it demonstrated that smooth reaction fields can be recovered.

Chapter 3 extends the method that was introduced in Chapter 2 to the analysis of immersed periodic unit cell of phononic crystals. To that end, Bloch-Floquet boundary conditions are *strongly* prescribed on non-matching edges, similar to the Dirichlet boundary conditions in Chapter 2 The proposed approach is studied for analyzing phononic crystals in 1-D, 2-D, and 3-D. It shows that both the phononic crystal geometry and periodicity can be modified without changing the underlying discretization.

Chapter 4 introduces a level set-based topology optimization framework using IGFEM analysis and Radial Basis Functions (RBFs). The sensitivities are derived analytically. This chapter demonstrates the use of the topology optimization procedure for minimum compliance in 2-D and 3-D, and for the optimization of a heat sink.

In Chapter 5, the importance of using smooth boundaries for the computational design of phononic crystals is demonstrated. Furthermore, the topology optimization procedure introduced in Chapter 4 is adapted to optimize PnCs. The computation of the sensitivities for bandgap maximization are derived and the final designs are evaluated.

Chapter 6 contains a discussion and conclusions on DE-FEM as an immersed method for the analysis and design of phononic crystals. Furthermore, recommendations for future work are given.

1

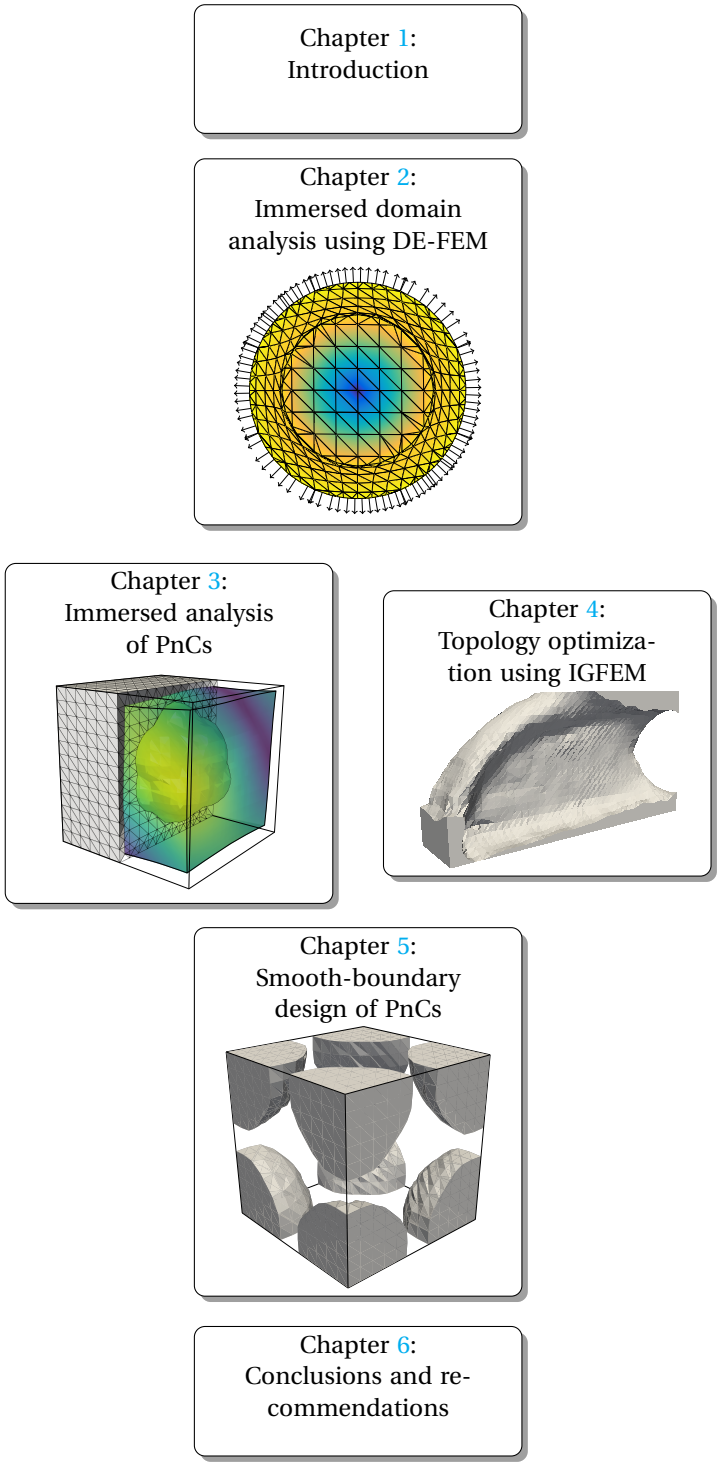

Figuur 1.2: Visual overview of the thesis outline. Chapter 2 establishes IGFEM/DE-FEM as an immersed method. In Chapter 3 this method is extended to PnCs, and in Chapter 4 a topology optimization approach is described. Chapter 5 combines this work into the optimization of PnCs.

2

An Interface-enriched Finite Element Method for Immersed Problems

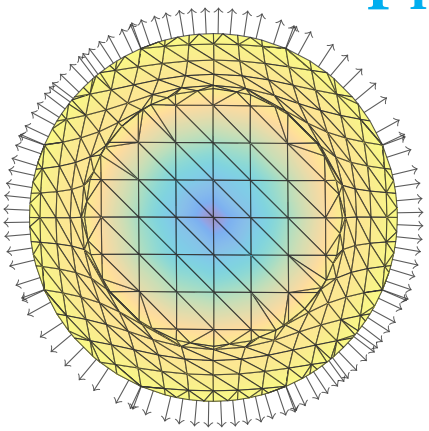

In order to fully decouple the analysis mesh from the design of phononic crystals using IGFEM, it has to be used in an immersed setting. In this chapter, IGFEM and DE-FEM are introduced as immersed domain methods. A formulation is derived in Section 2.2.2 for the *strong* enforcement of Dirichlet boundary conditions on edges that are non-matching to the discretization mesh. Numerical examples are provided in section 2.3 that demonstrate that the method is stable and optimally convergent.

This chapter has been published in
International Journal for Numerical Methods in Engineering
2019 (120) 1163 – 1183

2

A Stable Interface-Enriched Formulation for Immersed Domains with Strong Enforcement of Essential Boundary Conditions

Abstract *Generating matching meshes for finite element analysis is not always a convenient choice, for instance in cases where the location of the boundary is not known a priori or when the boundary has a complex shape. In such cases, enriched finite element methods can be used to describe the geometric features independently from the mesh. The Discontinuity Enriched Finite Element Method (DE-FEM) was recently proposed for solving problems with both weak and strong discontinuities within the computational domain. In this paper we extend DE-FEM to treat fictitious domain problems, where the mesh-independent boundaries might either describe a discontinuity within the object, or the boundary of the object itself. These boundaries might be given by an explicit expression or an implicit level set. We demonstrate the main assets of DE-FEM as an immersed method by means of a number of numerical examples; we show the method is not only stable and optimally convergent, but most importantly, that essential boundary conditions can be prescribed strongly.*

2.1. INTRODUCTION

Immersed boundary techniques eliminate the need for intricate meshing algorithms by decoupling the external boundary description from the discretization mesh. In this paper we introduce a novel method for immersed problems, where enrichments to the finite element approximation are associated to locations on the immersed boundary. This facilitates the strong enforcement of essential boundary conditions on non-matching edges, which was not possible in immersed methods until now.

The Finite Element Method (FEM) is a well-established numerical procedure for the analysis of a wide range of problems in physics and engineering. It requires a discretization mesh whose elements align with the domain's external boundaries and internal interfaces. However, for problems with complex geometries, creating a good-quality *matching* or *geometry-conforming* mesh is a demanding procedure, where admissible element aspect ratios have to be guaranteed. The burden of meshing increases even further in cases where the domain boundaries are changing in subsequent analyses, as is the case in optimization procedures. Local mesh-adaption techniques (Auricchio *et al.*, 2015; Basting and Weismann, 2014; Frei and Richter, 2014; Gangl and Langer, 2018) such as Universal Meshes (Rangarajan and Lew, 2014) and the Conforming to Interface Structured Adaptive Mesh Refinement (CISAMR) (Nagarajan and Soghrati, 2018; Sog-

hrati *et al.*, 2017) have been proposed to account for changing boundaries. These methods ensure elements with proper aspect ratio are created. Alternatively, immersed boundary methods alleviate the burden of remeshing by describing the external boundaries independently from a usually structured discretization mesh (Hansbo and Hansbo, 2002; Parvizian *et al.*, 2007), which is less sensitive to aspect ratio. In doing so, part of the complexity is merely shifted from the mesh generation to the integration scheme and mesh interactions. This shift is reasonable in cases where mesh generation is cumbersome, such as for complex-shaped problem domains (Heinze *et al.*, 2015) and for moving interfaces during optimization (Villanueva and Maute, 2017).

A number of immersed boundary techniques have been proposed which deal with *external* boundaries independently from the mesh. In the unfitted finite element method, first introduced by Barrett and Elliot (1987) and later improved by Hansbo and Hansbo (2002), the basis functions in the intersected elements are restricted to the respective integration domains, resulting in a doubling of the number of basis functions in intersected elements. This method was developed further into the Cut Finite Element Method (CutFEM) (Burman and Hansbo, 2010, 2012; Burman *et al.*, 2015) by adding ghost penalty terms to improve the condition number of the resulting matrices. CutFEM has been studied in the context of both solid (Burman *et al.*, 2015, 2018) and fluid mechanics (Villanueva and Maute, 2017), and has recently been applied to the topology optimization of flow problems (Villanueva and Maute, 2017). The Finite Cell Method (FCM) (Düster *et al.*, 2008; Parvizian *et al.*, 2007) is a fictitious domain procedure based on the p–version of the finite element method (p–FEM) where the field variables extend smoothly outside the physical domain. FCM has also been used in topology optimization (Parvizian and Rank, 2012), and has been extended to handle NURBS-based geometries (Ruess *et al.*, 2013; Schillinger *et al.*, 2012). While all of these methods undoubtedly allow greater flexibility by decoupling the discretization from the problem's geometric features, one of the core challenges remains prescribing essential (Dirichlet) boundary conditions. To the best of our knowledge, in the existing immersed boundary methods there is currently no way to *strongly* prescribe essentialm boundary conditions to a non-matching element side. Instead, several methods have been proposed to weakly impose essential boundary conditions, such as utilizing Lagrange multipliers (Burman and Hansbo, 2010; Glowinski *et al.*, 1994; Tur *et al.*, 2014) or employing Nitsche's method (Burman and Hansbo, 2012; Hansbo, 2005). Natural (Neumann) boundary conditions, on the other hand, do not pose generally much of an issue, as the only requirement is a means to integrate them accurately over the immersed boundary.

In parallel, the mesh-independent analysis of discontinuities that are *internal* to the domain has become established practice in enriched methods such as the eXtended/Generalized FEM (X/GFEM) (Aragón *et al.*, 2010; Belytschko *et al.*, 2009; Duarte *et al.*, 2001; Fries, 2008; Moës *et al.*, 1999, 2003), which originated from partition of unity methods (Babuška and Melenk, 1997; Melenk and Babuška, 1996). They provide an elegant solution to handling *strong* or *weak* discontinuities, referring to whether the discontinuity is present in the field itself (*e.g.*, a crack) or in its gradient (*e.g.*, a material interface), respectively. When modeling discontinuities with X/GFEM, the standard finite element approximation is augmented by enrichment functions that incorporate the desired behavior otherwise missing by the use of a non-matching mesh—in this case the

jump in the field and/or its gradient. It has been shown that this method outperforms the standard FEM in situations where changing topologies are involved, such as solidification problems (Chessa *et al.*, 2002), fluid-structure-contact-interaction problems (Mayer *et al.*, 2010), and topology optimization (van Dijk *et al.*, 2013; Villanueva and Maute, 2014). However, X/GFEM comes with its own set of challenges, such as the need for choosing appropriate enrichment functions that do not degrade accuracy (Fries, 2008) and the need for special formulations for prescribing interface conditions and essential boundary conditions (Babuška *et al.*, 2003). More recently, research efforts have focused on obtaining stable formulations through Stable Generalized Finite Element Methods (SGFEM) to address issues inherent to the formulation that result in ill-conditioned matrices (Babuška and Banerjee, 2012; Gupta *et al.*, 2013; Kergrene *et al.*, 2016). X/GFEM has been studied in the context of immersed domain problems. However, as explained in Cuba Ramos *et al.* (2015), it suffers from *boundary locking* as the Lagrange multiplier space overconstrains the problem.

The Interface Enriched Generalized Finite Element Method (IGFEM) (Soghrati *et al.*, 2012a) was introduced as a particular type of enriched FEM for the mesh-independent modeling of weak discontinuities(Aragón *et al.*, 2013; Soghrati, 2014; Soghrati and Geubelle, 2012). It differs from X/GFEM in that it places the enrichments exclusively on nodes collocated along discontinuities, instead of associating them to nodes of the original mesh. This significantly simplifies implementation, as enrichment functions are straightforward to construct by using Lagrange shape functions of *integration elements*, *i.e.*, subdomains created for the purpose of integrating the element local stiffness matrix and force vector. IGFEM, which converges optimally with mesh refinement (Soghrati and Geubelle, 2012; Soghrati *et al.*, 2012a), has been demonstrated successfully in the modeling of fibre-reinforced composites (Soghrati and Geubelle, 2012), the multi-scale damage evolution in heterogeneous adhesives (Aragón *et al.*, 2013), and microvascular materials with active cooling (Soghrati and Geubelle, 2012; Soghrati *et al.*, 2012a,b). Multiple interfaces crossing a single element can be resolved recursively by using a hierarchical implementation of IGFEM called the Hierarchical Interface-enriched Finite Element Method (HIFEM) (Soghrati, 2014). This makes it straightforward to analyze interfaces that are very close together, or even n-junctions, where n interfaces meet at a single point inside an element, allowing for crack branching in arbitrary locations, and for the analysis of cracks in composite materials. However, special treatment is required at crack tips to achieve optimal convergence. IGFEM has also been used in combination with adaptive meshing (Soghrati *et al.*, 2015), with NURBS interfaces (Tan *et al.*, 2015), and in an optimization setting (Najafi *et al.*, 2015; Tan and Geubelle, 2017). Cuba Ramos *et al.* (2015) demonstrated IGFEM as an immersed boundary method, by using Lagrange multipliers to weakly impose Dirichlet boundary conditions on IGFEM edges. More recently, Aragón and Simone (2017) introduced the Discontinuity Enriched Finite Element Method (DE-FEM) as a generalization of IGFEM to treat both weak and strong discontinuities with a unified formulation. In addition to the flexibility of dealing with both discontinuity types, DE-FEM inherits all of the virtues of IGFEM/HIFEM:

- The construction of *both* weak and strong enrichment functions is straightforward, as they are based on the standard Lagrange shape functions of integration elements;

- Because enrichment functions vanish at original mesh nodes, the Kronecker-delta property is maintained in standard nodes, allowing essential boundary condition to be applied in the same way as in standard FEM;
- With the use of a diagonal preconditioner, or a proper scaling factor for the enrichment functions (Aragón *et al.*, 2020), the formulation used for treating weak discontinuities is stable, *i.e.*, the conditioning number increases at the same rate as that of standard FEM under mesh refinement;
- A hierarchical implementation of DE-FEM can analyze multiple discontinuities and n-junctions within a single element. Cracks and interfaces are allowed to intersect each other as well.

In this paper, we place IGFEM, HIFEM, and DE-FEM in the context of *immersed* problems, using a strong enforcement of essential boundary conditions based on multiple point constraints. In the absence of strong discontinuities, the DE-FEM formulation simplifies to that of IGFEM/HIFEM. As external boundaries are weak discontinuities, the method for imposing Dirichlet BCs holds for IGFEM, HIFEM, and DE-FEM alike. We demonstrate the versatility of DE-FEM by means of an immersed-discontinuous patch test that includes a material interface and a crack, within just one element. Convergence of immersed IGFEM is demonstrated by means of the Eshelby inclusion problem. An example with a slightly rotated background mesh is used to demonstrate the stability of the method. Lastly, it is shown that the method is capable of dealing with complex 3-D geometries by means of immersing an intricate level set function within the volumetric mesh. Summarizing, the main novelties in this paper are:

- The use of DE-FEM as an immersed boundary method, where a material is only assigned to the physical parts of the domain. We include cracks and material interfaces in the immersed problems as well.
- To the best of the authors' knowledge, this is the first immersed method where Dirichlet boundary conditions can be applied on non-matching boundaries in a strong manner, by means of multiple point constraints.

2.2. DE-FEM AS AN IMMERSED METHOD

2.2.1. DISCRETIZATION

Consider a solid body, represented by an open domain $\Omega \in \mathbb{R}^d$ referenced by a Cartesian coordinate system spanned by $\{\boldsymbol{e}_i\}_{i=1..d}$, as shown in Figure 2.1. The body is composed by matrix and inclusion materials, denoted as Ω_m and Ω_i, respectively, such that the domain closure, denoted by an overbar, is defined as $\overline{\Omega} = \overline{\Omega}_\mathrm{m} \cup \overline{\Omega}_\mathrm{i}$ and $\Omega_\mathrm{m} \cap \Omega_\mathrm{i} = \emptyset$. The boundary of the domain $\partial\Omega \equiv \Gamma = \overline{\Omega} \setminus \Omega$, with outward unit normal $\boldsymbol{n}$, is composed by disjoint lower-dimensional manifolds Γ_u and Γ_t, such that $\overline{\Gamma} = \overline{\Gamma}_\mathrm{u} \cup \overline{\Gamma}_\mathrm{t}$ and $\Gamma_\mathrm{u} \cap \Gamma_\mathrm{t} = \emptyset$. We assume $\Gamma_\mathrm{u} \neq \emptyset$ is the region where essential (Dirichlet) boundary conditions are prescribed. Similarly, Γ_t is the region with prescribed natural (Neumann) boundary conditions. The figure also shows a traction-free crack $\Gamma_\mathrm{c} \subseteq \Gamma_\mathrm{t}$ that interacts with both materials, and might also coincide with the material interface Γ_i. The crack is parameterized by the

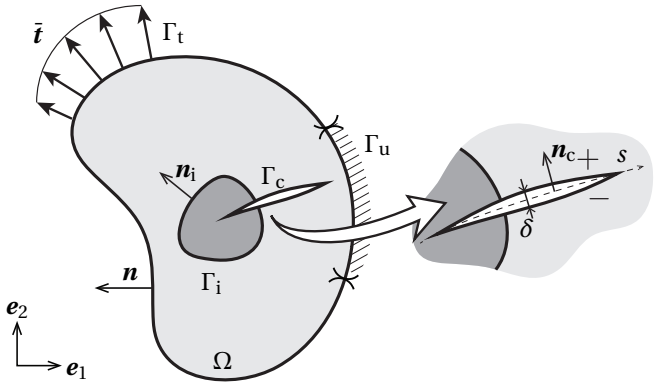

Figuur 2.1: Mathematical representation of a cracked solid composed by materials Ω_m and Ω_i, which represent the matrix and an inclusion, respectively. A crack Γ_c is also illustrated interacting with both faces. The schematic shows a problem containing both weak and strong discontinuities.

curve s, which also serves to define the orientation of the crack in space so that a unique normal $\boldsymbol{n}_c$ can be defined. The normal vector field is also used to identify two regions in the immediate vicinity of the crack, shown in the figure with positive (+) and negative (-) symbols. Thus, two points that coincide in space but are situated at each side of the crack are separated after deformation by a distance $\boldsymbol{\delta}$, which denotes the displacement jump as a function of a local coordinate s through the crack centerline.

The setting just described corresponds to that of a solid that contains both weak and strong discontinuities. The weak discontinuity results from the mismatch in material properties between the matrix and the inclusion, while the strong discontinuity arises from the crack. In this work, we restrict ourselves to traction-free cracks, but extension to cohesive or pressure-loaded cracks is straightforward. For simplicity the graphical representation of the problem shows a single inclusion and a single crack, but the generalization to multiple inclusions and cracks is straightforward as well. We are interested in solving the linear elastostatics problem on Ω. We denote the displacement field $\boldsymbol{u}$ in the matrix (Ω_m) and inclusion (Ω_i) by $\boldsymbol{u}_m$ and $\boldsymbol{u}_i$, respectively, *i.e.*, $\boldsymbol{u}_j \equiv \boldsymbol{u}|_{\Omega_j}$, $j = m,i$. Given the prescribed displacement $\bar{\boldsymbol{u}}_j : \Gamma_{u,j} \equiv \Gamma_u \cap \Gamma_j \to \mathbb{R}^d$ and traction $\bar{\boldsymbol{t}}_j : \Gamma_{t,j} \to \mathbb{R}^d$ fields, and the body force $\boldsymbol{b}_j : \Omega_j \to \mathbb{R}^d$, the strong form of the boundary value problem is: Find $\boldsymbol{u}$ such that

$$\nabla \cdot \boldsymbol{\sigma}_j + \boldsymbol{b}_j = \boldsymbol{0} \qquad \text{in } \Omega_j, \tag{2.1}$$

$$\boldsymbol{u}_j = \bar{\boldsymbol{u}} \qquad \text{on } \Gamma_{u,j}, \tag{2.2}$$

$$\boldsymbol{t}_j = \bar{\boldsymbol{t}} \qquad \text{on } \Gamma_{t,j}, \tag{2.3}$$

with interface conditions

$$\boldsymbol{u}_m = \boldsymbol{u}_i \qquad \text{on } \Gamma_i = \overline{\Omega}_m \cap \overline{\Omega}_i, \tag{2.4}$$

$$\boldsymbol{\sigma}_m \cdot \boldsymbol{n}_i = \boldsymbol{\sigma}_i \cdot \boldsymbol{n}_i \qquad \text{on } \Gamma_i, \tag{2.5}$$

and constitutive and continuity relation

$$\boldsymbol{\sigma} = \lambda \operatorname{tr}(\boldsymbol{\varepsilon})\,\boldsymbol{\varepsilon} + 2\mu\boldsymbol{\varepsilon}, \tag{2.6}$$

$$\boldsymbol{\varepsilon} = \frac{1}{2}\left(\nabla\boldsymbol{u} + \nabla\boldsymbol{u}^{\intercal}\right). \tag{2.7}$$

In Equation (2.1), $\nabla\cdot$ denotes the divergence operator and $\boldsymbol{\sigma}_j : \Omega_j \to \mathbb{R}^d \times \mathbb{R}^d$ is the second-order stress tensor that follows Hooke's law for isotropic linear elastic materials, which can be fully characterized by the Lamé parameters λ and μ.

Let $\mathcal{V}(\Omega) \equiv [\mathcal{V}(\Omega)]^d$ be a vector-valued function space on Ω, where each vector component of $\boldsymbol{v} \in \mathcal{V}$ belongs to the first-order Sobolev function space $H^1(\Omega)$. Similarly, let $\mathcal{V}_0(\Omega) \subset \mathcal{V}$ be the subset that satisfies homogeneous boundary conditions on Γ_u. To deal with non-homogeneous boundary conditions, we define the linear variety $\mathcal{V}^\star = \tilde{\boldsymbol{u}} + \mathcal{V}_0$ as a translation of $\mathcal{V}_0$ by the vector-valued function $\tilde{\boldsymbol{u}} : \tilde{u}_i \in H^1(\Omega)$, $\tilde{\boldsymbol{u}}|_{\Gamma_\mathrm{u}} = \bar{\boldsymbol{u}}$, *i.e.*, every element of $\mathcal{V}^\star$ satisfies the non-homogeneous essential boundary condition.

The weak formulation is: Find $\boldsymbol{u} \in \mathcal{V}^\star$ such that

$$B(\boldsymbol{u}, \boldsymbol{v}) = L(\boldsymbol{v}), \qquad \forall\, \boldsymbol{v} \in \mathcal{V}_0, \tag{2.8}$$

or equivalently: Find $\boldsymbol{u} \in \mathcal{V}_0$ such that $B(\boldsymbol{u}, \boldsymbol{v}) = L(\boldsymbol{v}) - B(\tilde{\boldsymbol{u}}, \boldsymbol{v})$, $\forall\, \boldsymbol{v} \in \mathcal{V}_0$. The linear and bilinear forms are given by

$$L(\boldsymbol{v}) = \sum_{j=\mathrm{m,i}} \int_{\Omega_j} \boldsymbol{v}_j \cdot \boldsymbol{b}_j \,\mathrm{d}\Omega + \int_{\Gamma_\mathrm{t}} \boldsymbol{v}_\mathrm{i} \cdot \bar{\boldsymbol{t}} \,\mathrm{d}\Omega \tag{2.9}$$

and

$$B(\boldsymbol{u}, \boldsymbol{v}) = \sum_{j=\mathrm{m,i}} \int_{\Omega_j} \boldsymbol{\sigma}_j(\boldsymbol{u}_j) : \boldsymbol{\varepsilon}_j(\boldsymbol{v}_j) \,\mathrm{d}\Omega. \tag{2.10}$$

For solving the problem we choose a domain $\Delta \subset \mathbb{R}^d$ that fully encloses our original problem domain ($\Delta \supseteq \Omega$), as illustrated in Figure 2.2a. This *hold-all domain* is discretized by finite elements so that $\Delta^h = \operatorname{int}\left(\bigcup_i \overline{e}_i\right)$, where e_i is the ith element and $e_i \cap e_j = \emptyset$, $\forall\, i \neq j$. An interaction between the discretization Δ^h and the problem's geometric features (boundary, interfaces, and/or cracks) then takes place, resulting in *new nodes*, created at the intersection of the discontinuities with the edges of elements in the discretization. Similarly, intersected—or cut—elements are divided into subdomains (called *integration elements*), which are added to a hierarchical data structure. For instance, Figure 2.2a shows an element e_i that is traversed by the interface Γ_i and the crack Γ_c. First, this *background element* e_i is split into three integration elements ($e_i^{(1)}, i = 1,2,3$) according to the crack Γ_c. Integration element $e_1^{(1)}$ is in turn split into three integration elements ($e_i^{(2)}, i = 1,2,3$). The resulting hierarchy is shown in Figure 2.2b. The new discretization containing new nodes and the element hierarchy will be denoted henceforth as Δ_H^h. Despite their name, integration elements are used for more than just integration. In fact, the purpose of these integration elements is fourfold: *i)* they are used for integration of the element matrices; *ii)* enrichment functions are constructed as linear combinations of their standard Lagrange shape functions; *iii)* they

2

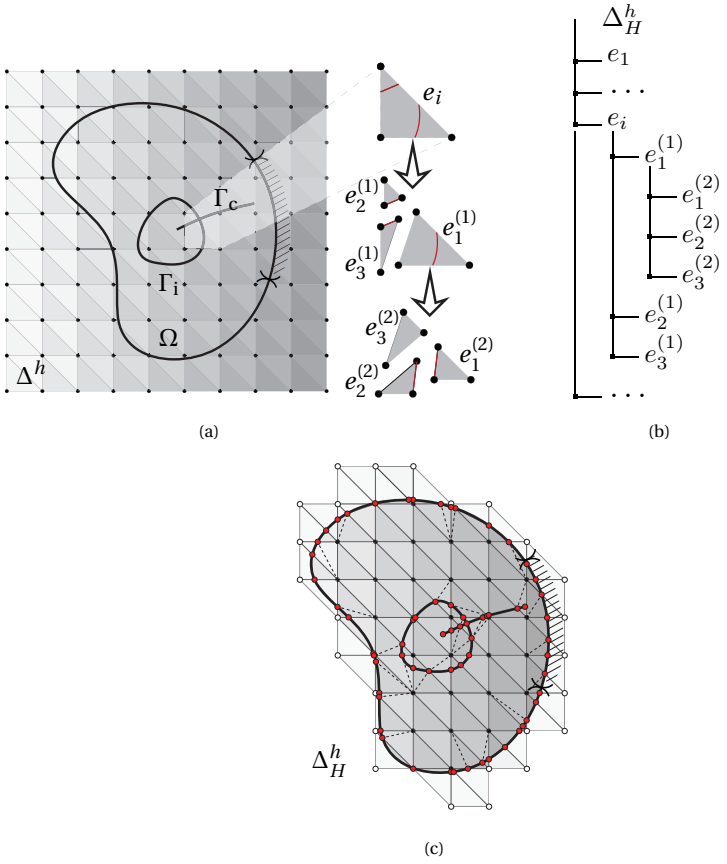

Figuur 2.2: Schematic representation of the mesh interaction: (a) the original mesh is hierarchically interacted with the discontinuities, (b) integration elements are stored in a tree structure, (c) new nodes and integration elements are added to the discretization.

ensure that the enrichment functions are smooth, and can thus be integrated with the least number of Gauss points; and *iv)* they are used to ensure the field can be displayed correctly after postprocessing.

The finite-dimensional form of Equation (2.8) is then solved on Δ_H^h by choosing our trial solution $\boldsymbol{u}^h$ and our weight function $\boldsymbol{w}^h$ from the Discontinuity-Enriched Finite Element space

$$\mathcal{V}^h = \left\{ \boldsymbol{v}^h : \boldsymbol{v}^h = \underbrace{\sum_{i\in\iota_h} N_i(\boldsymbol{x})\,\boldsymbol{U}_i}_{\text{std. FEM}} + \underbrace{\overbrace{\sum_{i\in\iota_w} \psi_i(\boldsymbol{x})\,\boldsymbol{\alpha}_i}^{\text{weak}} + \overbrace{\sum_{i\in\iota_s} \chi_i(\boldsymbol{x})\boldsymbol{\beta}_i}^{\text{strong}}}_{\text{enriched}}, \quad \boldsymbol{U}_i, \boldsymbol{\alpha}_i, \boldsymbol{\beta}_i \in \mathbb{R}^d \right\} \subset \mathcal{V}. \tag{2.11}$$

In Equation (2.11), ι_h represents the index set of all nodes in Δ_H^h from the original discretization (shown in Figure 2.2c with ○ and ● symbols for the degrees of freedom (DOFs) outside and inside the domain, respectively). Similarly, ι_w and ι_s denote index sets of weak and strong enriched nodes, respectively, which are the result of the aforementioned interactions with the background mesh (shown with ● and ● symbols in Figure 2.2c, respectively). The first term in (2.11) corresponds to the standard FEM part, where N_i and $\boldsymbol{U}_i$ are the Lagrange shape functions and DOF vector, respectively, associated with the ith mesh node. The standard FEM space is augmented by enrichment functions. The result is an enriched space that is spanned by enrichment functions that contain the kinematic description of the discontinuities. In the approximation, ψ_i (χ_i) are the enrichment functions that reproduces the weak (strong) discontinuity with associated enriched DOF vector $\boldsymbol{\alpha}_i$ ($\boldsymbol{\beta}_i$). Notice that if Δ^h is a linear triangulation, then $\boldsymbol{v}^h\big|_e \in [P_1(e)]^d$, $\forall e \in \Delta_H^h$, where P_1 represents the space of first-order polynomials on e.

As previously stated, DE-FEM is a particularly versatile method which allows arbitrary configurations of interfaces, domain boundaries, and cracks. Any number of interfaces and domain boundaries are allowed to come arbitrarily close to one another, and intersections of domain boundaries with cracks are allowed. As a result, an element $e_i \in \Delta_H^h$ can be intersected by an arbitrary number of discontinuities. The method has this advantage by virtue of the hierarchical construction of the shape functions in elements split by multiple interfaces, as illustrated earlier in Figure 2.2a, and in Figure 2.3. Here, we follow the work of Soghrati (2014) for the hierarchical construction of enrichment functions. At the element level, the approximate solution $\boldsymbol{u}^h \in \mathcal{V}^h$ can be written as

$$\boldsymbol{u}^h(\boldsymbol{x}) = \sum_{i\in\iota_h} N_i(\boldsymbol{x})\,\boldsymbol{U}_i + \sum_{k\in h}\sum_{i\in\iota_w} \psi_{ki}(\boldsymbol{x})\,\boldsymbol{\alpha}_{ki} + \sum_{k\in h_s}\sum_{i\in\iota_s} \chi_{ki}(\boldsymbol{x})\boldsymbol{\beta}_{ki}, \tag{2.12}$$

where $h \equiv \mathbb{Z}^+ = \{1, 2, \ldots, D\}$ is the index set of hierarchical levels resulting from D discontinuities that interact with the element, and $h_s \subseteq h$ represents the subset associated with strong discontinuities—since strong DOFs are not present in weak discontinuities. Note that an element intersected by D discontinuities will have D levels of hierarchy in the ordered tree. Because enrichment functions are constructed with the aid of Lagrange shape functions in integration elements, these functions are non-zero only in the domain of the cut element by construction; the functions attain their maximum absolute value at the location of the enriched node, and ramp linearly to zero at nodes of cut ele-

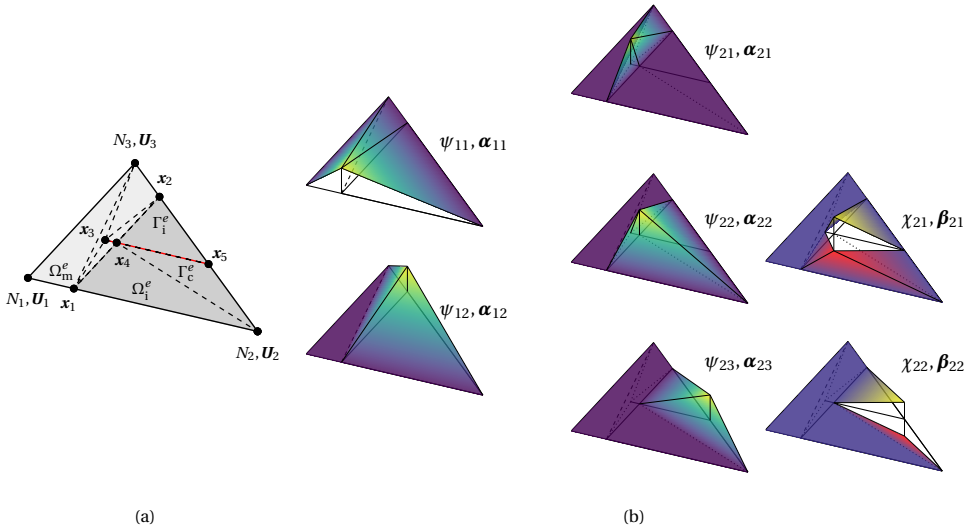

Figuur 2.3: Hierarchical splitting of an element crossed by a material interface (Γ_{i}^e), defined by element subdomains Ω_{i}^e and Ω_{m}^e, and a crack Γ_{c} (shown in red). The hierarchical construction of the corresponding enrichment functions ψ_{ki} and χ_{ki} is illustrated. Observe that all enrichment functions can be written as linear combinations of Lagrangian shape functions of the integration elements. Also, note that there is no strong enrichment function associated with the crack tip.

ment. The procedure for constructing hierarchical shape functions for both weak and strong enrichments is outlined in Figure 2.3.

The numerical quadrature of every integration element $e_i \in \Delta_H^h$ is conducted hierarchically in order to obtain the local stiffness matrix $\boldsymbol{k}_i$ and force vector $\boldsymbol{f}_i$ as

$$\boldsymbol{k}_e = \int_{\Omega_i} \begin{bmatrix} \mathrm{d}\boldsymbol{N} \\ \mathrm{d}\boldsymbol{\psi} \\ \mathrm{d}\boldsymbol{\chi} \end{bmatrix} \boldsymbol{C} \begin{bmatrix} \mathrm{d}\boldsymbol{N} & \mathrm{d}\boldsymbol{\psi} & \mathrm{d}\boldsymbol{\chi} \end{bmatrix} \mathrm{d}\Omega, \qquad \boldsymbol{f}_e = \int_{\Gamma_{\mathrm{t}}} \begin{bmatrix} \mathrm{d}\boldsymbol{N} \\ \mathrm{d}\boldsymbol{\psi} \\ \mathrm{d}\boldsymbol{\chi} \end{bmatrix} \bar{\boldsymbol{t}} \, \mathrm{d}\Gamma, \tag{2.13}$$

where $\boldsymbol{C}$ is the constitutive matrix. In the Appendix, pseudo-code is given for the computer implementation, where the traversal over the hierarchy is executed in a loop. Subsequently, following standard procedures, the discrete system of linear equations $\boldsymbol{K}\boldsymbol{U} = \boldsymbol{F}$ is obtained, where

$$\boldsymbol{K} = \mathop{\mathbb{A}}_{i} \boldsymbol{k}_i, \qquad \boldsymbol{F} = \mathop{\mathbb{A}}_{i} \boldsymbol{f}_i, \tag{2.14}$$

and $\mathbb{A}$ denotes the standard finite element assembly operator.

An important issue in immersed boundary methods is the ill-conditioning of the resulting system matrices, which can hinder obtaining a solution. Immersed methods suffer from conditioning issues due to nearly-zero contributions to the system matrix, originating from intersected elements with low volume fractions belonging to the physical domain. Several strategies have been proposed to prevent ill-conditioning in immersed methods. A possible solution is to add an artificial stiffness to the fictitious part of the

domain. However, adding stiffness to void regions modifies the problem at hand, and it is not straightforward to strike a balance between stability and accuracy. Another option is to modify the FE function space; one could either simply remove all basis functions that deteriorate the condition number, or scale the FE basis functions. Lastly, a preconditioner could be employed to improve the condition number of system matrices. In this work we use a diagonal preconditioner to avoid ill-conditioning. We also choose to remove all DOFs belonging to nodes in void areas from the system matrices, while setting the material properties in the void regions to zero. However, an optimal scaling for enrichment functions, which is a function of the geometric properties of the intersection and the material properties on each side of the interface, was proposed recently and could be used instead of the preconditioner (Aragón *et al.*, 2020).

2.2.2. TREATMENT OF BOUNDARY CONDITIONS

An important issue in immersed methods relates to prescribing boundary conditions on the non-matching boundaries Γ_u and Γ_t, which may coincide with the interface Γ_i and crack Γ_c. In immersed methods, in general, it is not straightforward to apply boundary conditions on these edges, as no degrees of freedom are explicitly related to the boundaries. Consequently, boundary conditions have to be imposed in a weak manner. In DE-FEM, on the contrary, prescribing boundary conditions is straightforward due to the fact that enrichment functions vanish at nodes of the background mesh, and that their associated enriched nodes are collocated exclusively along discontinuities. In fact, in DE-FEM it is possible to impose Dirichlet conditions in a strong manner by solving local problems, which is a distinctive asset that gives DE-FEM an advantage over other immersed domain methods.

DIRICHLET BOUNDARY CONDITIONS

We first start our discussion on prescribing essential boundary conditions on enriched nodes placed along the immersed boundary—which is a weak discontinuity described by weak enriched DOFs alone. By denoting $\boldsymbol{x}_\alpha$ the spatial coordinate of an enriched node associated with DOFs $\boldsymbol{\alpha}_{kj}$, we simply solve for the latter using (2.12) since $\boldsymbol{u}^h(\boldsymbol{x}_\alpha) = \bar{\boldsymbol{u}}(\boldsymbol{x}_\alpha)$:

$$\boldsymbol{\alpha}_{kj} = \frac{1}{\psi_{kj}} \left[\bar{\boldsymbol{u}}(\boldsymbol{x}_\alpha) - \sum_{i \in \iota_h} N_i(\boldsymbol{x}_\alpha) \boldsymbol{U}_i - \sum_{n \in h, n<k} \sum_{i \in \iota_w, i \neq j} \psi_{ni}(\boldsymbol{x}_\alpha) \boldsymbol{\alpha}_{ni} - \sum_{n \in h, n<k} \sum_{i \in \iota_s} \chi_{ni}\left(\boldsymbol{x}_{\alpha_j}\right) \boldsymbol{\beta}_{ni} \right]. \tag{2.15}$$

Note that, only the enrichment functions that are non-zero at $\boldsymbol{x}_\alpha$ need to be taken into account. In practice, this means that only the higher levels of hierarchy ($n < k$) need to be considered. Equation (2.15) can be used to find the value $\boldsymbol{\alpha}_{kj}$ for all prescribed nodes, as a function of $\boldsymbol{U}_i, \boldsymbol{\alpha}_{ni}$ and $\boldsymbol{\beta}_{ni}$. The resulting system of equations can subsequently be written in the form of a multiple point constraint (MPC):

$$\begin{bmatrix} \boldsymbol{U} \\ \boldsymbol{\alpha} \\ \boldsymbol{\beta} \end{bmatrix} = \boldsymbol{T} \begin{bmatrix} \tilde{\boldsymbol{U}} \\ \tilde{\boldsymbol{\alpha}} \\ \tilde{\boldsymbol{\beta}} \end{bmatrix} + \boldsymbol{g}, \tag{2.16}$$

where the vector $\begin{bmatrix} \tilde{\boldsymbol{U}} & \tilde{\boldsymbol{\alpha}} & \tilde{\boldsymbol{\beta}} \end{bmatrix}^\intercal$ contains only the remaining non-prescribed DOFs. The matrix $\boldsymbol{T}$ contains the contributions of other nodes, both original and enriched, to the

prescribed DOFs. The vector $\boldsymbol{g}$ contains the prescribed values $\bar{\boldsymbol{u}}$ and $\boldsymbol{\beta}$. The modified system matrix and right-hand side can then be computed as

$$\begin{aligned} \tilde{\boldsymbol{K}} &= \boldsymbol{T}^{\intercal} \boldsymbol{K} \boldsymbol{T} \\ \tilde{\boldsymbol{F}} &= \boldsymbol{T}^{\intercal} \left(\boldsymbol{F} - \boldsymbol{K} \boldsymbol{g} \right). \end{aligned} \tag{2.17}$$

In these reduced matrices, the displacements are strongly enforced.

To illustrate the procedure, consider the triangular element e in Figure 2.3, split by a boundary Γ_i so that part of the element lies in the domain Ω_m and part lies in the domain Ω_i. In this example, Ω_m is void. The element is also split by a crack Γ_c so that multiple integration elements are created hierarchically. We now prescribe the primary field variable $\boldsymbol{u}$ over Γ_i (*i.e.*, $\boldsymbol{u}|_{\Gamma_\mathrm{i}} = \bar{\boldsymbol{u}}$) which is discontinuous at the crack. To obtain the DOF values that should be prescribed on the first level of hierarchy—corresponding to coordinates $\boldsymbol{x}_1$ and $\boldsymbol{x}_2$ in the figure—we evaluate (2.15) for $\boldsymbol{\alpha}_{11}$ and $\boldsymbol{\alpha}_{12}$, respectively. Note that the DOFs in the void area are set to zero, and are therefore removed from the system. Furthermore, enrichment functions from deeper levels of the hierarchy vanish at these coordinates, so only the function N_2 corresponding to $\boldsymbol{U}_2$ will have a contribution:

$$\begin{aligned} \boldsymbol{\alpha}_{11} &= \frac{1}{\psi_{11}(\boldsymbol{x}_1)} \left[\bar{\boldsymbol{u}}(\boldsymbol{x}_1) - N_2(\boldsymbol{x}_1) \boldsymbol{U}_2 \right], \\ \boldsymbol{\alpha}_{12} &= \frac{1}{\psi_{12}(\boldsymbol{x}_2)} \left[\bar{\boldsymbol{u}}(\boldsymbol{x}_2) - N_2(\boldsymbol{x}_2) \boldsymbol{U}_2 \right]. \end{aligned} \tag{2.18}$$

For the next hierarchy level, only the coordinate $\boldsymbol{x}_4$ is located on Γ_i, but here, both weak ($\boldsymbol{\alpha}$) and strong ($\boldsymbol{\beta}$) DOFs are present. Because $\boldsymbol{\beta}$ physically represents the crack opening displacement (Aragón and Simone, 2017), their values are readily available once the jump in the displacement is known, *i.e.*, $\boldsymbol{\beta}_{21} = [\![\boldsymbol{u}(\boldsymbol{x}_4)]\!] = \left(\bar{\boldsymbol{u}}(\boldsymbol{x}_4)|_{\Gamma_\mathrm{c}^+} - \bar{\boldsymbol{u}}(\boldsymbol{x}_4)|_{\Gamma_\mathrm{c}^-} \right)$. Then solving for $\boldsymbol{\alpha}$ at $\boldsymbol{x}_4$ follows the same procedure just described for $\boldsymbol{\alpha}_{11}$ and $\boldsymbol{\alpha}_{12}$. Because the prescribed field $\bar{\boldsymbol{u}}(\boldsymbol{x}_\alpha)$ is discontinuous at this location, we prescribe here the average displacement $\bar{\boldsymbol{u}}_\mathrm{avg}(\boldsymbol{x}_4)$. The strong DOF $\boldsymbol{\beta}_{21}$ then vanishes from the equation. These DOFS can later be interpreted as the crack opening around the average displacements. The resulting expression for $\boldsymbol{\alpha}_{22}$ is written as

$$\boldsymbol{\alpha}_{22} = \frac{1}{\psi_{22}(\boldsymbol{x}_4)} \left[\bar{\boldsymbol{u}}_\mathrm{avg}(\boldsymbol{x}_4) - N_2(\boldsymbol{x}_4) \boldsymbol{U}_2 - \psi_{11}(\boldsymbol{x}_4) \boldsymbol{\alpha}_{11} - \psi_{12}(\boldsymbol{x}_4) \boldsymbol{\alpha}_{12} \right]. \tag{2.19}$$

Note that ψ_{11} and ψ_{12} (belonging to a higher hierarchy level) also have a contribution, as their values are nonzero at $\boldsymbol{x}_4$. However, the deeper levels of hierarchy can never influence the higher ones.

Upon inspection, it becomes clear that the only DOFs that are not prescribed are $\boldsymbol{U}_2$, $\boldsymbol{\alpha}_{23}$ and $\boldsymbol{\beta}_{22}$, all other DOFs can be written as a function of these remaining DOFs. For

this example, these vectors and matrices become:

$$\begin{bmatrix} \boldsymbol{U}_1 \\ \boldsymbol{U}_2 \\ \boldsymbol{U}_3 \\ \boldsymbol{\alpha}_{11} \\ \boldsymbol{\alpha}_{12} \\ \boldsymbol{\alpha}_{21} \\ \boldsymbol{\alpha}_{22} \\ \boldsymbol{\alpha}_{23} \\ \boldsymbol{\beta}_{21} \\ \boldsymbol{\beta}_{22} \end{bmatrix} = \begin{bmatrix} \boldsymbol{0} & \boldsymbol{0} & \boldsymbol{0} \\ \boldsymbol{I} & \boldsymbol{0} & \boldsymbol{0} \\ \boldsymbol{0} & \boldsymbol{0} & \boldsymbol{0} \\ -\frac{N_2(\boldsymbol{x}_1)}{\psi_{11}(\boldsymbol{x}_1)}\boldsymbol{I} & \boldsymbol{0} & \boldsymbol{0} \\ -\frac{N_2(\boldsymbol{x}_2)}{\psi_{12}(\boldsymbol{x}_2)}\boldsymbol{I} & \boldsymbol{0} & \boldsymbol{0} \\ \boldsymbol{0} & \boldsymbol{0} & \boldsymbol{0} \\ \left(N_2(\boldsymbol{x}_4) - \frac{\psi_{11}(\boldsymbol{x}_4)}{\psi_{11}(\boldsymbol{x}_1)}N_2(\boldsymbol{x}_1) - \frac{\psi_{12}(\boldsymbol{x}_4)}{\psi_{12}(\boldsymbol{x}_2)}N_2(\boldsymbol{x}_2)\right)\boldsymbol{I} & \boldsymbol{0} & \boldsymbol{0} \\ \boldsymbol{0} & \boldsymbol{I} & \boldsymbol{0} \\ \boldsymbol{0} & \boldsymbol{0} & \boldsymbol{0} \\ \boldsymbol{0} & \boldsymbol{0} & \boldsymbol{I} \end{bmatrix} \begin{bmatrix} \boldsymbol{U}_2 \\ \boldsymbol{\alpha}_{23} \\ \boldsymbol{\beta}_{22} \end{bmatrix} + \begin{bmatrix} \boldsymbol{0} \\ \boldsymbol{0} \\ \boldsymbol{0} \\ \frac{1}{\psi_{11}(\boldsymbol{x}_1)}\bar{\boldsymbol{u}}(\boldsymbol{x}_1) \\ \frac{1}{\psi_{12}(\boldsymbol{x}_2)}\bar{\boldsymbol{u}}(\boldsymbol{x}_2) \\ \boldsymbol{0} \\ \frac{1}{\psi_{22}(\boldsymbol{x}_4)}\bar{\boldsymbol{u}}_{\text{avg}}(\boldsymbol{x}_4) \\ \boldsymbol{0} \\ \left(\bar{\boldsymbol{u}}(\boldsymbol{x}_4)|_{\Gamma_c^+} - \bar{\boldsymbol{u}}(\boldsymbol{x}_4)|_{\Gamma_c^-}\right) \\ \boldsymbol{0} \end{bmatrix}. \tag{2.20}$$

NEUMANN BOUNDARY CONDITIONS

As stated before, tractions on the boundary Γ_t follow the same element-wise assembly procedure into $\boldsymbol{f}$ as in standard FEM. In order to apply a traction $\bar{\boldsymbol{t}}$ on $\Gamma_t \subset e$, one would simply compute

$$\boldsymbol{f}_e = \int_{\Gamma_t} \boldsymbol{v} \cdot \bar{\boldsymbol{t}} \, \mathrm{d}\Omega = \int_{\Gamma_t} \boldsymbol{N}^\intercal \bar{\boldsymbol{t}} \, \mathrm{d}\Gamma, \tag{2.21}$$

where $\boldsymbol{N}^\intercal$ contains not only the element's Lagrange shape functions N_i, but also enrichment functions ψ_{ki} and χ_{ki}, as $\boldsymbol{N}^\intercal = \left[N_i \; \psi_{ki} \; \chi_{ki}\right]^\intercal$. As a result, $\boldsymbol{f}_e$ will add contributions to DOFs that are not located on the boundary Γ_t. For example, if a traction were to be applied on Γ_i in Figure 2.3 (still assuming Ω_m to be void, and therefore removing $\boldsymbol{U}_1$ and $\boldsymbol{U}_3$), contributions would appear on DOFs $\boldsymbol{U}_2, \boldsymbol{\alpha}_{11}, \boldsymbol{\alpha}_{12}, \boldsymbol{\alpha}_{22}$ and $\boldsymbol{\beta}_{21}$, as all of their corresponding functions are non-zero on the boundary.

In the case of Neumann boundary conditions, DE-FEM also benefits from placing nodes on the interface and creating integration elements, as the boundary Γ_t is explicitly known, and therefore can be used for integration. Note that, as the partition of unity is not retained in cut elements, the sum of all contributions will be higher than the total applied traction. However, the obtained solutions are correct, as demonstrated in Section 2.3.

2.3. NUMERICAL EXAMPLES

In the following examples, a consistent unit system is assumed. Furthermore, plane-strain conditions are used for the 2-D examples, and a quadrature rule that exactly integrates integration elements is adopted, *i.e.*, one integration point is used for the linear triangular (integration) elements.

2.3.1. THE "ULTIMATE" DISCONTINUITY PATCH TEST

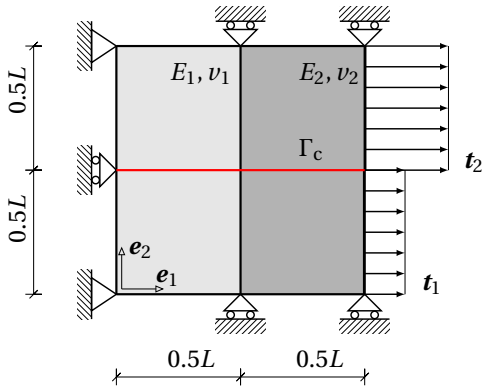

Figuur 2.4: A plate composed of two materials is split in two by a crack Γ_c, denoted by the red line. Tractions $\bar{t}_1$ and $\bar{t}_2$ are applied to the right edge, and the displacement is prescribed as shown.

In order to establish that DE-FEM can indeed recover constant states of stress, and to demonstrate the flexibility provided by DE-FEM, we devise an immersed patch test aiming at recovering multiple independent kinematic fields; the problem contains an interface and a crack that intersect each other within an immersed domain. The problem, schematically shown in Figure 2.4, consists of a square domain of area $L \times L$. The material to the left (right) of the interface has a Young's modulus $E_1 = 2$ ($E_2 = 20$), and both materials have Poisson ratio $\nu_1 = \nu_2 = 0$, to ensure that the vertical strain ε_{22} is zero in both materials, and a constant analytical stress is obtained above and below the crack. Regarding boundary conditions, the plate is constrained in displacement as shown in the figure, and subjected to a traction per unit length $\|\bar{t}_1\| = 1$ and $\|\bar{t}_2\| = 2$, respectively, below and above a crack Γ_c at $x_2 = 0.5L$.

The analytical displacement field of this patch test is given by

$$u_1 = \begin{cases} \dfrac{\|\bar{t}_1\| x_1}{E_1} & \text{for} \quad x_1 \le \dfrac{1}{2}L, \quad x_2 < \dfrac{1}{2}L, \\ \dfrac{\|\bar{t}_1\| \frac{1}{2}L}{E_1} + \dfrac{\|\bar{t}_1\| \left(x_1 - \frac{1}{2}L\right)}{E_2} & \text{for} \quad x_1 \ge \dfrac{1}{2}L, \quad x_2 < \dfrac{1}{2}L, \\ \dfrac{\|\bar{t}_2\| x_1}{E_1} & \text{for} \quad x_1 \le \dfrac{1}{2}L, \quad x_2 > \dfrac{1}{2}L, \\ \dfrac{\|\bar{t}_2\| \frac{1}{2}L}{E_1} + \dfrac{\|\bar{t}_1\| \left(x_1 - \frac{1}{2}L\right)}{E_2} & \text{for} \quad x_1 \ge \dfrac{1}{2}L, \quad x_2 > \dfrac{1}{2}L, \end{cases} \tag{2.22}$$

$$u_2 = 0,$$

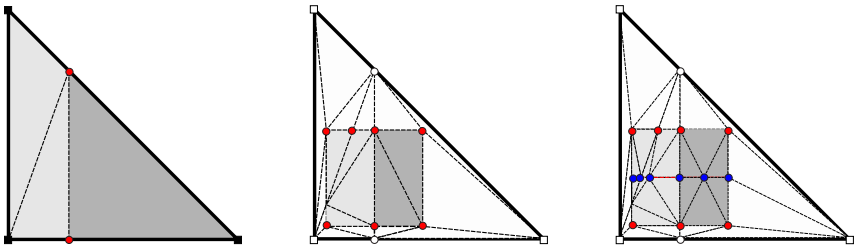

(a) (b) (c)

Figuur 2.5: Hierarchical creation of the integration elements within a single background element, for each discontinuity type: (a) The first level of hierarchy: the material interface is immersed in a single triangular background element, enriched nodes are added, shown as ●, and three integration elements are created; (b) the second level of hierarchy: the square material domain is interacted with the mesh that was obtained in (a), enriched nodes are placed on the intersection of element edges and the square discontinuity, and the next level of integration elements is created. Standard nodes and enriched nodes that lie completely outside the square domain are shown as ○ and ○, respectively, and will not be considered in the analysis; (c) the third level of hierarchy: the crack is added: weak and strong enriched nodes, shown as ● , are placed at intersections along the crack, and the final layer of integration elements is created.

and the stresses within the domain are given analytically as

$$\begin{aligned} \sigma_{11} &= \begin{cases} 2 & \text{for} \quad x_2 < 0.5 \\ 1 & \text{for} \quad x_2 > 0.5 \end{cases}, \\ \sigma_{22} &= 0, \\ \sigma_{12} &= 0. \end{aligned} \tag{2.23}$$

This problem is then discretized within a *single* background element. This is possible because in this case, the linear displacement field, combined with these material properties, will induce a constant state of stress. It has to be noted that, in physical problems containing multiple discontinuities, the interaction between these is likely to be more complex. A finer mesh would then be preferred to accurately capture the physics in that region. Even then, it is important to be able to describe multiple discontinuities within a single element for several reasons:

- A crossing between two non-matching discontinuities will typically occur in a single element, even after refinement. This may occur, for example, in composite materials, crack branching (or merging), and in crack propagation in composite materials or immersed domains.
- The method is more robust when discontinuities can come arbitrarily close to one another. While a mesh refinement step might be required, a linear interpolation between two interfaces might give a reasonable first estimate of the solution.

The hierarchical immersion of the problem in a single 3-node triangular element is illustrated in Figure 2.5, together with the integration elements that result from the interaction with the mesh at each level of the hierarchy. Figure 2.6a shows the numerical displacement field, that matches the analytical one exactly. Note that, although only

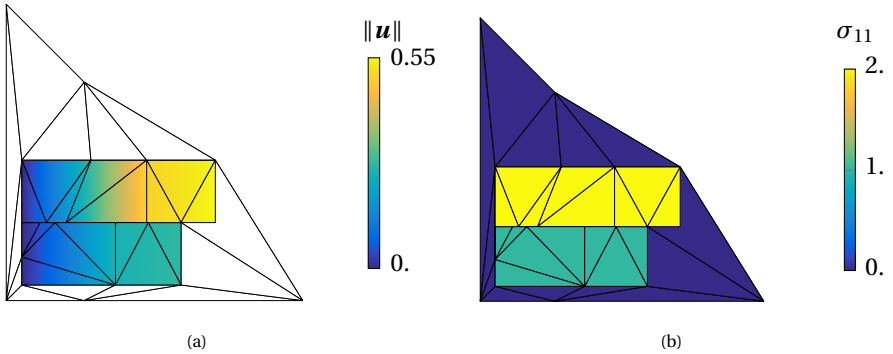

(a) (b)

Figuur 2.6: Numerical results for the 'ultimate' patch test: (a) The deformations exactly match the analytic deformations, as given in 2.22. (b) A constant state of stress, that corresponds to the analytical solution as given in (2.23), is retrieved at either side of the cracked domain. The deformations of the integration elements that lie outside the physical domain do not induce any stress.

the physical domain is colored, the integration elements outside the domain clearly undergo deformation as well. However, because Young's modulus in that region is exactly zero, these deformations do not lead to any stress. As shown in Figure 2.6b, DE-FEM is able to recover the analytic displacements and stresses exactly, despite the fact that this problem contains an interface and a crack and is immersed in a single, non-matching, background element.

2.3.2. CONVERGENCE: IMMERSED ESHELBY INCLUSION PROBLEM

The accuracy and convergence of the formulation are tested on the classical Eshelby inclusion problem, as illustrated in Figure 2.7a. A circular inclusion of a compliant material ($E_1 = 1$, $\nu_1 = 0.25$) and radius $r_\mathrm{i} = 0.9$ is immersed in a stiffer material ($E_2 = 10$, $\nu_2 = 0.3$) with a radius of $r_\mathrm{o} = 2$. The circular boundary is subjected to a prescribed displacement along the outer radius

$$\begin{aligned} u_r(r_\mathrm{o},\theta) &= r_\mathrm{o}, \\ u_\theta(r_\mathrm{o},\theta) &= 0. \end{aligned} \tag{2.24}$$

The analytic solution for the displacement field is

$$\begin{aligned} u_r &= \begin{cases} \left((1-\frac{r_\mathrm{o}^2}{r_\mathrm{i}^2})\alpha + \frac{r_\mathrm{o}^2}{r_\mathrm{i}^2}\right) r & \text{for} \quad 0 \le r \le r_\mathrm{i}, \\ \left(r - \frac{r_\mathrm{o}^2}{r}\right)\alpha + \frac{r_\mathrm{o}^2}{r} & \text{for} \quad r_\mathrm{i} \le r \le r_\mathrm{o}, \end{cases} \\ u_\theta &= 0, \end{aligned} \tag{2.25}$$

where α is a function of the Lamé parameters of the materials λ_1, λ_2 and μ_1, μ_2:

$$\alpha = \frac{\left(\lambda_1 + \mu_1 + \mu_2\right) r_\mathrm{o}^2}{\left(\lambda_2 + \mu_2\right) r_\mathrm{i}^2 + \left(\lambda_1 + \mu_1\right)\left(r_u^2 - r_\mathrm{i}^2\right) + \mu_2 r_u^2}, \tag{2.26}$$

and the Lamé parameters are defined as $\lambda = {}^{E\nu}/_{(1+\nu)(1-2\nu)}$ and $\mu = {}^{E}/_{2(1+\nu)}$.The analytic displacement field (2.25) is non-linear in terms of spatial coordinates, and therefore cannot be recovered exactly by the linear interpolation space of the discretized model.

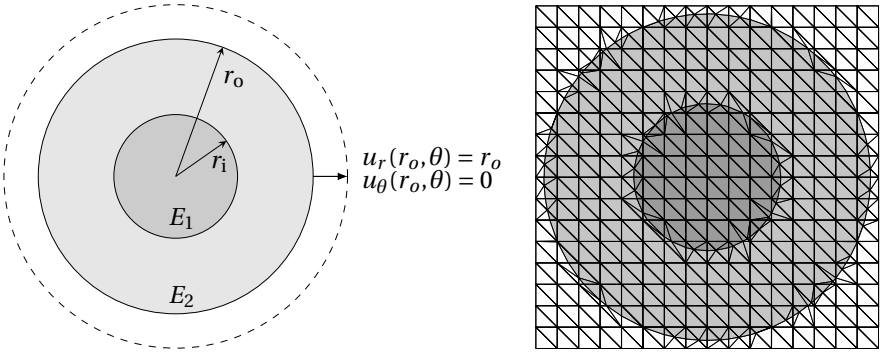

Figuur 2.7: (a) Schematic of the Eshelby inclusion problem: A circular domain with a concentric circular inclusion and prescribed displacements along the radial and tangential directions; and (b) The immersed discretization on a structured triangular mesh, and sub-triangulation into integration elements shown with thinner lines.

This circular domain is immersed in a square structured mesh as shown in Figure 2.7b, creating non-matching edges for both the internal material interface Γ_i as well as the external domain boundary Γ_o. On the boundary, the exact solution is prescribed in the form of a Dirichlet boundary condition. Contrary to the weak enforcement of non-homogeneous Dirichlet boundary conditions in Cuba Ramos *et al.* (2015), here we prescribe it using multiple point constraints, as described in Section 2.2.2. The numerically obtained displacement field is shown in Figure 2.8. Furthermore, the tractions on the Dirichlet boundary are recovered by mapping the nodal forces (obtained as $\boldsymbol{KU} = \boldsymbol{F}$) back to $d-1$ elements. The recovered traction profile is smooth, as illustrated in Figure 2.8.

Figure 2.9 shows an element-wise evaluation of the error fields in both the energy-norm and the L^2-norm, which we define for an element e as

$$\| \boldsymbol{e} \|^2_{L^2(e)} \equiv \frac{\| \boldsymbol{u} - \boldsymbol{u}^h \|^2_{L^2}}{\| \boldsymbol{u} \|^2_{L^2}} = \frac{\int_e \left(\boldsymbol{u} - \boldsymbol{u}^h\right)^\intercal \left(\boldsymbol{u} - \boldsymbol{u}^h\right) \mathrm{d}e}{\int_e \| \boldsymbol{u} \|^2 \, \mathrm{d}e}, \tag{2.27}$$

and

$$\| \boldsymbol{e} \|^2_{\mathcal{E}(e)} \equiv \frac{\| \boldsymbol{u} - \boldsymbol{u}_h \|^2_{\mathcal{E}}}{\| \boldsymbol{u} \|^2_{\mathcal{E}}} = \frac{\int_e \left(\boldsymbol{\varepsilon}(\boldsymbol{u}) - \boldsymbol{\varepsilon}(\boldsymbol{u}^h)\right)^\intercal \boldsymbol{C} \left(\boldsymbol{\varepsilon}(\boldsymbol{u}) - \boldsymbol{\varepsilon}(\boldsymbol{u}^h)\right) \mathrm{d}e}{\int_e \boldsymbol{\varepsilon}(\boldsymbol{u})^\intercal \boldsymbol{C} \boldsymbol{\varepsilon}(\boldsymbol{u}) \, \mathrm{d}e}, \tag{2.28}$$

where $\boldsymbol{u}$ is the analytic solution, $\boldsymbol{u}^h$ is the numerical solution, $\boldsymbol{\varepsilon}(\boldsymbol{u})$ is the strain due to displacement field and $\boldsymbol{C}$ the elasticity tensor, here written in Voigt notation. As this error evaluation is done on the level of integration elements, all elements are either completely inside or completely outside the physical domain. As we are not interested in the latter, we simply omit them from the error analysis. It is clear that the error is concentrated mostly along the material interface, as the circular interface is discretized as a piece-wise linear discontinuity. Particularly, the error in the energy norm may be large in integration

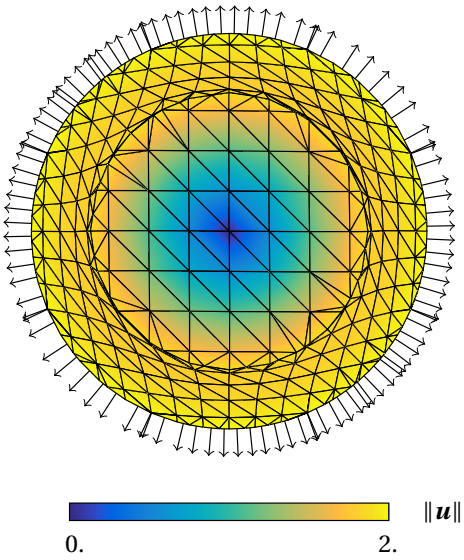

Figuur 2.8: Deformed configuration of the immersed Eshelby inclusion problem including the recovered smooth traction profile.

elements with bad aspect ratios, due to inaccurate computations of the derivatives of the field (Nagarajan and Soghrati, 2018; Soghrati *et al.*, 2017). Note, however, that the error on the domain boundary is relatively low, as the enriched DOFs are prescribed to represent exactly the imposed displacement there.

To further investigate the influence of aspect ratio on the error, we analyze a series of Eshelby inclusion problems on a single mesh that is matching to the material interface, but non-matching to the outer boundary. Figure 2.10 shows that the error on the matching interface is of a similar order as the error in DE-FEM. Changing the radius of the outer boundary while keeping the background mesh fixed changes the aspect ratio of the integration elements. The error in an integration element close to the immersed boundary—indicated with a red outline—is plotted as a function of the aspect ratio in Figure 2.11. Both the absolute error $\| \boldsymbol{u} - \boldsymbol{u}^h \|^2_{(e)}$ and the normalized error $\| \boldsymbol{u} - \boldsymbol{u}^h \|^2_{(e)} / \| \boldsymbol{u} \|^2_{(e)}$ are shown. From the former, it can be seen that the absolute error in the element decreases with aspect ratio, as the volume of the elements decreases. From the normalized error it becomes clear that the aspect ratio indeed has an influence, but the error remains bounded. Therefore, bad aspect ratio elements are expected to not have much influence on the global error measure under mesh refinement, as is investigated next.

In order to analyze convergence under mesh refinement, we use the standard L^2-

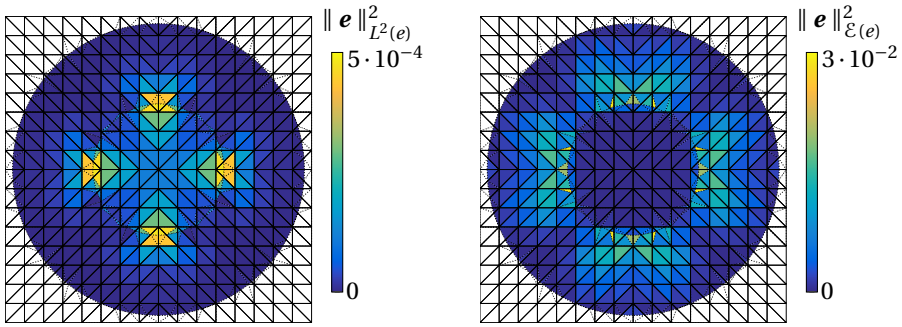

(a) (b)

Figuur 2.9: Element-wise error fields in the immersed Eshelby inclusion problem; (a) L^2-norm and (b) Energy-norm

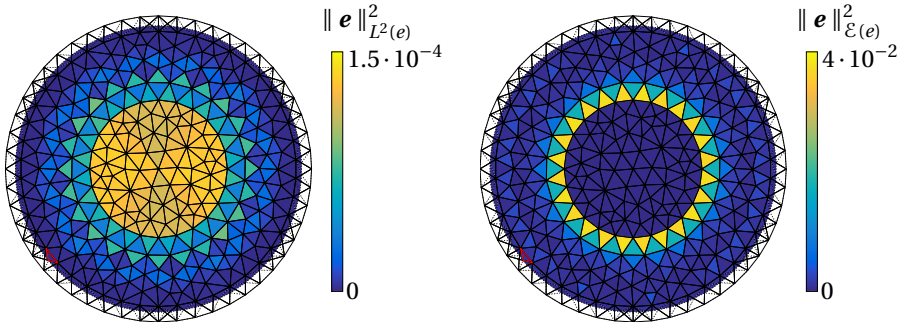

(a) (b)

Figuur 2.10: Element-wise error for an immersed Eshelby problem, where the outer boundary is non-matching to an unstructured background mesh that is aligned with the inclusion;(a) L^2-norm and (b) Energy-norm. The integration element indicated with a red outline is used in the aspect ratio study of Figure 2.11.

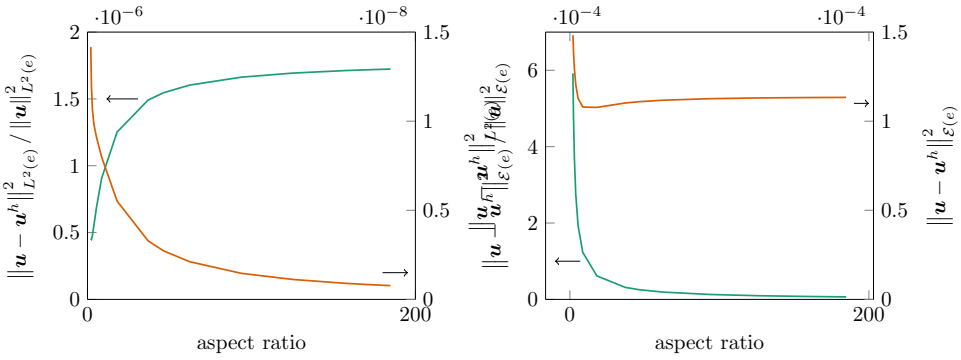

(a) (b)

Figuur 2.11: Error in an integration element (normalized by the integration element area) as a function of aspect ratio. Figure (a) shows the error in the *L2*-norm and (b) shows the error in the energy norm.

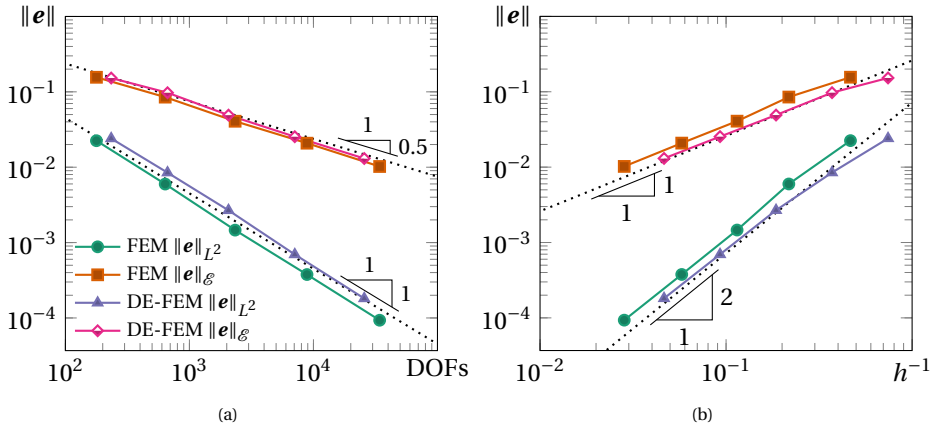

Figuur 2.12: DE-FEM shows optimal convergence for the immersed Eshelby inclusion problem with strongly prescribed nonzero Dirichlet boundary conditions: (a) Convergence with respect to the number of DOFs, and (b) the mesh size h.

and energy-norms of the relative error, given respectively by

$$\| \boldsymbol{e} \|_{L^2} \equiv \frac{\| \boldsymbol{u} - \boldsymbol{u}^h \|_{L^2}}{\| \boldsymbol{u} \|_{L^2}} = \sqrt{\frac{\sum_{e \in \Delta_H^h} \int_e (\boldsymbol{u} - \boldsymbol{u}^h)^\intercal (\boldsymbol{u} - \boldsymbol{u}^h) \, \mathrm{d}e}{\sum_{e \in \Delta_H^h} \int_e \| \boldsymbol{u} \|^2 \, \mathrm{d}e}}, \tag{2.29}$$

and

$$\| \boldsymbol{e} \|_{\mathcal{E}} \equiv \frac{\| \boldsymbol{u} - \boldsymbol{u}_h \|_{\mathcal{E}}}{\| \boldsymbol{u} \|_{\mathcal{E}}} = \sqrt{\frac{\sum_{e \in \Delta_H^h} \int_e (\boldsymbol{\varepsilon}(\boldsymbol{u}) - \boldsymbol{\varepsilon}(\boldsymbol{u}^h))^\intercal \boldsymbol{C} (\boldsymbol{\varepsilon}(\boldsymbol{u}) - \boldsymbol{\varepsilon}(\boldsymbol{u}^h)) \, \mathrm{d}e}{\sum_{e \in \Delta_H^h} \int_e \boldsymbol{\varepsilon}(\boldsymbol{u})^\intercal \boldsymbol{C} \boldsymbol{\varepsilon}(\boldsymbol{u}) \, \mathrm{d}e}}. \tag{2.30}$$

The convergence behavior under mesh refinement of the method is illustrated in Figure 2.12. Immersed DE-FEM, where both the domain boundary and the material interface are non-matching, as described before, is compared with standard FEM, where a mesh that conforms to both circular boundaries is used. In Figure 2.12a the error in both norms is plotted against the number of DOFs, while in Figure 2.12b the error is plotted against the mesh size h. Dotted lines with slopes corresponding to optimal convergence rates are provided for reference. It is clear from the results that immersed DE-FEM has an optimal rate of convergence. Furthermore, it performs comparable with the standard FEM with respect to accuracy. For h-convergence, DE-FEM has a slightly better accuracy, as details within a background element can be captured by DE-FEM, without a change in h.

In summary, this example demonstrates that the method is optimally convergent for cases without singularities such as crack tips. For the same number of DOFs, a similar error is obtained as with standard FEM, without the burden of creating a matching mesh. Furthermore, this example shows that the MPC method for prescribing Dirichlet boundary conditions in a strong manner is also able to correctly prescribe non-homogeneous displacements on a non-matching boundary.

2.3.3. STABILITY: SLIGHTLY ROTATED MESH

Here we study the stability, meaning the influence of refinement on the condition number, of the proposed methodology by looking at the condition number of the system matrices. A rectangular domain is evaluated on a background mesh that was rotated by 3°, as illustrated in Figure 2.13a, to ensure that integration elements of all shapes and sizes are present. The background mesh is then refined in multiple steps, creating different irregular-shaped elements in each level of refinement. The stability is then evaluated. The problem is not subjected to any boundary conditions, but rigid body motions are accounted for by discarding the lowest three eigenvalues in the system, which are zero within numerical precision.

As stated earlier, in this method we remove all DOFs belonging to nodes in the void area of the system. The remaining stiffness matrix can in general be written as

$$\boldsymbol{K} = \begin{pmatrix} \boldsymbol{K}_{uu} & \boldsymbol{K}_{u\alpha} & \boldsymbol{K}_{u\beta} \\ \boldsymbol{K}_{u\alpha}^{\top} & \boldsymbol{K}_{\alpha\alpha} & \boldsymbol{K}_{\alpha\beta} \\ \boldsymbol{K}_{u\beta}^{\top} & \boldsymbol{K}_{\alpha\beta}^{\top} & \boldsymbol{K}_{\beta\beta} \end{pmatrix}, \tag{2.31}$$

where $\boldsymbol{K}_{uu}$ is the portion that corresponds purely to the standard FEM, $\boldsymbol{K}_{\alpha\alpha}$ corresponds to weak enrichments, and $\boldsymbol{K}_{\beta\beta}$ corresponds to strong enrichments. The off-diagonal matrices $\boldsymbol{K}_{u\alpha}, \boldsymbol{K}_{u\beta}, \boldsymbol{K}_{\alpha\beta}$ contain coupling terms. Note that in this particular example, no strong discontinuities are present, and therefore the matrices $\boldsymbol{K}_{u\beta}, \boldsymbol{K}_{\alpha\beta}$ and $\boldsymbol{K}_{\beta\beta}$ are absent. Following the work of Kergrene *et al.* (2016), we study the condition number of $\boldsymbol{K}$ and a modified matrix $\hat{\boldsymbol{K}} = \boldsymbol{DKD}$, where D is a diagonal matrix, defined such that $D_{ii} = 1/\sqrt{K_{ii}}$ and thus $\hat{\boldsymbol{K}}$ has unit values on the diagonal. The condition number is then obtained as

$$\kappa = \frac{\lambda_{\max}}{\lambda_{\min}}, \qquad \lambda_{\min} \neq 0, \tag{2.32}$$

where $\lambda_{\max}$ and $\lambda_{\min}$ are the maximum and minimum (non-zero) eigenvalues of either $\boldsymbol{K}$ or $\hat{\boldsymbol{K}}$. Ideally, the condition number of a DE-FEM matrix would scale under mesh refinement at the same rate as standard FEM does: $\mathcal{O}\left(h^{-2}\right)$.

In Figure 2.13b the results are shown: we compare the conditioning of the full system without any preconditioner ($\boldsymbol{K}$) and the preconditioned system ($\hat{\boldsymbol{K}}$) with the part of the matrix ($\boldsymbol{K}_{uu}$) that corresponds to the standard part of the approximation. From these results, it is clear that the method indeed suffers from ill-conditioning if no measures are taken to prevent it. This happens because when an enriched node is placed close to an original node, integration elements with a small measure are created. The condition number grows with j^{-1}, were j is the Jacobian of these small integration elements, as was shown by Aragón and Simone (2017). In DE-FEM without a preconditioner, the condition number is not a straight line as a function of h^{-1}, suggesting that the condition number is highly dependent on the intersection geometry in each particular background mesh. However, the results also show that a simple diagonal pre-conditioner suffices in reducing the conditioning number of the full matrix to that of standard FEM. Alternatively, a local scaling of the enrichment functions has been proposed by Aragón *et al.* (2020) that results in the same reduction of the conditioning number. Consequently, the method is stable, and complex conditioning schemes are unnecessary in DE-FEM.

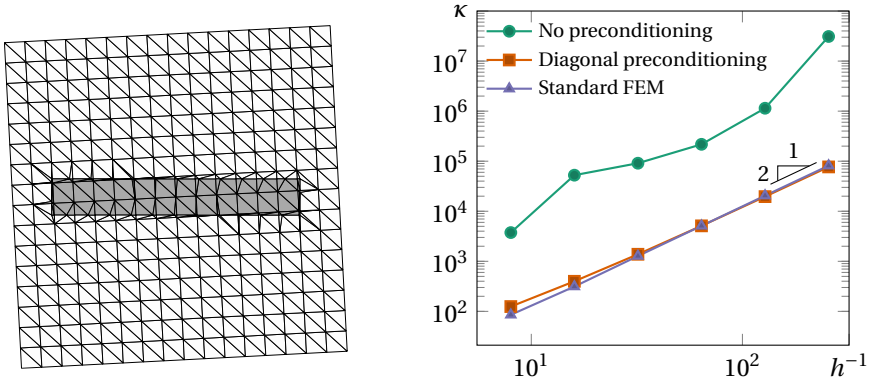

(a) (b)

Figuur 2.13: Stability of DE-FEM: a) Model problem showing a rectangular domain immersed in a structured background mesh that was rotated by 3°; b) Condition number as a function of the reciprocal of mesh size h. It is visible that, while the condition number $\kappa(\boldsymbol{K})$ of the raw matrix is unstable, $\kappa(\hat{\boldsymbol{K}})$—which uses the diagonal preconditioner—is close to the condition number of the standard FEM component $\kappa(\boldsymbol{K}_{uu})$.

2.3.4. A 3-D IMMERSED THERMO-MECHANICAL "POPCORN"

As a final example, we demonstrate the method in 3-D. To this end, we immerse a level set description of a popcorn shape (Annavarapu *et al.*, 2012; Burman *et al.*, 2015; Chern and Shu, 2007; Hautefeuille *et al.*, 2012) (Figure 2.14a) into a structured cubic mesh, as illustrated in Figure 2.14b. This geometry is described by the function

$$\phi(\boldsymbol{x}) = \sqrt{\|\boldsymbol{x}\|} - r - \sum_{k=0}^{11} A \exp\left[-\frac{\|\boldsymbol{x}-\boldsymbol{x}^{(k)}\|}{\sigma^2}\right], \tag{2.33}$$

where

$$\boldsymbol{x}^{(k)} = \begin{cases} \frac{r}{\sqrt{5}}\left[2\cos\left(\frac{2k\pi}{5}\right) \quad 2\sin\left(\frac{2k\pi}{5}\right) \quad 1\right]^\intercal & \text{for} \quad 0 \le k \le 4, \\ \frac{r}{\sqrt{5}}\left[2\cos\left(\frac{(2(k-5)-1)\pi}{5}\right) \quad 2\sin\left(\frac{(2(k-5)-1)\pi}{5}\right) \quad -1\right]^\intercal & \text{for} \quad 5 \le k \le 9, \\ \begin{bmatrix}0 & 0 & r\end{bmatrix}^\intercal & \text{for} \quad k = 10, \\ \begin{bmatrix}0 & 0 & -r\end{bmatrix}^\intercal & \text{for} \quad k = 11. \end{cases} \tag{2.34}$$

Following Burman *et al.* (2015), we choose $r = 0.6$, $\sigma = 0.2$ and $A = 4$.

The material inside the domain is assigned a Young's modulus $E = 2$, a Poisson ratio $\nu = 0$, and a thermal expansion coefficient $\alpha = 0.01$. A uniform temperature is applied on the surface Γ_i of the popcorn, described by the zero level set. A simple thermal solve leads to a constant temperature throughout the domain, such that the material will try to expand uniformly. However, a homogeneous Dirichlet boundary condition is prescribed for the displacement field on the entire surface Γ_i, preventing the popcorn from expanding.

The analytic result of this problem is a constant state of stress throughout the entire physical domain with stress magnitude $\|\boldsymbol{\sigma}\| = 0.346$. In Figure 2.15, the numerical results are illustrated. It is clear that the constant temperature field with a value of $T = 1$, and the state of stress, with magnitude $\|\boldsymbol{\sigma}\| = 0.346$ are indeed retrieved.

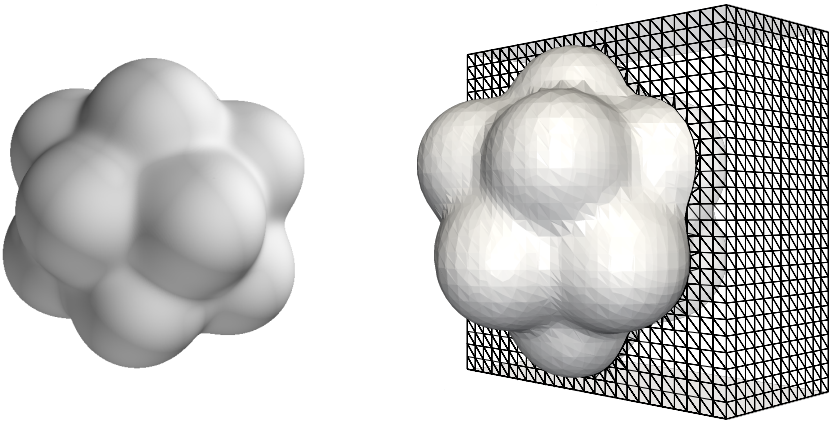

(a) (b)

Figuur 2.14: Immersed DE-FEM applied to a complex 3-D shape: (a) the zero contour of the level set function; (b) computational domain, resulting from the interaction between the zero level set and a structured mesh.

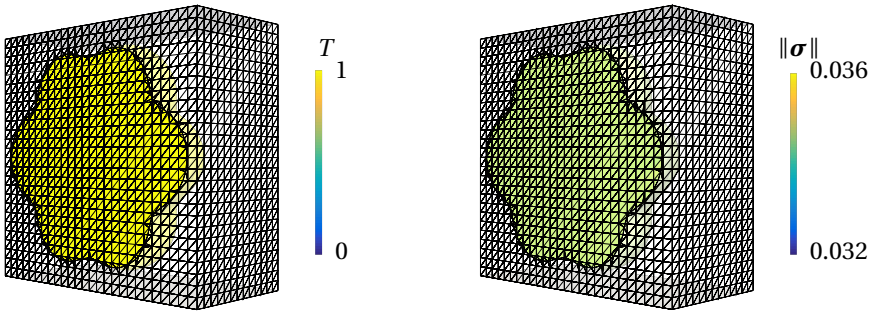

(a) (b)

Figuur 2.15: A constant temperature field (a) and a constant state of stress (b) are obtained throughout the domain.

2.4. SUMMARY AND CONCLUSIONS

In this work we extended the Discontinuity-Enriched Finite Element Method to treat immersed domain problems. The formulation, combined with a hierarchical implementation, results in an extremely versatile mesh-independent method for solving problems containing both weak and strong discontinuities with a unified formulation.

We have demonstrated, by means of a complex patch test, that a domain containing interfaces and cracks can be analyzed by enclosing it by a discretization that disregards completely all discontinuities. With the immersed Eshelby inclusion problem, we showed that non-homogeneous essential boundary conditions on a non-matching boundary can be prescribed in a strong manner. Furthermore, this example was used to show that optimal convergence is attained. The stability of the method was investigated by means of a rotated mesh example, and it was found that the method remains stable under mesh refinement with the use of a diagonal preconditioner. Lastly, the extension to complex 3-D structures was demonstrated. Discontinuities were represented both implicitly (via level sets as in the Eshelby and popcorn examples) and explicitly (through line segments, in the immersed patch test and in the stability example).

As any other computational method, DE-FEM has advantages and disadvantages:

Pros

- The most remarkable merit of DE-FEM as an immersed method is the strong enforcement of Dirichlet boundary conditions. In this respect, DE-FEM is unique amongst other immersed boundary methods. With strong enforcement, essential boundary conditions are fulfilled exactly on the nodes.
- DE-FEM is also the first method in the field of enriched finite element methods that can be applied succesfully as an immersed method with strong enforcement of Dirichlet boundary conditions. Previously, Cuba Ramos *et al.* (2015) had demonstrated the use as an immersed method with weak enforcement of essential boundary conditions.
- DE-FEM is a particularly versatile enriched method due to the hierarchical construction of enrichment functions. The method is truly mesh independent: different types of weak and strong discontinuities are allowed to lie arbitrarily close to one another or even intersect, within a single element. This makes the method robust against any placement of discontinuities, and suitable for the analysis of complex geometries, such as fracture analysis in immersed domains.
- The method is stable, *i.e.* the conditioning number increases at the same rate as that of standard FEM, $\mathcal{O}\left(h^{-2}\right)$.

Cons

- Compared to existing immersed boundary methods—for example the finite cell method—the geometric operations are more complex. Enriched nodes need to be placed along the boundary, and integration elements need to be created. These geometric operations can be done efficiently, but require specialized code: a "geometric engine".

- The hierarchical construction of enrichment functions calls for a dedicated data structure—such as an ordered tree—to store the hierarchy. However, this small overhead enables the hierarchical implementation, which is a major asset.

- For problems with material interfaces, it has been shown that IGFEM/HIFEM may overestimate stresses in integration elements with bad aspect ratios (Nagarajan and Soghrati, 2018; Soghrati *et al.*, 2017). This issue, however, is not significant near Dirichlet boundaries, where the essential boundary condition are enforced exactly.

Considering DE-FEM's many interesting properties, the advantages over other immersed methods strongly depend on the application. As a final remark, for the same functionality, the complexity of the geometric operations is similar to X/GFEM. Any increased complexity in the geometric operations of DE-FEM immediately opens up a wide range of new capabilities, such as the hierarchical implementation, interface with sharp corners and crack tips inside an element, and immersed domains inside a single element. This trade-off between generality of the method and simplicity of implementation is to be expected, and in cases where this flexibility is not needed, simplified geometric operations might be executed. This makes DE-FEM suitable as an all-purpose immersed domain method, and especially suitable for problems with complex configurations of discontinuities.

APPENDIX: PSEUDO CODE FOR HIERARCHICAL IMPLEMENTATION

For completeness, pseudo code for the hierarchical implementation of DE-FEM is provided. This algorithm assembles a leaf integration element by looping over the hierarchical tree and assembling all contributions. This pseudocode works in all dimensions and is based on the pseudo-code given by Zhang *et al.* (2019a).

In Algorithm 1 the general assembly loop for integration elements is described. This procedure is the same as for standard FEM, except that a check is done to confirm that the integration element lies within the physical domain. To assemble the contributions of integration element $e^{(k)}$ inside the physical domain at hierarchy level k, local arrays are initialized. Then, in a loop over integration points, the Jacobian, the shape/enrichment function matrix $\boldsymbol{N}$ and its derivative $\boldsymbol{B}$, are computed as described next.

Algorithm 2 describes the computation of $\boldsymbol{N}$ and $\boldsymbol{B}$ at every integration point. As a first step, the nodal coordinates of the integration elements are obtained. Then, in a loop over the enriched nodes of the integration element, the contribution is found for each level in the hierarchy. Starting from the leaf element we obtain the global coordinate, the Jacobian matrix, the Lagrange shape functions, and their derivatives. If the current hierarchy level is a leaf, the Jacobian determinant is also computed and stored. Furthermore, the enrichment function and its derivatives, corresponding to the current enriched node, are appended to an array. Finally, the level of hierarchy is decreased, the parent of the current element is found, and an inverse mapping is conducted to find the local coordinate in the parent element. Once all hierarchical levels and enriched nodes

have been visited, the shape & enrichment functions and their derivatives are expanded, according the number of DOFs per node, into the $\boldsymbol{N}$ and $\boldsymbol{B}$ matrix.

Algorithm 1 Element-wise assembly of the force vector $\boldsymbol{f}$ and stiffness matrix $\boldsymbol{k}$ in an integration element

Input: Modified mesh $\mathcal{M} = \{\mathcal{N} \cup \mathcal{N}_e, \mathcal{E} \cup \mathcal{H}\}$, ordered tree $\mathcal{H}$, leaf integration element $e^{(k)}$ at hierarchical level k, quadrature point weights $\boldsymbol{\gamma}$ and coordinates $\boldsymbol{\xi}$, constitutive matrix $\boldsymbol{C}$ and body force $\boldsymbol{b}$;
Output: Local stiffness matrix $\boldsymbol{k}$ and local force vector $\boldsymbol{f}$.

```
function GETLOCALARRAYS(M, H, e^(k), γ, ξ, C, b)
    Check if the element lies outside the physical domain:
    if C = 0 then return
    Initialize local arrays:
    {k, f} ← {0, 0}
    Loop over integration points:
    for i ← 1, ..., |ξ| do
        Get shape/enrichment functions (and their derivatives) and Jacobian:
        {j, N, B} ← functions(M, H, W, e^(k), ξ_i)
        Add contributions to stiffness matrix and force vector:
        k ← k + γ_i j B^T C B                    - Update stiffness matrix
        f ← f + γ_i j N^T b                      - Update nodal load vector
    return k, f
end function
```

Algorithm 2 Shape and enrichment functions, together with their derivatives

```
Input: Modified mesh M := {N ∪ N_e, E ∪ H}, ordered tree H, leaf integration
  element e^(k) at hierarchical level k, quadrature point at this level
  labeled ξ_i^(k);
Output: Jacobian determinant j, and arrays of shape and enrichment functions
  N together with their derivatives B.

  function FUNCTIONS(M, H, e^(k), ξ_i^(k))
    Get element coordinates:
    X = [x_1 ... x_4]^T  ← (N ∪ N_e) ∩ e^(k)
    Loop over element's enriched nodes:
    for n_j ← N_e ∩ e^(k) do
      do
        Shape functions and their derivatives:
        {N^(k), N^(k)_,ξ} ← Lagrange(e^(k), ξ_i^(k))
        x ← X^T N^(k)                                  - Obtain global coordinate
        J^(k) ← X^T N^(k)_,ξ                           - Obtain Jacobian matrix
        if not j then                                  - check if leaf Jacobian is set
          j ← det(J^(k))                               - Save leaf Jacobian
        N^(k)_,x ← N^(k)_,ξ [J^(k)]^-1                 - Compute derivatives with respect to x
        Add child contribution:
        Compute enrichments/derivatives at level k:
        {ψ^(k), ψ^(k)_,x}, {χ^(k), χ^(k)_,x} ← enrich(N^(k), N^(k)_,x)
        Stack functions and derivatives:
        {F, F_,x} ← {[F  ψ^(k)  χ^(k)], [F_,x  ψ^(k)_,x  χ^(k)_,x]}
        k ← k − 1                                      - Decrease level of hierarchy
        e^(k) ← H(k, e^(k))                            - Get parent element in the hierarchy
        ξ_i^(k) ← invert(x, e^(k))                     - Obtain local master coordinate
      while k ≠ 0                                      - If k ← 0, parent mesh element reached
    Add parent contribution:
    Shape functions and their derivatives:
    {N^(0), N^(0)_,ξ} ← Lagrange(e^(0), ξ_i^(0))
    Stack parent shape functions and their derivatives:
    {F, F_,x} ← {[N^(0)  F], [N^(0)_,x, F_,x]}
    Expand to multiple DOFs per node:
    {N, B} ← {expand(F), expand(F_,x)}
    return j, N, B
  end function
```

3

IMMERSED ANALYSIS OF PHONONIC CRYSTALS USING IGFEM

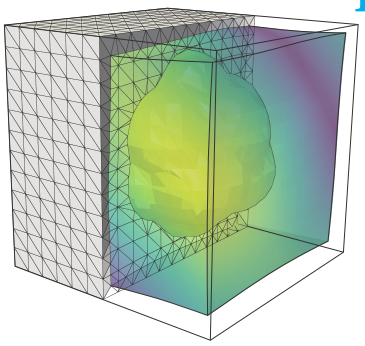

The formulation for immersed IGFEM, that was developed in Chapter 2, is extended in this chapter to the immersed analysis of phononic crystals. To that end, periodic unit cells are immersed in structured background meshes. In Section 3.2.1 a formulation is derived for the *strong* application of Bloch-Floquet boundary conditions on non-matching boundaries by means of multiple point constraints, analogous to the Dirichlet boundary conditions of Section 2.2.2. In Section 3.3, the proposed approach tested on the analysis of phononic crystals in 1-D, 2-D, and 3-D, and found to converge at the same rate as standard FEM. It is shown that both the phononic crystal geometry and periodicity can be modified without the burden of changing the underlying discretization.

This chapter has been published in
Computer Methods in Applied Mechanics and Engineering
doi.org/10.1016/j.cma.2021.113848

Fully decoupling geometry from discretization in the Bloch-Floquet finite element analysis of phononic crystals

3

Abstract *An immersed enriched finite element method is proposed for the analysis of phononic crystals (PnCs) with finite element (FE) meshes that are completely decoupled from geometry. Particularly, a technique is proposed to prescribe Bloch-Floquet periodic boundary conditions strongly on non-matching edges of the periodic unit cell (PUC). The enriched finite element formulation effectively transforms a periodic non-confirming discretization into an enriched node-to-node periodic discretizations where periodicity is enforced by any standard procedure. The enriched formulation is also used to describe the interior material interface. This completely eliminates the tedious process of generating matching or fitted meshes during the design process, as it allows changing the inclusion's geometry as well as the PnC's lattice type without changing the FE mesh. The proposed approach, which is used to analyze phononic crystals in 1-D, 2-D and 3-D using structured meshes, exhibits the same performance as the standard finite element analysis on fitted meshes.*

3.1. INTRODUCTION

Efficient analysis of phononic crystals (PnCs) is essential to their design for engineering applications. Specifically, computational design and optimization require the analysis of many variations of a design. In such cases, the fully immersed analysis of PnCs proposed in this work prevents the cumbersome procedure of generating matching meshes. As in the proposed method Bloch-Floquet boundary conditions are applied to non-matching edges in a *strong* manner, the lattice type as well as the inclusion can be altered without remeshing. Therefore, the computational design of PnCs is greatly simplified.

Phononic crystals have distinctive effects on waves traveling through them, and their design and optimization has therefore seen a recent increase in interest (Li *et al.*, 2019b; Yi and Youn, 2016). They exhibit bandgaps, *i.e.*, ranges of frequencies for which no waves can propagate through the material due to Bragg scattering. A negative effective density and modulus can also be attained (Mokhtari *et al.*, 2019). PnCs can be applied in many fields of engineering and across many length scales. For example, they can be used for thermal control (Davis and Hussein, 2014) at one end of the frequency spectrum, and for seismic engineering at the other end (Yan *et al.*, 2015). New sensing schemes for liquids based on PnCs have also been introduced for biological samples and for hazardous chemicals such as gasoline (Lucklum and Li, 2009; Oseev *et al.*, 2013). Additional appli-

cations can be found in vibrationless environments for high-precision systems, sound protection devices, and acoustic waveguides and lenses (Rupp *et al.*, 2010). Tuneable behavior may also be achieved: *in situ* changing of the impulse transmission can be achieved (Chaunsali *et al.*, 2017), and amplitude-tunable PnCs are optimized in (Manktelow *et al.*, 2013). Using a wave-like modulation of the constitutive parameters, symmetry and reciprocity of the wave propagation may even be broken (Nassar *et al.*, 2017).

In order to optimally utilize the full potential of PnCs, efficient and accurate models that capture the wave propagation properties are invaluable. Furthermore, methods for the systematic design of such crystals are required. For the analysis of PnCs, a large variety of modeling techniques is available. Examples are the Finite Element Method (FEM) (Veres *et al.*, 2013), the Boundary Element Method (BEM) (Isakari *et al.*, 2016; Li *et al.*, 2013a,b), Finite Differences - Time Domain (FDTD) (Su *et al.*, 2010; Tanaka *et al.*, 2000), Plane Wave Expansion (PWE) technique (Economou and Sigalas, 1993; Kushwaha *et al.*, 1994), the monodromy matrix method (Kutsenko *et al.*, 2013, 2011), the Spectral Element Method (SEM) (Shi *et al.*, 2016), IGA (Alberdi *et al.*, 2018), and meshfree methods (Zheng *et al.*, 2016). Homogenization approaches for the effective dynamic properties of PnCs are also being developed (Hu and Oskay, 2019; Nassar *et al.*, 2016; Sridhar *et al.*, 2018). While all of these methods have advantages and disadvantages, FEM is widely used for complex geometries, as it extends effortlessly to inclusions of any shape. With FEM, periodic structures are generally studied by analyzing a PUC, whereby requiring the displacements at opposite sides of the PUC to be equal, periodicity is enforced. In the case of wave propagation problems, Bloch-Floquet periodic BCs are used instead; these impose a phase difference between both edges of the unit cell, and as a result they can describe traveling waves.

Despite the ease of implementation of standard FEM, it has a big disadvantage: the procedure calls for a *matching* (or *fitted* or *geometry-conforming*) mesh, *i.e.*, the edges of finite elements *must* align to material interfaces and PUC's sides. Creating such a mesh is undesirable in many situations, for instance during an iterative design process, where the unit cell geometry is not known *a priori*. Moreover, even when the geometry is known, the process of generating matching meshes is computationally expensive and prone to errors when complex geometries are involved. The issue of remeshing can be avoided completely by non-fitted or enriched finite element approaches. Wang *et al.* (2019) have shown the use of a non-fitted Petrov-Galerkin interface approach for the analysis of PnCs. Similarly, the eXtended/Generalized Finite Element Method (X/GFEM) (Duarte *et al.*, 2000; Moës *et al.*, 1999) provides a means to decouple material discontinuities from the FE discretization, by enriching the finite element formulation with discontinuous functions that are associated to nodes of intersected elements. For PnCs, this was demonstrated by Zhao *et al.* (2015). However, X/GFEM has many disadvantages: as enrichment functions do not vanish at original mesh nodes, their degrees of freedom (DOFs) do not retain their physical meaning. Therefore, essential (Dirichlet) boundary conditions generally need to be imposed *weakly*, *e.g.*, by means of Lagrange multipliers or the penalty method (Cuba Ramos *et al.*, 2015). In the former case, positive definiteness of the system matrices is lost. Sanders *et al.* (2009) discuss various methods for applying and stabilizing interface constraints. For the Bloch-Floquet periodic analysis of quantum-mechanical problems, Sukumar and Pask (2009) proposed

a formulation for classical and enriched finite element methods by constructing Bloch-Floquet periodic trial and test spaces. Additionally, X/GFEM can lead to ill-conditioned system matrices, which may be remedied by the use of Stable Generalized FEM (SG-FEM) (Babuška and Banerjee, 2012; Gupta *et al.*, 2013; Kergrene *et al.*, 2016). Lastly, the accuracy of the approximation in blending elements—elements for which not all nodes are enriched—may deteriorate (Fries, 2008).

There is another family of enriched finite element methods that can fully decouple the discretization from the problem's geometric features (Aragón and Simone, 2017; van den Boom *et al.*, 2019b; Soghrati, 2014; Soghrati *et al.*, 2012a; Zhang *et al.*, 2019a); contrary to what is done in X/GFEM, enriched DOFs are collocated along discontinuities, eliminating many of the aforementioned issues. The Interface Enriched Generalized Finite Element Method (IGFEM) (Soghrati *et al.*, 2012a) was first proposed to solve problems with weak discontinuities, *i.e.*, where the gradient of the primal field is discontinuous as in problems containing perfectly bonded material interfaces. Enrichment functions in IGFEM are local to intersected elements by construction and they vanish at the original mesh nodes and at edges which are not crossed by material interfaces. As a result, Dirichlet boundary conditions are as straightforward to prescribe as in standard FEM. Dirichlet boundary conditions were prescribed weakly on enriched edges by Cuba-Ramos *et al.* (Cuba Ramos *et al.*, 2015), who first proposed IGFEM as an immersed (fictitious domain) method. In the context of computational design, the use of IGFEM for shape optimization has been shown for a range of engineering applications (Pejman *et al.*, 2019; Tan and Geubelle, 2017; Tan *et al.*, 2018a,b), and has been demonstrated for NURBS-based geometries as well (Najafi *et al.*, 2017). Recently, IGFEM was also proposed for level-set based topology optimization (van den Boom *et al.*, 2021b). The benefits of assigning enrichments to enriched nodes along the discontinuities have inspired two important extensions to the method: the Hierarchical Interfaced-enriched Finite Element Method (HIFEM) (Soghrati, 2014), that can resolve multiple interfaces interacting within a single finite element, and the Discontinuity-Enriched Finite Element Method (DE-FEM) (Aragón and Simone, 2017; Zhang *et al.*, 2019a). The latter is able to handle not only weak but also strong discontinuities—those where the field itself is discontinuous as in fracture problems—with a single unified formulation. DE-FEM inherits all assets of IGFEM and HIFEM, and in the absence of strong discontinuities (*e.g.*, cracks), it simplifies to these methods. Curved cracks and interfaces may also be analysed using DE-FEM with NURBS-based discontinuities (De Lazzari *et al.*, 2021).

In this paper, which builds on the recently proposed immersed DE-FEM with strong enforcement of Dirichlet boundary conditions (van den Boom *et al.*, 2019b), we introduce the Interface-enriched Generalized Finite Element Method for the fully immersed analysis of PnCs, for which we derive a method for applying Bloch-Floquet BCs along non-matching PUC edges, similar to the strong enforcement of Dirichlet BCs introduced in (van den Boom *et al.*, 2019b). We first verify the procedure by comparing the analytical and computed shear and pressure wave velocities obtained by means of an enriched immersed analysis of a homogeneous material. We then compare the convergence rates of IGFEM to those of standard FEM for a 1-D PnC and for the 2-D homogeneous PUCs, and demonstrate that the same rates of convergence are achieved for 2-D PnCs. Furthermore, we analyze a range of immersed 2-D phononic crystals with different lattice

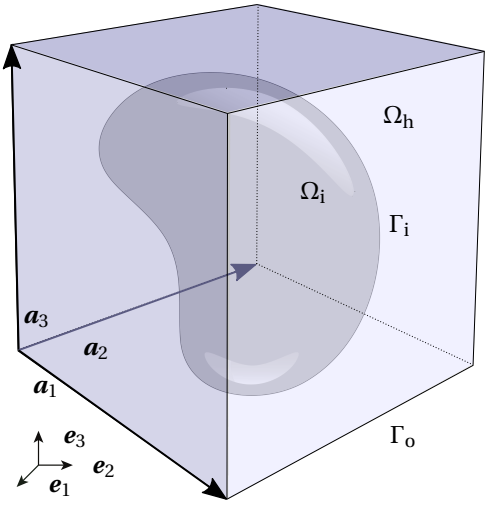

Figuur 3.1: Schematic representation of a PUC: a 3-D cube with lattice vectors $\boldsymbol{a}_1$, $\boldsymbol{a}_2$ and $\boldsymbol{a}_3$. The domain Ω consists of a host phase Ω_h and an inclusion Ω_i. The boundary between the two is denoted Γ_i, and Γ_o is the boundary of the PUC.

vectors, using the same background mesh, to demonstrate that full decoupling of mesh and PUC geometry is achieved. Finally, it is demonstrated that the formulation extends to complex 3-D phononic crystals, by means of an immersed cubic PUC with a "popcorn" shaped inclusion.

3.2. PROBLEM FORMULATION

In this work, we analyze PnCs by means of their periodic unit cell, represented by a d-dimensional parallelotope (line segment in 1-D, parallelogram in 2-D, or parallelepiped in 3-D). The PUC is replicated in d-dimensional space along the directions defined by lattice vectors $\boldsymbol{a}_i$, $i = \{1, \ldots, d\}$. The PUC, illustrated in Figure 3.1, will be denoted by an open domain $\Omega \subset \mathbb{R}^d$. It is composed by a host phase Ω_h and an inclusion phase Ω_i, such that $\Omega_h \cap \Omega_i = \emptyset$; the closure of the domain is denoted $\overline{\Omega} = \overline{\Omega}_h \cup \overline{\Omega}_i$. The boundary of the domain Ω is given by $\partial\Omega \equiv \Gamma_o = \overline{\Omega} \setminus \Omega$. We denote by Γ_i the interface separating the two material phases that is responsible for the weak discontinuity. Fields such as the displacement field $\boldsymbol{u}$ are defined over the entire domain Ω, whereas the restriction of the field to the subdomain Ω_j is denoted $\boldsymbol{u}_j(\boldsymbol{x}, t) \equiv \boldsymbol{u}|_{\Omega_j}$.

The governing equations that describe the linear behavior of the PnC are the homogeneous elastodynamic wave equation, the constitutive equation, and the linear continuity relation, which hold on both parts of the domain:

$$\rho_j \frac{\partial^2 \boldsymbol{u}_j}{\partial t^2} = \nabla \cdot \boldsymbol{\sigma}_j \qquad \text{in } \Omega_j,\ j = \mathrm{i}, \mathrm{h}, \tag{3.1}$$

$$\boldsymbol{\sigma}_j = \lambda_j \operatorname{tr}(\boldsymbol{\varepsilon}_j)\boldsymbol{\varepsilon}_j + 2\mu_j \boldsymbol{\varepsilon}_j, \tag{3.2}$$

$$\boldsymbol{\varepsilon}_j = \frac{1}{2}\left(\nabla \boldsymbol{u}_j + \nabla \boldsymbol{u}_j^{\mathsf{T}}\right), \tag{3.3}$$

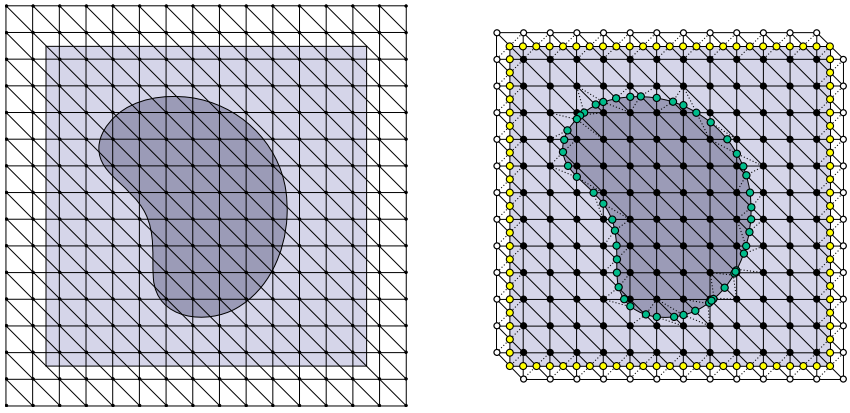

(a) (b)

Figuur 3.2: Mesh-independent periodic unit cell: (a) The PUC is immersed in a non-matching structured mesh; (b) Enriched nodes are placed along the discontinuities (● and ●) and integration elements are created. Elements that lie completely outside the PUC are removed, and nodes outside the PUC (○) are fixed. Bloch-Floquet periodic BCs are applied to enriched nodes on the PUC boundary (●).

with Bloch-Floquet periodic boundary conditions

$$\boldsymbol{u}(\boldsymbol{x}+\boldsymbol{a}_i, t) = e^{i(\mathbf{k}\cdot\boldsymbol{a}_i)}\boldsymbol{u}(\boldsymbol{x}, t) \qquad \text{on } \Gamma_o. \tag{3.4}$$

In (3.1) ρ_j is the material density, $\nabla\cdot$ is the divergence operator, $\boldsymbol{u}_j(\boldsymbol{x}, t)$ is the displacement as a function of position $\boldsymbol{x}$ and time t; similarly, $\boldsymbol{\sigma}_j(\boldsymbol{x}, t) \equiv \boldsymbol{\sigma}|_{\Omega_j}$ is the Cauchy stress tensor, described by the linearized strain tensor $\boldsymbol{\varepsilon}_j(\boldsymbol{x}, t) \equiv \boldsymbol{\varepsilon}|_{\Omega_j}$ and Lamé parameters λ_j and ν_j. In (3.4) $\mathbf{k}$ denotes the wave vector of the traveling wave. In accordance with Bloch-Floquet theory, the displacement field $\boldsymbol{u}$ corresponds to a traveling wave, modulated by some unknown periodic function $\boldsymbol{\Psi}(\boldsymbol{x})$ with the same periodicity as the medium:

$$\boldsymbol{u}(\boldsymbol{x}, t) = e^{i(\mathbf{k}\cdot\boldsymbol{x}-\omega t)}\boldsymbol{\Psi}(\boldsymbol{x}), \tag{3.5}$$

where ω is the angular frequency.

In weak form, the elastodynamic wave equation reads: Find $\boldsymbol{u} \in \mathcal{V}^\star$ such that

$$\sum_{j=\mathrm{h,i}} \left[\int_{\Omega_j} \rho_j\, \ddot{\boldsymbol{u}}_j\, \boldsymbol{v}_j \,\mathrm{d}\Omega + \int_{\Omega_j} \boldsymbol{\sigma}_j(\boldsymbol{u}_j) : \boldsymbol{\varepsilon}_j(\boldsymbol{v}_j) \,\mathrm{d}\Omega \right] = 0, \qquad \forall \boldsymbol{v} \in \mathcal{V}_0, \tag{3.6}$$

where $\mathcal{V}^\star$ is a *linear variety* that accounts for the non-homogeneous Bloch-Floquet BCs (Aragón and Simone, 2017), and $\mathcal{V}_0$ is a vector-valued function space on Ω_j, so that

$$\mathcal{V}_0 = \left\{ \boldsymbol{v} \in \left[\mathcal{L}^2(\Omega)\right]^d,\ \boldsymbol{v}|_{\Omega_i} \in \left[\mathcal{H}^1(\Omega_i)\right]^d,\ \boldsymbol{v}|_{\Gamma_o} = \mathbf{0},\ i = \mathrm{h,i} \right\}, \tag{3.7}$$

where $\mathcal{L}^2(\Omega)$ is the space of square-integrable functions and $\mathcal{H}^1(\Omega_i)$ is the first-order Sobolev space.

We solve the problem on a domain $\Delta \supseteq \Omega$ that fully encloses the PUC. The discretized domain Δ^h, or *background mesh*, does not necessarily conform to the geometric features of the PUC. To account for the mismatch between the discretization and the PUC's geometry, we choose our weight function and trial solution from the finite-dimensional IGFEM space $\mathcal{S}_e^h \subset \mathcal{V}_0$:

$$\mathcal{S}_e^h = \left\{ \boldsymbol{v}^h(\boldsymbol{x}) \,\middle|\, \boldsymbol{v}^h(\boldsymbol{x}) = \underbrace{\sum_{i \in \iota_h}^{n} N_i(\boldsymbol{x}) \boldsymbol{U}_i}_{\text{standard FEM}} + \underbrace{\sum_{i \in \iota_w} s_i \psi_i(\boldsymbol{x}) \boldsymbol{\alpha}_i}_{\text{enrichment}}, \quad \boldsymbol{U}_i, \boldsymbol{\alpha}_i \in \mathbb{R}^d \right\}, \tag{3.8}$$

where ι_h refers to the index set of all original mesh nodes, ι_w is the set of enriched nodes, and s_i refers to a scaling factor that produces well-conditioned system matrices and thus makes the formulation *stable* (Aragón *et al.*, 2020). The space $\mathcal{S}_e^h$ consists of the standard FEM approximation—the first term with standard Lagrange shape functions N_i and standard DOFs $\boldsymbol{U}_i$—that is augmented with an enriched term that introduces, by means of enrichment functions ψ_i and associated enriched DOFs $\boldsymbol{\alpha}_i$, the required jumps in the gradient of the solution field.

In order to construct the IGFEM enrichment functions, operations on the background mesh using the PUC geometry are required, as illustrated in Figure 3.2: new nodes (shown by ● and ● symbols) are created at intersections of the boundaries (Γ_o and Γ_i) with edges of elements of the background mesh; the cut elements are subdivided into *integration elements* accordingly, as illustrated with dotted lines. The purpose of these integration elements is fourfold:

- as their name suggests, the integration elements are used for integration of the elements' local arrays;
- the enrichment functions ψ_i are constructed as linear combinations of standard Lagrange shape functions of those integration elements;
- the integration elements are used to ensure the field can be displayed correctly after postprocessing; and
- the triangular or tetrahedral integration elements are easy to split, thus facilitating a hierarchical implementation when multiple discontinuites cross a single element.

Elements that lie completely outside the PUC are removed from the analysis, as are DOFs corresponding to outside nodes (shown with ○ symbols). In the case that an element is intersected by multiple discontinuities, this procedure can simply be applied hierarchically, as described in detail in Soghrati (2014) and Aragón *et al.* (2020).

Following a Bubnov-Galerkin approach, the discretized system of linear equations, $\boldsymbol{M}\ddot{\boldsymbol{U}} - \boldsymbol{K}\boldsymbol{U} = \boldsymbol{0}$, can now be obtained via standard procedures, with global stiffness and mass matrix, $\boldsymbol{K}$ and $\boldsymbol{M}$, respectively:

$$\boldsymbol{K} = \bigwedge_i \boldsymbol{k}_i, \quad \boldsymbol{M} = \bigwedge_i \boldsymbol{m}_i. \tag{3.9}$$

The finite element assembly operator is here written as $\mathbb{A}$ and $\boldsymbol{k}_i$, $\boldsymbol{m}_i$ denote element local stiffness and mass matrices, respectively, which are obtained by numerical quadrature.

Once $\boldsymbol{K}$ and $\boldsymbol{M}$ are assembled, Bloch-Floquet periodicity is enforced by means of a transformation matrix $\boldsymbol{T}$. This complex matrix contains the complex exponent of the Bloch-Floquet BCs and is therefore a function of the wave vector $\mathbf{k}$. The modified system matrices $\tilde{\boldsymbol{K}}$ and $\tilde{\boldsymbol{M}}$ can be found by pre- and post-multiplying the original matrices with $\boldsymbol{T}$, resulting in complex Hermitian matrices:

$$\begin{aligned} \tilde{\boldsymbol{K}}(\mathbf{k}) &= \boldsymbol{T}(\mathbf{k})^{\mathsf{H}} \boldsymbol{K} \boldsymbol{T}(\mathbf{k}), \\ \tilde{\boldsymbol{M}}(\mathbf{k}) &= \boldsymbol{T}(\mathbf{k})^{\mathsf{H}} \boldsymbol{M} \boldsymbol{T}(\mathbf{k}). \end{aligned} \tag{3.10}$$

This rectangular transformation matrix $\boldsymbol{T}$ reduces the size of the system of linear equations, as subordinate periodic boundary DOFs are removed (*e.g.*, in contrast to Lagrange multiplier methods, where the system of linear equations is augmented). The costs of these operations are relatively low, as the transformation matrix $\boldsymbol{T}(\mathbf{k})$ is very sparse; for the internal part of the domain it is the identity matrix, and the only off-diagonal terms relate to the boundary DOFs. Due to the sparsity of $\boldsymbol{T}$ as well as $\boldsymbol{K}$ and $\boldsymbol{M}$, these operations can be performed very efficiently. As the boundaries of the PUC are lower-dimensional manifolds (*e.g.*, lines in 2-D and surfaces in 3-D), the cost of these transformations relative to the cost of solving the system reduces with mesh refinement. The dispersion relation—or band structure—is subsequently obtained by performing a series of eigenvalue analyses for a set of wave vectors $\mathbf{k}_j$, defined along the edge of the irreducible Brillouin zone (Brillouin, 1930):

$$\left[\tilde{\boldsymbol{K}}(\mathbf{k}_j) - \omega_j^2 \tilde{\boldsymbol{M}}(\mathbf{k}_j)\right] \boldsymbol{V}_j = \mathbf{0}, \tag{3.11}$$

where $\boldsymbol{V}_j$ are complex eigenvectors that represent traveling waves and ω_j are the corresponding eigenfrequencies.

Although IGFEM has not been used in phononic crystal analysis before, it can be readily used to describe the material interfaces within the periodic unit cell. However, when a discontinuity crosses the PUC boundary, or when the PUC itself is non-matching, enriched nodes are subject to Bloch-Floquet periodicity as well, as explained in the next section.

3.2.1. BLOCH-FLOQUET PERIODICITY ON ENRICHED NODES

Bloch-Floquet periodic BCs enforce periodicity of the PUC, but allow for a phase difference of the traveling wave between unit cells; they guarantee that the displacements $\boldsymbol{u}$ take the form of a Bloch wave throughout the entire domain, while only operating on the boundaries. As these BCs operate directly on the field $\boldsymbol{u}$, we follow the procedure for Dirichlet BCs on immersed IGFEM edges using multiple point constraints (MPCs), as described by van den Boom *et al.* (2019b). On the boundary nodes of the PUC, Bloch-Floquet periodic boundary conditions are applied as

$$\boldsymbol{u}(\boldsymbol{x}_{\mathrm{s}}) = e^{i\mathbf{k}\cdot\boldsymbol{a}} \boldsymbol{u}(\boldsymbol{x}_{\mathrm{m}}), \tag{3.12}$$

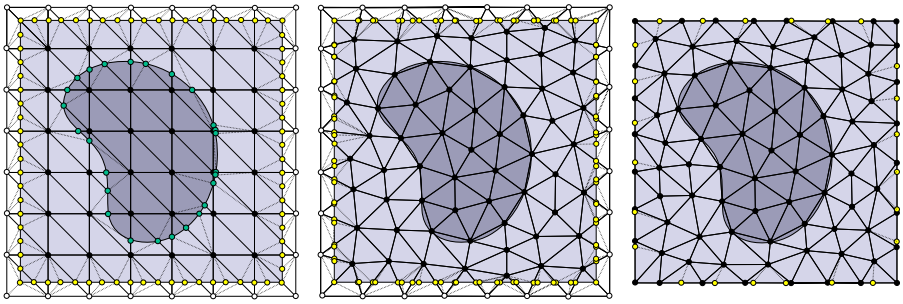

(a) (b) (c)

Figuur 3.3: Cases where boundary nodes are not spaced exactly one lattice vector apart: (a,b) PUCs immersed in a structured (a) and unstructured (b) meshes, where additional enriched nodes are added to properly enforce periodicity; (c) PUC were the mesh conforms to both the inclusion and the outer PUC edge, but the nodes on either side do not coincide, so enriched nodes are added.

where $\boldsymbol{u}(\boldsymbol{x}_\mathrm{m})$ and $\boldsymbol{u}(\boldsymbol{x}_\mathrm{s})$ are displacements corresponding to a main and a subordinate node, respectively. These two nodes are assumed to be separated by exactly one lattice vector $\boldsymbol{a}$, as attempting to apply periodicity to non-matching nodes would result in inaccurate results. In general, enriched nodes are not guaranteed to coincide on either side of the PUC, thus Bloch-Floquet periodicity cannot be enforced directly. In such cases, supplementary enriched nodes can be added to ensure that every enriched boundary node has a counterpart. These extra enriched nodes can easily be accounted for by creating additional integration elements, and as such they do not change the rest of the procedure. Figure 3.3 illustrates some situations where the enriched nodes do not coincide exactly. Figure 3.3a is similar to Figure 3.2 in that it shows a square unit cell immersed in a structured mesh. The difference is that the PUC edges do not lie exactly in the middle of the background elements, so that the intersections with the diagonal element edges do not coincide on either side of the PUC. Other cases where the boundary nodes do not coincide are found in unstructured meshes, regardless of whether the edges are immersed, as in Figure 3.3b, or conforming, as in Figure 3.3c. In cases where the nodes do not coincide, the full procedure to prescribe the Bloch-Floquet periodic boundary conditions on immersed edges is:

- Find the intersections between the immersed edges and the background elements;
- Find the counterpart of these nodes by adding the lattice vector to the coordinate vector of the node;
- Create integration elements taking into account all enriched nodes.

In IGFEM, the enriched DOFs do not directly represent the displacement field at their location because the *partition of unity* property is lost in intersected elements [1]. Instead,

[1] In IGFEM, enrichment functions $\psi_i(x)$ are added to the standard FEM approximation, breaking the partition of unity. The original shape function N_i do not vanish at the locations of the enriched nodes, and as a result, the displacements at those locations are computed per Eq. (3.13). However, because enrichment functions vanish at original mesh nodes, the Kronecker-δ property on those nodes is retained and therefore standard DOFs keep their physical meaning.

the solution also depends on the DOFs of the parent cut element, as given by (3.8). The solution at the enriched locations can therefore be written for $j = \mathrm{m}, \mathrm{s}$ as:

$$\boldsymbol{u}(\boldsymbol{x}_j) = \sum_{i \in \iota_j} N_i(\boldsymbol{x}_j)\boldsymbol{U}_i + s_j \psi_j(\boldsymbol{x}_j)\boldsymbol{\alpha}_j, \tag{3.13}$$

where the index set $\iota_j \subset \iota_h$ refers to the parent nodes which have a non-zero contribution on the enriched node location $\boldsymbol{x}_j$, and $\psi_j(\boldsymbol{x}_j) = 1$. Expanding (3.12) in terms of this IGFEM approximation results in an expression from which the subordinate DOFs of the system can be calculated:

$$\boldsymbol{\alpha}_\mathrm{s} = \frac{e^{i\mathbf{k}\cdot\boldsymbol{r}}}{s_\mathrm{s}\psi_\mathrm{s}(\boldsymbol{x}_\mathrm{s})}\left[\sum_{i\in\iota_\mathrm{m}} N_i(\boldsymbol{x}_\mathrm{m})\boldsymbol{U}_i + s_\mathrm{m}\psi_\mathrm{m}(\boldsymbol{x}_\mathrm{m})\boldsymbol{\alpha}_\mathrm{m}\right] - \frac{1}{s_\mathrm{s}\psi_\mathrm{s}(\boldsymbol{x}_\mathrm{s})}\sum_{i\in\iota_\mathrm{s}} N_i(\boldsymbol{x}_\mathrm{s})\boldsymbol{U}_i. \tag{3.14}$$

Writing such a constraint equation for every subordinate node results in a system of equations, that can be written in the form:

$$\begin{bmatrix}\boldsymbol{U}\\ \boldsymbol{\alpha}\end{bmatrix} = \boldsymbol{T}\begin{bmatrix}\tilde{\boldsymbol{U}}\\ \tilde{\boldsymbol{\alpha}}\end{bmatrix}, \tag{3.15}$$

where $\boldsymbol{T}$ is a complex-valued transformation matrix that is a function of wave vector $\mathbf{k}$, and that maps between the free system $\begin{bmatrix}\boldsymbol{U} & \boldsymbol{\alpha}\end{bmatrix}^\mathsf{T}$ and the constrained system $\begin{bmatrix}\tilde{\boldsymbol{U}} & \tilde{\boldsymbol{\alpha}}\end{bmatrix}^\mathsf{T}$. The system matrices can now be modified as described in Eq. (3.10). A one-dimensional example on the construction of $\boldsymbol{T}$ is given in the Appendix.

In cases where the parent elements of the outer edges of the PUC are intersected by multiple discontinuities, *e.g.*, when the immersed inclusion crosses the PUC edge, a hierarchical implementation of the multiple point constraint is required. This implementation follows naturally from the HIFEM approximation, and is described for Dirichlet boundary conditions by van den Boom *et al.* (2019b).

3.3. NUMERICAL RESULTS

3.3.1. 1-D PHONONIC CRYSTAL

Consider in Figure 3.4 a 1-D phononic crystal composed of two materials of dissimilar properties. A PUC of length $L \equiv \|a_1\|$ can be defined such that its boundaries lie on the host and the other material outlines an inclusion of length b. The materials used are polycarbonate and lead for the host and inclusion, respectively. Polycarbonate (lead) has an elasticity modulus $E_1 = 2.3\,\mathrm{GPa}$ ($E_2 = 16\,\mathrm{GPa}$) and density $\rho_1 = 1200\,\mathrm{kg/m^3}$ ($\rho_2 = 11\,340\,\mathrm{kg/m^3}$). This phononic crystal has a total unit cell length $L = 25\,\mathrm{mm}$, with an inclusion of length $b = 14\,\mathrm{mm}$. Therefore, the length of the two sections are $l_\mathrm{h} = 11\,\mathrm{mm}$ and $l_\mathrm{i} = 14\,\mathrm{mm}$, respectively.

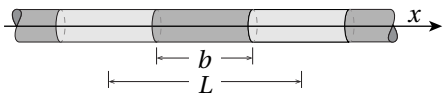

Figuur 3.4: One-dimensional phononic crystal with PUC of length L.

Following Nielsen and Sorokin (2015) for the analytic solution, we scale the lengths by l_h and time by $l_\mathrm{h}/c_\mathrm{h}$, where c_h is the wave speed in the host material. This problem can then be described by the non-dimensionalized 1-D wave equation on both material domains ($i = \mathrm{h}, \mathrm{i}$):

$$\frac{\partial^2 u_i(x,t)}{\partial x^2} = \frac{1}{c_i/c_\mathrm{h}} \frac{\partial^2 u_i(x,t)}{\partial t^2}, \tag{3.16}$$

with the wave speeds

$$c_i = \sqrt{E_i/\rho_i}, \tag{3.17}$$

interface conditions

$$u_\mathrm{h}(1,t) = u_\mathrm{i}(1,t), \tag{3.18}$$

$$u'_\mathrm{h}(1,t) = \frac{E_2}{E_1} u'_\mathrm{i}(1,t), \tag{3.19}$$

Bloch-Floquet periodic boundary conditions

$$u_\mathrm{h}(0,t) = u_\mathrm{i}(1 + \frac{L_\mathrm{i}}{L_\mathrm{h}}, t)\, \lambda, \tag{3.20}$$

$$u'_\mathrm{h}(0,t) = \frac{E_\mathrm{i}}{E_\mathrm{h}} u'_2(1 + \frac{L_\mathrm{i}}{L_\mathrm{h}}, t)\, \lambda, \tag{3.21}$$

and with the propagation constant $\lambda = e^{ikL}$. A non-trivial solution to the system of equations can be found if λ is a solution to the characteristic equation

$$\lambda^2 + q(\hat{\omega})\lambda + 1 = 0, \tag{3.22}$$

with

$$q(\hat{\omega}) = -2\cos(\hat{\omega})\cos(\tau\hat{\omega}) + \left(\kappa + \frac{1}{\kappa}\right)\sin(\hat{\omega})\sin(\tau\hat{\omega}), \tag{3.23}$$

where $\tau = l_\mathrm{i} c_\mathrm{h}/l_\mathrm{h} c_\mathrm{i}$ is the ratio of propagation times, and $\kappa = E_\mathrm{i} c_\mathrm{h}/E_\mathrm{h} c_\mathrm{i}$ is the ratio of impedances of the two materials. Looping over $\hat{\omega}$ and solving for λ, the analytic solution can be computed.

The numerical results are obtained using two different approaches:

- standard FEM using matching meshes;
- IGFEM using meshes that do not match to the PUC edges nor to the material interfaces.

We define the error with respect to the analytic solution as

$$\epsilon = \sqrt{\frac{1}{|K|N} \frac{\sum_{\mathrm{k}\in K}\sum_n (\omega_{\mathrm{k},n} - \hat{\omega}_{\mathrm{k},n})^2}{\sum_{\mathrm{k}\in K}\sum_n \hat{\omega}^2_{\mathrm{k},n}}} \qquad n = 1, 2, \ldots, N, \tag{3.24}$$

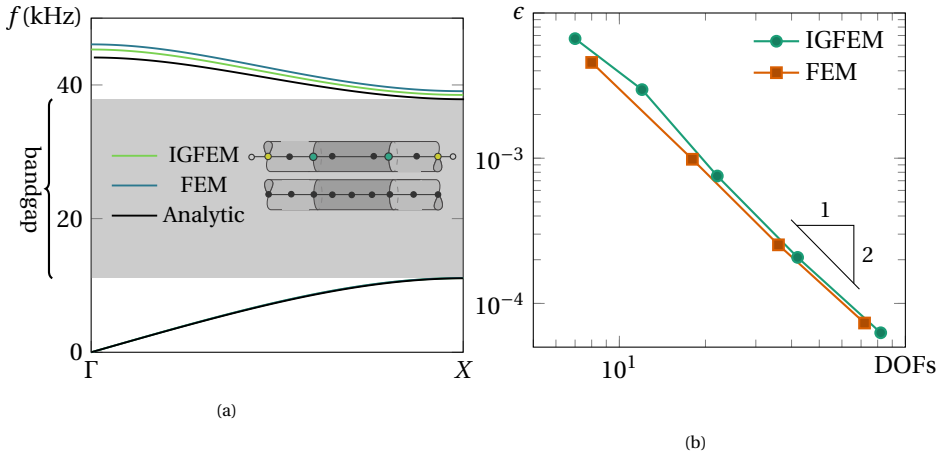

Figuur 3.5: (a) Dispersion curve (band structure) and bandgap for the 1-D phononic crystal, where the IGFEM result on a 5-element background mesh is compared to a matching mesh with a comparable number of DOFs; (b) Mesh convergence for the relative error in the first two bands given by Eq. (3.24).

where K is the set of wave numbers in the Brillouin zone, $K = \{\Gamma, \ldots, X\}$, with cardinality $|K|$, $\hat{\omega}_{\mathrm{k},n}$ denotes the nth analytic frequency for a given wave number k and $\omega_{\mathrm{k},n}$ is the numerical counterpart. In other words, Eq. (3.24) is the relative error in the L^2-norm of the first N bands evaluated at $|K|$ wave numbers.

The first two bands of the band structure are shown in Figure 3.5a for the analytical solution and the two numerical results that were obtained on a fixed mesh size with meshes composed of 5 elements. Both FEM and IGFEM give more accurate results for lower frequencies, so more deviation from the analytic result is expected in the higher bands. Figure 3.5b considers mesh refinement and shows the convergence for the error (3.24) as a function of the number of DOFs, with $N = 5$ and $|K| = 100$. It is shown that IGFEM has the same rate of convergence as the standard FEM on matching meshes.

3.3.2. 2-D UNIFORM MATERIAL

To investigate the performance of the enriched boundary conditions in 2-D, we consider the velocity of pressure and shear waves through a uniform polycarbonate slab, with a Poisson ratio $\nu = 0.37$ and, as in the previous example, $E = 2.3\,\mathrm{GPa}$ and $\rho = 1200\,\mathrm{kg/m^3}$. It should be noted that this is not a PnC, and as such, no dispersion is expected. This material is analyzed using a square PUC with a side length $L = 0.025\,\mathrm{m}$, so that the lattice vectors $\boldsymbol{a}_i$ and reciprocal lattice vectors $\boldsymbol{b}_i$ are given by

$$\boldsymbol{a}_1 = \begin{bmatrix} 0.025 \\ 0 \end{bmatrix} \mathrm{m},\ \boldsymbol{a}_2 = \begin{bmatrix} 0 \\ 0.025 \end{bmatrix} \mathrm{m},\ \boldsymbol{b}_1 = \begin{bmatrix} 251.33 \\ 0 \end{bmatrix} \mathrm{m}^{-1},\ \boldsymbol{b}_2 = \begin{bmatrix} 0 \\ 251.33 \end{bmatrix} \mathrm{m}^{-1}. \tag{3.25}$$

The vertices of the irreducible Brillouin zone are therefore located at $\Gamma = \begin{bmatrix} 0 & 0 \end{bmatrix}^\mathsf{T} \mathrm{m}^{-1}$, $X = \begin{bmatrix} 125.66 & 0 \end{bmatrix}^\mathsf{T} \mathrm{m}^{-1}$ and $M = \begin{bmatrix} 125.66 & 125.66 \end{bmatrix}^\mathsf{T} \mathrm{m}^{-1}$. The PUC is analyzed using standard FEM and IGFEM using a 60×60 structured mesh with triangular elements for both cases, and results are reported in Figure 3.6. The nature of each band, which

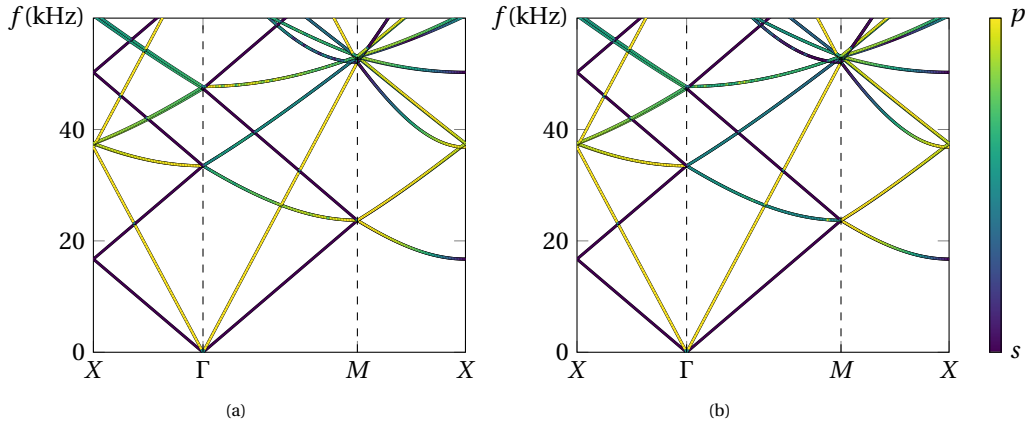

Figuur 3.6: Band structure for a PUC of uniform polycarbonate, obtained on a 60 × 60 matching mesh (a), and on a 60 × 60 non-matching mesh with enriched Bloch-Floquet boundary conditions (b). The nature of each wave in the uniform material is investigated in more detail: the color of each line signifies whether the wave is an s-wave (blue), a p-wave (yellow), or a combination thereof. Both matching and non-matching meshes recover the same wave types for each band.

is found by projecting the normalized displacements in the vibration mode onto the wave vector using a dot product and averaging the nodal results, is plotted in Figures 3.6a and 3.6b, for standard FEM and IGFEM, respectively. Blue refers to a pure shear wave and yellow refers to a pure pressure wave. It is clear that both methods recover the same wave types for each band.

The velocities of shear and pressure waves are now recovered numerically as

$$v_s = \frac{2\pi f_s}{\|\mathbf{k}\|} \text{ and } v_p = \frac{2\pi f_p}{\|\mathbf{k}\|}. \tag{3.26}$$

The numerical wave velocities, computed using IGFEM (or FEM) as $v_s = 836.53\,\mathrm{m/s}$ and $v_p = 1841.53\,\mathrm{m/s}$, are in close agreement with the exact velocities,

$$\hat{v}_s = \sqrt{\frac{G}{\rho}} = 836.37\,\mathrm{m\,s^{-1}} \text{ and } \hat{v}_p = \sqrt{\frac{M}{\rho}} = 1841.18\,\mathrm{m\,s^{-1}}, \tag{3.27}$$

where the shear modulus G and pressure wave modulus M are given, respectively, by

$$G = \frac{E}{2(1-2\nu)} \text{ and } M = \frac{E(1-\nu)}{(1+\nu)(1-2\nu)}. \tag{3.28}$$

To study the convergence of the wave velocities, we define an error norm for the shear and pressure waves:

$$\epsilon_s = \sqrt{\frac{(v_s - \hat{v}_s)^2}{\hat{v}_s^2}}\ ,\ \epsilon_p = \sqrt{\frac{\left(v_p - \hat{v}_p\right)^2}{\hat{v}_p^2}}. \tag{3.29}$$

In the results of Figure 3.7 it is shown that IGFEM and standard FEM converge towards the exact solution at the same terminal convergence rate. Furthermore, the absolute

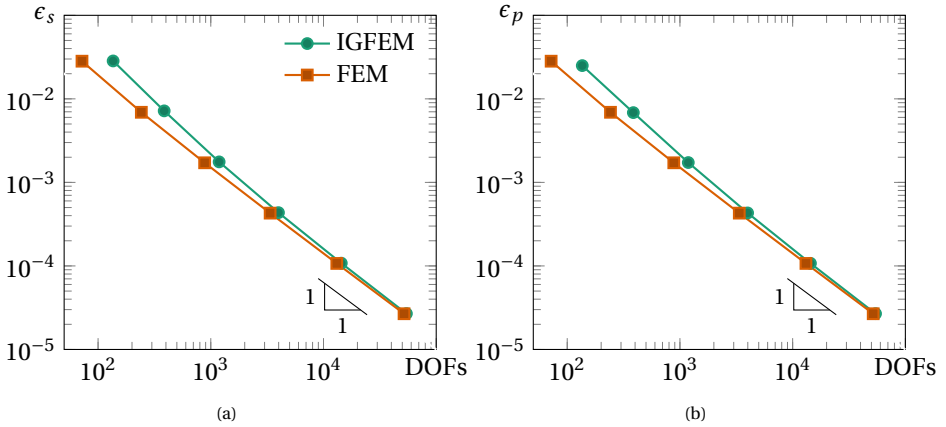

Figuur 3.7: Convergence of the shear wave velocity (a) and pressure wave velocity (b) for a uniform material. Both the shear wave velocity and the pressure wave velocity converge at the same rate for standard FEM and IGFEM.

value of the error is similar for FEM and IGFEM. Therefore, it can be concluded that the enriched boundary conditions do not influence the solution in 2-D.

3.3.3. 2-D PHONONIC CRYSTAL WITH A CIRCULAR INCLUSION

A 2-D phononic crystal containing a circular inclusion of radius r in a square lattice is now analyzed. A PUC of size $L \times L$ can be defined, as illustrated in Figure 3.8. The same materials as for the 1-D phononic crystal are used for the host and inclusion; polycarbonate and lead ($E_1 = 2.3\,\text{GPa}$, $E_2 = 16\,\text{GPa}$, $\nu_1 = 0.37$, $\nu_2 = 0.44$, $\rho_1 = 1200\,\text{kg/m}^3$, $\rho_2 = 11\,340\,\text{kg/m}^3$). The dimensions of this PnC are $L = 25\,\text{mm}$ and $r = 7\,\text{mm}$. The lattice vectors and reciprocal lattice vectors for this problem are the same as in the previous example, as the unit cell is of the same dimensions. Therefore, the locations of the Brillouin zone vertices are also the same, located at $\Gamma = \begin{bmatrix}0 & 0\end{bmatrix}^\intercal \text{m}^{-1}$, $X = \begin{bmatrix}125.66 & 0\end{bmatrix}^\intercal \text{m}^{-1}$ and $M = \begin{bmatrix}125.66 & 125.66\end{bmatrix}^\intercal \text{m}^{-1}$.

The numerical results, obtained using IGFEM on different mesh sizes, are compared to the results obtained using standard FEM on a very fine (overkill) matching mesh, which we will regard to be the correct result. From the band structure in Figure 3.8c, it can be seen that a bandgap opens in the range 18 kHz to 28 kHz. Some propagation bands appear in the bandgap for very coarse meshes, but with mesh refinement, the bandgap converges towards that of the reference matching mesh. The error for each band n with respect to the reference solution is defined by

$$\epsilon_n = \sqrt{\frac{1}{|K|}\frac{\sum_{\mathbf{k}\in K}(\omega_{\mathbf{k},n} - \omega^*_{\mathbf{k},n})^2}{\sum_{\mathbf{k}}\omega^{*2}_{\mathbf{k},n}}}, \tag{3.30}$$

where K defines a set of wave vectors $\mathbf{k}$ along the irreducible Brillouin zone ($X \rightarrow \Gamma \rightarrow M \rightarrow X$). Furthermore, an error norm is defined for the frequencies that define the band-

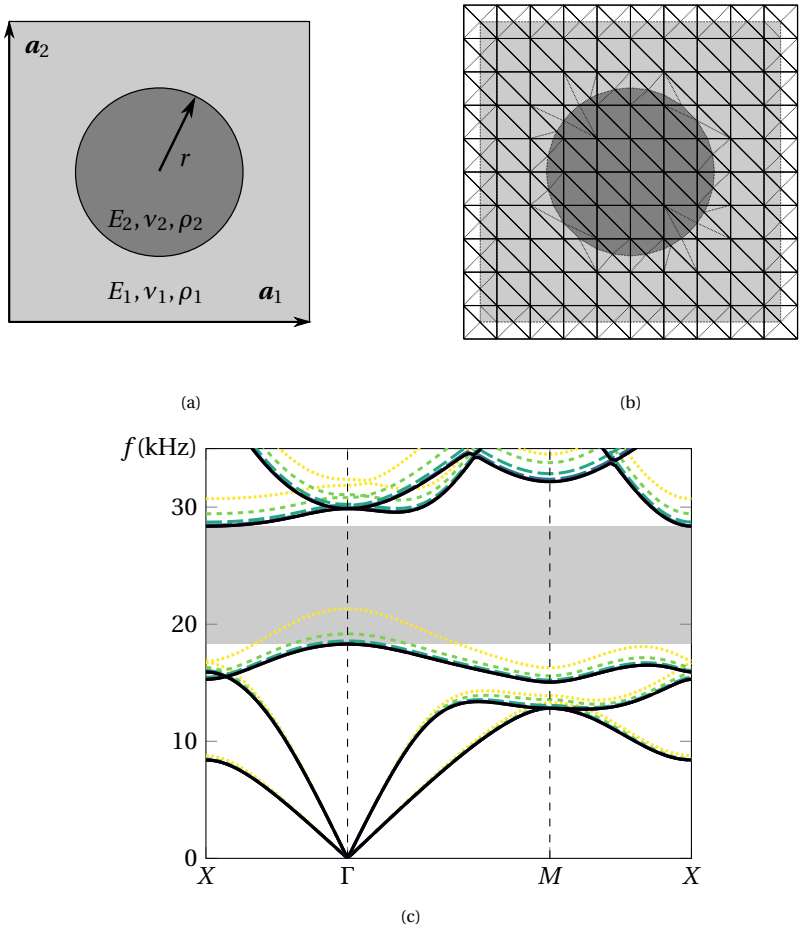

Figuur 3.8: (a) Schematic of a square PUC with lattice vectors $\boldsymbol{a}_1$ and $\boldsymbol{a}_2$ and a circular inclusion of radius r; (b) the PUC is immersed in a 10×10 non-matching structured mesh; (c) Band structure for a square PUC with a circular inclusion, obtained by multiple non-matching meshes consisting of $5 \times 5 \times 2$ ( ), $10 \times 10 \times 2$ ( ), $20 \times 20 \times 2$ ( ), $40 \times 40 \times 2$ ( ), $80 \times 80 \times 2$ ( ), and $160 \times 160 \times 2$ ( ) triangular elements and a very fine matching mesh ( ). The bandgap is plotted for the finest matching mesh. Clearly, a coarse representation of a non-matching mesh results in propagation bands inside the gap. However, the bandgap converges with mesh refinement.

gap between the third and the fourth propagation bands:

$$\epsilon_{\text{low}} = \sqrt{\frac{\left(\max\left(\omega_{\mathbf{k},3}\right) - \max\left(\omega^*_{\mathbf{k},3}\right)\right)^2}{\max\left(\omega^*_{\mathbf{k},3}\right)^2}} \quad \text{and} \quad \epsilon_{\text{high}} = \sqrt{\frac{\left(\min\left(\omega_{\mathbf{k},4}\right) - \min\left(\omega^*_{\mathbf{k},4}\right)\right)^2}{\min\left(\omega^*_{\mathbf{k},4}\right)^2}}. \tag{3.31}$$

The convergence of the first 5 bands is shown in Figure 3.9a. The error increases slightly

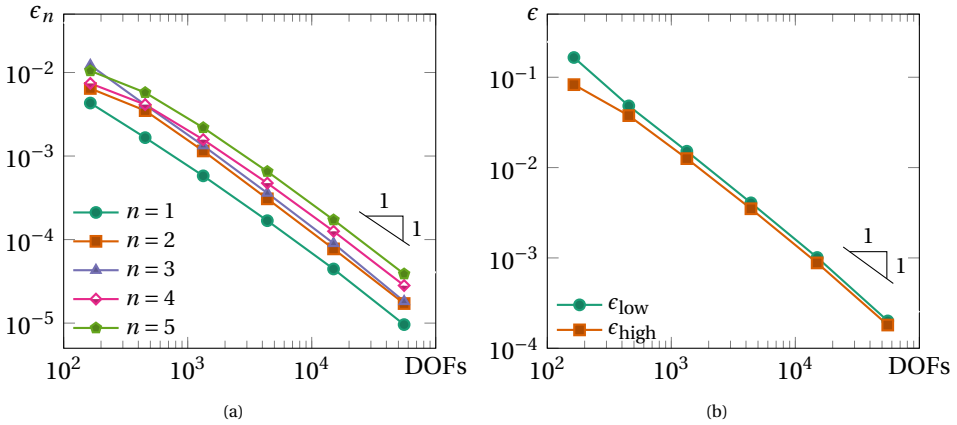

Figuur 3.9: Convergence for the PnC with a circular inclusion in a square lattice. In (a), the error for the first five propagation bands as defined in Eq (3.30) is shown to have the same rate of convergence. In (b) the convergence of the error defined in Eq. (3.31) is shown for the frequencies that define the bandgap.

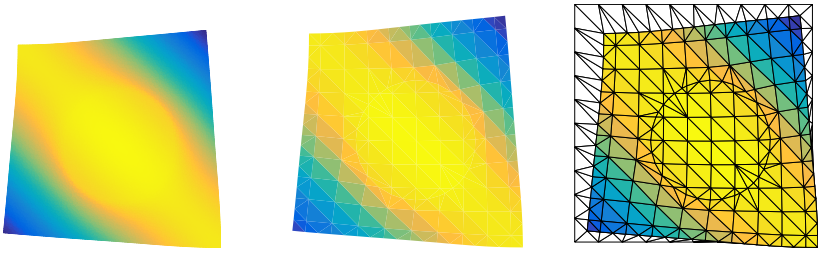

Figuur 3.10: Snapshot of a traveling wave on the lowest band between Γ and M on (a) a fine matching mesh; (b) a 10×10 non-matching structured mesh; the non-matching mesh is also shown in (c). The same mode shapes are obtained for both analyses.

for the higher bands, which is to be expected in eigenvalue analysis because the higher frequencies correspond to shorter wave lengths which are not captured accurately by the relatively coarse discretizations. Nonetheless, all bands converge at the same rate. In Figure 3.9b it is shown that the frequencies that define the bandgap converge at a slightly higher rate (1.5).

The motion of a wave traveling between Γ and X ($\mathbf{k} = \begin{bmatrix}62.83 & 62.83\end{bmatrix}^\mathsf{T}\,\mathrm{m}^{-1}$) on the first propagation band, obtained from a coarse IGFEM mesh and a fine FEM mesh, are now compared. Figure 3.10a shows a snapshot of a traveling wave for the very fine matching mesh, while Figures 3.10b and 3.10c show the same wave at the same time on a non-matching mesh defined over a 10×10 grid. The same mode is indeed resolved on both meshes.

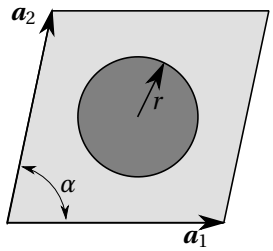

Figuur 3.11: General periodic unit cell for the phononic crystal with a varying lattice: the angle α between lattice vectors $\boldsymbol{a}_1$ and $\boldsymbol{a}_2$ is varied while the inclusion with radius r is kept the same.

Tabel 3.1: Lattice vectors $\boldsymbol{a}_i$ and reciprocal lattice vectors $\boldsymbol{b}_i$ for the different lattice angles α that were analyzed on the same structured meshes.

Lattice angle α	Lattice vectors		Reciprocal lattice vectors	
	$\boldsymbol{a}_1$ (m)	$\boldsymbol{a}_2$ (m)	$\boldsymbol{b}_1$ (m^{-1})	$\boldsymbol{b}_2$ (m^{-1})
60° (Triangular lattice)	$\begin{bmatrix}0.027\\0.000\end{bmatrix}$	$\begin{bmatrix}0.013\\0.023\end{bmatrix}$	$\begin{bmatrix}233.89\\-135.03\end{bmatrix}$	$\begin{bmatrix}0.00\\270.07\end{bmatrix}$
70° (Rhombic lattice)	$\begin{bmatrix}0.026\\0.000\end{bmatrix}$	$\begin{bmatrix}0.009\\0.024\end{bmatrix}$	$\begin{bmatrix}243.63\\-88.67\end{bmatrix}$	$\begin{bmatrix}0.00\\259.27\end{bmatrix}$
80° (Rhombic lattice)	$\begin{bmatrix}0.025\\0.000\end{bmatrix}$	$\begin{bmatrix}0.004\\0.024\end{bmatrix}$	$\begin{bmatrix}249.41\\-43.98\end{bmatrix}$	$\begin{bmatrix}0.00\\253.26\end{bmatrix}$
90° (Square lattice)	$\begin{bmatrix}0.025\\0.000\end{bmatrix}$	$\begin{bmatrix}0.000\\0.025\end{bmatrix}$	$\begin{bmatrix}251.33\\0.00\end{bmatrix}$	$\begin{bmatrix}0.00\\251.33\end{bmatrix}$

3.3.4. 2-D PHONONIC CRYSTAL WITH A VARYING LATTICE

In previous examples, the combinations of PUC and background mesh were chosen such that enriched nodes, placed at intersections of the background elements with the PUC edge, were separated by exactly one lattice vector. This means that only certain configurations of PnCs could be analyzed within a given mesh. However, to achieve true mesh-geometry decoupling this requirement is now removed. Additional enriched DOFs are placed on either side of the PUC to ensure that each enriched node has a periodic counterpart. In this numerical example, phononic crystals with different lattices, with a variable angle α between both lattice vectors, are analyzed on the same square structured mesh, for which the general PUC is illustrated in Figure 3.11. The different PnCs, with a circular inclusion ($r = 7$ mm), are chosen such that the volume fraction of the inclusion versus the host material is the same ($\phi = 0.2463$). Furthermore, for each phononic crystal, the magnitude of both lattice vectors are chosen to be the same ($\|\boldsymbol{a}_1\| = \|\boldsymbol{a}_2\|$), such that the lattices are triangular ($\alpha = 60°$), square ($\alpha = 90°$), or rhombic ($\alpha = 70°$ and $\alpha = 80°$). The lattice vectors that were used for the four cases, and their corresponding reciprocal lattice vectors, are given in Table 3.1.

The material properties of the inclusion and host are the same as in previous examples. In the discretization of these PUCs, extra enriched nodes are placed along the PUC edge, such that all enrichments are spaced exactly one lattice vector apart. Only

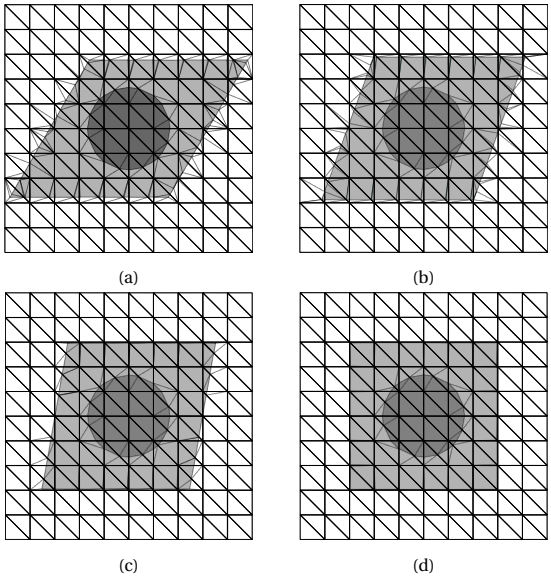

Figuur 3.12: Integration meshes for the four periodic unit cells, analyzed on the coarsest structured mesh defined on a 10×10 grid.

then can Bloch-Floquet periodic boundary conditions be applied as described in § 3.2.1. Figure 3.12 illustrates the coarsest integration mesh for each periodic unit cell.

Each layout is analyzed on a square grid of $10 \times 10 \times 2$, $20 \times 20 \times 2$, $40 \times 40 \times 2$, and $80 \times 80 \times 2$ triangular elements, and on a fine matching mesh. Figure 3.13 summarizes the results of the different PnCs. On the left, the PUC and corresponding irreducible Brillouin zone are illustrated. The middle figures show the band structures for the different PnCs, computed on different mesh sizes. The results given on the right in Figure 3.13 show that the convergence rates of these dispersion bands are the same as those in previous examples. In Figure 3.14, snapshots of waves are given for the same wave vector in different phononic crystals: Figure 3.14(a-d) correspond to the Brillouin zone vertex M of the triangular lattice, and Figure 3.14(e-f) correspond to the Brillouin zone vertex M of the square lattice. For the rhombic lattices, neither wave vector corresponds to a symmetry point. Therefore, Figures 3.14a and 3.14h correspond to standing waves, whereas the other figures represent traveling waves. This is confirmed by the fact that the modes in Figures 3.14a and 3.14h are symmetric, and the rest are not.

3.3.5. 3-D PHONONIC CRYSTAL

To demonstrate the method in 3-D, we analyze a cubic PUC with a popcorn-shaped inclusion. This geometry is described by the function

$$\phi(\boldsymbol{x}) = \sqrt{\|\boldsymbol{x}\|} - r - \sum_{k=0}^{11} A \exp\left[-\frac{\|\boldsymbol{x} - \boldsymbol{x}^{(k)}\|}{\varsigma^2}\right], \tag{3.32}$$

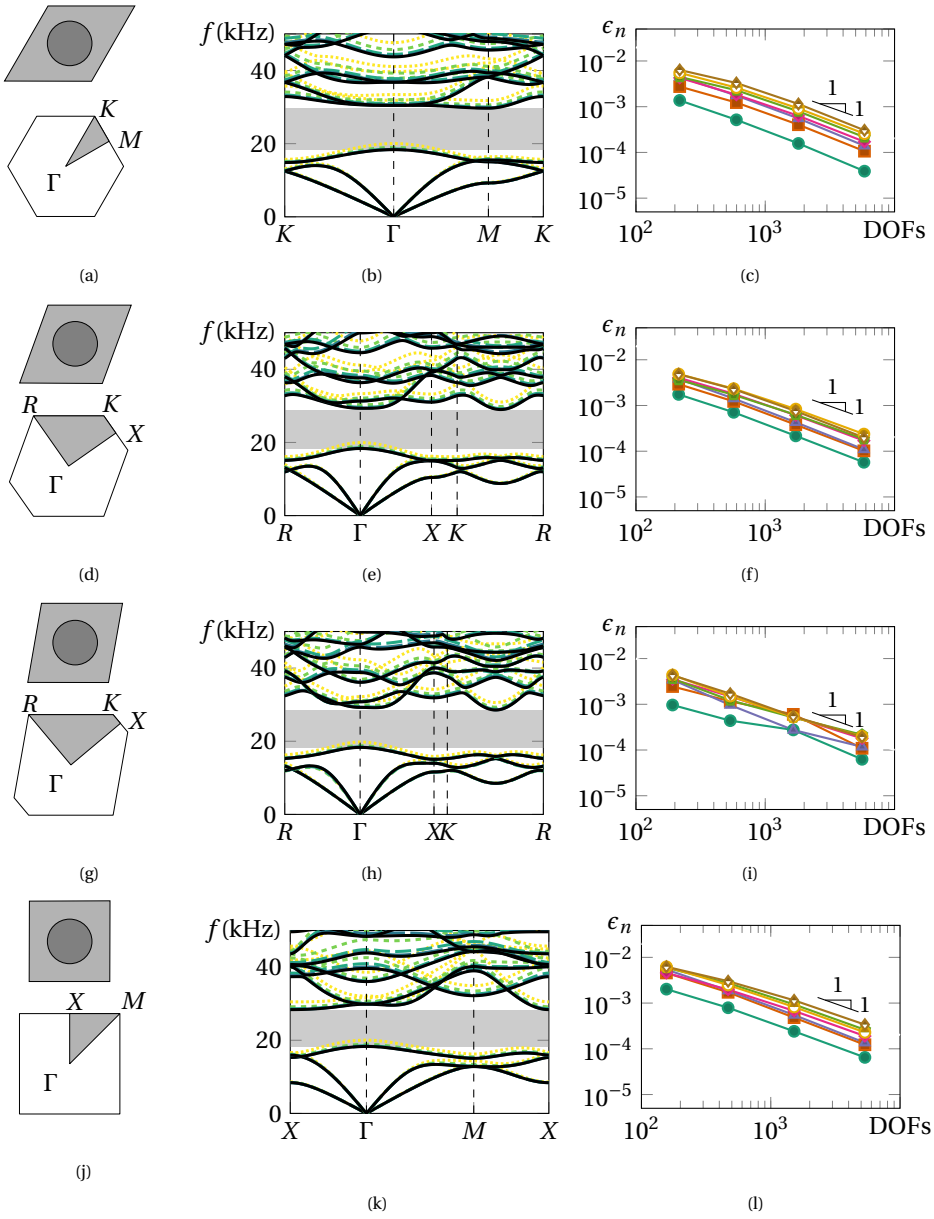

Figuur 3.13: Phononic crystals with the same volume fractions but with different lattice types (*i.e.*, with PUCs of different shapes) are analyzed on structured meshes. In (a), (d), (g), and (j) periodic unit cells and their corresponding (irreducible) Brillouin zones are shown. Their corresponding dispersion curves are shown in (b),(e),(h), and (k), where results of structured meshes consisting of $10 \times 10 \times 2$ ( ), $20 \times 20 \times 2$ ( ), $40 \times 40 \times 2$ ( ), $80 \times 80 \times 2$ ( ) triangular elements, and a matching mesh ( ) are compared. The convergence rates of the first seven bands, as defined in (3.30), are plotted in (c),(f),(i), and (l).

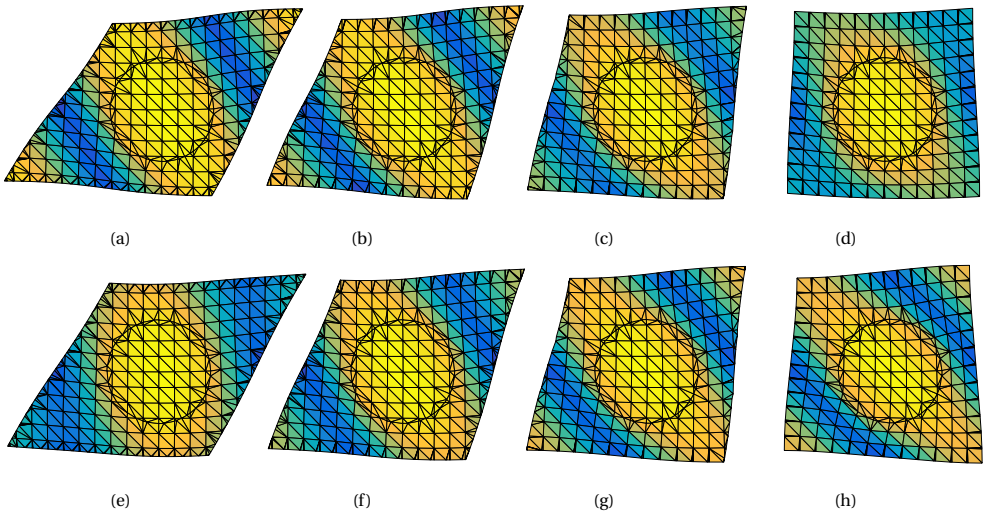

Figuur 3.14: Snapshots of a wave with wave vector $[116.94, 67.52]^\mathsf{T}\,\mathrm{m}^{-1}$, *i.e.*, M for the triangular lattice (a)-(d), and with wave vector $[125.67, 125.67]^\mathsf{T}\,\mathrm{m}^{-1}$, *i.e.*, M for the square lattice (e)-(h). Figures (a) and (h) correspond to standing waves, whereas the others to traveling waves. This illustrates the different behavior of the same wave vector in different periodic media.

where $r = 0.6$, $\varsigma = 0.2$, $A = 4$, and

$$\boldsymbol{x}^{(k)} = \begin{cases} \frac{r}{\sqrt{5}}\left[2\cos\left(\frac{2k\pi}{5}\right) \quad 2\sin\left(\frac{2k\pi}{5}\right) \quad 1\right]^\mathsf{T} & \text{for } 0 \le k \le 4, \\ \frac{r}{\sqrt{5}}\left[2\cos\left(\frac{(2(k-5)-1)\pi}{5}\right) \quad 2\sin\left(\frac{(2(k-5)-1)\pi}{5}\right) \quad -1\right]^\mathsf{T} & \text{for } 5 \le k \le 9, \\ \left[0 \quad 0 \quad r\right]^\mathsf{T} & \text{for } k = 10, \\ \left[0 \quad 0 \quad -r\right]^\mathsf{T} & \text{for } k = 11. \end{cases} \tag{3.33}$$

The PUC has volume $L \times L \times L$, where $L = 25\,\mathrm{mm}$, and is immersed in a larger background mesh. The PUC is illustrated in Figure 3.15a. As constituent materials, we again use polycarbonate (lead) for the host (inclusion). The vertices of the 3-D irreducible zone are located at $\Gamma = \left[0 \quad 0 \quad 0\right]^\mathsf{T}\mathrm{m}^{-1}$, $X = \left[125.66 \quad 0 \quad 0\right]^\mathsf{T}\mathrm{m}^{-1}$, $M = \left[125.66 \quad 125.66 \quad 0\right]^\mathsf{T}\mathrm{m}^{-1}$ and $R = \left[125.66 \quad 125.66 \quad 125.66\right]^\mathsf{T}\mathrm{m}^{-1}$. The resulting band structure is obtained on non-matching tetrahedral meshes defined on $6\times6\times6$, $8\times8\times8$, $10\times10\times10$ and $12\times12\times12$ grids (with 6 tetrahedra per cubic unit in the grid), and on a matching mesh composed of 33610 tetrahedral elements. Figure 3.16 illustrates the results, where it is shown that even on coarse meshes, reasonable approximations can be made on non-matching meshes in 3-D.

3.4. SUMMARY AND CONCLUSIONS

In this paper we achieved, for the first time, full decoupling of mesh and geometry in the analysis of phononic crystals in 1-D, 2-D, and 3-D by means of immersed analysis

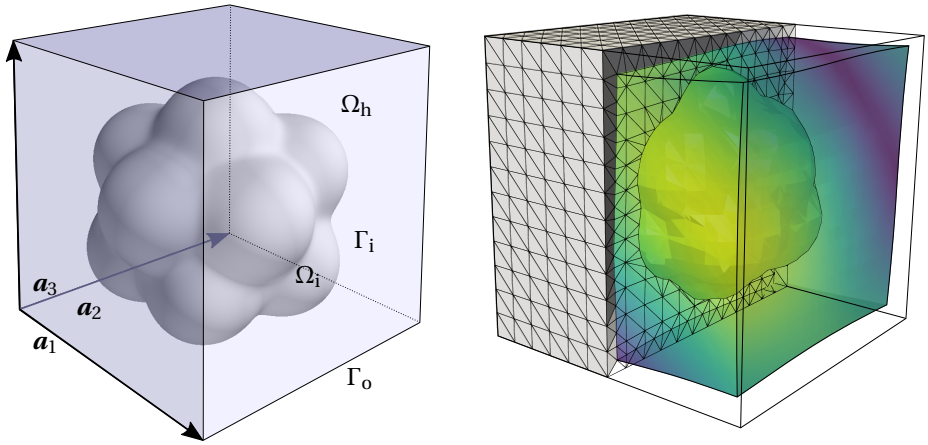

Figuur 3.15: Three dimensional phononic crystal: (a) Schematic of the cubic PUC with lattice vectors $\boldsymbol{a}_1$, $\boldsymbol{a}_2$ and $\boldsymbol{a}_3$ and a popcorn-shaped inclusion. The host material is polycarbonate, and the inclusion is made of lead; (b) The deformed PUC is completely immersed in a non-matching background mesh. In this snapshot, a traveling wave in $\Gamma \rightarrow R$ is illustrated.

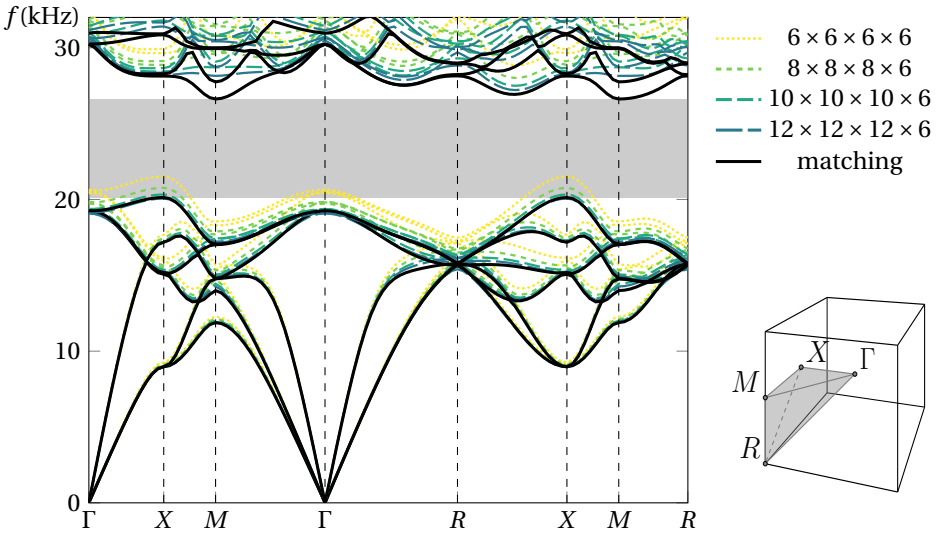

Figuur 3.16: Dispersion curve for a cubic PUC with a popcorn-shaped inclusion, obtained by multiple non-matching meshes and a matching mesh. The bandgap is plotted for the matching mesh. In different colors, IGFEM solutions for different mesh sizes are shown. The irreducible Brillouin zone of the cubic lattice is plotted to the right. It is found that even for coarse meshes, a reasonable prediction of the bandstructure can be obtained.

of periodic unit cells using the Interface-enriched Generalized Finite Element Method. Both the inclusion and the outer edges of the PUC are allowed to be defined independently from the background mesh, either explicitly (by line segments) or implicitly (by means of a level set function). Bloch-Floquet periodic boundary conditions are applied in a strong manner using multiple point constraints, reminiscent of the strong application of Dirichlet boundary conditions proposed recently in van den Boom *et al.* (2019b). As the IGFEM operations are restricted to lower-dimensional manifolds (*i.e.*, the material interfaces and PUC boundaries), they do not dominate the computational costs for sufficiently refined meshes; the computational costs are dominated by solving the eigenvalue problem. The resulting formulation provides considerable flexibility in the analysis of phononic crystals with varying inclusions and/or lattices.

The method's convergence properties were compared to standard FEM. This was done by means of two numerical examples: a 1-D phononic crystal, where the methods were compared against an analytic solution proposed in Kushwaha *et al.* (1994), and a 2-D uniform material, where the numerical band structures were used to compute velocities for shear and pressure waves that were compared to analytical velocities. In both 1-D and 2-D examples, the convergence rates of IGFEM and standard FEM were found to be the same. Therefore, the results obtained on a very fine matching mesh were used as reference solution for the following examples.

Several 2-D phononic crystals were analyzed. First, the strong enforcement of Bloch-Floquet periodic boundary conditions on non-matching edges was demonstrated on carefully chosen combinations of PUC and background mesh (§ 3.3.2); they were chosen such that enriched nodes on either side of the PUC matched up exactly, so that no extra steps were required for the enforcement of BCs. In the example of § 3.3.4, this requirement was released, and 2-D phononic crystals of different non-matching lattice shapes were analyzed. To that end, extra enriched nodes where added along the PUC edges to ensure periodicity could be enforced properly. In both cases, the results were shown to converge to those of the fine matching mesh at the same rate that was previously found. Lastly, a 3-D phononic crystal with a popcorn-shaped inclusion was analyzed. In the examples shown in this paper, the inclusions and PUC boundaries never intersect the same background element. Through the use of HIFEM (Soghrati, 2014), it is also possible to analyze unit cells where the inclusion crosses the PUC boundary. However, the boundary conditions would also need to be implemented hierarchically, as described for Dirichlet boundary conditions elsewhere (van den Boom *et al.*, 2019b).

As other enriched methods, IGFEM also has a number of drawbacks. For example, as shown in (Nagarajan and Soghrati, 2018; Soghrati *et al.*, 2017), IGFEM overestimates stresses in integration elements with bad aspect ratios. Although it has been shown that this effect is less prominent near Dirichlet boundaries (van den Boom *et al.*, 2019b), and in the context of DE-FEM near traction-free cracks (Zhang *et al.*, 2019a), the approximation of stresses in elements with bad aspect ratios is still an open research question. Furthermore, as in standard FEM, the higher bands are approximated less accurately. Higher order interpolation functions and enrichment functions could be investigated to mitigate this drawback.

To the best of our knowledge, this is the first work in which complete decoupling of the mesh and geometry in the analysis of phononic crystals with the same accuracy as

that of standard FEM with matching meshes is demonstrated. The advantage of decoupling the mesh from the geometry is most apparent in cases where the geometry of the PUC is not known *a priori*, such as during the design or optimization of the phononic crystal PUC. Using this method, a range of phononic crystals can readily be analyzed without the need for remeshing, and the immersed optimization of phononic crystals is a matter of computing sensitivities and including an optimization loop. As the geometry of the inclusion may be defined implicitly by a level set, the level-set based enriched topology optimization introduced by van den Boom *et al.* (2021b) may be employed. In fact, the topology optimization of PnCs using IGFEM is the subject of an incoming publication. Following Veres *et al.* (2013) it is also possible to extend the enriched method in a $\mathbf{k}(\omega)$-formulation, which can be used to also obtain the evanescent waves. In this method, dynamic condensation is used to reduce the problem to its boundary nodes. The properties of the wave vectors along the irriducible Brillouin zone are then used to write the problem as palindromic quadratic and quartic eigenvalue problems (polynomial eigenvalue problems where the coefficient matrices form a palindrome). For arbitrary wave vectors it is more challenging to solve. Finally, the proposed method may also be used for the analysis of locally resonant acoustic metamaterials. However, as their behavior does not depend on the lattice type, the benefit of being able to modify the outer boundary of the PUC is lost in this case.

The use of additional IGFEM nodes to prescribe periodic boundary conditions on non-conforming and immersed edges extends beyond the procedure described here for PnCs. In fact, a similar approach is used for the coupling between non-conforming meshes and contact, which is the subject of an incoming publication (Liu *et al.*, 2022).

APPENDIX: CONSTRUCTING A TRANSFORMATION MATRIX FOR A SIMPLE 1-D PUC

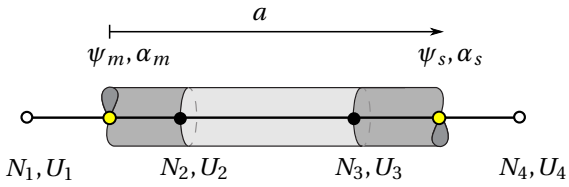

Figuur 3.17: One-dimensional mesh that is non-matching to the PnC on the outer boundaries for the demonstration of the construction of the $\boldsymbol{T}$ matrix.

The construction of the $\boldsymbol{T}$ matrix for a simple 1-D PUC as in Figure 3.17 is explained in detail in this section. For simplicity, a very coarse mesh is used that is matching to the internal material interfaces. However, the extension to more complex problems in higher dimensions is straightforward.

In order to apply Bloch-Floquet boundary conditions on the two nodes shown as ○, the general condition

$$u(x_\mathrm{s}) = e^{i\mathbf{k}\cdot a} u(x_\mathrm{m}), \tag{3.34}$$

has to be satisfied, where $u(x_\mathrm{m})$ and $u(x_\mathrm{s})$ are displacements corresponding to the left

and right enriched nodes, respectively. These nodes are separated by the lattice constant a. Using the IGFEM approximation, $u(x_\mathrm{m})$ and $u(x_\mathrm{s})$ are found as:

$$\begin{aligned} u(x_\mathrm{m}) &= N_1(x_\mathrm{m})U_1 + N_2(x_\mathrm{m})U_2 + s_\mathrm{m}\psi_\mathrm{m}(x_\mathrm{m})\alpha_\mathrm{m} \\ u(x_\mathrm{s}) &= N_3(x_\mathrm{s})U_3 + N_4(x_\mathrm{s})U_4 + s_\mathrm{s}\psi_\mathrm{s}(x_\mathrm{s})\alpha_\mathrm{s} \end{aligned} \tag{3.35}$$

Substituting Equation (3.35) into Equation (3.34) yields

$$N_3(x_\mathrm{s})U_3 + N_4(x_\mathrm{s})U_4 + s_\mathrm{s}\psi_\mathrm{s}(x_\mathrm{s})\alpha_\mathrm{s} = e^{i\mathrm{k}\cdot a}\left(N_1(x_\mathrm{m})U_1 + N_2(x_\mathrm{m})U_2 + s_\mathrm{m}\psi_\mathrm{m}(x_\mathrm{m})\alpha_\mathrm{m}\right), \tag{3.36}$$

which can then be rewritten as

$$\alpha_\mathrm{s} = \frac{e^{i\mathrm{k}\cdot a}}{s_\mathrm{s}\psi_\mathrm{s}(x_\mathrm{s})}\left(N_1(x_\mathrm{m})U_1 + N_2(x_\mathrm{m})U_2 + s_\mathrm{m}\psi_\mathrm{m}(x_\mathrm{m})\alpha_\mathrm{m}\right) - \frac{1}{s_\mathrm{s}\psi_\mathrm{s}(x_\mathrm{s})}\left(N_3(x_\mathrm{s})U_3 + N_4(x_\mathrm{s})U_4\right). \tag{3.37}$$

Written in the form $\boldsymbol{U} = \boldsymbol{T}\bar{\boldsymbol{U}}$, using a transformation matrix $\boldsymbol{T}$, the enriched subordinate DOF α_s can be eliminated:

$$\begin{bmatrix} U_1 \\ U_2 \\ U_3 \\ U_4 \\ \alpha_\mathrm{m} \\ \alpha_\mathrm{s} \end{bmatrix} = \begin{bmatrix} 1 & 0 & 0 & 0 & 0 \\ 0 & 1 & 0 & 0 & 0 \\ 0 & 0 & 1 & 0 & 0 \\ 0 & 0 & 0 & 1 & 0 \\ 0 & 0 & 0 & 0 & 1 \\ e^{i\mathrm{k}\cdot a}\frac{N_1(x_\mathrm{m})}{s_\mathrm{s}\psi_\mathrm{s}(x_\mathrm{s})} & e^{i\mathrm{k}\cdot a}\frac{N_2(x_\mathrm{m})}{s_\mathrm{s}\psi_\mathrm{s}(x_\mathrm{s})} & \frac{N_3(x_\mathrm{s})}{s_\mathrm{s}\psi_\mathrm{s}(x_\mathrm{s})} & \frac{N_4(x_\mathrm{s})}{s_\mathrm{s}\psi_\mathrm{s}(x_\mathrm{s})} & e^{i\mathrm{k}\cdot a}\frac{s_\mathrm{m}\psi_\mathrm{m}(x_\mathrm{m})}{s_\mathrm{s}\psi_\mathrm{s}(x_\mathrm{s})} \end{bmatrix} \begin{bmatrix} U_1 \\ U_2 \\ U_3 \\ U_4 \\ \alpha_\mathrm{m} \end{bmatrix}. \tag{3.38}$$

4

LEVEL SET-BASED TOPOLOGY OPTIMIZATION USING IGFEM

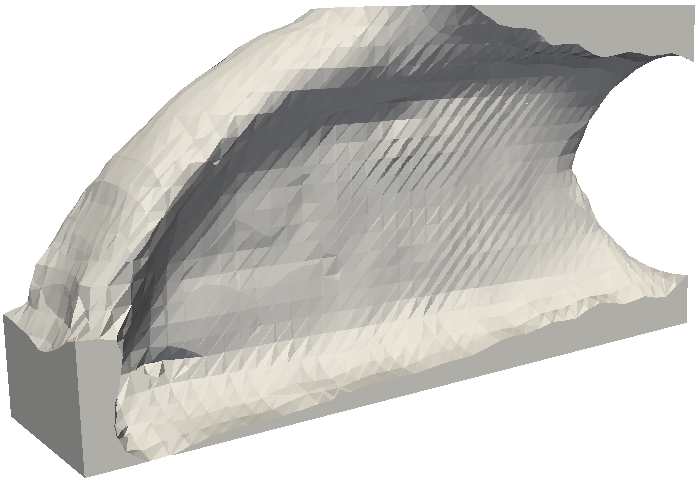

Whereas previous chapters concentrate on immersed *analysis*, this chapter focuses on immersed *design* using topology optimization. A level set based topology optimization framework using IGFEM is developed in Section 4.2.1, and applied to the design of minimum compliance structures in Section 4.3. The most challenging aspect of the formulation—the sensitivity analysis—is detailed in Section 4.2.3.

This chapter has been published in
Structural and Multidisciplinary Optimization
doi.org/10.1007/s00158-020-02682-5

An Interface-enriched Generalized Finite Element Method for Level Set-based Topology Optimization

Abstract *During design optimization, a smooth description of the geometry is important, especially for problems that are sensitive to the way interfaces are resolved, e.g., wave propagation or fluid-structure interaction. A level set description of the boundary, when combined with an enriched finite element formulation, offers a smoother description of the design than traditional density-based methods. However, existing enriched methods have drawbacks, including ill-conditioning and difficulties in prescribing essential boundary conditions. In this work we introduce a new enriched topology optimization methodology that overcomes the aforementioned drawbacks; boundaries are resolved accurately by means of the Interface-enriched Generalized Finite Element Method (IGFEM), coupled to a level set function constructed by radial basis functions. The enriched method used in this new approach to topology optimization has the same level of accuracy in the analysis as the standard finite element method with matching meshes, but without the need for remeshing. We derive the analytical sensitivities and we discuss the behavior of the optimization process in detail. We establish that IGFEM-based level set topology optimization generates correct topologies for well-known compliance minimization problems.*

4.1. INTRODUCTION

The use of enriched finite element methods in topology optimization approaches is not new; the eXtended/Generalized Finite Element Method (X/GFEM) (Aragón *et al.*, 2010; Belytschko *et al.*, 2009; Moës *et al.*, 1999, 2003; Oden *et al.*, 1998), for example, has been explored in this context. However, the Interface-enriched Generalized Finite Element Method (IGFEM) has been shown to have many advantages over X/GFEM (van den Boom *et al.*, 2019b; Soghrati *et al.*, 2012a). In this work we extend IGFEM to be used in a level set based topology optimization framework.

Topology optimization, first introduced by Bendsøe and Kikuchi (1988), has been widely used to obtain designs that are optimized for a certain functionality, *e.g.*, minimum compliance. In the commonly-used density-based methods, a continuous design variable that represents a material density is assigned to each element in the discretization. The design is pushed towards a *black and white* design by means of an interpolation function, *e.g.*, the Solid Isotropic Material with Penalisation (SIMP) (Bendsøe, 1989), that disfavors intermediate density values (also referred to as gray values). A filter is then required to prevent checkerboard-like density patterns, and to impose a minimum fea-

ture size. However, due to the filter, gray values are introduced. Density based topology optimization is straightforward to implement and widely available in both research and commercial software. However, because the topology is described by a density field on a (usually) structured mesh, material interfaces not only contain gray values but also suffer from *pixelization* or *staircasing*—staggered boundaries that follow the finite element mesh. Although a post-processing step can be performed to smoothen the final design, the analysis during optimization is still based on gray density fields and a staircased representation. This may be detrimental to the approximate solution's accuracy, especially in cases that are sensitive to the boundary description, such as flow problems (Villanueva and Maute, 2017). Furthermore, because the location of the material boundary is not well defined, it is difficult to track the evolving boundary during optimization, for example to impose contact constraints.

The aforementioned drawbacks could be alleviated by the use of geometry-fitted discretization methods, which have been widely used in shape optimization (Staten *et al.*, 2012). In these methods, the location of the material interface is known throughout the optimization, and the analysis mesh is modified to completely eliminate the pixalization and gray values. Mesh-morphing methods such as the deformable simplex method (Christiansen *et al.*, 2014, 2015; Misztal and Bundefinedrentzen, 2012; Zhou *et al.*, 2018), level set-based mesh evolution (Allaire *et al.*, 2014), anisotropic elements (Jensen, 2016), and r-refinement (Yamasaki *et al.*, 2017), have been demonstrated for topology optimization. Nevertheless, adapting the mesh in every design iteration remains a challenge. Not only is it an extra computational step, the changing discretization also introduces another complication in the optimization procedure because design variables need to be mapped to the new discretization (van Dijk *et al.*, 2013).

A more elegant option is to define material interfaces independently from the finite element discretization, *e.g., implicitly* by means of the zero-contour of a level set function. In level set methods, the material boundary is moved by evolving the level set function, and new holes can be nucleated by means of topological derivatives (Amstutz and Andrä, 2006). Although the required mapping between the geometry and the discretization mesh can be done with an Ersatz method using material density interpolation (Allaire *et al.*, 2004), this again introduces gray values and staircasing into the analysis. Similarly, NURBS-based topology optimization using the Finite Cell Method (FCM) (Gao *et al.*, 2019) provides a higher resolution boundary description, that is however, still staircased. Alternatively, there are methods that allow for a one-to-one mapping of the topology to the analysis mesh, resulting in a non-pixalized boundary description. These methods combine the advantages of clearly defined material interfaces with the benefits of a fixed discretization mesh used in density-based methods. In the literature, level set-based topology optimization has been established using for the analysis CutFEM (Burman *et al.*, 2018; Villanueva and Maute, 2017), where the basis functions are restricted to the physical domain, and X/GFEM (Belytschko *et al.*, 2003; Liu *et al.*, 2016a; Villanueva and Maute, 2014), where the approximation space is enriched.

In enriched finite element methods such as X/GFEM, the standard finite element space is augmented by enrichment functions that account for *a priori* knowledge of the discontinuity of the field or its gradient at cracks or material interfaces, respectively. Although X/GFEM has been shown to be advantageous in many applications, *e.g.*,

fluid-structure interaction (Mayer *et al.*, 2010) and fracture mechanics (Fries and Belytschko, 2010), the method has also weaknesses: degrees of freedom (DOFs) corresponding to original mesh nodes do not automatically retain their physical meaning, and non-zero essential boundary conditions mostly have to be prescribed *weakly*. Moreover, X/GFEM may result in ill-conditioned matrices, in which case Stable Generalized FEM (SGFEM) (Babuška and Banerjee, 2012; Gupta *et al.*, 2013; Kergrene *et al.*, 2016) or advanced preconditioning schemes (Lang *et al.*, 2014) are needed. Furthermore, the approximation of stresses can be highly overestimated near material boundaries (Noël and Duysinx, 2017; Sharma and Maute, 2018; Van Miegroet and Duysinx, 2007). Finally, as the enriched functions are associated with original mesh nodes, the accuracy of the approximation may degrade in blending elements, *i.e.* elements that do not have all nodes enriched (Fries, 2008).

The Interface-enriched General Finite Element Method (IGFEM) (Soghrati *et al.*, 2012a) was first introduced as a simplified generalized FEM to solve problems with weak discontinuities, *i.e.*, where the gradient field is discontinuous. The method overcomes most issues of X/GFEM for this kind of problems: In IGFEM, enriched nodes are placed along interfaces, and enrichment functions are non-zero only in *cut elements*, *i.e.*, elements that are intersected by a discontinuity. Furthermore, enrichment functions are exactly zero at original mesh nodes. Therefore, original mesh nodes retain their physical meaning and essential boundary conditions can be enforced directly on non-matching edges (Aragón and Simone, 2017; van den Boom *et al.*, 2019b; Cuba Ramos *et al.*, 2015). It was shown that IGFEM is optimally convergent under mesh refinement for problems without singularities (Soghrati and Geubelle, 2012; Soghrati *et al.*, 2012a). Moreover, IGFEM is stable by means of scaling enrichment functions or a simple diagonal preconditioner (Aragón *et al.*, 2020; van den Boom *et al.*, 2019b), meaning it has the same condition number as standard FEM. The method has been applied to the modeling of fibre-reinforced composites (Soghrati and Geubelle, 2012), multi-scale damage evolution in heterogeneous adhesives (Aragón *et al.*, 2013), microvascular materials with active cooling (Soghrati and Geubelle, 2012; Soghrati *et al.*, 2012a,b, 2013), and the transverse failure of composite laminates (Shakiba *et al.*, 2019; Zhang *et al.*, 2019b). IGFEM was later developed into the Hierarchical Interface-enriched Finite Element Method (HIFEM) (Soghrati, 2014), that allows for intersecting discontinuities, and into the Discontinuity-Enriched Finite Element Method (DE-FEM) (Aragón and Simone, 2017), which provides a unified formulation for both strong and weak discontinuities (*i.e.*, discontinuities in the field and its gradient, respectively). DE-FEM, which inherits the same advantages of IGFEM over X/GFEM, has successfully been applied to problems in fracture mechanics (Aragón and Simone, 2017; Zhang *et al.*, 2019a) and fictitious domain or immersed boundary problems with strongly enforced essential boundary conditions (van den Boom *et al.*, 2019b). A drawback of IGFEM is that quadratic enrichment functions are needed when the method is applied to background meshes composed of bilinear quadrangular elements (Aragón *et al.*, 2020). Another disadvantage of IGFEM, which is also shared by X/GFEM, is that it may yield inaccurate field gradients depending on how the enriched finite element space is constructed (Nagarajan and Soghrati, 2018; Soghrati *et al.*, 2017). Depending on the aspect ratio of integration elements, stresses may be overestimated, and the issue is more prominent near material interfaces. This

is not an issue along Dirichlet boundaries, where a smooth reaction field can be recovered (van den Boom *et al.*, 2019a,b), nor along traction-free cracks where stresses are negligible (Zhang *et al.*, 2019a).

In the context of optimization, IGFEM has been explored for NURBS-based shape optimization (Najafi *et al.*, 2017), the shape optimization of microvascular channels (Tan and Geubelle, 2017) and their combined shape and network topology optimization (Pejman *et al.*, 2019), the optimization of microvascular panels for nanosatellites (Tan *et al.*, 2018a), and optimal cooling of batteries (Tan *et al.*, 2018b). Nevertheless, IGFEM has not yet been used for continuum topology optimization. In this paper we show topology optimization based on a level set function, parametrized with Radial Basis Functions (RBFs) (Wang and Wang, 2006; Wendland, 1995), in combination with IGFEM. We demonstrate the method on benchmark compliance problems. The sensitivities are derived and the method is compared to density-based topology optimization and to the level set-based Ersatz method. It should be noted that no significant performance improvement is expected for these cases, as they are not sensitive to the way the boundaries are discretized. Cases that would benefit from our approach to topology optimization compared to density-based methods—and which may be shared among other methods that provide clearly defined interfaces—include those where the location of the boundary has to be known throughout the entire optimization. Examples include contact, problems where boundary conditions need to be enforced on evolving boundaries, or problems where an accurate boundary description is fundamental for resolving the fields at interfaces, such as fluid-structure interaction or wave scattering problems. Although no significant improvement in performance is expected for the compliance minimization cases in this paper, they should be seen as the necessary proof of concept before considering more complex cases.

4.2. FORMULATION

4.2.1. IGFEM-BASED ANALYSIS

In this work we focus on elastostatics and heat conduction problems on solid domains, as represented in Figure 4.1. A design domain $\Omega \subset \mathbb{R}^d$ is referenced by a Cartesian coordinate system spanned by base vectors $\{\boldsymbol{e}_i\}_{i=1}^d$. This domain is decomposed into a solid material domain and a void domain, denoted by Ω_m and Ω_v, respectively, such that the domain closure is $\overline{\Omega} = \overline{\Omega}_\mathrm{m} \cup \overline{\Omega}_\mathrm{v}$, and $\Omega_\mathrm{m} \cap \Omega_\mathrm{v} = \emptyset$. The boundary of the design domain, $\partial\Omega \equiv \Gamma = \overline{\Omega} \setminus \Omega$, is subjected to essential (Dirichlet) boundary conditions on Γ^D, and to natural (Neumann) boundary conditions on Γ^N, such that $\overline{\Gamma} = \overline{\Gamma}^\mathrm{D} \cup \overline{\Gamma}^\mathrm{N}$ and $\Gamma^\mathrm{D} \cap \Gamma^\mathrm{N} = \emptyset$. The material boundary, $\Gamma_\mathrm{m} = \left(\overline{\Omega}_\mathrm{m} \cap \overline{\Omega}_\mathrm{v}\right) \setminus \Gamma$, is defined implicitly by a level set function, $\phi(\boldsymbol{x}) = 0$, that is a function of the spatial coordinate $\boldsymbol{x}$.

For any iteration in the elastostatic optimization procedure, the boundary value problem is solved with prescribed displacements $\bar{\boldsymbol{u}} : \Gamma^\mathrm{D} \to \mathbb{R}^d$, prescribed tractions $\bar{\boldsymbol{t}} : \Gamma^\mathrm{N} \to \mathbb{R}^d$, and body forces $\boldsymbol{b}_i$ defined as the restriction of $\boldsymbol{b}$ to domain Ω_i as $\boldsymbol{b}_i \equiv \boldsymbol{b}|_{\Omega_i} : \Omega_i \to \mathbb{R}^d$, where $i = \mathrm{m}, \mathrm{v}$. Similarly, we denote the field $\boldsymbol{u}_i$ as the restriction of $\boldsymbol{u}$ to domain Ω_i, *i.e.* $\boldsymbol{u}_i \equiv \boldsymbol{u}|_{\Omega_i}$. Note that here the field is defined on both material and void domains. However, following the techniques described in van den Boom *et al.* (2019b), it is also possible to completely remove the void regions from the analysis.

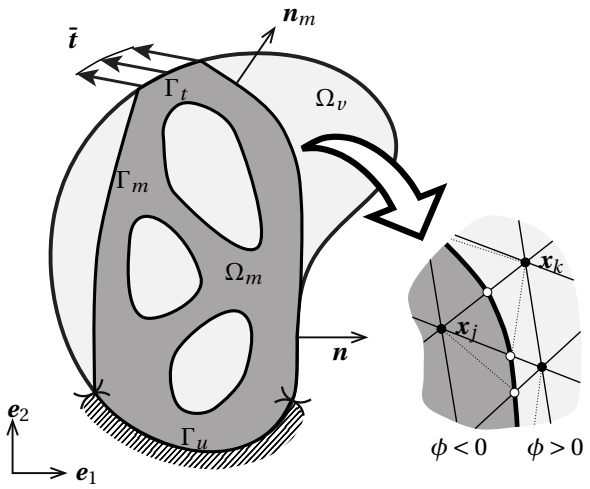

Figuur 4.1: Mathematical representation of a topology optimization design domain Ω. Essential and natural boundary conditions are prescribed on the part of the boundary denoted Γ^{D} and Γ^{N}, respectively. The material domain is referred to as Ω_{m}, while the void region is denoted Ω_{v}. The inset shows the discretization with a material interface, defined by the zero-contour of the level set function ϕ, that is non-matching to the mesh. Original mesh nodes and enriched nodes are denoted with ● and ○ symbols, respectively.

We define the vector-valued function space

$$\mathcal{V}_0 = \Big\{ \boldsymbol{v} \in \left[\mathcal{L}^2(\Omega)\right]^d,\ \boldsymbol{v}|_{\Omega_i} \in \left[\mathcal{H}^1(\Omega_i)\right]^d, \\ \boldsymbol{v}|_{\Gamma_i^{\mathrm{D}}} = \boldsymbol{0},\ i = \mathrm{m}, \mathrm{v} \Big\}, \tag{4.1}$$

where $\mathcal{L}^2(\Omega)$ is the space of square-integrable functions and $\mathcal{H}^1(\Omega_i)$ is the first-order Sobolev space. In this work we only focus on problems with homogeneous Dirichlet boundary conditions. For problems with non-homogeneous essential boundary conditions, the reader is referred to Aragón and Simone (2017). The weak form of the elastostatics boundary value problem can be written as: Find $\boldsymbol{u} \in \mathcal{V}_0$ such that

$$B(\boldsymbol{u}, \boldsymbol{v}) = L(\boldsymbol{v}) \qquad \forall\, \boldsymbol{v} \in \mathcal{V}_0, \tag{4.2}$$

where the bilinear and linear forms can be written as

$$B(\boldsymbol{u}, \boldsymbol{v}) = \sum_{i=\mathrm{m,v}} \int_{\Omega_i} \boldsymbol{\varepsilon}_i(\boldsymbol{v}_i) : \boldsymbol{\sigma}_i(\boldsymbol{u}_i)\, \mathrm{d}\Omega, \tag{4.3}$$

and

$$L(\boldsymbol{v}) = \sum_{i=\mathrm{m,v}} \int_{\Omega_i} \boldsymbol{v}_i \cdot \boldsymbol{b}_i\, \mathrm{d}\Omega + \int_{\Gamma^{\mathrm{N}}} \boldsymbol{v}_i \cdot \bar{\boldsymbol{t}}\, \mathrm{d}\Gamma, \tag{4.4}$$

respectively, where the stress tensor $\boldsymbol{\sigma}_i \equiv \boldsymbol{\sigma}|_{\Omega_i}$ follows Hooke's law for linear elastic materials, $\boldsymbol{\sigma}_i = \boldsymbol{C}_i : \boldsymbol{\varepsilon}_i$, and $\boldsymbol{C}_i$ is the elasticity tensor. Small strain theory is used for the strain tensor, *i.e.*, $\boldsymbol{\varepsilon}(\boldsymbol{u}) = \frac{1}{2}(\nabla \boldsymbol{u} + \nabla \boldsymbol{u}^{\mathrm{T}})$.

For heat conduction the variational problem is

$$B(u,v) = L(v) \qquad \forall\, v \in \mathcal{V}_0, \tag{4.5}$$

where trial and weight function are taken from the space $\mathcal{V}_0 = \left\{ v \in \mathcal{L}^2(\Omega),\ v|_{\Omega_i} \in \mathcal{H}^1(\Omega_i),\ v|_{\Gamma_i^{\mathrm{D}}} = 0,\ i = \mathrm{m}, \mathrm{v} \right\}$. For a prescribed temperature $u : \Gamma^{\mathrm{D}} \to \mathbb{R}$, prescribed heat flux $q : \Gamma^{\mathrm{N}} \to \mathbb{R}$, heat source $f_i : \Omega_i \to \mathbb{R}$, and conductivity tensor $\boldsymbol{\kappa}_i \equiv \boldsymbol{\kappa}|_{\Omega_i} \to \mathbb{R}^d \times \mathbb{R}^d$, the bilinear and linear forms for each iteration in heat compliance problems are given by

$$B(u,v) = \sum_{i=\mathrm{m},\mathrm{v}} \int_{\Omega_i} \nabla v_i \cdot (\boldsymbol{\kappa}_i \cdot \nabla u_i)\, \mathrm{d}\Omega \tag{4.6}$$

and

$$L(v) = \sum_{i=\mathrm{m},\mathrm{v}} \int_{\Omega_i} v_i\, f_i\, \mathrm{d}\Omega + \int_{\Gamma^{\mathrm{N}}} v_i\, \bar{q}\, \mathrm{d}\Gamma. \tag{4.7}$$

It is worth noting that interface conditions that satisfy continuity of the field and its tractions (or fluxes) do not appear explicitly in (4.3) or in (4.6), because they drop out due to the weight function $\boldsymbol{v}$ (or v) being continuous along the interface.

The design domain is discretized without prior knowledge of the topology as $\overline{\Omega}^h = \bigcup_{i \in \iota_E} \overline{e}_i$, where $\overline{e}_i$ is the ith finite element and ι_E is the index set corresponding to all elements in the original mesh. Similarly, we define the mesh nodes $\{\boldsymbol{x}_j\}_{j \in \iota_h}$, where ι_h is an index set corresponding to all the original nodes of the mesh. A partition of unity is defined by standard Lagrange shape functions N_j, associated to the mesh nodes. The result is a mesh that is non-matching to material boundaries. The level set function, whose zero contour defines the interface between void and material, is then evaluated on the same mesh. This is done for efficiency, as the mapping needs to be computed only once, and results in discrete nodal level set values. New *enriched nodes* are placed at the intersection between element edges and the zero contour of the level set. As illustrated in Figure 1, the locations of these enriched nodes, denoted $\boldsymbol{x}_n$, are found by linear interpolation between two nodes of the original mesh. Given two mesh nodes $\boldsymbol{x}_j$ and $\boldsymbol{x}_k$ with intersecting supports (*i.e.*, $\mathrm{supp}\left(N_j\right) \cap \mathrm{supp}\left(N_k\right) \neq \emptyset$) and level set values of different sign (*i.e.*, $\phi\left(\boldsymbol{x}_j\right)\phi\left(\boldsymbol{x}_k\right) < 0$), the enriched node is found as:

$$\boldsymbol{x}_n = \boldsymbol{x}_j - \frac{\phi_j}{\phi_k - \phi_j}\left(\boldsymbol{x}_k - \boldsymbol{x}_j\right), \tag{4.8}$$

where we adopt the notation $\phi_j \equiv \phi\left(\boldsymbol{x}_j\right)$. The material interface Γ_{m} is defined as the piece-wise linear representation of the zero contour of the level set function, discretized with enriched nodes $\{\boldsymbol{x}_n\}_{n \in \iota_w}$, where ι_w is the index set corresponding to all enriched nodes. Elements that are intersected by Γ_{m}, indexed by the index set ι_c, are then subdivided into *integration elements* by means of a constrained Delaunay algorithm. The index set referring to all integration elements is denoted ι_e. The complexity of finding intersections and creating integration elements is $\mathcal{O}(|\iota_E|)$, where $|\cdot|$ denotes set cardinality, since each element has to be processed only once per iteration.

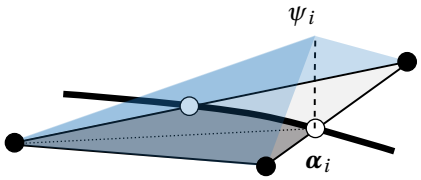

Figuur 4.2: Schematic representation of enrichment function ψ_i corresponding to enriched DOFs $\boldsymbol{\alpha}_i$, where enriched nodes are shown with ○ symbols. This enrichment function is constructed from standard Lagrange shape functions in integration elements.

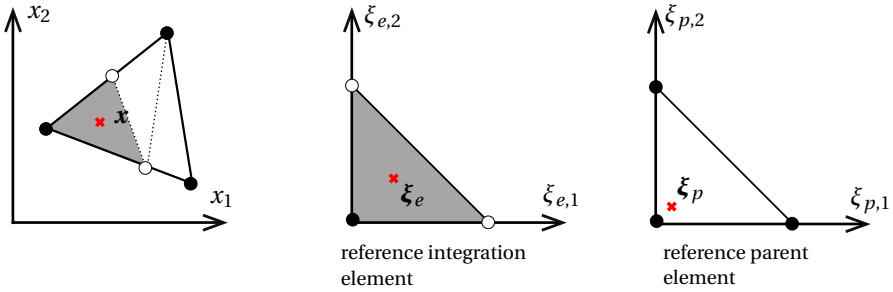

Figuur 4.3: Schematic of an integration element (shaded), whose local arrays are obtained by using an isoparametric mapping. Integration points in integration elements ($\boldsymbol{\xi}_e$) and parent elements ($\boldsymbol{\xi}_p$) are mapped to global coordinate $\boldsymbol{x}$.

Following a Bubnov-Galerkin procedure, the resulting finite dimensional problem is then solved by choosing trial and weight functions from the same enriched finite element space. The IGFEM approximation can then be written as

$$\boldsymbol{u}^h(\boldsymbol{x}) = \underbrace{\sum_{i \in \iota_h} N_i(\boldsymbol{x})\, \boldsymbol{U}_i}_{\text{standard FEM}} + \underbrace{\sum_{i \in \iota_w} \psi_i(\boldsymbol{x})\, \boldsymbol{\alpha}_i}_{\text{enrichment}}, \tag{4.9}$$

for elastostatics, or

$$u^h(\boldsymbol{x}) = \underbrace{\sum_{i \in \iota_h} N_i(\boldsymbol{x})\, U_i}_{\text{standard FEM}} + \underbrace{\sum_{i \in \iota_w} \psi_i(\boldsymbol{x})\, \alpha_i}_{\text{enrichment}}, \tag{4.10}$$

for heat conduction problems. The first term in (4.9) and (4.10) corresponds to the standard finite element approximation, with shape functions $N_i(\boldsymbol{x})$ and corresponding standard degrees of freedom $\boldsymbol{U}_i$ (or U_i), and the second term refers to the enrichment, characterized by enrichment functions $\psi_i(\boldsymbol{x})$ and associated enriched DOFs $\boldsymbol{\alpha}_i$ (or α_i). Enrichment functions ψ_i can be conveniently constructed from Lagrange shape functions of integration elements, as illustrated in Figure 4.2, while the underlying partition of unity shape functions are kept intact.

Subsequently, the local stiffness matrix $\boldsymbol{k}_e$ and force vector $\boldsymbol{f}_e$ are obtained numerically; elements that are not intersected follow standard FEM procedures. An isoparametric procedure is used in integration elements to obtain the local arrays. Figure 4.3 shows a schematic of a triangular integration element (shaded) within an original cut element—the parent element—in global coordinates. The reference triangular domains for both integration and parent elements are also shown. Each reference domain shows the master coordinate associated to a given global coordinate $\boldsymbol{x}$. In elastostatics (heat conductivity follows an analogous procedure), $\boldsymbol{k}_e$ and $\boldsymbol{f}_e$ are computed on each integration element's reference triangle $\triangleright$ as

$$\begin{aligned} \boldsymbol{k}_e &= \int_{\triangleright} j_e \boldsymbol{B}^\top \boldsymbol{D} \boldsymbol{B} \mathrm{d}\boldsymbol{\xi}, \\ &\text{and} \\ \boldsymbol{f}_e &= \int_{\triangleright} j_e \begin{bmatrix} \boldsymbol{N} \\ \boldsymbol{\psi} \end{bmatrix} \boldsymbol{b} \,\mathrm{d}\boldsymbol{\xi} + \int_{\triangleright \cap \Gamma^{\mathrm{N}}} j_e \begin{bmatrix} \boldsymbol{N} \\ \boldsymbol{\psi} \end{bmatrix} \bar{\boldsymbol{t}} \,\mathrm{d}\partial\boldsymbol{\xi} \end{aligned} \tag{4.11}$$

where $\boldsymbol{B} = \begin{bmatrix} \boldsymbol{\Delta}_{\boldsymbol{\xi}}^\top \boldsymbol{N}^\top \boldsymbol{J}^{-\top} & \boldsymbol{\Delta}_{\boldsymbol{\xi}}^\top \boldsymbol{\psi}^\top \boldsymbol{J}_e^{-\top} \end{bmatrix}$ and $\boldsymbol{D}$ is the constitutive matrix. The parental shape functions vector $\boldsymbol{N}$ and enrichment functions $\boldsymbol{\psi}$ are stacked together. Note that j_e and $\boldsymbol{J}_e^{-1}$ are the determinant and the inverse of the Jacobian of the isoparamatric mapping of the integration element respectively, and $\boldsymbol{J}^{-1}$ is the inverse of the Jacobian of the mapping of the parent element. The isoparametric mapping is a standard procedure in FEM; however, as the steps are important for the derivation of the sensitivites in §4.2.3, it is explained in more detail in Appendix B. The differential operator $\boldsymbol{\Delta}_{\boldsymbol{\xi}}$ is defined as:

$$\begin{aligned} \boldsymbol{\Delta}_{\boldsymbol{\xi}} &\equiv \begin{bmatrix} \frac{\partial}{\partial \xi_1} & 0 & \frac{\partial}{\partial \xi_2} \\ 0 & \frac{\partial}{\partial \xi_2} & \frac{\partial}{\partial \xi_1} \end{bmatrix}^\top, \\ \boldsymbol{\Delta}_{\boldsymbol{\xi}} &\equiv \begin{bmatrix} \frac{\partial}{\partial \xi_1} & 0 & 0 & \frac{\partial}{\partial \xi_2} & 0 & \frac{\partial}{\partial \xi_3} \\ 0 & \frac{\partial}{\partial \xi_2} & 0 & \frac{\partial}{\partial \xi_1} & \frac{\partial}{\partial \xi_3} & 0 \\ 0 & 0 & \frac{\partial}{\partial \xi_3} & 0 & \frac{\partial}{\partial \xi_2} & \frac{\partial}{\partial \xi_1} \end{bmatrix}^\top, \end{aligned} \tag{4.12}$$

for elastostatics in 2-D and 3-D, respectively, and

$$\boldsymbol{\Delta}_{\boldsymbol{\xi}} \equiv \begin{bmatrix} \frac{\partial}{\partial \xi_1} & \frac{\partial}{\partial \xi_2} \end{bmatrix}^\top, \; \boldsymbol{\Delta}_{\boldsymbol{\xi}} \equiv \begin{bmatrix} \frac{\partial}{\partial \xi_1} & \frac{\partial}{\partial \xi_2} & \frac{\partial}{\partial \xi_3} \end{bmatrix}^\top, \tag{4.13}$$

for heat conductivity in 2-D and 3-D, respectively.

In this work, we are concerned with linear triangular elements, for which a single integration point in standard and integration elements is sufficient. The discrete system of linear equations $\boldsymbol{K}\boldsymbol{U} = \boldsymbol{F}$ is finally obtained through standard procedures, where

$$\boldsymbol{K} = \bigwedge_{i \in \iota_A} \boldsymbol{k}_i, \qquad \boldsymbol{F} = \bigwedge_{i \in \iota_A} \boldsymbol{f}_i, \tag{4.14}$$

where $\iota_A = (\iota_E \setminus \iota_c) \cup \iota_e$ and $\mathbb{A}$ denotes the standard finite element assembly operator.

For a more detailed description on IGFEM, the reader is referred to Soghrati *et al.* (2012a).

RELATION TO X/GFEM

IGFEM is closely related to X/GFEM: The general X/GFEM approximation can be written as

$$\boldsymbol{u}^h(\boldsymbol{x}) = \underbrace{\sum_{i\in\iota_h} N_i(\boldsymbol{x})\,\boldsymbol{U}_i}_{\text{standard FEM}} + \underbrace{\sum_{i\in\iota_h} N_i(\boldsymbol{x}) \sum_{j\in\iota_g} E_{ij}(\boldsymbol{x})\,\hat{\boldsymbol{U}}_{ij}}_{\text{enrichment}}, \tag{4.15}$$

where enrichment functions E_{ij} are associated to generalized DOFs $\hat{\boldsymbol{U}}_{ij}$—the latter assigned to nodes of the mesh. While the X/GFEM approximation uses partition of unity shape functions to localize the effect of enrichment functions, in IGFEM this is not necessary because enrichment functions are local to cut elements by construction. In addition, enriched nodes in IGFEM are collocated along the discontinuities, resulting in less DOFs than required by (4.15).

It is worth noting, however, that IGFEM is not only closely related to X/GFEM, it can actually be derived from it by means of a proper choice of enrichment functions E_{ij} and by clustering enriched DOFs (Duarte *et al.*, 2007). Appendix A shows this with a simple 1-D example.

IGFEM has several benefits over X/GFEM:

- Enrichment functions in IGFEM are local by construction, *i.e.*, they are non-zero only in elements cut by the interface and exactly zero elsewhere. Therefore, IGFEM has no issues with blending elements, which is an issue for X/GFEM for some choices of enrichment functions (Fries, 2008);
- In IGFEM the enrichment functions vanish at the nodes of background elements. Therefore, the original mesh node conserve the Kronecker property, and the DOFs associated to these nodes maintain their physical interpretation;
- In X/GFEM, prescribing non-zero Dirichlet boundary conditions is usually done weakly by means of penalty, Lagrange, or Nitsche methods (Cuba Ramos *et al.*, 2015). In IGFEM, on the contrary, these boundary conditions can be prescribed strongly, both on original nodes and, by means of a multipoint constraint, on enriched edges (Aragón and Simone, 2017; van den Boom *et al.*, 2019b);
- Smooth traction profiles can be recovered when Dirichlet boundary conditons are prescribed on enriched edges (van den Boom *et al.*, 2019a,b; Cuba Ramos *et al.*, 2015). This is currently not possible in X/GFEM even with stabilization techniques (Haslinger and Renard, 2009);
- IGFEM is stable, *i.e.*, the condition number of the system matrix grows as $\mathcal{O}\left(h^{-2}\right)$, which is the same order as that of standard FEM. This is accomplished by means of a proper scaling of enrichment functions or by using a simple diagonal preconditioner (Aragón *et al.*, 2020);
- The computer implementation is simpler: data structures of standard FEM can be reused to store enriched DOFs, post-processing is required for enriched DOFs only, and no special treatment of Dirichlet boundary conditions is needed (Aragón and Simone, 2017).

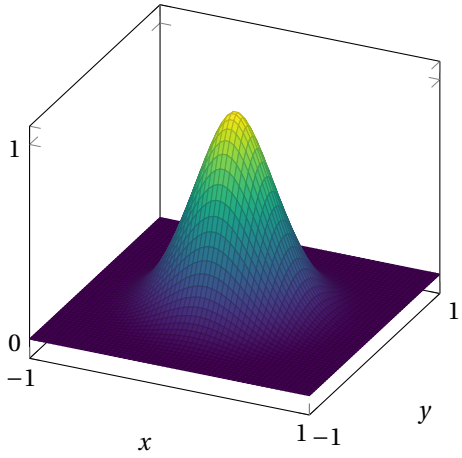

Figuur 4.4: Compactly supported RBF given by (4.16) with coordinates $\boldsymbol{x} = [0\,0]^\mathsf{T}$ and radius of influence $r_\mathrm{s} = 1$.

4.2.2. RADIAL BASIS FUNCTIONS

Although it is possible to directly use the level set values ϕ_j on original nodes of the finite element mesh as design variables, we choose to use compactly supported radial basis functions for the level set parametrization for a number of reasons (Wang and Wang, 2006):

- RBFs give control over the complexity of the designs, and as such, they act similarly to a filter in density-based topology optimization;
- By decoupling the finite element analysis mesh from the RBF grid, the design space can be restricted without deteriorating the finite element approximation. This can be used to mitigate approximation errors discretizations that are too coarse; and
- By tuning the radius of support of RBFs, we can ensure that the influence of each design variable extends over multiple elements. This allows the optimizer to move the boundary further and therefore converge faster, while using fewer design variables. This effect is similar to that of a filter radius in standard density-based topology optimization.

Figure 4.4 illustrates a compactly supported RBF θ (Wendland, 1995) described by

$$\theta_i(r_i) = (1 - r_i)^4 (4r_i + 1), \tag{4.16}$$

where the radius r_i is defined as

$$r_i(\boldsymbol{x}, \boldsymbol{x}_i) = \frac{\sqrt{\|\boldsymbol{x} - \boldsymbol{x}_i\|}}{r_\mathrm{s}}, \tag{4.17}$$

and r_s is the radius of support. In (4.17) $\|\cdot\|$ denotes the Euclidian norm, and $\boldsymbol{x}_i$ is the center coordinates corresponding to RBF θ_i.

The scalar-valued level set function $\phi(\boldsymbol{x})$ is found as a summation of every non-zero RBF θ_i, scaled with its corresponding design variable s_i:

$$\phi(\boldsymbol{x}) = \boldsymbol{\Theta}(\boldsymbol{x})^\top \boldsymbol{s} = \sum_{i \in \iota_s} \theta_i(\boldsymbol{x})\, s_i, \tag{4.18}$$

where ι_s is the index set corresponding to all design variables, and

$$\boldsymbol{s} \in \mathcal{D} = \left\{ \boldsymbol{s} \middle| \boldsymbol{s} \in \mathbb{R}^{|\iota_s|}, -1 \leq s_i \leq 1 \right\} \tag{4.19}$$

is a vector of design variables, with lower and upper bounds -1 and 1 that prevent the level set from becoming too steep. Finally, evaluating this function at the original nodes of the finite element mesh results in the level set vector

$$\boldsymbol{\phi} = \boldsymbol{\theta}^\top \boldsymbol{s}, \tag{4.20}$$

where $\boldsymbol{\theta}$ is a matrix that needs to be computed only once, as the original mesh nodes do not move throughout the optimization.

4.2.3. OPTIMIZATION

The optimization problem is chosen as a minimization of the compliance C with respect to the design variables $\boldsymbol{s}$ that scale the RBFs. It needs to be emphasized that compliance minimization is merely a demonstrator problem, and the method is not limited to it. The minimization problem is subject to equilibrium and to a volume constraint V_c. This problem can be written as

$$\begin{aligned} \boldsymbol{s}^\star = \underset{\boldsymbol{s} \in \mathcal{D}}{\arg\min} \quad & C = \boldsymbol{U}^\top \boldsymbol{K} \boldsymbol{U}, \\ \text{subject to} \quad & \boldsymbol{K}\boldsymbol{U} = \boldsymbol{F}, \\ & V_{\Omega_\mathrm{m}} \leq V_c. \end{aligned} \tag{4.21}$$

The Method of Moving Asymptotes (MMA) (Svanberg, 1987)[1], a method commonly used in density-based topology optimization, is employed to solve this optimization problem.

SENSITIVITY ANALYSIS

The compliance minimization problem is self-adjoint (Bendsøe and Sigmund, 2004), resulting in the sensitivity of the compliance C with respect to the design variables $\boldsymbol{s}$ as

$$\frac{\partial C}{\partial \boldsymbol{s}} = -\boldsymbol{U}^\top \frac{\partial \boldsymbol{K}}{\partial \boldsymbol{s}} \boldsymbol{U} + 2\boldsymbol{U}^\top \frac{\partial \boldsymbol{F}}{\partial \boldsymbol{s}}. \tag{4.22}$$

Applying the chain rule, the sensitivity of the compliance C with respect to design variable s_i can be written at the level of integration elements in terms of the nodal level set values ϕ_j:

$$\frac{\partial C}{\partial s_i} = \sum_{j \in \iota_i} \sum_{e \in \iota_j} \sum_{n \in \iota_n} \left(-\boldsymbol{u}_e^\top \frac{\partial \boldsymbol{k}_e}{\partial \boldsymbol{x}_n} \frac{\partial \boldsymbol{x}_n}{\partial \phi_j} \boldsymbol{u}_e + 2\boldsymbol{u}_e^\top \frac{\partial \boldsymbol{f}_e}{\partial \boldsymbol{x}_n} \frac{\partial \boldsymbol{x}_n}{\partial \phi_j} \right) \frac{\partial \phi_j}{\partial s_i}. \tag{4.23}$$

In (4.23), a summation is done over all the nodes in the index set ι_i which contains all the original mesh nodes that are in the support of the RBF corresponding to design variable

[1] The author would like to thank Krister Svanberg for providing us with the MMA implementation.

s_i. Then, a summation is done over ι_j, which refers to the index set of all integration elements e in the support of original mesh node j, *i.e.*, the region where the original shape function N_j is nonzero. Lastly, a summation is done over the index set ι_n, which contains all the enriched nodes n in integration element e. The location of these enriched nodes is denoted $\boldsymbol{x}_n$. Note that a number of terms can be identified in the sensitivity formulation: the derivatives of nodal level set values with respect to the design variables, $\partial\phi_j/\partial s_i$, the design velocities $\partial\boldsymbol{x}_n/\partial\phi_j$, and the sensitivity of the element stiffness matrix and force vector with respect to the location of the nth enriched node, $\partial\boldsymbol{k}_e/\partial\boldsymbol{x}_n$ and $\partial\boldsymbol{f}_e/\partial\boldsymbol{x}_n$, respectively.

First, the sensitivity of the nodal level set values with respect to the design variables is simply computed by taking the derivative of (4.20) with respect to $\boldsymbol{s}$ as

$$\frac{\partial\boldsymbol{\phi}}{\partial\boldsymbol{s}} = \boldsymbol{\theta}^\mathsf{T}. \tag{4.24}$$

The design velocities $\partial\boldsymbol{x}_n/\partial\phi_j$ also remain straightforward as they are computed by taking the derivative of (4.8) as

$$\frac{\partial\boldsymbol{x}_n}{\partial\phi_j} = -\frac{\phi_k}{\left(\phi_j-\phi_k\right)^2}\left(\boldsymbol{x}_j-\boldsymbol{x}_k\right). \tag{4.25}$$

Note that the enriched nodes remain on the element edges of the finite element mesh, and thus the direction of the design velocity is known *a priori*.

More involved is the sensitivity of the eth integration element stiffness matrix $\boldsymbol{k}_e$ with respect to the location of enriched node n, which can be computed on the reference domain as:

$$\frac{\partial\boldsymbol{k}_e}{\partial\boldsymbol{x}_n} = \int_{\square}\left(\frac{\partial j_e}{\partial\boldsymbol{x}_n}\boldsymbol{B}^\mathsf{T}\boldsymbol{D}\boldsymbol{B} + j_e\frac{\partial\boldsymbol{B}^\mathsf{T}}{\partial\boldsymbol{x}_n}\boldsymbol{D}\boldsymbol{B} + j_e\boldsymbol{B}^\mathsf{T}\boldsymbol{D}\frac{\partial\boldsymbol{B}}{\partial\boldsymbol{x}_n}\right)\mathrm{d}\boldsymbol{\xi}, \tag{4.26}$$

where $\boldsymbol{B} = \left[\boldsymbol{\Delta}_{\boldsymbol{\xi}}^\mathsf{T}\boldsymbol{N}^\mathsf{T}\boldsymbol{J}^{-\mathsf{T}}\boldsymbol{\Delta}_{\boldsymbol{\xi}}^\mathsf{T}\boldsymbol{\psi}^\mathsf{T}\boldsymbol{J}_e^{-\mathsf{T}}\right]$ as defined in §4.2.1. In this work, a single integration point is used for numerical quadrature, with $\boldsymbol{\xi}_e = [1/3, 1/3]$ and $w_g = 1/2$. Recall that the material within each integration element remains constant, and therefore $\partial\boldsymbol{D}/\partial\boldsymbol{x}_n = \boldsymbol{0}$. The first term in (4.26) contains the sensitivity of the Jacobian determinant, and represents the effect of the changing integration element area; the second and third terms contain the sensitivity of the element $\boldsymbol{B}$ matrix, and represent the effect of the changing shape and enrichment functions. The latter is computed as

$$\frac{\partial\boldsymbol{B}}{\partial\boldsymbol{x}_n} = \begin{bmatrix}\boldsymbol{0} & \boldsymbol{\Delta}_{\boldsymbol{\xi}}^\mathsf{T}\boldsymbol{\psi}^\mathsf{T}\dfrac{\partial\boldsymbol{J}_e^{-\mathsf{T}}}{\partial\boldsymbol{x}_n}\end{bmatrix}. \tag{4.27}$$

Observe that only the enriched part of the formulation has an influence, as for linear elements the background shape function derivatives are constant throughout the integration element, and thus

$$\frac{\partial\boldsymbol{\Delta}_{\boldsymbol{\xi}}\boldsymbol{N}}{\partial\boldsymbol{x}_n} = \frac{\partial\boldsymbol{\Delta}_{\boldsymbol{\xi}}\boldsymbol{N}}{\cancel{\partial\boldsymbol{\xi}_p}}\overset{0}{\cancel{\frac{\partial\boldsymbol{\xi}_p}{\partial\boldsymbol{x}}}}\frac{\partial\boldsymbol{x}}{\partial\boldsymbol{x}_n} = \boldsymbol{0}. \tag{4.28}$$

The Jacobian of the parent element is not influenced by the enriched node location either ($\partial \boldsymbol{J}/\partial \boldsymbol{x}_n = \boldsymbol{0}$). Similarly to (4.28), the enrichment functions are constant throughout the integration element, so that

$$\frac{\partial \boldsymbol{\Delta}_{\xi} \boldsymbol{\psi}}{\partial \boldsymbol{x}_n} = \frac{\partial \boldsymbol{\Delta}_{\xi} \boldsymbol{\psi}}{\partial \boldsymbol{\xi}_e}^{0} \frac{\partial \boldsymbol{\xi}_e}{\partial \boldsymbol{x}} \frac{\partial \boldsymbol{x}}{\partial \boldsymbol{x}_n} = \boldsymbol{0}. \tag{4.29}$$

Appendix C describes how to compute the derivative of the Jacobian inverse and determinant, $\partial \boldsymbol{J}_e^{-1}/\partial \boldsymbol{x}_n$ and $\partial j_e/\partial \boldsymbol{x}_n$, respectively, by straightforward differentiation.

Finally, the sensitivity of the design-dependent force vector $\boldsymbol{f}_e$ is evaluated. Due to the IGFEM discretization, enriched nodes whose support is subjected to a line or body load contribute to the force vector, implying that the derivatives of the force vector are nonzero for cases with line loads or body forces. Similarly to the sensitivity of the element stiffness matrix, each integral in the sensitivity of the element force vector consists of two terms, one related to the Jacobian derivative, and another containing the function derivatives:

$$\begin{aligned} \frac{\partial \boldsymbol{f}_e}{\partial \boldsymbol{x}_n} = &\int_{\square} \left(\frac{\partial j_e}{\partial \boldsymbol{x}_n} \begin{bmatrix} \boldsymbol{N} \\ \boldsymbol{\psi} \end{bmatrix} \boldsymbol{b} + j_e \begin{bmatrix} \partial \boldsymbol{N}/\partial \boldsymbol{x}_n \\ \boldsymbol{0} \end{bmatrix} \boldsymbol{b} \right) \mathrm{d}\boldsymbol{\xi} \\ &+ \int_{\square \cap \Gamma^{\mathrm{N}}} \left(\frac{\partial j_e}{\partial \boldsymbol{x}_n} \begin{bmatrix} \boldsymbol{N} \\ \boldsymbol{\psi} \end{bmatrix} \bar{\boldsymbol{t}} + j_e \begin{bmatrix} \partial \boldsymbol{N}/\partial \boldsymbol{x}_n \\ \boldsymbol{0} \end{bmatrix} \bar{\boldsymbol{t}} \right) \mathrm{d}\partial \boldsymbol{\xi}. \end{aligned} \tag{4.30}$$

In the second term of the integrals, only the parent shape functions have a contribution. This is because enrichment functions in reference coordinates are not influenced by the enriched node in global coordinates, *i.e.*, $\partial \boldsymbol{\psi}/\partial \boldsymbol{x}_n = \boldsymbol{0}$. However, as the mapping to the parent reference domain is influenced by the enriched node location, $\partial \boldsymbol{N}/\partial \boldsymbol{x}_n$ is nonzero, and can be evaluated as

$$\frac{\partial \boldsymbol{N}}{\partial \boldsymbol{x}_n} = \frac{\partial \boldsymbol{N}}{\partial \boldsymbol{\xi}_p} \frac{\partial \boldsymbol{\xi}_p}{\partial \boldsymbol{x}} \frac{\partial \boldsymbol{x}}{\partial \boldsymbol{x}_n} = \frac{\partial \boldsymbol{N}}{\partial \boldsymbol{\xi}_p} \boldsymbol{A}_p^{-1} \frac{\partial \boldsymbol{x}_e}{\partial \boldsymbol{x}_n} \boldsymbol{N}_e, \tag{4.31}$$

where $\boldsymbol{A}_p^{-1}$ is the inverse isoparametric mapping that maps global coordinates to the local master coordinate system of the parent element as explained in Appendix B.

Although the sensitivity analysis seems involved, the partial derivatives are relatively straightforward to compute on local arrays.

4.3. NUMERICAL EXAMPLES

The enriched method outlined above is demonstrated on a number of classical compliance optimization problems. The results generated by this approach are compared to those generated by open source optimization codes, and the influence of the design discretization is investigated. A 3-D compliance optimization case and a heat sink problem are also considered. It should be noted that no holes can be nucleated in the method presented in this paper. Therefore, initial designs containing a relatively large number of holes are used for the numerical examples. However, the method could be extended to also nucleate holes by means of topological derivatives (Amstutz and Andrä, 2006).

In this section, no units are specified; therefore, any consistent unit system can be assumed. For the MMA optimizer (Svanberg, 1987), the following settings are used unless otherwise specified:

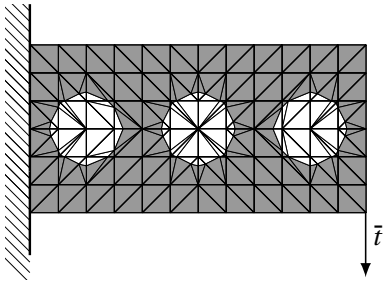

Figuur 4.5: Test problem for the finite difference check of the analytical sensitivities. The relative differences δ_i as per (4.32) are illustrated in Figure 4.6.

- The lower and upper bounds on the design variables s_i are given by -1 and 1, as defined in the design variable space in (4.19)
- The move limit used by MMA is set to 0.01;
- A value of 10 is used for the Lagrange multiplier on the auxiliary variables in the MMA sub-problem that controls how aggressively the constraints are enforced.

4.3.1. NUMERICAL VERIFICATION OF THE SENSITIVITIES

The analytically computed sensitivities $\partial C/\partial s_i$ are checked against central finite differences C_i' for a small test problem as illustrated in Figure 4.5. This test problem consists of a beam of size $2L \times L$ that is clamped on the left, and subjected to a downward force $|\bar{\boldsymbol{t}}| = 1$ on the bottom right. The material phase of this beam has Young's modulus $E_1 = 1$. We consider the initial design with three holes, as shown in Figure 4.5, with Young's modulus $E_2 = 10^{-6}$. The problem is solved on a symmetric mesh of $12 \times 6 \times 2$ triangles. The RBFs are defined on a 13×7 grid, and have a radius of $0.15L$.

The relative differences of the non-zero design variable sensitivities are computed as

$$\delta_i = \frac{C_i' - \partial C/\partial s_i}{\partial C/\partial s_i}, \tag{4.32}$$

and illustrated in Figure 4.6 for different finite different step sizes Δs_i. For a step size of $\Delta s_i = 10^{-5}$ the relative difference is minimized and takes a value of $\delta \approx 5 \times 10^{-6}$.

4.3.2. CANTILEVER BEAM

Our approach to enriched level set-based topology optimization is compared to the following open source codes:

- the 99-line SIMP-based code by Sigmund (2001);
- an 88-line code for parameterized level set optimization using radial-basis functions and density mapping, proposed by Wei *et al.* (2018); and
- a code for discrete level set topology optimization with topological derivatives by Challis (2010).

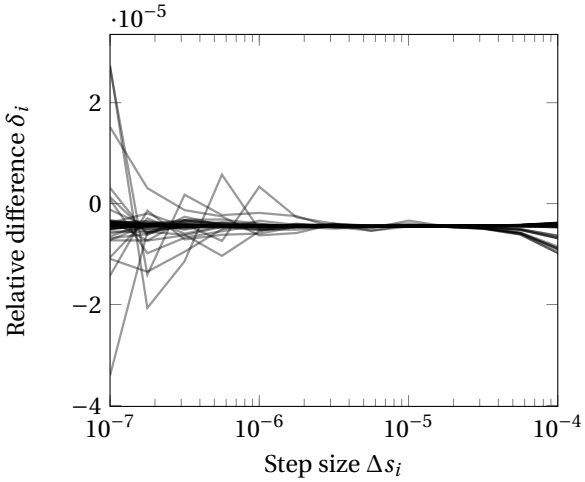

Figuur 4.6: Relative difference δ_i between the analytically computed sensitivities for node i and central finite differences, as a function of the step size Δs_i.

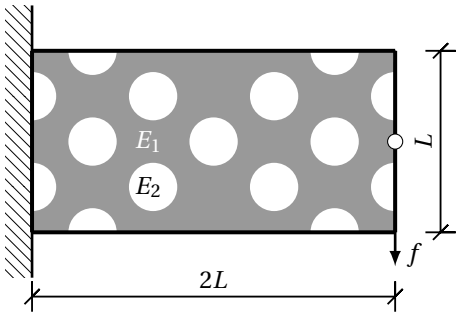

Figuur 4.7: Problem description and initial design for the cantilever beam example in §4.3.2. The domain is clamped on the left and a downward force is applied in the middle of the right side.

Figuur 4.8: Final designs for a cantilever beam obtained by the proposed method and the other methods considered in this study, shown in the columns. The rows show designs obtained on meshes defined on grids of 21, 41 × 21, 61 × 31, 81 × 41, and 101 × 51 nodes, respectively.

The optimization problem for this comparison is the widely-used cantilever beam problem, as illustrated in Figure 4.7. It consists of a $2L \times L$ rectangular domain that is clamped on the left and subjected to a downward point load $\bar{\boldsymbol{t}}$ in the middle of the right side. We set L equal to 1, the volume constraint to 55% of the design domain volume, and use $|\bar{\boldsymbol{t}}| = 1$. The material domain Ω_{m} is assigned a Young's modulus $E_1 = 1$, whereas the void domain Ω_{v} has Young's modulus $E_2 = 10^{-6}$. Both domains have a Poisson ratio $\nu_1 = \nu_2 = 0.3$. Note that it is also possible to give the void regions a stiffness of exactly zero by removing DOFs (van den Boom *et al.*, 2019b). However, this would entail extra overhead, and to ensure a fair comparison with the other models, in this work it is chosen to use a small value for the void stiffness.

Figure 4.7 shows the initial design that is used for the IGFEM-based optimization, which is the same as that used in the paper describing the 88-line code (Wei *et al.*, 2018). The other two codes do not require an initial design, as they are able to nucleate holes. The optimization problem is solved on meshes defined on rectangular grids of 21×11, 41×21, 61×31, 81×41, and 101×51 nodes. Our proposed method makes use of triangular meshes, whereas the other methods use quadrilateral meshes. The RBF mesh used in the IGFEM-based solutions is the same as the analysis mesh, and a radius of influence of $r_s = \sqrt{2} \cdot a$ is used, where a is the distance between two RBFs.

The results for each code are illustrated in Figure 4.8. For all methods, the design becomes more detailed when the mesh resolution is increased. Furthermore, the topologies obtained by each method are roughly the same. It is observed that the resulting designs are similar to those given by the code of Wei *et al.*, especially for the finer meshes. Indeed, our proposed method yields results that have clearly defined (black and white) non-staircased boundaries. It should be noted, however, that the coarsest IGFEM result shows jagged boundaries. This zigzagging effect reduces with mesh refinement and is investigated in detail in §4.4.2. Figure 4.9a shows the convergence behavior of the different codes for the finest mesh. It is observed that our method leads to the lowest objective function value, which again is similar to that obtained by the code by Wei *et al.*, while initially converging faster in the volume fraction.

Figure 4.9b shows the final compliance as a function of the number of DOFs. Initially, the different methods all find lower compliance values as the mesh is refined, but the method by Wei *et al.* and our method find slightly higher values for the finest mesh sizes. This may be explained by the optimizer converging to a local optimum. For each mesh size, the proposed method finds the lowest compliance value at the cost of adding some enriched DOFs.

4.3.3. MBB BEAM

The influence of the number of radial basis functions is investigated on the well-known MBB beam[2], which is illustrated in Figure 4.10. The optimization problem consists of a $3L \times L$ domain with symmetry conditions on the left. On the bottom right corner, the domain is simply supported, and a downward force $\bar{\boldsymbol{t}}$ is applied on the top left corner. As

[2] The original Messerschmitt-Bölkow-Blohm (MBB) beam problem, as introduced by Olhoff *et al.* (1991), also specified that the upper and lower surfaces have to remain planar, in addition to a maximum allowable deflection and maximum stress. Over the years a more free interpretation of the problem formulation has become commonplace.

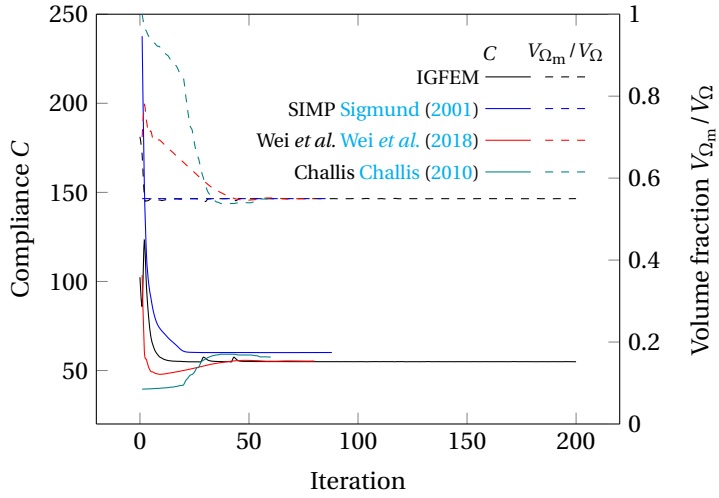

(a)

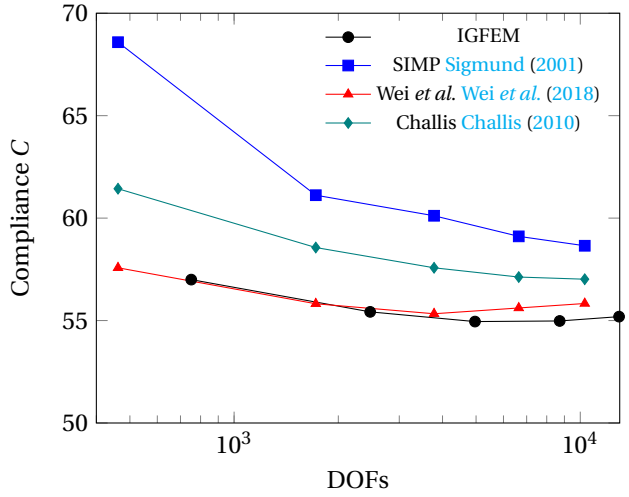

(b)

Figuur 4.9: Results of the cantilever beam problem for the different methods considered in §4.3.2; (a) shows the compliance and volume ratio convergence during optimization, (b) illustrates the final compliance as a function of the number of DOFs.

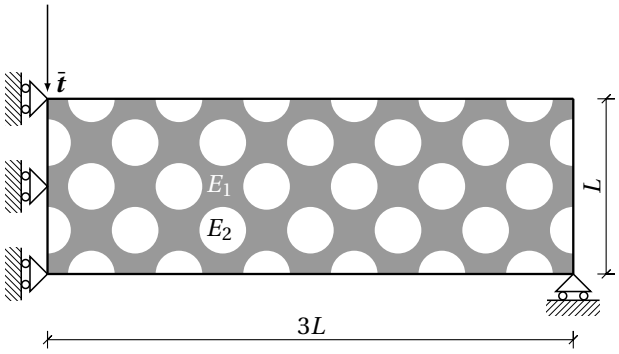

Figuur 4.10: Problem description and initial design for the MBB beam example in §4.3.3. Symmetry conditions are applied on the left of the domain, and the bottom-right corner is simply supported. A downward force is applied at the top-left side on the domain, in the middle of the beam.

in the previous example, the volume constraint is set to 55% of the volume of the total design domain. The initial design is also indicated in Figure 4.10, and the same material properties as in the previous example are used.

This optimization problem is solved on a triangular analysis mesh defined on a grid of 151×51 nodes, using a discretization of the design space consisting of 61×21, 91×31, 121×41 and 151×51 radial basis functions, so that only for the finest design space discretization, both resolutions match, and an RBF is assigned to every node in the analysis mesh. The support radius r_s is changed together with the design grid so that the overlap of RBFs is the same in each case: $r_s = \sqrt{2} \cdot a$, where a is again the distance between two RBFs.

Figure 4.11 shows the optimized designs. As expected, the level of detail in the design can be controlled by the RBF discretization. However, it is noted that in the finest RBF mesh, artifacts appear on the design boundary. This behavior will be further analysed in §4.4.2. In Figure 4.12a the convergence behavior of the different RBF meshes is shown. Although the coarsest RBF mesh shows some initial oscillations, the overall convergence behavior is similar in all cases. Moreover, as shown in Figure 4.12b, the compliance no longer significantly improves for the finest RBF discretization.

4.3.4. 3-D CANTILEVER BEAM

To show that the method is not restricted to 2-D, a 3-D cantilever beam example is also considered. The material properties are the same as those of previous examples. The size of this cantilever beam is $2L \times L \times 0.5L$, and a structured mesh with $40 \times 20 \times 10 \times 6$ tetrahedral elements is used to discretize the model. The design space is discretized using a grid of $21 \times 11 \times 6$ RBFs, with $r_s = \sqrt{2} \cdot a$. Figure 4.13 shows the initial design, along with the boundary conditions; the right surface is clamped, and a distributed line load with $|\bar{t}| = 0.2$ per unit length is applied on the bottom-left edge. The move limit for MMA in this example is set to 0.001 to prevent the optimizer from moving the boundaries too fast, as only a small number of RBFs is used with a large r_s compared to the analysis mesh.

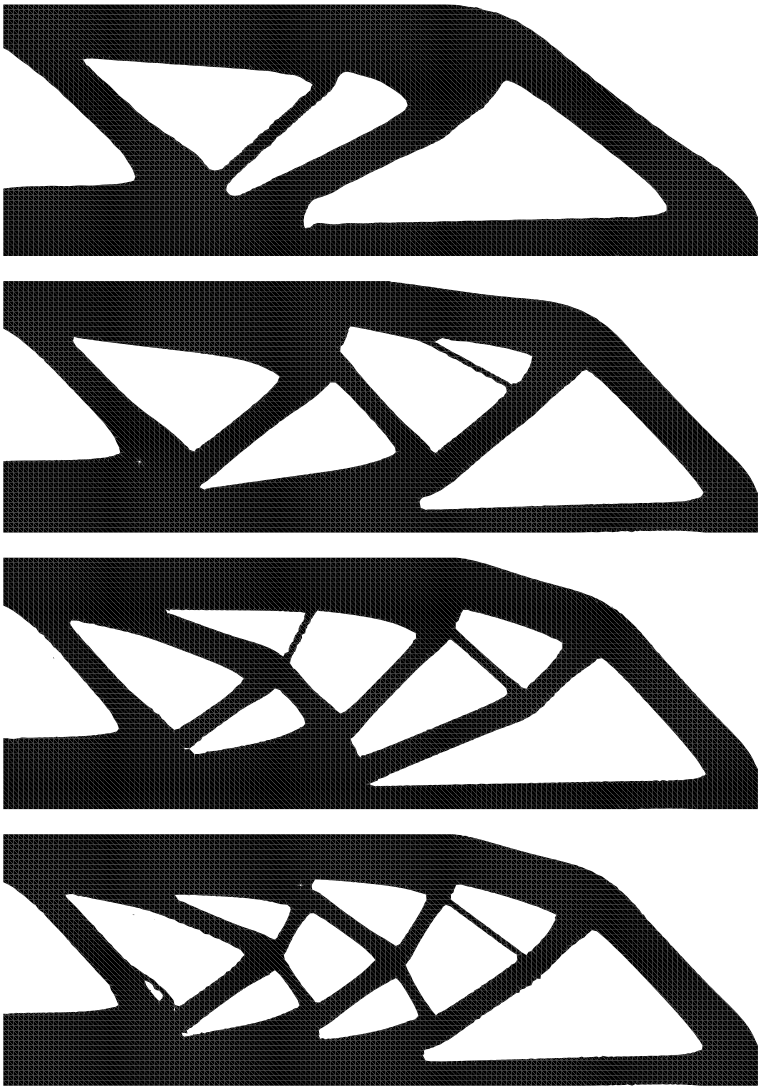

Figuur 4.11: Influence of the RBF mesh on the final design. Using symmetry conditions, only half of the MBB-beam is considered in the optimization. For each optimization, a structured mesh consisting of $150 \times 50 \times 2$ triangular finite elements is used. From top to bottom, final designs are shown obtained with design meshes consisting of 61×21, 91×31, 121×41 and 151×51 RBFs.

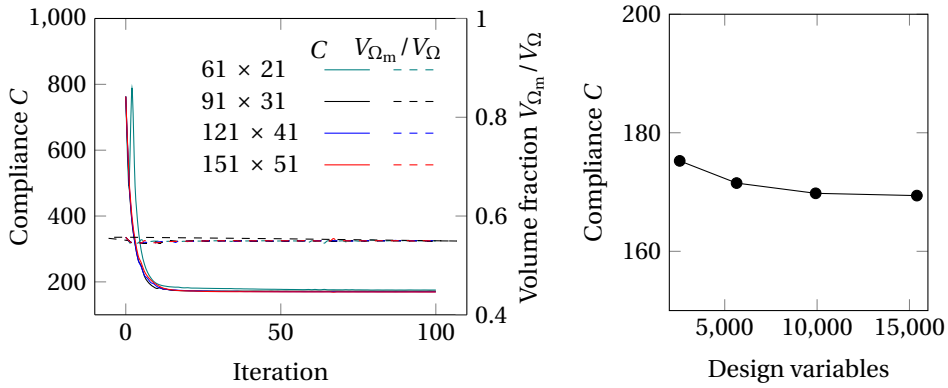

(a) (b)

Figuur 4.12: Subfigure (a) shows the convergence of the compliance C and volume fraction V_{Ω_m}/V_Ω of the MBB beam using different discretizations of the design space; (b) shows the final compliance of the MBB beam as a function of the number of design variables.

The objective function is again the structural compliance, and the volume constraint is set to 40% of the total design domain.

Figure 4.14a displays the optimized design; the corresponding convergence plot is shown in Figure 4.14b, where it can be seen that the volume satisfied the constraint, and the objective function converges smoothly.

4.3.5. HEAT SINK

Lastly, we consider a heat compliance minimization problem, illustrated in Figure 4.15. In this two-material problem, a highly conductive material ($\kappa_1 = 1$) is distributed within an $L \times L$ square domain with a lower conductivity ($\kappa_2 = 0.01$). The bottom-right corner of the domain has a heat sink, with $u = 0$, whereas the domain edges are adiabatic boundaries, *i.e.*, $\bar{q} = 0$. The entire domain is subjected to uniform heat source $f = 1$. The problem is solved on a 41×41 node analysis mesh, using 31×31 RBFs with $r_s = \sqrt{2} \cdot a$.

As this problem considers a case with a body load, the load vector also contains enriched degrees of freedom that depend on the locations of the enriched nodes. Therefore, the right hand side is design dependent, *i.e.*, $\partial \boldsymbol{F}/\partial \boldsymbol{s} \neq \boldsymbol{0}$, even though the body load is constant throughout the entire domain.

The results of this optimization problem are shown in Figure 4.16. In the optimized design, narrow features can be distinguished that follow the edges of original elements in the background mesh. This is an effect caused by how the intersections are detected, and is investigated in more detail in §4.4.1. The convergence plot shows that, although there are initially some oscillations in both the objective and constraint (also investigated further in §4.4.1), they converge in the end.

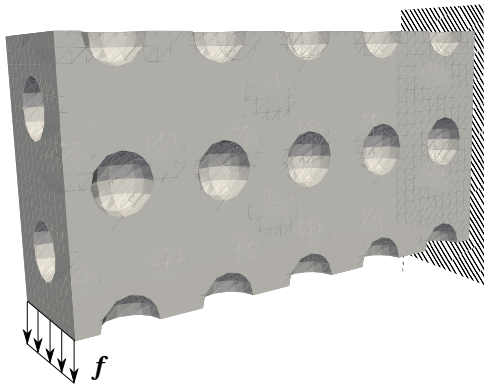

Figuur 4.13: Initial design of the 3-D example with a schematic illustration of the boundary conditions: the right side is fixed and a vertical downward line load is applied on the bottom-left edge.

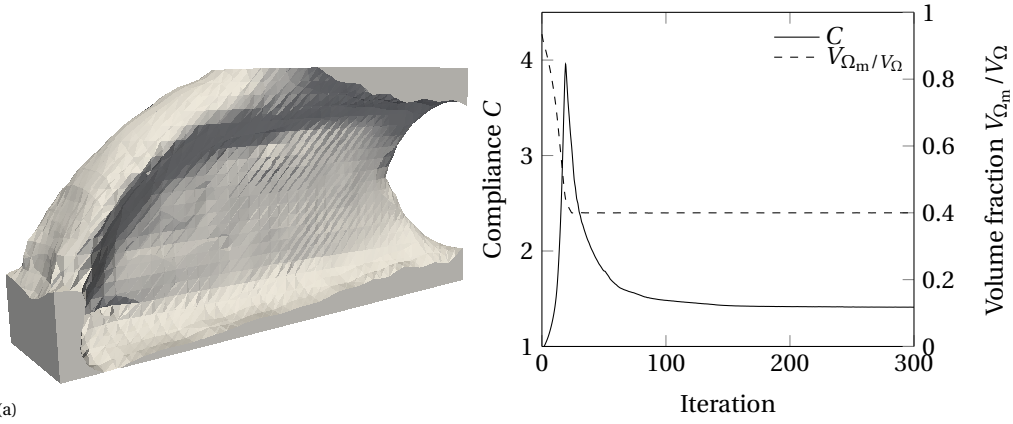

(a)

(b)

Figuur 4.14: Optimized design for the 3-D cantilever beam optimization example (a), and the convergence of the compliance C and volume fraction V_{Ω_m}/V_Ω (b).

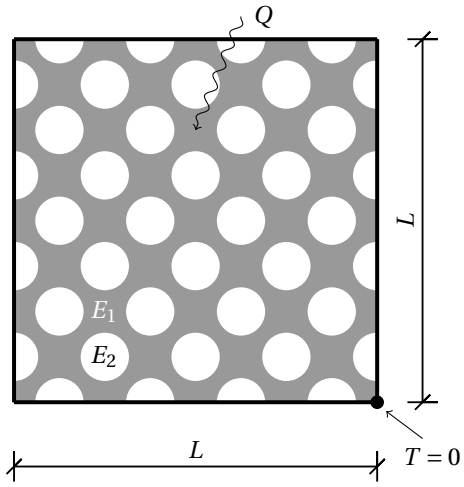

Figuur 4.15: Problem description and initial design for the heat sink. A fixed temperature is applied to the bottom right corner, and a uniform heat source is applied throughout the entire square domain.

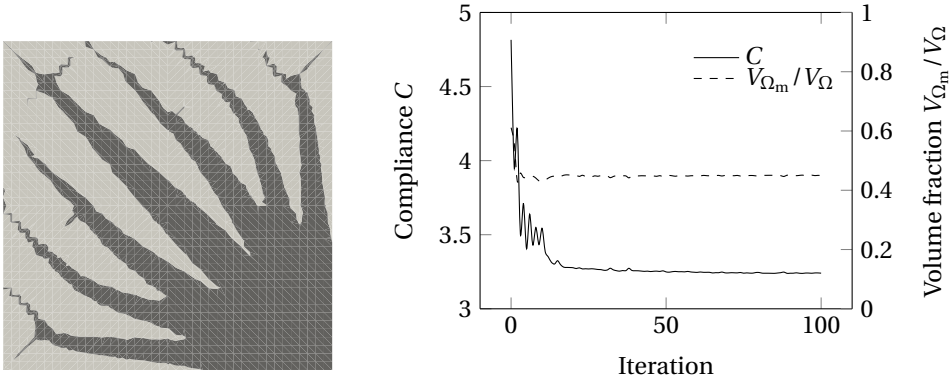

Figuur 4.16: Subfigure (a) shows the optimized design of the heat sink problem, where narrow features are created along the edges of the original mesh element. The convergence plot in (b) shows initially some small oscillations that can be prevented by the use of a smaller move limit.

4.4. DISCUSSION

4.4.1. OSCILLATIONS: THE LEVEL SET DISCRETIZATION

Oscillations in the objective functions are visible in the convergence of the heat sink problem in Figure 4.16, and in the coarsest RBF mesh of the MBB beam in Figure 4.12. As these oscillations might point to inaccurate modeling or sensitivities, the phenomenon is discussed here in more detail.

Recall that intersections between the zero contour of the level set function and element edges are found using a linear interpolation of nodal level set values. Because the level set function is discretized, no intersections can be found if two adjacent nodes have the same sign, as (4.8) does not hold for $\phi_j \phi_k \geq 0$. This effect is illustrated in Figure 4.17. On the left, the zero-contour of a level set function is shown in red, which defines a design shown in white/gray. The white arrows indicate the movement of the material boundary during the next design update. On the right, the updated level set contour is shown in red. As the level set values ϕ_j and ϕ_k on the two adjacent original nodes $\boldsymbol{x}_j$ and $\boldsymbol{x}_k$ now have the same sign, the two intersections between them, shown as ● cannot be found.

The sudden disconnection of the structure due to the level set discretization is a discontinuous event that cannot be captured by the sensitivity information. Therefore, as soon as such discontinuous event occurs, the sensitivities and the modeling deviate, and oscillations may occur.

This problem can be alleviated by using a smaller move limit, as was done in the 3-D MBB example. Another approach that could mitigate this issue is to evaluate the parametrized level set function on a finer grid, so that multiple intersections are found on an element edge. However, the procedure that creates integration elements would also need to allow for these more complex intersections. It should be noted that neither of these methods completely eliminates the problem of discontinuous events. Rather, the methods alleviate the problem by limiting their chance of occurrence. On the contrary, the use of a length scale control could eliminate this issue completely by enforcing material and void features to be larger than the element size. Besides eliminating the issue of numerical oscillations, length scale control can also ensure the mesh is sufficiently fine with respect to the design's features to properly describe its physical behavior. Methods for length scale control in parametrized level set methods have recently been proposed (Dunning, 2018; Jansen, 2019).

A related observation can be made in the zigzagged features in the heat sink design of Figure 4.16. As illustrated in Figure 4.18, this pattern occurs when the optimizer tries to make a narrow diagonal feature in the opposite direction of the mesh diagonals. The red intersections cannot be detected, and therefore the structure is disconnected. As a result, the optimizer can only create diagonal narrow features by zigzagging them along element edges, as illustrated in Figure 4.18 on the right.

4.4.2. ZIGZAGGING: APPROXIMATION ERROR

In the final designs of some of the numerical examples, zigzagging of the edges occurred where the zero contour of the level set function is not perfectly smooth, as detailed in Figure 4.19. To investigate the cause of this artifact, the test problem of a clamped beam

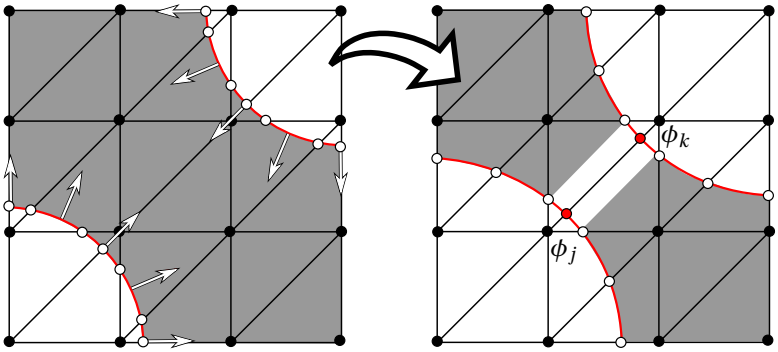

Figuur 4.17: Illustration of the structure disconnecting due to the level set discretization. On the left the zero-contour of the level set, shown in red, defines the design shown in gray. The white arrows indicate the update of the level set in the next iteration. On the right, the next iteration is shown, where the narrowest part of the zero-contour lies within a single element, and the nodal level set values ϕ_j and ϕ_k have the same sign. Therefore, the two intersections shown as ● are not found, and the structure disconnects, as shown by the new gray design.

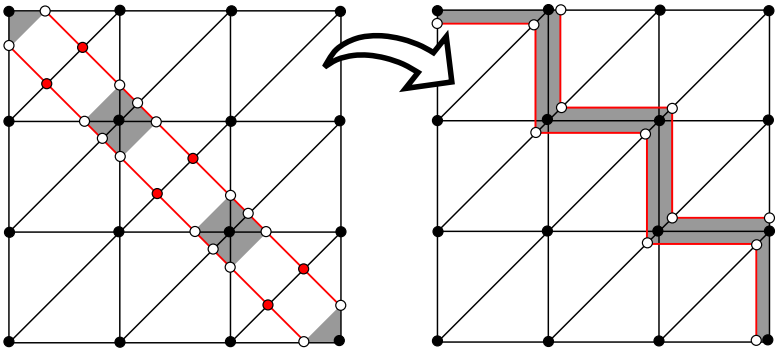

Figuur 4.18: Illustration of the zigzagged pattern that appears in Figure 4.16. When a narrow diagonal line is desired in the opposite direction of the diagonal lines of the mesh, the problem illustrated in Figure 4.17 results in a disconnected line, as shown on the left. Instead, the optimizer will create narrow features along element edges, as illustrated on the right.

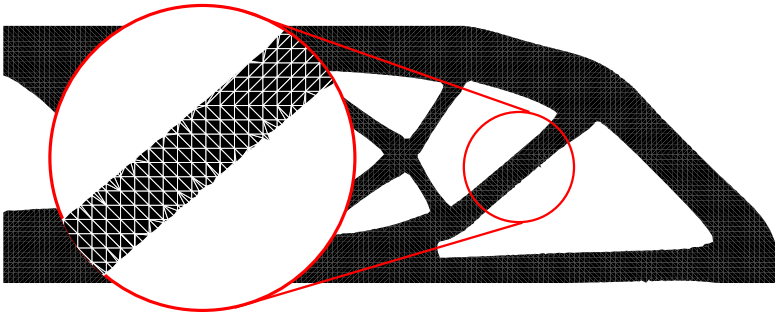

Figuur 4.19: Detail of zigzagging that might occur when the design space is not reduced with respect to the FE mesh.

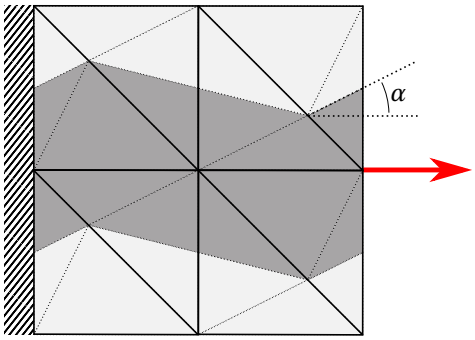

Figuur 4.20: Schematic for the zigzagging approximation error. A beam with zigzagging angle β is clamped on the left, while a concentrated axial loading is applied on the right. The angle β is varied without changing the material volume, and the compliance is evaluated.

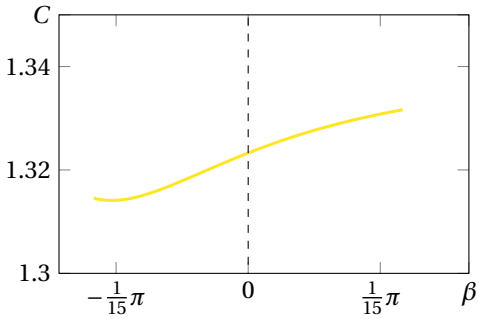

Figuur 4.21: The compliance of the test case, illustrated in Figure 4.20, as a function of the zigzagging angle β. The compliance for this coarse test case is non-symmetric with respect to 0.

loaded axially shown in Figure 4.20 was investigated. The compliance was computed for a varying zigzagging angle β while keeping the material volume constant.

The results in Figure 4.21 show that the minimum compliance is not found at $\beta = 0$, as one would expect, but instead it is found at a negative value of β. Furthermore, the compliance is not symmetric with respect to $\beta = 0$ due to the asymmetry of the analysis mesh. The cause of this zigzagging is an approximation error, as the mesh is too coarse to accurately describe the deformations and stresses in the structure, similarly to the effect described for nodal design variables in Braibant and Fleury (1984). This effect can be resolved by reducing the design space with respect to the analysis mesh, for example with the use of RBFs, or by increasing the element order. Furthermore, as the non-smoothness is confined to a single layer of background elements, mesh-refinement makes the issue less pronounced.

4.5. SUMMARY AND CONCLUSIONS

In this work we introduced a new enriched topology optimization approach based on the Interface-enriched Generalized Finite Element Method (IGFEM). The technique yields

non-pixelized black and white designs, that do not require any post-processing. We have derived an analytic expression for the sensitivities for compliance minimization problems in elastostatics and heat conduction, and have shown that they can be computed with relatively low computational effort. Furthermore, the method was compared to a number of open source topology optimization codes, based on SIMP, the Ersatz approach, and discrete level sets. The influence of decoupling the design discretization from the analysis mesh was investigated using the classical MBB beam optimization problem. A 3-D cantilever beam and a heat sink problem were also demonstrated. The convergence behavior was provided for each numerical example. Any numerical artifacts, such as approximation errors and discretization errors of the level set, as discussed in §4.4, can be mitigated by means of suitable move limits and radial basis functions, where the latter serve as a sort of filter because they can control the design complexity.

A number of conclusions can be drawn from this work:

- The combination of IGFEM with the level set topology optimization based on RBFs results in crisp boundaries in both the design representation and the modeling. Because the RBF mesh and analysis mesh are completely decoupled, the resolution of the design and the modeling can be chosen independently, as is the case in any parametrized level set optimization. In addition, the radial basis functions help in reducing numerical artifacts, as they act like a black-and-white filter. Lastly, as the RBFs may extend over multiple elements, they allow the boundary to move further and the optimizer to converge faster;

- As only one intersection can be detected per element edge, due to the mapping of the level set to the original mesh nodes, features smaller than a single element might not be described correctly. As discussed in §4.4.1, this may lead to oscillations in the convergence. Using a finer grid for evaluating the level sets, more intersection may be found, allowing for narrower features. However, this will require a more involved procedure for creating integration elements. Similarly, the method may be extended to be used on quadrilateral elements, which also requires more involved integration element procedures. Furthermore, for quadrilateral elements, higher order enrichment functions are needed (Aragón *et al.*, 2020);

- Due to approximation error, numerical artifacts may occur that may be exploited by the optimizer when the RBF mesh is too fine with respect to the analysis mesh. Another known issue in IGFEM and other enriched methods, which may be exploited by the optimizer, is the fact that the computation of stresses near material interfaces may yield inaccurate results (Nagarajan and Soghrati, 2018; Soghrati *et al.*, 2017);

- In this work, we chose to model the void together with the material domain for a number of reasons, including ease of implementation, and ease of comparing to other methods. However, we could have chosen to completely remove the void from the analysis (van den Boom *et al.*, 2019b), which would reduce computation times and eliminate the artificial stiffness in the void.

Compared to the commonly-used density-based methods, our proposed approach does not introduce staircasing nor gray values. The location of the boundary is there-

fore known throughout the entire optimization, and no post-processing of the design is required. However, additional complexity is introduced in the creation of integration elements. Furthermore, the extra enriched nodes slightly increase the size of system matrices, which is an effect that diminishes with mesh refinement. Lastly, in density-based methods for linear elasticity, the local element arrays can simply be scaled with the density, and need to be computed only once. In our approach, local arrays for integration elements have to be computed at every iteration.

In an optimization context, IGFEM has a number of advantages:

- The IGFEM formulation provides a natural distinction between original mesh nodes, which are stationary and on which the level set is evaluated, and enriched nodes, which define the material boundary and are allowed to move during optimization. Enriched DOFs are directly related to the discontinuity in the gradient of the field;
- As the background mesh does not change during optimization, the mapping of the design variables to nodal level set values has to be computed only once; and
- As the location of enriched nodes is known to remain on the background element edges, and the enriched node location is computed as a linear interpolation between background mesh nodes, the direction of the design velocities is known *a priori*. This simplifies the sensitivity computations;

Regarding the benefits of IGFEM with respect to X/GFEM, in addition to those regarding the analysis phase described in §4.2.1, the first item above must also be added. In X/GFEM the distinction is less clear, as enrichments are associated to nodes of the background mesh.

As mentioned in §4.1, the benefits of using an enriched formulation are expected to be more pronounced for problems that rely heavily on an accurate boundary description, such as fluid-structure interaction and wave scattering. In fact, the optimization of the latter is the subject of an incoming publication.

4.6. REPLICATION OF RESULTS

This manuscript is self-contained, in that it contains all necessary theory to reproduce the results, including the preliminaries, *i.e.*, the IGFEM approximation and the theory on radial basis functions. The sensitivity computation is described in detail, and all parameters for the numerical examples are provided. Furthermore, the sensitivities are verified using central finite differences, and appendices detailing the relation of IGFEM to X/GFEM, the isoparametric mapping of integration elements, and the derivatives of the Jacobian inverse and determinant have been included. Lastly, designs of intermediate iterations are supplied in the supplementary material.

APPENDIX A: DERIVATION OF IGFEM FROM X/GFEM

Here we derive the IGFEM formulation from the X/GFEM approximation for a single 1-D linear finite element with nodes x_1 and x_2 that contains a weak discontinuity at x_n. For

this element, the X/GFEM approximation can be written as

$$u^h(x) = \underbrace{\sum_{i=1}^{2} N_i(x)\, U_i}_{\text{std. FEM}} + \underbrace{\sum_{i=1}^{2} N_i(x)\, E_i(x)\, \hat{U}_i}_{\text{enrichment}}, \tag{4.33}$$

where E_i denotes the enrichment functions and $\hat{U}_i$ are the generalized DOFs. In order to derive the IGFEM formulation, the key is to select appropriate enrichment functions E_i. We use scaled Heaviside enrichments, as shown in Figure 4.22.

By clustering DOFs, *i.e.*, $\hat{U}_1 = \hat{U}_2 = \alpha$, we reduce the number of enriched DOFs (Duarte *et al.*, 2007). The enrichment term is then given by

$$\begin{aligned} \sum_{i=1}^{2} N_i E_i \hat{U}_i &= (N_1 E_1 + N_2 E_2)\,\alpha, \\ &= \underbrace{[N_1 c_1 H(x - x_n) + N_2 c_2 H(x_n - x)]}_{\psi}\,\alpha \end{aligned} \tag{4.34}$$

where H is the Heaviside function and the constants $c_1 = 1/(1-w)$ and $c_2 = 1/w$, with $w = x_n/(x_2 - x_1)$, yield a C^0–continuous function that attains a maximum value of one regardless of the discontinuity location within the element. The final approximation is therefore

$$u^h(x) = \sum_{i=1}^{2} N_i(x)\, U_i + \psi\alpha, \tag{4.35}$$

which is equivalent to the IGFEM approximation for a 1-D bar containing a weak discontinuity. Similar considerations can be made for higher-dimensional problems.

APPENDIX B: ISOPARAMETRIC MAPPING OF INTEGRATION ELEMENTS

In order to make this manuscript self-contained, here we describe the isoparametric mapping and numerical integration of an IGFEM integration element, as explained in more detail in §4.2.1 and illustrated in Figure 4.3.

The integration element's stiffness matrix $\boldsymbol{k}_e$ can be computed in terms of the reference integration element as

$$\begin{aligned} \boldsymbol{k}_e &= \int_{\Omega_e} \begin{bmatrix} \boldsymbol{\Delta}_{\boldsymbol{x}} \boldsymbol{N} \\ \boldsymbol{\Delta}_{\boldsymbol{x}} \boldsymbol{\psi} \end{bmatrix} \boldsymbol{D} \begin{bmatrix} \boldsymbol{\Delta}_{\boldsymbol{x}}^{\intercal} \boldsymbol{N}^{\intercal} & \boldsymbol{\Delta}_{\boldsymbol{x}}^{\intercal} \boldsymbol{\psi}^{\intercal} \end{bmatrix} \mathrm{d}\boldsymbol{x}, \\ &= \int_{\triangle} j_e \boldsymbol{B}^{\intercal} \boldsymbol{D} \boldsymbol{B} \mathrm{d}\boldsymbol{\xi}, \end{aligned} \tag{4.36}$$

with $\boldsymbol{B} = \begin{bmatrix} \boldsymbol{\Delta}_{\boldsymbol{\xi}}^{\intercal} \boldsymbol{N}^{\intercal} \boldsymbol{J}^{-\intercal} & \boldsymbol{\Delta}_{\boldsymbol{\xi}}^{\intercal} \boldsymbol{\psi}^{\intercal} \boldsymbol{J}_e^{-\intercal} \end{bmatrix}$, and the element force vector $\boldsymbol{f}_e$ is computed in terms of the reference integration element as

$$\begin{aligned} \boldsymbol{f}_e &= \int_{\Omega_e} \begin{bmatrix} \boldsymbol{N} \\ \boldsymbol{\psi} \end{bmatrix} \boldsymbol{b} \mathrm{d}\boldsymbol{x} + \int_{\Gamma_e} \begin{bmatrix} \boldsymbol{N} \\ \boldsymbol{\psi} \end{bmatrix} \bar{\boldsymbol{t}} \mathrm{d}\boldsymbol{x} \\ &= \int_{\triangle} j_e \begin{bmatrix} \boldsymbol{N} \\ \boldsymbol{\psi} \end{bmatrix} \boldsymbol{b} \mathrm{d}\boldsymbol{\xi} + \int_{\triangle \cap \Gamma^{\mathrm{N}}} j_e \begin{bmatrix} \boldsymbol{N} \\ \boldsymbol{\psi} \end{bmatrix} \bar{\boldsymbol{t}} \mathrm{d}\partial\boldsymbol{\xi}. \end{aligned} \tag{4.37}$$

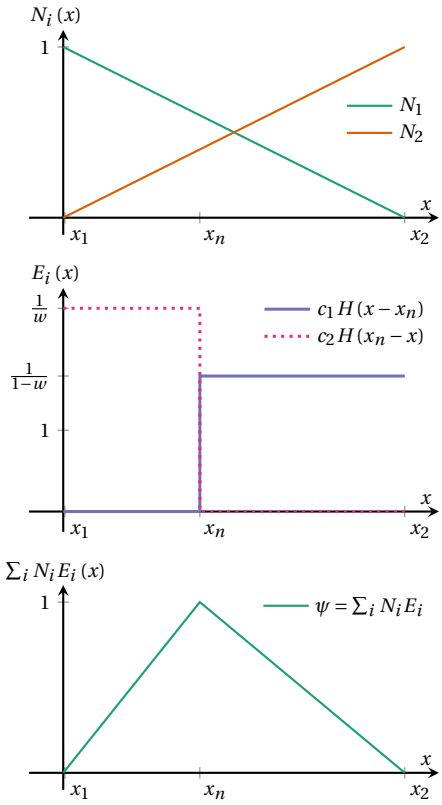

Figuur 4.22: Construction of IGFEM enrichment function from X/GFEM formulation.

A global coordinate $\boldsymbol{x}$, in terms of the isoparametric mappings of the integration and parent elements, can be written as

$$\boldsymbol{x} = \boldsymbol{x}_e^{\mathsf{T}} N_e(\boldsymbol{\xi}_e) = \boldsymbol{x}_p^{\mathsf{T}} N(\boldsymbol{\xi}_p), \tag{4.38}$$

where $\boldsymbol{N}_e$ are the linear Lagrange shape functions associated to the nodes of the integration element, with global coordinates $\boldsymbol{x}_e$. Similarly, $\boldsymbol{N}$ are the shape functions associated to the parent's nodes with global coordinates $\boldsymbol{x}_p$.

The Jacobians of these mappings and their determinants are computed as

$$\boldsymbol{J}_e = \frac{\partial \boldsymbol{x}}{\partial \boldsymbol{\xi}_e} = \boldsymbol{x}_e^{\mathsf{T}} \frac{\partial \boldsymbol{N}_e(\boldsymbol{\xi}_e)}{\partial \boldsymbol{\xi}_e}, \qquad j_e = \det(\boldsymbol{J}_e), \tag{4.39}$$

and

$$\boldsymbol{J} = \frac{\partial \boldsymbol{x}}{\partial \boldsymbol{\xi}_p} = \boldsymbol{x}_p^{\mathsf{T}} \frac{\partial \boldsymbol{N}(\boldsymbol{\xi}_p)}{\partial \boldsymbol{\xi}_p}, \qquad j = \det(\boldsymbol{J}), \tag{4.40}$$

respectively, where $\boldsymbol{x}_e$ contains the integration element nodes and $\boldsymbol{x}_p$ contains the parent element nodes.

Numerical integration is performed in the reference integration element by means of Gauss quadrature. Using (4.38) it is straightforward to map the Gauss integration point's reference coordinates $\boldsymbol{\xi}_e$ to its corresponding global coordinates $\boldsymbol{x}$. The inverse mapping from $\boldsymbol{x}$ to the location in the parent reference coordinate system $\boldsymbol{\xi}_p$ is more involved. For a 2-D triangular element the procedure can be written as

$$\begin{aligned}
\boldsymbol{x} &= \begin{bmatrix} x_{i,1} & x_{j,1} & x_{k,1} \\ x_{i,2} & x_{j,2} & x_{k,2} \end{bmatrix} \begin{bmatrix} 1-\xi_1-\xi_2 \\ \xi_1 \\ \xi_2 \end{bmatrix} \\
\boldsymbol{x} &= \begin{bmatrix} x_{i,1} + \xi_1(x_{j,1}-x_{i,1}) + \xi_2(x_{k,1}-x_{i,1}) \\ x_{i,2} + \xi_1(x_{j,2}-x_{i,2}) + \xi_2(x_{k,2}-x_{i,2}) \end{bmatrix}, \\
\boldsymbol{x} - \begin{bmatrix} x_{i,1} \\ x_{i,2} \end{bmatrix} &= \underbrace{\begin{bmatrix} x_{j,1}-x_{i,1} & x_{k,1}-x_{i,1} \\ x_{j,2}-x_{i,2} & x_{k,2}-x_{i,2} \end{bmatrix}}_{\boldsymbol{A}} \begin{bmatrix} \xi_1 \\ \xi_2 \end{bmatrix}
\end{aligned} \tag{4.41}$$

Inverting this isoparametric mapping leads to the following equation for the integration point in parent coordinates $\boldsymbol{\xi}_p$

$$\boldsymbol{\xi}_p = \begin{bmatrix} \xi_1 \\ \xi_2 \end{bmatrix} = \boldsymbol{A}^{-1}\boldsymbol{x} - \boldsymbol{A}^{-1} \begin{bmatrix} x_{i,1} \\ x_{i,2} \end{bmatrix}. \tag{4.42}$$

APPENDIX C: DERIVATIVES OF THE JACOBIAN INVERSE AND DETERMINANT

In the sensitivity computation discussed in §4.2.3, the derivative of the Jacobian inverse and determinant are required. According to Jacobi's formula (Magnus and Neudecker, 2007), the derivative of the determinant of a matrix can be computed as the trace of the

adjugate of the matrix ($\text{adj}(\boldsymbol{J}_e) = j_e \boldsymbol{J}_e^{-\mathsf{T}}$), multiplied by the derivative of the matrix. For the Jacobian determinant j_e, the derivative can thus be computed as:

$$\frac{\partial j_e}{\partial \boldsymbol{x}_n} = \text{tr}\left(\text{adj}(\boldsymbol{J}_e)\frac{\partial \boldsymbol{J}_e}{\partial \boldsymbol{x}_n}\right), \tag{4.43}$$

The sensitivity of the Jacobian inverse can be computed by realizing that $\boldsymbol{J}_e \boldsymbol{J}_e^{-1} = \boldsymbol{I}$:

$$\frac{\partial \boldsymbol{J}_e \boldsymbol{J}_e^{-1}}{\partial \boldsymbol{x}_n} = \frac{\partial \boldsymbol{J}_e}{\partial \boldsymbol{x}_n}\boldsymbol{J}_e^{-1} + \boldsymbol{J}_e \frac{\partial \boldsymbol{J}_e^{-1}}{\partial \boldsymbol{x}_n} = \frac{\partial \boldsymbol{I}}{\partial \boldsymbol{x}_n} = 0, \tag{4.44}$$

and solving for $\partial \boldsymbol{J}_e^{-1}/\partial \boldsymbol{x}_n$:

$$\frac{\partial \boldsymbol{J}_e^{-1}}{\partial \boldsymbol{x}_n} = -\boldsymbol{J}_e^{-1}\frac{\partial \boldsymbol{J}_e}{\partial \boldsymbol{x}_n}\boldsymbol{J}_e^{-1}. \tag{4.45}$$

For both (4.43) and (4.45), the sensitivity of the Jacobian is required; as the Jacobian of the integration element is computed as $\boldsymbol{J}_e = \boldsymbol{x}_e^{\mathsf{T}} \partial \boldsymbol{N}_e / \partial \boldsymbol{\xi}_e$ it can be computed as

$$\frac{\partial \boldsymbol{J}_e}{\partial \boldsymbol{x}_n} = \frac{\partial \boldsymbol{x}_e^{\mathsf{T}}}{\partial \boldsymbol{x}_n}\frac{\partial \boldsymbol{N}_e}{\partial \boldsymbol{\xi}_e} + \boldsymbol{x}_e^{\mathsf{T}}\cancelto{0}{\frac{\partial^2 \boldsymbol{N}_e}{\partial \boldsymbol{\xi}_e \partial \boldsymbol{x}_n}}, \tag{4.46}$$

where $\partial \boldsymbol{x}_e / \partial \boldsymbol{x}_n$ is simply a selection array consisting of zeros except for a one on the entries of interest for enriched node n.

5

TOPOLOGY OPTIMIZATION OF PHONONIC CRYSTALS

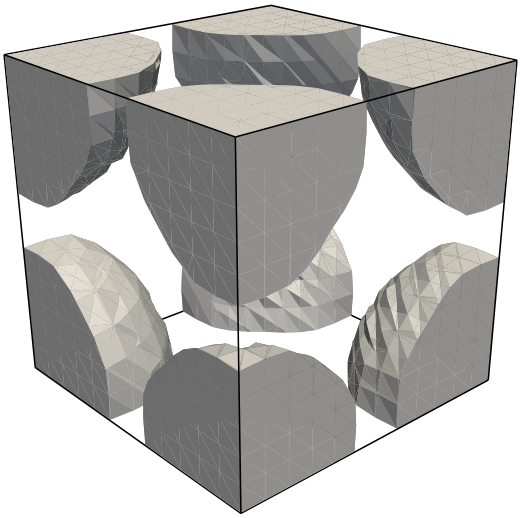

In this chapter, the theory developed in previous chapters is brought together for the computational design of phononic crystals—architected bandgap materials that interact with mechanical waves. In this chapter it is demonstrated how the enriched analysis of phononic crystals, introduced in Chapter 3, shows superior accuracy compared to density-based methods that are generally used in topology optimization. Furthermore, it is shown how the level set-based topology optimization using IGFEM, introduced in Chapter 4, can be used for the computational design of phononic crystals.

This chapter will be submitted for publication

On the importance of boundary smoothness for the computational design of phononic crystals

Abstract *Phononic crystals can be designed to show bandgaps—ranges of frequencies whose propagation is strongly attenuated in the material. In essence, their working principle is based on destructive interference of waves reflecting from the periodic arrangement of material interfaces (i.e Bragg scattering). Consequently, capturing accurately the behavior at material interfaces requires appropriate numerical modeling and computational design techniques. However, the commonly used density-based representation in popular topology optimization methods results in a diffuse staircased boundary. The heavily refined finite element meshes required to compensate for this boundary description results in exceedingly large and expensive optimization problems. In this paper, we demonstrate the adverse effect of the density-based boundary description. Furthermore, we propose a level set-based topology optimization procedure with an enriched finite element method that shows improved performance when compared to the density-based approach.*

5.1. INTRODUCTION

Since their introduction in the seminal papers by Sigalas and Economou (1993); Sigalas and Economou (1992) and Kushwaha *et al.* (1993), phononic crystals have gained increased attention due to their peculiar effect on traveling waves. Because bandgaps can be tuned to any mechanical wavelength, applications can vary from thermal control by operating on the nano scale (Davis and Hussein, 2014), to seismic engineering (Yan *et al.*, 2015) on the other side of the wavelength spectrum. These materials can be designed for vibrationless environments (Hussein *et al.*, 2014), and for specialized control over the traveling waves, which can be used for energy harvesting (Park *et al.*, 2019; Tol *et al.*, 2019) and for efficient sound radiation (Jung *et al.*, 2019). For instance, these periodic media can be used to develop new sensing technology for the characterization of biological samples and sensitive chemicals (Lucklum and Li, 2009; Lucklum *et al.*, 2021; Oseev *et al.*, 2013), and are sometimes also combined with photonics to form phoxonic sensors (Pennec *et al.*, 2019). For an overview of the historical development of phononic crystal research, see the review by Hussein *et al.* (2014), the more recent reviews by Vasileiadis *et al.* (2021) and Muhammad and Lim (2021), and the review that focusses on tunable and active PnCs by Wang *et al.* (2020).

To design these materials for specific functionality, *ad hoc* trial-and-error design procedures based on intuition are not an option due to the complexity of the structure in these *bandgap materials*. Instead, systematic computational procedures are needed

for their design that can generate candidate solutions and quantitatively discriminate among them. Topology Optimization (TO) (Bendsøe and Kikuchi, 1988; Eschenauer and Olhoff, 2001; Rozvany, 2009; Sigmund, 1994) is a powerful numerical tool widely used for designing complex materials and structures that can be used to unlock the full potential of phononic crystals (PnCs). A first categorization of TO procedures can be made on whether or not gradient information is used during a numerical optimization process. Single- and multi- objective optimization of phononic crystals is successfully demonstrated using Non-Gradient-based Topology Optimization (NGTO) techniques, such as Genetic Algorithms (GAs). GAs have been used for maximizing absolute and relative bandgaps (Bilal and Hussein, 2011, 2017; Gazonas *et al.*, 2006; Hedayatrasa *et al.*, 2016a, 2017; Hussein *et al.*, 2007; Qian *et al.*, 2020; **?**), for designing tunable PnCs (Bortot *et al.*, 2018; Hedayatrasa *et al.*, 2016b), PnCs with prestress (Pascalis *et al.*, 2020), PnCs with seperate bandgaps with different polarizations (Liu *et al.*, 2016b), and PnCs with reduced symmetry (Dong *et al.*, 2014, 2015). It has also be used for multiobjective optimization (Xu *et al.*, 2020), including the optimization for bandgaps and thermal expansion (Zhang *et al.*, 2021). It has been used in a two-scale approach (Liang and Du, 2020), and in combination with Kriging (Zhang *et al.*, 2021). As an alternative for NGTO, in recent years machine learning techniques have been introduced for the design of PnCs (Li *et al.*, 2019a, 2020; Liu *et al.*, 2019; Sadat and Wang, 2020). NGTO methods can handle discrete design variables, and can therefore be used to assign a material to each element. Although this avoids diffuse boundaries, these methods generally still suffer from staircasing. Furthermore, NGTO methods are usually population-based, and as such, they require vast computational resources despite being *embarrassingly parallel*.

Gradient-based Topology Optimization (GTO), on the other hand, has the advantage of requiring considerably less function evaluations, although it generally cannot handle discrete design variables. Consequently, simply assigning a discrete material to each element is not possible, and other means of describing the geometry are required. Most commonly, the material properties in each element are continuously interpolated to ensure differentiability. Sigmund and Jensen (Sigmund and Jensen, 2002, 2003) were the first to propose density-based topology optimization designing both PnC unit cells and finite sized phononic crystals. Density-based TO has been used for maximizing the absolute or relative width of bandgaps (Li *et al.*, 2019c, 2018; Lu *et al.*, 2017; Rupp *et al.*, 2007; Yuksel and Yilmaz, 2020), the spatial decay of evanescent waves (Chen *et al.*, 2017a), and the wave attenuation in viscoelastic materials (Chen *et al.*, 2018). It has also been used to design PnCs that show self-collimation of elastic waves (Park *et al.*, 2015), piezoelectric PnCs (Vatanabe *et al.*, 2014), PnCs with different properties in different directions(Chen *et al.*, 2017b; He and Kang, 2018), and PnCs that are robust to imperfections (Ma *et al.*, 2021; Xie *et al.*, 2017, 2018; Zhang *et al.*, 2018, 2019c). Extensive reviews on the developments of topology optimization of PnCs were written by Yi and Youn (2016) and Li *et al.* (2019b), where the latter also includes works on the topology optimization of Photonic Crystals (PtCs). Despite its popularity, GTO with a density approach leads to boundary descriptions that are both staircased and diffuse, *i.e.* they have intermediate (gray) values in the design.

Yera *et al.* (2021) achieve a better description of the boundaries by combining a level set-based approach with local mesh refinements during the topology optimization.

However, this method only improves the mesh resolution near the boundaries, it does not remove the staircasing or intermediate densities. Alternatively, to avoid staircased boundaries, enriched finite element methods can be used in combination with a level-set topology optimization approach. The enriched analysis of PnCs was demonstrated by Zhao *et al.* (2015) and van den Boom *et al.* (2021a), but to the best of our knowledge, topology optimization of PnCs using an enriched finite element method has not yet been described in literature despite its great potential. The Interface-enriched Generalized Finite Element Method (IGFEM) Soghrati *et al.* (2012a), is such an enriched finite element method that has advantages over the well known eXtended/Generalized Finite Element Method (X/GFEM) (Belytschko *et al.*, 2003; Liu *et al.*, 2016a; Villanueva and Maute, 2014). In IGFEM, the standard finite element approximation is enriched with an additional term which accounts for *a priori* knowledge about the kinematics of material interfaces.Contrary to X/GFEM, where enrichment functions are associated to nodes of the standard FEM mesh, IGFEM place enrichments to nodes collocated along discontinuities, providing considerable benefits over X/GFEM with respect to the enforcement of boundary conditions on non-matching edges (Aragón and Simone, 2017; van den Boom *et al.*, 2019b, 2021a; Cuba Ramos *et al.*, 2015). IGFEM has been shown to converge optimally with mesh refinement (Soghrati and Geubelle, 2012; Soghrati *et al.*, 2012a), and has previously been demonstrated for the topology optimization for compliance minimization (van den Boom *et al.*, 2021b), and for the immersed design of PnC (van den Boom *et al.*, 2021a).

In this work we study the importance of smooth and non-diffuse boundaries in the analysis and design of phononic crystals. To that end, the governing equations, simulation techniques, and boundary representation methods are described briefly in §5.2. The influence of a staircased and diffuse boundary description is investigated in detail in §5.3 and it is demonstrated that highly refined meshes are needed to reach the same level of accuracy in staircased and diffuse cases. Therefore, a level-set based topology optimization procedure is proposed in combination with IGFEM in order to find optimized unit cell topologies for bandgap maximization without staircased boundaries. The topology optimization problem and corresponding sensitivity analysis are then specified in §5.4. Finally, the procedure is employed to generate optimized phononic crystal topologies with non-staircased boundaries in 2-D and 3-D for bandgap maximization in §5.5. We show that the method can generate designs with bandgaps between desired bands, despite numerical challenges. These challenges are discussed in detail in §5.6.

5.2. COMPUTATIONAL ANALYSIS OF PHONONIC CRYSTALS

The computational analysis of the effect that phononic crystals have on traveling waves can be divided into two categories: approaches considering the full finite sized phononic crystal, and approaches using a periodic unit cell (PUC), where the PnC is assumed to be infinite. In this paper, the latter approach is used, using the governing equations, modeling approach, and boundary representations described in this section.

Figure 5.1 illustrates a 3-D finite-sized PnC and its corresponding PUC. The phononic crystal consists of a periodic array of inclusions Ω_i inside a host material Ω_h, where material interfaces are denoted Γ_i. To obtain this phononic crystal, the PUC is repeated along the lattice vectors $\boldsymbol{a}_i, i = \{1,\dots 3\}$.

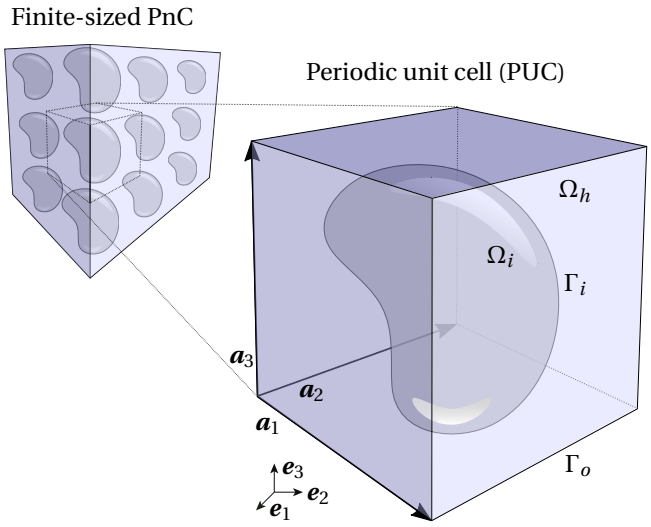

Figuur 5.1: Schematic representation of a PnC: the finite-sized phononic crystal consists of a periodic array of periodic unit cells. The PUC itself is a cube with lattice vectors $\boldsymbol{a}_1$, $\boldsymbol{a}_2$ and $\boldsymbol{a}_3$. The domain Ω consists of a host phase Ω_h and an inclusion Ω_i. The boundary between the two is denoted Γ_i, and Γ_o is the boundary of the PUC.

5.2.1. GOVERNING EQUATION AND FORMULATION

On both the host domain (Ω_h) and the inclusion (Ω_i), the behavior is governed by the elastodynamic wave equation:

$$\rho_j \, \ddot{\boldsymbol{u}}_j - \nabla \cdot \boldsymbol{\sigma}_j = \boldsymbol{0} \,, \quad j = h, i, \tag{5.1}$$

where material density is denoted ρ_j, $\boldsymbol{u}_j(\boldsymbol{x}, t) \equiv \boldsymbol{u}|_{\Omega_j}$ is the restriction of the displacement field $\boldsymbol{u}$ to the domain Ω_j, $\boldsymbol{x}$ indicates spatial coordinate, t indicates time, $\boldsymbol{\sigma}_j = \lambda_j \operatorname{tr}(\boldsymbol{\varepsilon}_j)\boldsymbol{\varepsilon}_j + 2\mu_j \boldsymbol{\varepsilon}_j$ is the stress tensor, $\nabla\cdot$ is the divergence operator, and $\boldsymbol{\varepsilon}_j = \frac{1}{2}\left(\nabla \boldsymbol{u}_j + \nabla \boldsymbol{u}_j^\intercal\right)$ is the linearized strain tensor. Boundary and initial conditions depend on the analysis approach.

For band structure analysis of PnCs a periodic unit cell is used as illustrated in Figure 5.1. Bloch-Floquet periodic boundary conditions are prescribed on the outer boundary Γ_o of this PUC:

$$\boldsymbol{u}(\boldsymbol{x} + \boldsymbol{a}_i, t) = e^{i(\mathbf{k}\cdot\boldsymbol{a}_i)} \boldsymbol{u}(\boldsymbol{x}, t) \,, \tag{5.2}$$

where $\boldsymbol{a}_i$ is the lattice vector between two periodic edges and $\mathbf{k}$ is a wave vector. These boundary conditions enforce periodicity on the displacement field while accommodating the phase difference of the traveling wave on the two sides of the PUC. The band structure can then be evaluated by performing an eigenvalue analysis for all the wave vectors along the irreducible Brillouin zone (Brillouin, 1930).

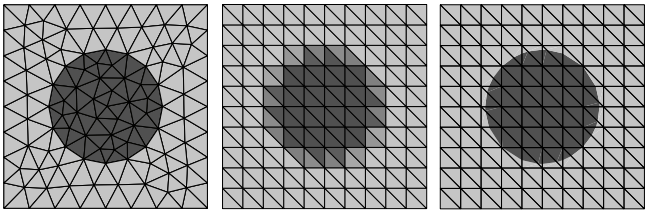

Fitted Density Immersed

Figuur 5.2: The three boundary representations used in this paper: the left figure shows a fitted mesh, the middle figure illustrates the density-based approach, and the figure on the right shows an immersed boundary representation.

5.2.2. BOUNDARY REPRESENTATIONS

Three types of boundary representation are considered in this work, as illustrated in Figure 5.2 for a 2-D PUC:

- **Fitted meshes** In these discretizations the material boundary is piece-wise linearly represented by the edges of elements in the mesh. This method would require remeshing in every design iteration in an optimization setting;
- **Density-based meshes** In these meshes, boundaries are represented based on a pseudo-density ρ of the material within each element. A density of 0 is used to represent the host material, while a density of 1 represents the inclusion material. Intermediate density values are assigned to elements that are intersected by the boundary, corresponding to the volume percentage of the element that lies inside the inclusion. For this boundary representation no remeshing is needed during optimization, but the resulting boundaries are staircased and diffuse;
- **Immersed boundaries** The material boundary is decoupled from the analysis mesh by means of the Interface-enriched Generalized Finite Element Method (IGFEM). This leads to a non-staircased black-and-white piece-wise linear boundary representation. The use of IGFEM for analysis of phononic crystals is described in mode detail in the next section and in van den Boom *et al.* (2021a)

5.2.3. ENRICHED BAND STRUCTURE ANALYSIS

For the enriched analysis of PnCs, IGFEM is used. In IGFEM, both the trial an weight functions in the weak form of (5.1) are chosen from the same enriched finite element space, where the enriched part of the approximation reproduces the kinematics of a material interface Γ_i, *i.e.* a discontinuity in the field gradient (a weak discontinuity). The IGFEM approximation is written as

$$\boldsymbol{u}^h(\boldsymbol{x}) = \underbrace{\sum_{i\in\iota_h} N_i(\boldsymbol{x})\,\boldsymbol{U}_i}_{\text{standard FEM}} + \underbrace{\sum_{i\in\iota_w} \psi_i(\boldsymbol{x})\,\boldsymbol{\alpha}_i}_{\text{enrichment}}. \tag{5.3}$$

The enriched DOFs $\boldsymbol{\alpha}_i$ are associated to new enriched nodes collocated along material interfaces, at the intersection with element edges in the mesh. The material interface is

located at the zero contour of a level set function ϕ, that is discretized on the nodes of the background mesh. The location of the intersection $\boldsymbol{x}_l$ between the node locations $\boldsymbol{x}_j$ and $\boldsymbol{x}_k$, with level-set values ϕ_j and ϕ_k, respectively, is found as

$$\boldsymbol{x}_l = \boldsymbol{x}_j - \frac{\phi_j}{\phi_k - \phi_j}\left(\boldsymbol{x}_k - \boldsymbol{x}_j\right). \tag{5.4}$$

Standard FEM procedures can then be employed to obtain the element mass matrix $\boldsymbol{m}_e$ and stiffness matrix $\boldsymbol{k}_e$. For elements that are intersected by a material interface, standard shape functions $\boldsymbol{N}$ and enrichment functions $\boldsymbol{\psi}$ are stacked as

$$\begin{aligned} \boldsymbol{k}_e &= \int_e \begin{bmatrix} \boldsymbol{\Delta N} \\ \boldsymbol{\Delta \psi} \end{bmatrix} [\boldsymbol{D}] \begin{bmatrix} \boldsymbol{\Delta N}^\mathsf{T} & \boldsymbol{\Delta \psi}^\mathsf{T} \end{bmatrix} \mathrm{d}\Omega, \text{ and} \\ \boldsymbol{m}_e &= \int_{\partial e} \rho_e \begin{bmatrix} \boldsymbol{N} \\ \boldsymbol{\psi} \end{bmatrix} \begin{bmatrix} \boldsymbol{N}^\mathsf{T} & \boldsymbol{\psi}^\mathsf{T} \end{bmatrix} \mathrm{d}\Omega, \end{aligned} \tag{5.5}$$

where $[\boldsymbol{D}]$ is the constitutive matrix, ρ_e is the element mass density, and the differential operator $\boldsymbol{\Delta}$ is defined as:

$$\begin{aligned} \boldsymbol{\Delta}_{\boldsymbol{\xi}} &\equiv \begin{bmatrix} \frac{\partial}{\partial \xi_1} & 0 & \frac{\partial}{\partial \xi_2} \\ 0 & \frac{\partial}{\partial \xi_2} & \frac{\partial}{\partial \xi_1} \end{bmatrix}^\mathsf{T}, \\ \boldsymbol{\Delta}_{\boldsymbol{\xi}} &\equiv \begin{bmatrix} \frac{\partial}{\partial \xi_1} & 0 & 0 & \frac{\partial}{\partial \xi_2} & 0 & \frac{\partial}{\partial \xi_3} \\ 0 & \frac{\partial}{\partial \xi_2} & 0 & \frac{\partial}{\partial \xi_1} & \frac{\partial}{\partial \xi_3} & 0 \\ 0 & 0 & \frac{\partial}{\partial \xi_3} & 0 & \frac{\partial}{\partial \xi_2} & \frac{\partial}{\partial \xi_1} \end{bmatrix}^\mathsf{T}, \end{aligned} \tag{5.6}$$

for 2-D and 3-D respectively. The global mass matrix $\boldsymbol{M}$ and stiffness matrix $\boldsymbol{K}$ are subsequently assembled using the standard FEM procedure.

Finally, Bloch-Floquet periodicity, as described in (5.2) is enforced by a transformation matrix $\boldsymbol{T}$ as

$$\begin{aligned} \tilde{\boldsymbol{K}}(\mathbf{k}) &= \boldsymbol{T}(\mathbf{k})^\mathsf{H} \boldsymbol{K} \boldsymbol{T}(\mathbf{k}), \text{ and} \\ \tilde{\boldsymbol{M}}(\mathbf{k}) &= \boldsymbol{T}(\mathbf{k})^\mathsf{H} \boldsymbol{M} \boldsymbol{T}(\mathbf{k}), \end{aligned} \tag{5.7}$$

where $\boldsymbol{T}$ is complex valued and dependent on the wave vector $\mathbf{k}$. A series of eigenvalue analysis is performed to find the band structure, where wave vectors along the edge of the irreducible Brillouin zone are considered:

$$\left(\tilde{\boldsymbol{K}}(\boldsymbol{k}) - \omega_{\mathbf{k}j}^2 \tilde{\boldsymbol{M}}(\mathbf{k})\right) \tilde{\boldsymbol{V}}_{\mathbf{k}j} = \mathbf{0}. \tag{5.8}$$

For more details on IGFEM, the reader is referred to Soghrati *et al.* (2012a) and Aragón *et al.* (2020). The IGFEM analysis of immersed phononic crystals is described in more detail in van den Boom *et al.* (2021b).

5.3. COMPARISON OF BOUNDARY REPRESENTATIONS

To illustrate that the benefits of piece-wise linear representations in an immersed setting, IGFEM is compared to staircased meshes for a band structure analysis. The effect

of these boundary approximations is investigated in Figure 5.3, which shows the predicted band structure for a coarse staircased unit cell (green) and a unit cell with an immersed representation, analyzed on the same discretization mesh (blue). Both methods are compared to the results of a very fine standard FEM mesh (black). As apparent from the figure, the bandgap obtained by the IGFEM procedure is much closer to the real bandgap than the staircased approximation.

Noteworthy, the result given by the enriched formulation requires marginally more DOFs than the result of the density-based approach, because additional enriched nodes are used. However, as these enriched nodes are placed only along the boundary, the number of enriched nodes relative to the number of standard nodes reduces with mesh refinement. To better assess the performance with respect to computational cost, Figure 5.4 shows the rate of convergence, where the error in the bands that define the band gap is defined by

$$\epsilon = \sqrt{\frac{1}{|K|N}\frac{\sum_{\boldsymbol{k}\in K}\sum_j(\omega_{\boldsymbol{k}j}-\omega^*_{\boldsymbol{k}j})^2}{\sum_{\boldsymbol{k}\in K}\sum_j\omega^{*2}_{\boldsymbol{k}j}}}, \tag{5.9}$$

where K is the set of wave vectors in the Brillouin zone, with cardinality $|K|$, $\omega^*_{\boldsymbol{k}j}$ is the jth frequency for wave vector $\boldsymbol{k}$, obtained by a matching mesh and $\omega_{\boldsymbol{k}j}$ is the approximated frequency. As apparent from Figure 5.4, not only does the IGFEM analysis provide better accuracy, the rate of convergence is also higher. In fact, for some levels of accuracy, the density-based approach requires almost an order of magnitude more DOFs.

To conclude, the use of piece-wise linear representations of the material boundary results in a more accurate solution in the band structure analysis. As a result, much coarser meshes may be used in the analysis and computational design of PnCs when piece-wise linear representations are used. In the context of topology optimization, this does not only drastically reduce the computational effort for the analysis part of the optimization, but it also reduces the number of design variables, as in the density-based topology optimization, the number of design variables is directly coupled to the number of finite elements. Therefore, level set-based topology optimization using IGFEM may help to mitigate *the curse of dimensionality* in the computational design of phononic crystals.

5.4. OPTIMIZATION PROBLEM

Now that the importance of using a non-staircased and non-diffuse boundary is demonstrated a level set based topology optimization using IGFEM for the boundary description is formulated. In this work we aim to maximize the width of the bandgap between the nth and $(n+1)$th propagation bands, on a set of wave vectors K. Henceforward we denote the frequencies corresponding to the nth band that defines the bandgap from below $\hat{f}_{\boldsymbol{k}}$, and the $(n+1)$th, that defines the bandgap from above $\check{f}_{\boldsymbol{k}}$, where $f_{\boldsymbol{k}} = \omega_{\boldsymbol{k}}/(2\pi)$. The optimization problem is now formally stated as

$$\begin{aligned} \boldsymbol{s}^\star \underset{\boldsymbol{s}\in\mathcal{D}}{\arg\min} \quad & \mathcal{F} = \max\left(\hat{f}_{\boldsymbol{k}}\right) - \min\left(\check{f}_{\boldsymbol{k}}\right) \\ \text{such that} \quad & \left(\tilde{\boldsymbol{K}}(\boldsymbol{s}) - \omega^2_{\boldsymbol{k}j}\tilde{\boldsymbol{M}}(\boldsymbol{s})\right)\tilde{\boldsymbol{V}}_{\boldsymbol{k}j} = \boldsymbol{0} \\ & \boldsymbol{s}_{\min} \le \boldsymbol{s} \le \boldsymbol{s}_{\max}, \end{aligned} \tag{5.10}$$

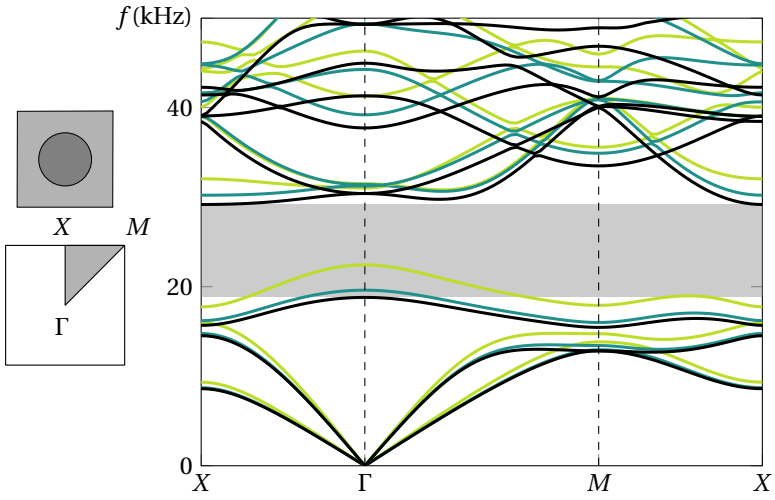

Figuur 5.3: Comparison of band structures computed with a stair-cased boundary representation (green) and a crisp description of the boundary (blue) to the band structure computed on a very fine matching mesh (black). The bandgap for a matching mesh is shown in gray. Clearly, the two approximations show propagation bands within the bandgap. For a comparable number of DOFs, the crisp representation performs considerably better than the staircased boundary. On the left, the irreducible Brillouin zone is illustrated.

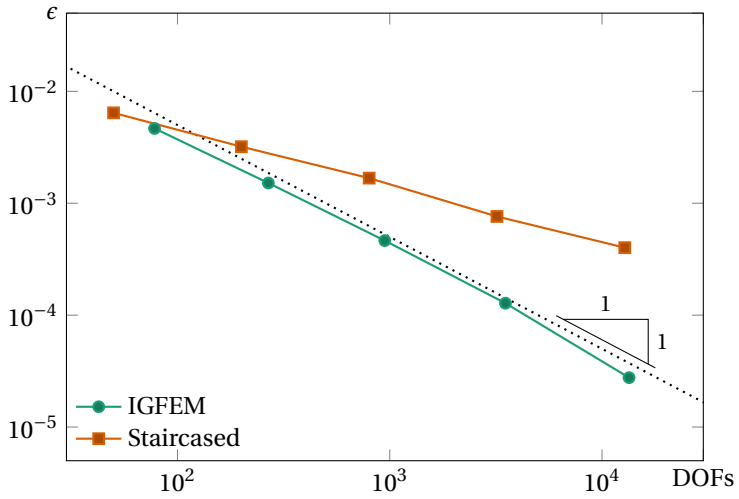

Figuur 5.4: Convergence of the staircased representation, compared to an enriched formulation. Not only is the enriched representation more accurate, a higher rate of convergence is found.

where $\boldsymbol{k} \in K$. The level set function is parametrized using a number of radial basis functions (RBFs) (van den Boom *et al.*, 2021b; Wang and Wang, 2006), that are scaled using the design variables $\boldsymbol{s}$ (see also §4.2.2). The value of $\boldsymbol{s}$ is bounded between $\boldsymbol{s}_{\min} = -1$ and $\boldsymbol{s}_{\max} = 1$. Note that the optimization problem is self-constrained in the sense that the optimal design does not correspond to a fully empty or a fully filled domain. Therefore, this formulation does not require a volume constraint. It was found that this formulation where the bandgap is optimized using $\check{f}_{\boldsymbol{k}}$ and $\hat{f}_{\boldsymbol{k}}$ (or $\check{\omega}_{\boldsymbol{k}}$ and $\hat{\omega}_{\boldsymbol{k}}$), scales better than using $\check{\omega}^2_{\boldsymbol{k}}$ and $\hat{\omega}^2_{\boldsymbol{k}}$ (see Appendix A). A bandgap has opened up when the objective function is negative.

The maximum operator is implemented as the α-smoothmax function,

$$S_\alpha\left(\hat{f}_{\boldsymbol{k}}\right) = \frac{\sum_{\boldsymbol{k}\in K} \hat{f}_{\boldsymbol{k}} e^{\alpha \hat{f}_{\boldsymbol{k}}}}{\sum_{\boldsymbol{k}\in K} e^{\alpha \hat{f}_{\boldsymbol{k}}}}, \tag{5.11}$$

which has the property $S_\alpha\left(\hat{f}_{\boldsymbol{k}}\right) \to \max$ for $\alpha \to \infty$. Similarly, it tends to a minimum for $\alpha \to -\infty$, and thus, the smooth minimum is implemented analogously. In this work we use $\alpha = 40$ and $\alpha = -40$ for smooth maximum and minimum functions, respectively.

This optimization problem is solved using the Method of Moving Asymptotes (MMA) (Svanberg, 1987)[1], which is a widely used optimizer in topology optimization. It requires information of the response function values, as well as their gradients or *sensitivities*. The derivation of the sensitivities for bandgap maximization can be found in §5.4.1. The move limit for MMA that is suitable for the optimization of PnCs depends on the design resolution compared to the mesh resolution.

5.4.1. SENSITIVITY ANALYSIS

The objective function described in this paper can be written as a function of the smooth minimum and maximum function as

$$\mathcal{F} = S_\alpha\left(\hat{f}_{\boldsymbol{k}}\right) - S_{-\alpha}\left(\check{f}_{\boldsymbol{k}}\right). \tag{5.12}$$

The derivative of this objective function with respect to the design variables $\boldsymbol{s}$ can be expressed as

$$\frac{\partial \mathcal{F}}{\partial s_i} = \left(\frac{\partial S_\alpha}{\partial \hat{f}_{\boldsymbol{k}}} \frac{\partial \hat{f}_{\boldsymbol{k}}}{\partial \hat{\omega}^2_{\boldsymbol{k}}} \frac{\partial \hat{\omega}^2_{\boldsymbol{k}}}{\partial \boldsymbol{x}_l} - \frac{\partial S_{-\alpha}}{\partial \check{f}_{\boldsymbol{k}}} \frac{\partial \check{f}_{\boldsymbol{k}}}{\partial \check{\omega}^2_{\boldsymbol{k}}} \frac{\partial \check{\omega}^2_{\boldsymbol{k}}}{\partial \boldsymbol{x}_l} \right) \frac{\partial \boldsymbol{x}_l}{\partial \phi_j} \frac{\partial \phi_j}{\partial s_i}, \tag{5.13}$$

where the chain rule is applied. Here, the partial derivative $\partial S_\alpha / \partial f_{\boldsymbol{k}}$ corresponds to the sensitivity of the smooth maximum/minimum function when an eigenfrequency in the band is changed, $\partial f_{\boldsymbol{k}} / \partial \omega^2_{\boldsymbol{k}} = 1/(4\pi\omega)$ describes the sensitivity of the eigenfrequency $f_{\boldsymbol{k}}$ with respect to the eigenvalue $\omega^2_{\boldsymbol{k}}$, $\partial \omega^2_{\boldsymbol{k}} / \partial \boldsymbol{x}_l$ denotes the change in eigenfrequency when an enriched node is moved, $\partial \boldsymbol{x}_l / \partial \phi_j$ are the design velocities, and $\partial \phi_j / \partial s_i$ are the derivatives of the nodal level set values to the design parameters.

First, the derivative of the smooth maximum function can be computed simply as the derivative of Eq. (5.11):

$$\frac{\partial S_\alpha}{\partial \hat{f}_{\boldsymbol{k}}} = \frac{e^{\alpha \hat{f}_{\boldsymbol{k}}}}{\sum_{\boldsymbol{k}} e^{\hat{f}_{\boldsymbol{k}\star}}} \left(1 + \alpha\left(\hat{f}_{\boldsymbol{k}} - S_\alpha\right)\right), \tag{5.14}$$

[1] The author would like to thank Krister Svanberg for providing us with the MMA implementation.

where $\boldsymbol{k}^\star \neq \boldsymbol{k}$. The derivative of the smooth minimum function is computed analogously.

The derivative of the eigenfrequencies with respect to the enriched node locations $\boldsymbol{x}_l$ can be written as

$$\frac{\partial \omega_{\boldsymbol{k}j}^2}{\partial \boldsymbol{x}_n} = \frac{1}{m_{jj}} \tilde{\boldsymbol{V}}_{\boldsymbol{k}j}^{\mathsf{H}} \boldsymbol{T}_{\boldsymbol{k}}^{\mathsf{H}} \left(\frac{\partial \boldsymbol{K}}{\partial \boldsymbol{x}_l} - \omega_{\boldsymbol{k}j}^2 \frac{\partial \boldsymbol{M}}{\partial \boldsymbol{x}_l} \right) \boldsymbol{T}_{\boldsymbol{k}} \tilde{\boldsymbol{V}}_{\boldsymbol{k}j}, \tag{5.15}$$

where the modal mass $m_{jj} = \tilde{\boldsymbol{V}}_{\boldsymbol{k}i}^{\mathsf{H}} \boldsymbol{T}_{\boldsymbol{k}}^{\mathsf{H}} \boldsymbol{M} \boldsymbol{T}_{\boldsymbol{k}} \tilde{\boldsymbol{V}}_{\boldsymbol{k}j} = 1$ due to mass orthogonality of the eigenvectors. Note that $\boldsymbol{V}_{\boldsymbol{k}j} = \boldsymbol{T}_{\boldsymbol{k}} \tilde{\boldsymbol{V}}_{\boldsymbol{k}j}$, and $\partial \boldsymbol{K}/\partial \boldsymbol{x}_l$ and $\partial \boldsymbol{M}/\partial \boldsymbol{x}_l$ are independent of the wave vector $\boldsymbol{k}$. Omitting the index j and the dependence on wave vector $\boldsymbol{k}$ for clarity, this derivative can now be computed element-wise as

$$\frac{\partial \omega^2}{\partial \boldsymbol{x}_l} = \sum_{e \in \iota_l} \boldsymbol{v}_e^{\mathsf{H}} \left(\frac{\partial \boldsymbol{k}_e}{\partial \boldsymbol{x}_l} - \omega^2 \frac{\partial \boldsymbol{m}_e}{\partial \boldsymbol{x}_l} \right) \boldsymbol{v}_e, \tag{5.16}$$

where ι_l denotes the set of integration elements in the support of enriched node $\boldsymbol{x}_l$, and $\boldsymbol{v}_e$.

The derivative of the element stiffness matrix can be computed as

$$\frac{\partial \boldsymbol{k}_e}{\partial \boldsymbol{x}_n} = \frac{\partial j_e}{\partial \boldsymbol{x}_n} \boldsymbol{B}_e^{\mathsf{T}} \boldsymbol{D}_e \boldsymbol{B}_e + j_e \left(\frac{\partial \boldsymbol{B}_e^{\mathsf{T}}}{\partial \boldsymbol{x}_n} \boldsymbol{D}_e \boldsymbol{B}_e + \boldsymbol{B}_e^{\mathsf{T}} \boldsymbol{D}_e \frac{\partial \boldsymbol{B}_e}{\partial \boldsymbol{x}_n} \right). \tag{5.17}$$

For the element mass matrix, following a similar approach, the derivative is written as:

$$\frac{\partial \boldsymbol{m}_e}{\partial \boldsymbol{x}_n} = \frac{\partial j_e}{\partial \boldsymbol{x}_n} \rho_e \boldsymbol{N}_e^{\mathsf{T}} \boldsymbol{N}_e + j_e \rho_e \left(\frac{\partial \boldsymbol{N}_e^{\mathsf{T}}}{\partial \boldsymbol{x}_n} \boldsymbol{N}_e + \boldsymbol{N}_e^{\mathsf{T}} \frac{\partial \boldsymbol{N}_e}{\partial \boldsymbol{x}_n} \right). \tag{5.18}$$

For details on the remaining terms in the sensitivity analysis see Appendix B and van den Boom *et al.* (2021b).

5.5. OPTIMIZED PHONONIC CRYSTAL DESIGNS

The previously described topology optimization procedure is now used to design of phononic crystals in 2-D and 3-D with maximized bandgaps.

5.5.1. BANDGAP MAXIMIZATION IN 2-D PNCS

First, the maximization of bandgaps between different bands in a 2-D PnC is considered. To that end, a square periodic unit cell is optimized with an arbitrary topology that has 8-fold symmetry. The periodic unit cell has dimensions of 25 mm × 25 mm, and consists of polycarbonate ($E_1 = 2.3\,\text{GPa}$, $\nu_1 = 0.37$, $\rho_1 = 1200\,\text{kg/m}^3$) and lead ($E_2 = 16\,\text{GPa}$, $\nu_2 = 0.44$, $\rho_2 = 11\,340\,\text{kg/m}^3$). The phononic crystal is optimized for maximized bandgap between the 3rd and 4th, and 6th and 7th bands. Because the method cannot nucleate inclusions, initial designs with a number of inclusions are defined. Two types of initial designs are used: lead inclusions in a polycarbonate matrix, and polycarbonate inclusions in a lead matrix. Each optimization problem is solved on two sizes of symmetric triangular analysis meshes, consisting of 20 × 20 × 2 and 40 × 40 × 2 triangular elements, respectively.

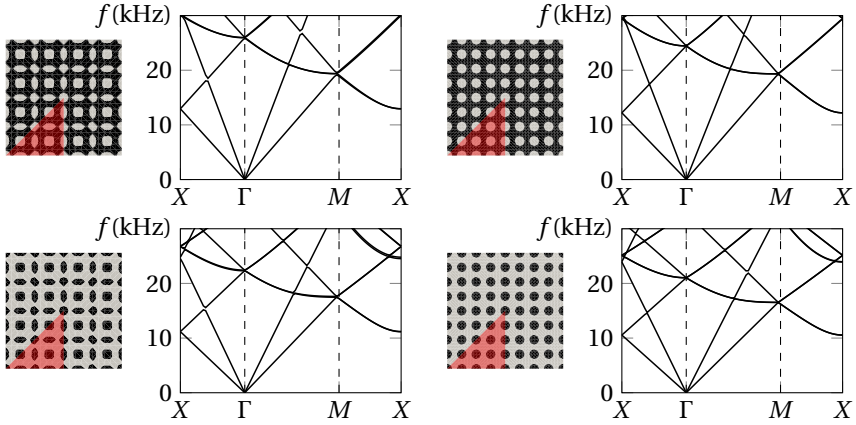

Figuur 5.5: Initial designs for the 2-D phononic crystal optimization. On the left (right), 20×20×2 (40×40×2) triangular elements are used. The top row shows initial conditions with a lead matrix (black) and polycarbonate inclusions(gray). In the bottom row the inclusions (black) are made of lead and the matrix is polycarbonate (gray). The red triangle indicates the reduced design area due to symmetry.

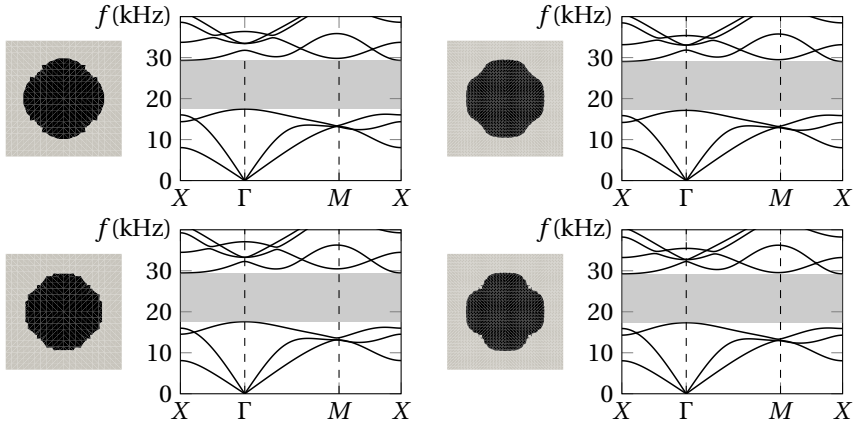

Figuur 5.6: Optimized results for a bandgap maximization between the 3rd and 4th bands starting from the initial designs shown in Figure 5.5. A large bandgap has opened up in all four optimizations, and the designs have a similar shape.

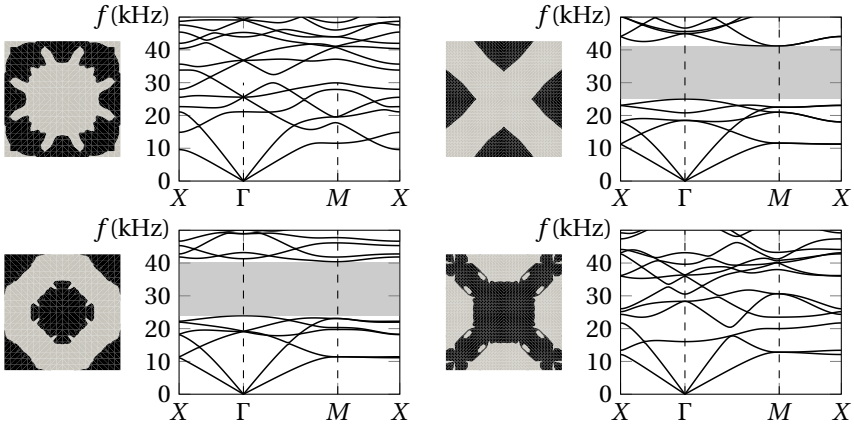

Figuur 5.7: Optimized results for a bandgap maximization between the 6th and 7th bands starting from the initial designs shown in Figure 5.5. A large bandgap has opened up between these bands for two optimization cases, while in the other two cases no bandgap was created.

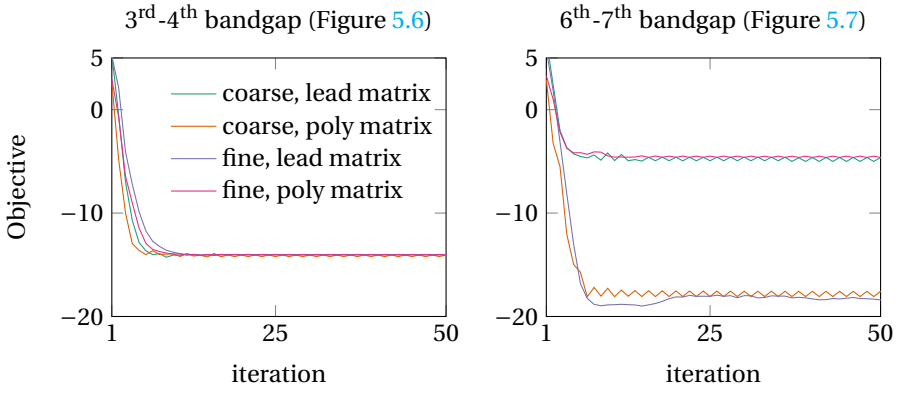

Figuur 5.8: Convergence of the optimization problems of Figures 5.6, and 5.7. The figure on the left shows the convergence for a bandgap between the 3rd and 4th bands, the figure on the right show the convergence for a bandgap between the 6th and 7th bands.

The initial designs and their corresponding band structures, without a bandgap, are shown in Figure 5.5. The red triangles indicate the reduced design area due to the 8-fold symmetry in which the inclusion can be optimized. The full PUC topology is recovered by unfolding the design in this red area. In these figures, the polycarbonate is shown in gray, and lead is shown as black.

Figures 5.6, and 5.7 show the optimized designs for maximized bandgap between band 3-4, and 6-7, respectively. For the bandgap between the 3rd and 4th band, both mesh sizes and both initial designs result in a design that roughly resembles a single circular lead inclusion in a polycarbonate matrix. The band structures show that a large bandgap has indeed opened up between the 3rd and 4th bands. As demonstrated earlier in Figures 5.3 and 5.4, this design would be poorly represented by a density-based approach. Although all four designs are very similar, they are not exactly the same, indicating that the optimizer has found a local optimum.

The effect of local optima is more clearly observed in the results for bandgaps between the 6th and 7th bands. In two of the four cases, the optimizer did not succeed in opening up a bandgap. This effect of local optima will be further discussed in §5.6. In the two cases where the optimizer succeeded to create a bandgap between the 6th and 7th bands, top right and bottom left, it did so by creating a total of two inclusions in the unit cell. In the case of the top right figure, four halves of the inclusion are visible in the unit cell. The figure on the bottom left has a full inclusion in the center and four quarters in the corners. In both cases, large bandgaps open up between the 6th and 7th bands, as was the objective of the optimization.

Figure 5.8 illustrates the convergence of the optimization cases. It is observed that the optimizer converges quickly in all cases, albeit sometimes to a local optimum. Note that the two cases without a bandgap still appear to have a negative objective value, which would indicate a bandgap. This can be explained by the fact that the smooth minimum and smooth maximum functions that are used in the optimization are approximations of the actual minimum and maximum functions respectively (see (5.11)). Increasing the value of α in (5.11) would improve this approximation, but it would simultaneously increase the nonlinearity of the problem, which could lead to instabilities.

5.5.2. BANDGAP MAXIMIZATION IN 3-D PNCS

To demonstrate the method for the design of 3-D phononic crystals, a bandgap maximization between the 6th and 7th bands is performed for a 3-D periodic unit cell with 16-fold symmetry. This example uses the same material properties and sizes, *i.e.* a $25 \times 25 \times 25$ mm unit cell, as the previous numerical example. Figure 5.9 shows the initial design with polycarbonate inclusions inside a lead matrix, and its corresponding band structure without a bandgap. The same figure also shows the final design after 50 iterations and the corresponding bandgap between the 6th and 7th bands. The final design has 8 sections of a single spherical inclusion. In Figure 5.10 the convergence of this optimization is shown. Initially, the optimization converges slowly, but after about 15 iterations it rapidly converges to form a large bandgap. This figure also shows an alternative representation of the optimized design that more clearly shows that the result resembles a spherical inclusion.

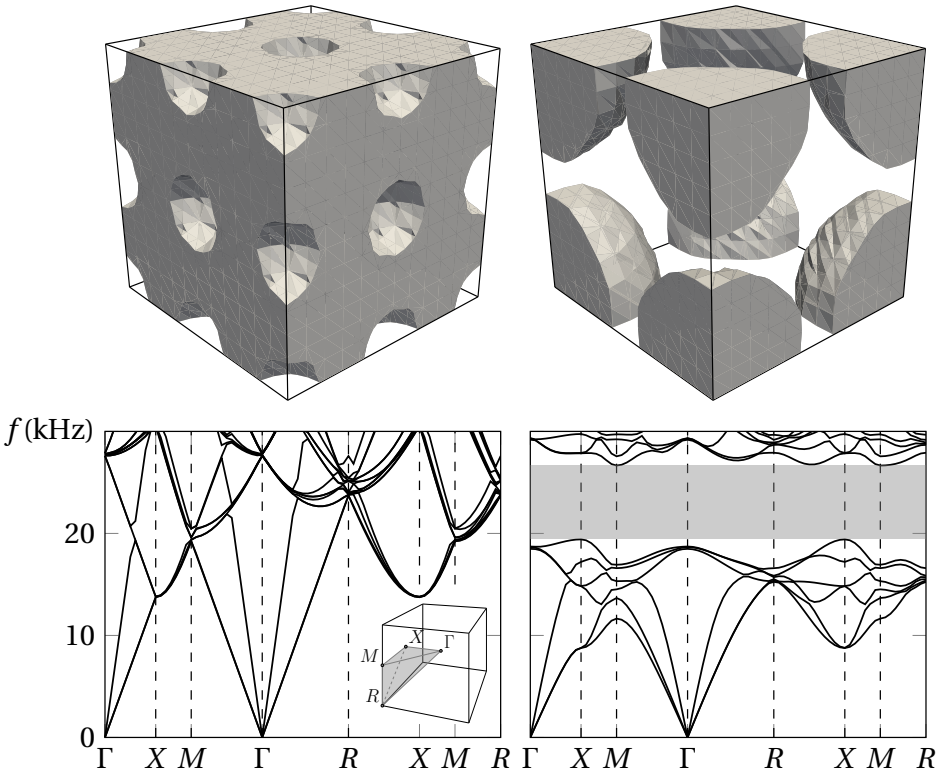

Figuur 5.9: 3-D results for bandgap maximization; on the left the initial design, irreducible Brillouin zone, and corresponding bandstructure are shown, the right shows the optimized design and bandstructure with bandgap.

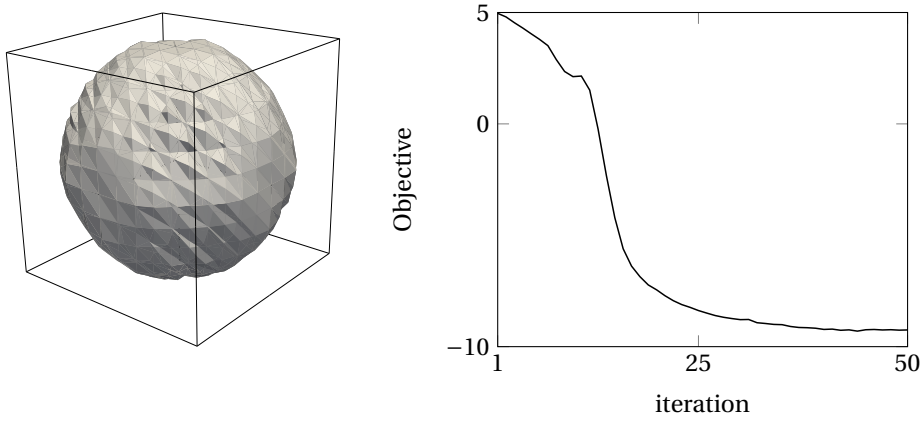

Figuur 5.10: On the right this figure shows the convergence of the 3D bandgap maximization problem, the left shows an alternative representation of the optimized design.

5.6. DISCUSSION AND CONCLUSIONS

In this work we have shown that the numerical analysis and design of phononic crystals relies heavily on the boundary description of material interfaces. The popular density-based topology optimization method results in staircased and diffuse boundaries that are detrimental for the analysis accuracy in periodic unit cell-based phononic crystals. As shown in this work, highly refined analysis meshes are needed when using a density-based approach to compensate for the loss of accuracy. These highly refined meshes lead to prohibitively expensive optimization problems.

The level set-based topology optimization that uses IGFEM for phononic crystals design proposed in this paper provides an alternative optimization method in which coarser meshes can be used to achieve the same level of accuracy compared to density methods. Furthermore, in this method the design variables are decoupled from the analysis mesh, which further reduces computational costs. The method was demonstrated for full bandgap maximization in 2-D and 3-D. However, there are still challenges.

The first observation is the fact that there are many local optima to which the optimizer may converge that may not even show a band gap at all. Small changes in the initial design or the move limit that is used in the MMA may result in a completely different optimized design. To illustrate this, Figure 5.11 shows the optimization for a bandgap between the 6th and 7th bands. On the left it shows the optimized result that converged to a solution without a bandgap. The right shows the same optimization problem, that started from the same initial design, but was optimized using a larger move limit. Starting from an initial design with slightly larger inclusions also has a similar effect in that it also results in the desired bandgap. This problem may therefore be partially alleviated by using a method to nucleate inclusions in the design, such as topological derivatives (Amstutz and Andrä, 2006).

The initial design and move limit are not the only factors for local optima to occur in the topology optimization of phononic crystals. Figure 5.12 shows on the left a 2×2 phononic crystal based on the unit cell that was optimized for a bandgap between the 6th and 7th bands. The unit cell with a green outline is the result of a topology optimization as presented in this work. The unit cell that is outlined in blue describes the exact same PnC, and therefore has the exact same performance. The unit cell shown with the red outline cannot be achieved during the optimization due to the symmetry constraints, but it would also have the same performance. In fact, any unit cell of the same dimensions would perform the same. Therefore, the number of local optima is amplified significantly when the symmetry is released. Additionally, reducing the symmetry would lead to another—larger—irreducible Brillouin zone, so more wave vectors should be considered during the optimization, increasing computation time.

Another observation that can be made is that there are small oscillations in the objective function. These oscillations are especially visible in Figure 5.8. Several explanations for these oscillations exist. First, as observed in the optimization of lattice-based PnCs in Quinteros *et al.* (2021), the oscillations may be caused by the MMA optimizer, in which case implementing a Globally Convergent Method of Moving Asymptotes (GCMMA) (Svanberg, 2002) in future work would help.

Another possible explanation is found in the fact that the sensitivities are not always accurate during the optimization. As described in van den Boom *et al.* (2021b) and Chap-

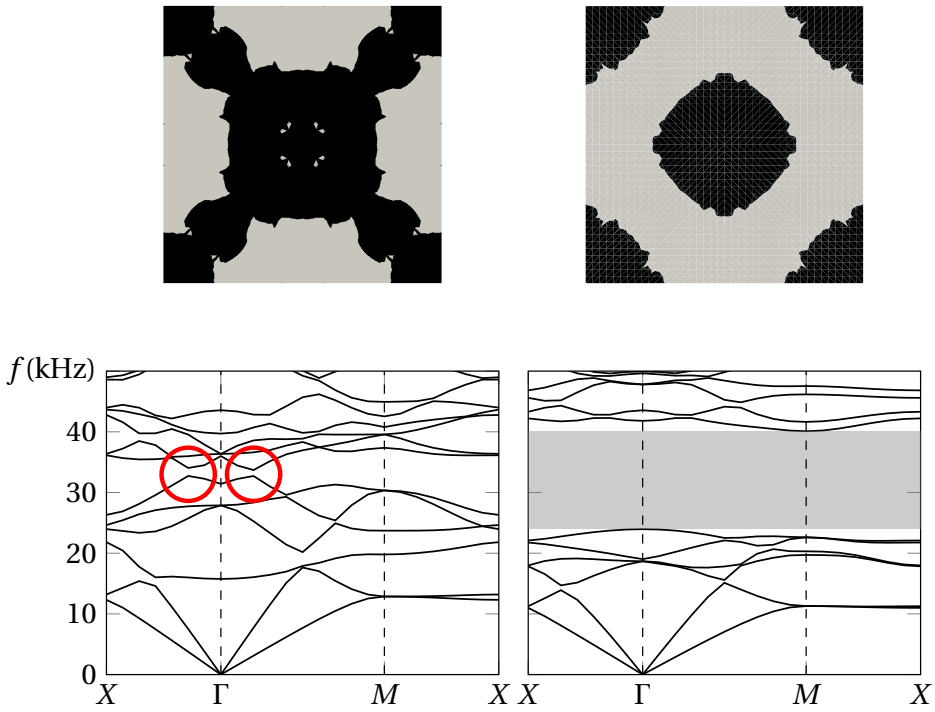

Figuur 5.11: Bandgap optimization for a bandgap between the 6th and 7th band. On the left the results as obtained in §5.5.1 are shown. The right shows the results for the same optimization problem with a larger move limit. The red circles on the left highlight mode switching in the band structure.

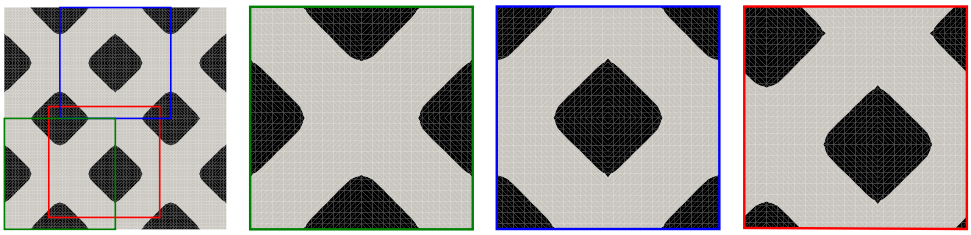

Figuur 5.12: Illustration of a few periodic unit cells that describe the same PnC, and cause the problem to have many local optima. Due to the symmetry constraint, the unit cell with a red outline cannot be achieved during optimization.

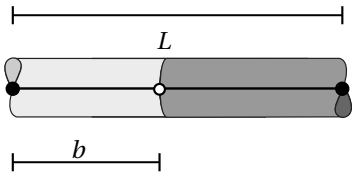

Figuur 5.13: Small 1D test problem to illustrate the scaling of the objective as a function of the interface location.

ter 4, this can be attributed to the discretization of the level set function. Figure 4.17 illustrates that in some cases enriched locations cannot be detected when a narrow feature falls within a single element. As suggested in §4.4.1, these oscillations can be alleviated by using a smaller move limit, using a finer grid for the level set discretization, or imposing a minimum length scale.

Another reason for inaccurate sensitivities is found in the multiplicity of eigenmodes and mode switching, which occurs often in the highly symmetric unit cells of the PnC. As discussed in Seyranian *et al.* (1994), these multiple eigenvalues are not differentiable in the normal sense. Instead they require a sensitivity analysis based on a perturbation technique to compute directional derivatives. For simplicity, this was not done in this work, but it could prove beneficial in further developments. Indeed, mode switching is observed in Figure 5.11 as illustrated with red circles. Alternatively, Quinteros *et al.* (2021) suggest that mode switching may be avoided when all the lower and upper bands are included in the approximation of the maximum and minimum, respectively.

Despite these challenges, this computational design procedure enables efficient generation of phononic crystal arrangements for specialized functionalities. Furthermore, the computational procedure may be extended to other problems that require a smooth description of the boundaries, such as fluid-structure interaction.

APPENDIX A: OBJECTIVE SCALING

The objective function for the maximization of absolute and relative bandgaps in literature is sometimes described in terms of ω^2, and sometimes in terms of ω or f. In this appendix it is illustrated why the optimizer converges better when using f (or ω) instead of ω^2. Figure 5.13 shows a small 1D PnC that is used for this purpose. It consists of a $L = 25$mm unit cell with lead and polycarbonate constituents (as also used in §5.5). It is meshed with a single 1D element and the material is described with an IGFEM enrichment at location b. Bloch-Floquet periodic boundary conditions are prescribed to both standard nodes, and the band structure is computed.

Figure 5.14 illustrates the scaling of the objective value in terms of ω^2 and f as a function of the location b. In the figure the absolute values of the objective function is shown, and the objective is scaled to 1 for an interface in the middle of the unit cell, $b = L/2 = 12.5$mm. The scaled objective value in terms of ω^2 crosses more than an order of magnitude, while the scaled objective value in terms of f has a less extreme curve. Therefore, in optimization it is preferred to remove the square from the objective function.

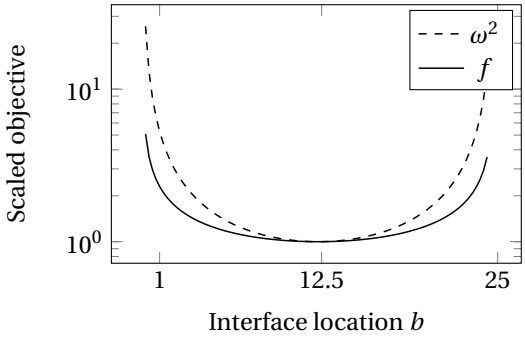

Figuur 5.14: Scaled objective values as a function of the interface location b

APPENDIX B: SENSITIVITY ANALYSIS

The sensitivity of the B-matrix with respect to the enriched node location is

$$\frac{\partial \boldsymbol{B}_e}{\partial \boldsymbol{x}_n} = \left[\boldsymbol{0} \quad \boldsymbol{\delta\psi}_e \frac{\partial \boldsymbol{J}_e^{-1}}{\partial \boldsymbol{x}_n} \right], \tag{5.19}$$

and the derivative of the Jacobian determinant can be written as:

$$\frac{\partial j_e}{\partial \boldsymbol{x}_n} = \mathrm{tr}\left(\mathrm{adj}\left(\boldsymbol{J}_e\right) \frac{\partial \boldsymbol{J}_e}{\partial \boldsymbol{x}_n} \right), \tag{5.20}$$

where the adjugate is the transpose of the cofactor matrix of $\boldsymbol{J}_e$. The sensitivity of the Jacobian inverse is computed as

$$\frac{\partial \boldsymbol{J}_e^{-1}}{\partial \boldsymbol{x}_n} = -\boldsymbol{J}_e^{-1} \frac{\partial \boldsymbol{J}_e}{\partial \boldsymbol{x}_n} \boldsymbol{J}_e^{-1}, \tag{5.21}$$

and the sensitivity of the Jacobian itself is defined as:

$$\frac{\partial \boldsymbol{J}_e}{\partial \boldsymbol{x}_n} = \frac{\partial \boldsymbol{x}_e}{\partial \boldsymbol{x}_n} \left[\boldsymbol{\delta N}_e \quad \boldsymbol{\delta\psi}_e \right]. \tag{5.22}$$

The derivatives of the N-matrix are found as:

$$\frac{\partial \boldsymbol{N}_e}{\partial \boldsymbol{x}_n} = \boldsymbol{\delta N}_e \boldsymbol{A} \frac{\partial \boldsymbol{x}_e}{\partial \boldsymbol{x}_n} \boldsymbol{N}_e, \tag{5.23}$$

where A is the inverse isoparametric mapping.

Finally, the design velocities can straightforwardly be found as

$$\frac{\partial \boldsymbol{x}_n}{\partial \phi_j} = -\frac{\phi_k}{\left(\phi_j - \phi_k\right)^2} \left(\boldsymbol{x}_j - \boldsymbol{x}_k \right), \tag{5.24}$$

and the derivative of the nodal level set values with respect to the design variables $\boldsymbol{s}$ are computed as

$$\frac{\partial \boldsymbol{\phi}}{\partial \boldsymbol{s}} = \boldsymbol{\theta}^{\mathsf{T}}. \tag{5.25}$$

For more information about the use of RBFs in the level set based topology optimization using IGFEM, see van den Boom *et al.* (2021b).

6

DISCUSSION AND CONCLUSIONS

The aim of this thesis was to develop a method for the analysis and systematic computational design of phononic crystals. This was achieved by using the Interface-enriched Generalized Finite Element Method in combination with a level set method, which allows material interfaces not to conform to the analysis mesh. This is an advantageous feature in computational design, where the optimized interfaces are unknown at the moment of mesh creation. In contrast to density-based topology optimization methods, the level set-based topology optimization using IGFEM developed in Chapter 5 of this thesis therefore does not suffer from staircasing. It has been shown in this thesis that staircasing is detrimental for the accuracy with which bandgaps are resolved.

A large part of the work presented in this thesis consisted of developing the methodology for immersed analysis and topology optimization using IGFEM. A procedure for the strong enforcement of Dirichlet and Bloch-Floquet boundary conditions on enriched nodes was developed and demonstrated in Chapters 2 and 3, respectively. Furthermore, a framework for level set-based topology optimization using IGFEM was established in Chapter 4. In Chapter 5, the developed methods were combined and applied to the topology optimization of PnCs.

6.1. SMOOTH BOUNDARIES IN PHONONIC CRYSTAL DESIGN

The present work showed that the analysis of phononic crystals is heavily dependent on the type of boundary description of the material interface. In Chapter 5, it was shown that the staircased and diffuse boundary description, that is often used in density-based topology optimization, is detrimental for the accuracy of the results. Consequently, highly refined meshes are needed for density-based topology optimization of PnCs, leading to prohibitively expensive optimization problems.

Chapter 5 also demonstrated that IGFEM requires significantly less refined meshes near interfaces to obtain the same level of accuracy. Moreover, the proposed IGFEM-based topology optimization method uses level sets to decouple the design variables from the mesh, which reduces the computational costs as well. The resulting computa-

tional design procedure facilitates efficient generation of optimized phononic crystal designs.

6.2. BOUNDARY CONDITIONS IN ENRICHED FORMULATIONS

Chapter 2 demonstrated that in contrast to other enriched methods it is straightforward to prescribe Dirichlet boundary conditions *strongly* in discontinuity-enriched finite element methods. More importantly, the method was also shown to recover a smooth reaction field. Thereby, this chapter established IGFEM/DE-FEM as an immersed finite element method.

Compared to other immersed methods, such as the finite cell method, the geometric operations in IGFEM/DE-FEM are more involved (they are of the same complexity as those in X/GFEM). This slight downside is counterbalanced by the tremendous versatility that interface-enriched finite element methods provide. Through the use of DE-FEM, both weak and strong discontinuities, *e.g.* material interfaces and cracks, can be handled. Additionally, using the hierarchical HIFEM implementation, discontinuities of different types are allowed to lie arbitrarily close to one another or even intersect. Furthermore, it has been shown that discontinuity-enriched methods are optimally convergent. They are also stable in the sense that the conditioning number grows with the same rate as in standard FEM, provided that a suitable preconditioner or scaling of the enrichment functions is chosen. These properties combined make IGFEM/DE-FEM very suitable as an all-purpose immersed analysis method for complex configurations of discontinuities and geometries.

Chapter 3 highlighted the versatility of IGFEM by using the immersed approach proposed in Chapter 2, and extending it to the analysis of phononic crystals. To that end, the formulation for boundary conditions on immersed edges is further developed to handle Bloch-Floquet periodic boundary conditions. It was demonstrated that *fully* immersed analysis of phononic crystals, where both the inclusion and the lattice type are decoupled from the mesh, is possible without loss of accuracy.

Despite the versatility, there are still open questions. For example, it is known that discontinuity-enriched finite element methods overestimate gradients in integration elements with bad aspect ratios (Nagarajan and Soghrati, 2018; Soghrati *et al.*, 2017). Although there are some cases where this has been shown not to be a problem (van den Boom *et al.*, 2019b; Zhang *et al.*, 2019a), this issue should be addressed to make the method truly general. Furthermore, in the analysis of phononic crystals, the higher bands are resolved less accurately than the lower bands, as is the case with standard FEM as well.

6.3. TOPOLOGY OPTIMIZATION USING IGFEM

This thesis introduced a framework for topology optimization using IGFEM and radial basis functions for compliance minimization problems, and later extended it to band-gap maximization of PnCs. In Chapter 4 the optimization procedure was described and investigated in detail. By combining IGFEM with a level set method, the proposed method yields black and white designs that do not suffer from staircasing, and the location of the material interface is clearly described throughout the entire optimization process.

It was also shown that the sensitivities, that are required to update the design, can be derived analytically and be computed with relatively low computational effort.

The influence of decoupling the analysis mesh from the design discretization was investigated by means of the classical MBB beam optimization problem. Because the design discretization and the analysis mesh are decoupled, the resolution of the design can be chosen independently from the mesh resolution (as is the case for any RBF-parametrized level set method). The resolution of the design should be sufficiently low compared to the resolution of the analysis to ensure that the designs are modelled accurately. In a way, the radial basis functions act similar to a filter in density-based topology optimization.

Chapter 4 also discussed two issues that are encountered when using IGFEM in a topology optimization setting: design oscillations, and "zig-zagging" of the material interfaces. Both issues were studied in detail and found to be caused by numerical artifacts due to the discretization. Strategies to mitigate these issues include using a finer grid to evaluate the intersections between the level set and the background mesh, and using a smaller move limit.

The use of IGFEM in a level set-based topology optimization framework has a number of advantages. Firstly, by virtue of the level set approach, the mapping of design variables to nodal level set values only needs to be computed once, as the background mesh is stationary during the entire optimization process. Secondly, IGFEM provides a natural distinction between nodes of the background mesh, whose locations are fixed during the optimization, and enriched nodes, which are defined by the location of the level set and move during the optimization. Because of this reason, the majority of the mesh undergoes no changes during optimization, and only the enrichments in elements that are intersected by an interface need to be updated in every iteration. Thirdly, as the enriched nodes are known (by definition) to only move along the edges of the background element, the direction of the design velocities is trivially computed. At the same time, as the original nodes are stationary, their design velocities are zero. This significantly simplifies the sensitivity computations. Lastly, using the immersed procedure described in Chapter 2, it is possible to completely remove void regions from the topology optimization. This would reduce computation time and remove artificial stiffness from the void regions. However, to achieve a fair comparison the other topology optimization methods this was not done in Chapter 4. In Chapter 5, this possibility does not apply, as PnCs consisting of two materials were optimized, and therefore there were no void regions.

The method proposed in this thesis also has some drawbacks and challenges. A drawback of the level set approach is the fact that it requires an initial design with a large number of holes. This choice of initial design can have a large influence on the final optimized design and its performance, due to non-convexity of the optimization problem at hand. However, it should be noted that the problem of non-convexity and local optima in topology optimization is not unique to level set-based approaches (Papadopoulos *et al.*, 2021; Zhang and Norato, 2018). Furthermore, topological derivatives may be used to nucleate new inclusions in level set methods (Amstutz and Andrä, 2006). Another drawback of the proposed approach compared to density-based methods is, the additional complexity that IGFEM introduces by requiring the creation of integra-

tion elements. As these integration elements change in every iteration, the local arrays for integration elements need to be reconstructed, whereas in density-based methods for linear elasticity, the element matrices can simply be scaled with density. Enriched degrees of freedom also cause a slight increase in the size of the system matrices, but the relative effect of this decreases with mesh refinement.

6.4. RELATED RESEARCH

The concepts described and developed in this thesis are useful in applications beyond the analysis and design of phononic crystals. This section briefly highlights some related topics that have been explored in collaboration with other researchers from our group:

- The foundation for any discontinuity-enriched finite element method is a fast, user-friendly, and robust tool for mesh interactions—a *geometric engine*. Considerable collaborative effort was put into creating such a versatile and robust geometric engine, which resulted in an object-oriented implementation. Zhang *et al.* (Submitted) have prepared a paper describing the geometric engine, investigating its complexity, and showcasing its capabilities. The geometric engine described in the paper can be used for research in discontinuity-enriched finite element methods, as well as other enriched and immersed methods, such as X/GFEM and CutFEM. Note that although this versatile geometric engine is relatively complex, for most applications only a small subset of the functionality is needed;

- The use of a NURBS-based discontinuity-enriched method to *exactly* represent the geometry of both weak and strong discontinuities was investigated by De Lazzari *et al.* (2021). It was found that although only slight modifications are required to the formulation to account for the spline-based discontinuities, the benefits in lower-order elements are only slight. The true potential of using NURBS to describe the discontinuities will therefore only be achieved when using higher-order interpolations;

- Finally, inspired by the recovery of smooth reaction fields described in Chapter 2, IGFEM enrichment functions have been investigated for contact problems and the coupling of non-matching meshes. Using IGFEM enrichments, the non-matching problem is transformed into an enriched problem that allows the use of multi-point constraints and standard node-to-node contact formulations. Liu *et al.* (2022) study this application of IGFEM enrichment functions. They show that the method works for linearized kinematics and frictionless contact, and properly transfers tractions from one mesh to the other.

6.5. RECOMMENDATIONS FOR FUTURE WORK

In addition to addressing the open challenges in discontinuity-enriched finite element methods and the IGFEM-based topology optimization procedure, there are more interesting directions for further development of this work. For instance, the methods described here can be used for topology optimization of other structures that consider wave propagation. One example is found in the computational design of locally resonant acoustic metamaterials (LRAMs). These metamaterials are also periodic materials

that interact with mechanical waves, and they provide sub-wavelength bandgaps. As LRAMs can also be analyzed using a PUC, the same procedure can be followed as for the analysis of PnCs. However, LRAMs are often made of more than two constituent materials, so this would entail extending the optimization procedure to a multi-material formulation.

Another type of problem that could benefit from an enriched approach is the computational design of structures with (self-) contact and large deformations. In such optimization procedures, it is important to track the boundary properly in every design iteration, such that contact can be detected and a contact formulation may be employed. More importantly, the use of IGFEM for such cases will ensure that tractions are transferred correctly, as is demonstrated in Liu *et al.* (2022).

Finally, other examples of optimization problems that may benefit from the procedure developed in this thesis are found in fluid-structure interaction problems, and the inverse analysis of material interfaces and/or fractures.

REFERENCES

Alberdi R, Zhang G, Khandelwal K (2018) An isogeometric approach for analysis of phononic crystals and elastic metamaterials with complex geometries. Comput Mech 62(3):285–307

Allaire G, Jouve F, Toader AM (2004) Structural optimization using sensitivity analysis and a level-set method. Journal of Computational Physics 194(1):363 – 393

Allaire G, Dapogny C, Frey P (2014) Shape optimization with a level set based mesh evolution method. Computer Methods in Applied Mechanics and Engineering 282:22 – 53

Amstutz S, Andrä H (2006) A new algorithm for topology optimization using a level-set method. Journal of Computational Physics 216(2):573 – 588

Annavarapu C, Hautefeuille M, Dolbow JE (2012) A robust nitsche's formulation for interface problems. Computer Methods in Applied Mechanics and Engineering 225-228:44 – 54

Aragón AM, Simone A (2017) The discontinuity-enriched finite element method. International Journal for Numerical Methods in Engineering 112(11):1589–1613

Aragón AM, Duarte CA, Geubelle PH (2010) Generalized finite element enrichment functions for discontinuous gradient fields. International Journal for Numerical Methods in Engineering 82(2):242–268

Aragón AM, Soghrati S, Geubelle PH (2013) Effect of in-plane deformation on the cohesive failure of heterogeneous adhesives. Journal of the Mechanics and Physics of Solids 61(7):1600 – 1611

Aragón AM, Liang B, Ahmadian H, Soghrati S (2020) On the stability and interpolating properties of the hierarchical interface-enriched finite element method. Computer Methods in Applied Mechanics and Engineering 362(112671)

Auricchio F, Brezzi F, Lefieux A, Reali A (2015) An "immersed" finite element method based on a locally anisotropic remeshing for the incompressible stokes problem. Computer Methods in Applied Mechanics and Engineering 294:428 – 448

Babuška I, Banerjee U (2012) Stable Generalized Finite Element method (SGFEM). Computer Methods in Applied Mechanics and Engineering 201–204:91–111

Babuška I, Melenk JM (1997) The partition of unity method. Int J Numer Methods Eng 40:727–758

Babuška I, Banerjee U, Osborn JE (2003) Survey of meshless and generalized finite element methods: A unified approach. Acta Numerica 12:1–125

Barrett JW, Elliot CM (1987) Fitted and unfitted finite-element methods for elliptic equations with smooth interfaces. IMA J Numer Anal 7(3):283–300

Basting S, Weismann M (2014) A hybrid level set/front tracking approach for finite element simulations of two-phase flows. Journal of Computational and Applied Mathematics 270:471 – 483

Belytschko T, Xiao SP, Parimi C (2003) Topology optimization with implicit functions and regularization. International Journal for Numerical Methods in Engineering 57(8):1177–1196

Belytschko T, Gracie R, Ventura G (2009) A review of extended/generalized finite element methods for material modeling. Modelling and Simulation in Materials Science and Engineering 17(043001)

Bendsøe M, Sigmund O (2004) Topology optimization. Theory, methods, and applications. 2nd ed., corrected printing

Bendsøe MP (1989) Optimal shape design as a material distribution problem. Structural optimization 1(4):193–202

Bendsøe MP, Kikuchi N (1988) Generating optimal topologies in structural design using a homogenization method. Computer Methods in Applied Mechanics and Engineering 71(2):197 – 224

Bilal OR, Hussein MI (2011) Ultrawide phononic band gap for combined in-plane and out-of-plane waves. Physical Review E - Statistical, Nonlinear, and Soft Matter Physics 84(6)

Bilal OR, Hussein MI (2017) Topology optimization of lattice materials

van den Boom SJ, Zhang J, van Keulen F, Aragón AM (2019a) Cover image. International Journal for Numerical Methods in Engineering 120(10):i–i

van den Boom SJ, Zhang J, van Keulen F, Aragón AM (2019b) A stable interface-enriched formulation for immersed domains with strong enforcement of essential boundary conditions. International Journal for Numerical Methods in Engineering 120(10):1163–1183

van den Boom SJ, van Keulen F, Aragón AM (2021a) Fully decoupling geometry from discretization in the bloch–floquet finite element analysis of phononic crystals. Computer Methods in Applied Mechanics and Engineering 382(113848)

van den Boom SJ, Zhang J, van Keulen F, Aragón AM (2021b) An interface-enriched generalized finite element method for level set-based topology optimization. Structural and Multidisciplinary Optimization 63:1–20

Bortot E, Amir O, Shmuel G (2018) Topology optimization of dielectric elastomers for wide tunable band gaps. International Journal of Solids and Structures 143:262–273

Braibant V, Fleury C (1984) Shape optimal design using b-splines. Computer Methods in Applied Mechanics and Engineering 44(3):247 – 267

Brillouin L (1930) Les électrons dans les métaux et le classement des ondes de de broglie correspondantes. Comptes Rendus Hebdomadaires des Seances de l'Academie des Sciences p 191:192

Burman E, Hansbo P (2010) Fictitious domain finite element methods using cut elements: I. A stabilized Lagrange multiplier method. Comput Methods Appl Mech Eng 199(41-44):2680–2686

Burman E, Hansbo P (2012) Fictitious domain finite element methods using cut elements: II. A stabilized Nitsche method. Appl Numer Math 62(4):328–341

Burman E, Claus S, Hansbo P, Larson MG, Massing A (2015) CutFEM: Discretizing geometry and partial differential equations. Proc 2011 Am Control Conf (104):472–501

Burman E, Elfverson D, Hansbo P, Larson MG, Larsson K (2018) Shape optimization using the cut finite element method. Computer Methods in Applied Mechanics and Engineering 328:242 – 261

Challis VJ (2010) A discrete level-set topology optimization code written in matlab. Structural and Multidisciplinary Optimization 41(3):453–464

Chaunsali R, Toles M, Yang J, Kim E (2017) Extreme control of impulse transmission by cylinder-based nonlinear phononic crystals. Journal of the Mechanics and Physics of Solids 107:21 – 32

Chen Y, Huang X, Sun G, Yan X, Li G (2017a) Maximizing spatial decay of evanescent waves in phononic crystals by topology optimization. Computers & Structures 182:430 – 447

Chen Y, Meng F, Sun G, Li G, Huang X, Huang X (2017b) Topological design of phononic crystals for unidirectional acoustic transmission. Journal of Sound and Vibration 410

Chen Y, Guo D, Li YF, Li G, Huang X (2018) Maximizing wave attenuation in viscoelastic phononic crystals by topology optimization. Ultrasonics 94:419–429

Chern IL, Shu YC (2007) A coupling interface method for elliptic interface problems. Journal of Computational Physics 225(2):2138 – 2174

Chessa J, Smolinski P, Belytschko T (2002) The extended finite element method (XFEM) for solidification problems. International Journal for Numerical Methods in Engineering 53(8):1959–1977

Christiansen AN, Nobel-Jørgensen M, Aage N, Sigmund O, Bærentzen JA (2014) Topology optimization using an explicit interface representation. Structural and Multidisciplinary Optimization 49(3):387–399

Christiansen AN, Bærentzen JA, Nobel-Jørgensen M, Aage N, Sigmund O (2015) Combined shape and topology optimization of 3d structures. Computers & Graphics 46:25 – 35

Cuba Ramos A, Aragón AM, Soghrati S, Geubelle PH, Molinari JF (2015) A new formulation for imposing dirichlet boundary conditions on non-matching meshes. International Journal for Numerical Methods in Engineering 103(6):430–444

Davis BL, Hussein MI (2014) Nanophononic metamaterial: Thermal conductivity reduction by local resonance. Physical Review Letters 112(5)

De Lazzari E, van den Boom SJ, Zhang J, van Keulen F, Aragón AM (2021) A critical view on the use of non-uniform rational b-splines to improve geometry representation in enriched finite element methods. International Journal for Numerical Methods in Engineering 122(5):1195–1216

van Dijk NP, Maute K, Langelaar M, van Keulen F (2013) Level-set methods for structural topology optimization: a review. Structural and Multidisciplinary Optimization 48(3):437–472

Dong HW, Su XX, Wang YS, Zhang C (2014) Topology optimization of two-dimensional asymmetrical phononic crystals. Physics Letters A 378(4):434 – 441

Dong HW, Dong HW, Wang YS, Wang YF, Zhang C (2015) Reducing symmetry in topology optimization of two-dimensional porous phononic crystals. AIP Advances 5

Duarte CA, Babuška I, Oden JT (2000) Generalized finite element methods for three-dimensional structural mechanics problems. Computers & Structures 77(2):215 – 232

Duarte CA, Hamzeh ON, Liszka TJ, Tworzydlo WW (2001) A generalized finite element method for the simulation of three-dimensional dynamic crack propagation. Computer Methods in Applied Mechanics and Engineering 190:2227–2262

Duarte CA, Liszka TJ, Tworzydlo WW (2007) Clustered generalized finite element methods for mesh unrefinement, non-matching and invalid meshes. International Journal for Numerical Methods in Engineering 69(11):2409–2440

Dunning P (2018) Minimum length-scale constraints for parameterized implicit function based topology optimization. Struct Multidiscip Optim 58(1):155–169

Düster A, Parvizian J, Yang Z, Rank E (2008) The finite cell method for three-dimensional problems of solid mechanics. Comput Methods Appl Mech Eng 197(45-48):3768–3782

Economou EN, Sigalas MM (1993) Classical wave propagation in periodic structures: Cermet versus network topology. Phys Rev B 48:13,434–13,438

Eschenauer HA, Olhoff N (2001) Topology optimization of continuum structures: A review*. Applied Mechanics Reviews 54(4):331–390

European Parliament Council of the European Union (2002) Directive 2002/44/ec of the european parliament and of the council of 25 june 2002 on the minimum health and safety requirements regarding the exposure of workers to the risks arising from physical agents (vibration). Tech. Rep. 2002/44/EC

Frei S, Richter T (2014) A locally modified parametric finite element method for interface problems. SIAM Journal on Numerical Analysis 52(5):2315–2334

Fries TP (2008) A corrected xfem approximation without problems in blending elements. International Journal for Numerical Methods in Engineering 75(5):503–532

Fries TP, Belytschko T (2010) The extended/generalized finite element method: An overview of the method and its applications. International Journal for Numerical Methods in Engineering 84(3):253–304

Gangl P, Langer U (2018) A local mesh modification strategy for interface problems with application to shape and topology optimization. In: Langer U, Amrhein W, Zulehner W (eds) Scientific Computing in Electrical Engineering, Springer International Publishing, Cham, pp 147–155

Gao Y, Guo Y, Zheng S (2019) A nurbs-based finite cell method for structural topology optimization under geometric constraints. Computer Aided Geometric Design 72:1 – 18

Gazonas GA, Weile DS, Wildman R, Mohan A (2006) Genetic algorithm optimization of phononic bandgap structures. International Journal of Solids and Structures 43(18-19):5851–5866

Glowinski R, Pan TW, Periaux J (1994) A fictitious domain method for Dirichlet problem and applications. Comput Methods Appl Mech Eng 111:283–303

Gupta V, Duarte CA, Babuška I, Banerjee U (2013) A stable and optimally convergent generalized FEM (SGFEM) for linear elastic fracture mechanics. Computer Methods in Applied Mechanics and Engineering 266:23–39

Hansbo A, Hansbo P (2002) An unfitted finite element method, based on Nitsche's method, for elliptic interface problems. Comput Methods Appl Mech Eng 191(47-48):5537–5552

Hansbo P (2005) Nitsche's method for interface problems in computational mechanics. GAMM-Mitteilungen 28(2):183–206

Haslinger J, Renard Y (2009) A new fictitious domain approach inspired by the extended finite element method. SIAM Journal on Numerical Analysis 47(2):1474–1499

Hautefeuille M, Annavarapu C, Dolbow JE (2012) Robust imposition of dirichlet boundary conditions on embedded surfaces. International Journal for Numerical Methods in Engineering 90(1):40–64

He J, Kang Z (2018) Achieving directional propagation of elastic waves via topology optimization. Ultrasonics 82:1–10

Hedayatrasa S, Abhary K, Uddin M, Ng CT (2016a) Optimum design of phononic crystal perforated plate structures for widest bandgap of fundamental guided wave modes and maximized in-plane stiffness. Journal of the Mechanics and Physics of Solids 89:31 – 58

Hedayatrasa S, Abhary K, Uddin MS, Guest JK (2016b) Optimal design of tunable phononic bandgap plates under equibiaxial stretch. Smart Materials and Structures 25(055025)

Hedayatrasa S, Kersemans M, Abhary K, Uddin M, Guest JK, Paepegem WV (2017) Maximizing bandgap width and in-plane stiffness of porous phononic plates for tailoring flexural guided waves: Topology optimization and experimental validation. Mechanics of Materials 105:188–203

Heinze S, Joulaian M, Düster A (2015) Numerical homogenization of hybrid metal foams using the finite cell method. "Computers & Mathematics with Applications" 70(7):1501 – 1517

Hu R, Oskay C (2019) Multiscale nonlocal effective medium model for in-plane elastic wave dispersion and attenuation in periodic composites. Journal of the Mechanics and Physics of Solids 124:220 – 243

Hussein MI, Hamza K, Hulbert GM, Saitou K (2007) Optimal synthesis of 2d phononic crystals for broadband frequency isolation. Waves in Random and Complex Media 17(4):491–510

Hussein MI, Leamy MJ, Ruzzene M (2014) Dynamics of Phononic Materials and Structures: Historical Origins, Recent Progress, and Future Outlook. Applied Mechanics Reviews 66(040802)

Isakari H, Takahashi T, Matsumoto T (2016) Periodic band structure calculation by the sakurai-sugiura method with a fast direct solver for the boundary element method with the fast multipole representation. Engineering Analysis with Boundary Elements 68:42–53

Jansen M (2019) Explicit level set and density methods for topology optimization with equivalent minimum length scale constraints. Struct Multidiscip Optim 59(5):1775–1788

Jensen KE (2016) Anisotropic mesh adaptation and topology optimization in three dimensions. Journal of Mechanical Design, Transactions of the ASME 138(6)

Jung J, Jeong CH, Jensen JS (2019) Efficient sound radiation using a bandgap structure. Applied Physics Letters 115(041903)

Kergrene K, Babuška I, Banerjee U (2016) Stable generalized finite element method and associated iterative schemes; application to interface problems. Computer Methods in Applied Mechanics and Engineering 305:1 – 36

Kushwaha MS, Halevi P, Dobrzynski L, Djafari-Rouhani B (1993) Acoustic band structure of periodic elastic composites. Phys Rev Lett 71:2022–2025

Kushwaha MS, Halevi P, Martínez G, Dobrzynski L, Djafari-Rouhani B (1994) Theory of acoustic band structure of periodic elastic composites. Phys Rev B 49:2313–2322

Kutsenko A, Shuvalov A, Norris A (2013) On the quasistatic effective elastic moduli for elastic waves in three-dimensional phononic crystals. Journal of the Mechanics and Physics of Solids 61(11):2260 – 2272

Kutsenko AA, Shuvalov AL, Norris AN (2011) Evaluation of the effective speed of sound in phononic crystals by the monodromy matrix method (l). The Journal of the Acoustical Society of America 130(6):3553–3557

Lang C, Makhija D, Doostan A, Maute K (2014) A simple and efficient preconditioning scheme for heaviside enriched xfem. Comput Mech 54(5):1357–1374

Li FL, Wang YS, Zhang C, Yu GL (2013a) Bandgap calculations of two-dimensional solid–fluid phononic crystals with the boundary element method. Wave Motion 50(3):525 – 541

Li FL, Wang YS, Zhang C, Yu GL (2013b) Boundary element method for band gap calculations of two-dimensional solid phononic crystals. Engineering Analysis with Boundary Elements 37(2):225 – 235

Li M, Cheng Z, Jia G, Shi Z (2019a) Dimension reduction and surrogate based topology optimization of periodic structures. Composite Structures 229(111385)

Li W, Meng F, Chen Y, Li Yf, Huang X (2019b) Topology optimization of photonic and phononic crystals and metamaterials: A review. Advanced Theory and Simulations 2(7)

Li W, Meng F, Li YF, Huang X (2019c) Topological design of 3d phononic crystals for ultra-wide omnidirectional bandgaps. Structural and Multidisciplinary Optimization 60:2405–2415

Li X, Ning S, Liu Z, Yan Z, Luo C, Zhuang Z (2020) Designing phononic crystal with anticipated band gap through a deep learning based data-driven method. Computer Methods in Applied Mechanics and Engineering 361(112737)

Li YF, Meng F, Li S, Jia B, Zhou S, Huang X (2018) Designing broad phononic band gaps for in-plane modes. Physics Letters A 382:679–684

Liang X, Du J (2020) Design of phononic-like structures and band gap tuning by concurrent two-scale topology optimization. Structural and Multidisciplinary Optimization 61:943–962

Liu CX, Yu GL, Zhao GY (2019) Neural networks for inverse design of phononic crystals. AIP Advances 9(085223)

Liu D, van den Boom SJ, Simone A, Aragón AM (2022) An interface-enriched generalized finite element formulation for locking-free coupling of non-conforming discretizations and contact. Computational Mechanics *accepted for publication*

Liu P, Luo Y, Kang Z (2016a) Multi-material topology optimization considering interface behavior via xfem and level set method. Computer Methods in Applied Mechanics and Engineering 308:113 – 133

Liu ZF, Wu B, He C (2016b) Systematic topology optimization of solid-solid phononic crystals for multiple separate band-gaps with different polarizations. Ultrasonics 65:249–257

Lu Y, Yang Y, Guest JK, Srivastava A (2017) 3-d phononic crystals with ultra-wide band gaps. Scientific Reports 7(43407)

Lucklum R, Li J (2009) Phononic crystals for liquid sensor applications. Measurement Science and Technology 20(12)

Lucklum R, Mukhin N, Rouhani BD, Pennec Y (2021) Phononic crystal sensors: A new class of resonant sensors—chances and challenges for the determination of liquid properties. Frontiers in Mechanical Engineering 7

Ma M, Wang L, Wang L (2021) Reliability-based topology optimization framework of two-dimensional phononic crystal band-gap structures based on interval series expansion and mapping conversion method. International Journal of Mechanical Sciences 196(106265)

Magnus JR, Neudecker H (2007) Matrix Differential Calculus with Applications in Statistics and Econometrics

Manktelow KL, Leamy MJ, Ruzzene M (2013) Topology design and optimization of nonlinear periodic materials. Journal of the Mechanics and Physics of Solids 61(12):2433 – 2453

Mayer UM, Popp A, Gerstenberger A, Wall WA (2010) 3d fluid–structure-contact interaction based on a combined xfem fsi and dual mortar contact approach. Computational Mechanics 46(1):53–67

Melenk JM, Babuška I (1996) The partition of unity finite element method: Basic theory and applications. Comput Methods Appl Mech Eng 139:289–314

Misztal MK, Bundefinedrentzen JA (2012) Topology-adaptive interface tracking using the deformable simplicial complex. ACM Trans Graph 31(3)

Moës N, Dolbow J, Belytschko T (1999) A finite element method for crack growth without remeshing. International Journal for Numerical Methods in Engineering 46(1):131–150

Moës N, Cloirec M, Cartraud P, Remacle JF (2003) A computational approach to handle complex microstructure geometries. Computer Methods in Applied Mechanics and Engineering 192(28):3163 – 3177

Mokhtari AA, Lu Y, Srivastava A (2019) On the emergence of negative effective density and modulus in 2-phase phononic crystals. Journal of the Mechanics and Physics of Solids 126:256 – 271

Muhammad, Lim CW (2021) From photonic crystals to seismic metamaterials: A review via phononic crystals and acoustic metamaterials. Archives of Computational Methods in Engineering 29:1137–1198

Nagarajan A, Soghrati S (2018) Conforming to interface structured adaptive mesh refinement: 3d algorithm and implementation. Computational Mechanics 62(5):1213–1238

Najafi AR, Safdari M, Tortorelli DA, Geubelle PH (2015) A gradient-based shape optimization scheme using an interface-enriched generalized fem. Computer Methods in Applied Mechanics and Engineering 296:1–17

Najafi AR, Safdari M, Tortorelli DA, Geubelle PH (2017) Shape optimization using a nurbs-based interface-enriched generalized fem. International Journal for Numerical Methods in Engineering 111(10):927–954

Nassar H, He QC, Auffray N (2016) A generalized theory of elastodynamic homogenization for periodic media. International Journal of Solids and Structures 84:139 – 146

Nassar H, Xu X, Norris A, Huang G (2017) Modulated phononic crystals: Non-reciprocal wave propagation and willis materials. Journal of the Mechanics and Physics of Solids 101:10 – 29

Nielsen RB, Sorokin SV (2015) Periodicity effects of axial waves in elastic compound rods. Journal of Sound and Vibration 353:135 – 149

Noël L, Duysinx P (2017) Shape optimization of microstructural designs subject to local stress constraints within an xfem-level set framework. Structural and Multidisciplinary Optimization 55(6):2323–2338

Oden JT, Duarte CAM, Zienkiewicz OC (1998) A new cloud-based hp finite element method. Computer Methods in Applied Mechanics and Engineering 153(1):117 – 126

Olhoff N, Bendsøe MP, Rasmussen J (1991) On cad-integrated structural topology and design optimization. Computer Methods in Applied Mechanics and Engineering 89(1):259 – 279

Oseev A, Zubtsov M, Lucklum R (2013) Gasoline properties determination with phononic crystal cavity sensor. Sensors and Actuators B: Chemical 189:208 – 212

Papadopoulos IPA, Farrell PE, Surowiec TM (2021) Computing multiple solutions of topology optimization problems. SIAM J Sci Comput 43(3):A1555–A1582

Park CS, Shin YC, Jo SH, Yoon H, Choi W, Youn BD, Kim M (2019) Two-dimensional octagonal phononic crystals for highly dense piezoelectric energy harvesting. Nano Energy 57

Park JH, Ma PS, Kim YY (2015) Design of phononic crystals for self-collimation of elastic waves using topology optimization method. Structural and Multidisciplinary Optimization 51(6):1199–1209

Parvizian J, Rank E (2012) Topology optimization using the finite cell method. Optim Eng 13:57–78

Parvizian J, Düster A, Rank E (2007) Finite cell method h- and p-extension for embedded domain problems in solid mechanics. Comput Mech 41:121–133

Pascalis RD, Donateo T, Ficarella A, Parnell WJ (2020) Optimal design of phononic media through genetic algorithm-informed pre-stress for the control of antiplane wave propagation. Extreme Mechanics Letters 40(100896)

Pejman R, Aboubakr SH, Martin WH, Devi U, Tan MHY, Patrick JF, Najafi AR (2019) Gradient-based hybrid topology/shape optimization of bioinspired microvascular composites. International Journal of Heat and Mass Transfer 144(118606)

Peng C, Zhao X, Liu G (2015) Noise in the sea and its impacts on marine organisms. Int J Environ Res Public Health 12(10):12,304–23

Pennec Y, Jin Y, Djafari-Rouhani B (2019) Phononic and photonic crystals for sensing applications 52:105–145

Qian C, Hui G, Yuan T, Pei S, Guo F, Yansong W (2020) Topological design of square lattice structure for broad and multiple band gaps in low-frequency range. Extreme Mechanics Letters 35(100632)

Quinteros L, Meruane V, Cardoso E (2021) Phononic band gap optimization in truss-like cellular structures using smooth p-norm approximations. Structural and Multidisciplinary Optimization 64:113–124

Rangarajan R, Lew AJ (2014) Universal meshes: A method for triangulating planar curved domains immersed in nonconforming meshes. International Journal for Numerical Methods in Engineering 98(4):236–264

Rozvany GIN (2009) A critical review of established methods of structural topology optimization. Structural and Multidisciplinary Optimization 37(3):217–237

Ruess M, Schillinger D, Bazilevs Y, Varduhn V, Rank E (2013) Weakly enforced essential boundary conditions for NURBS-embedded and trimmed NURBS geometries on the basis of the finite cell method. Int J Numer Methods Eng 95:811–846

Rupp CJ, Evgrafov A, Maute K, Dunn ML (2007) Design of phononic materials/structures for surface wave devices using topology optimization. Structural and Multidisciplinary Optimization 34

Rupp CJ, Dunn ML, Maute K (2010) Switchable phononic wave filtering, guiding, harvesting, and actuating in polarization-patterned piezoelectric solids. Applied Physics Letters 96(11):111902

Sadat SM, Wang RY (2020) A machine learning based approach for phononic crystal property discovery. Journal of Applied Physics 128:025,106

Sanders JD, Dolbow JE, Laursen TA (2009) On methods for stabilizing constraints over enriched interfaces in elasticity. International Journal for Numerical Methods in Engineering 78(9):1009–1036

Schillinger D, Dede L, Scott MA, Evans JA, Borden MJ, Rank E, Hughes TJR (2012) An isogeometric design-through-analysis methodology based on adaptive hierarchical refinement of NURBS, immersed boundary methods, and T-spline CAD surfaces. Comput Methods Appl Mech Eng 249-252:116–150

Seyranian AP, Lund E, Olhoff N (1994) Multiple eigenvalues in structural optimization problems. Structural optimization 8:207–227

Shakiba M, Brandyberry DR, Zacek S, Geubelle PH (2019) Transverse failure of carbon fiber composites: Analytical sensitivity to the distribution of fiber/matrix interface properties. International Journal for Numerical Methods in Engineering 120:650–665

Sharma A, Maute K (2018) Stress-based topology optimization using spatial gradient stabilized xfem. Structural and Multidisciplinary Optimization 57(1):17–38

Shi L, Liu N, Zhou J, Zhou Y, Wang J, Liu QH (2016) Spectral element method for bandstructure calculations of 3d phononic crystals. Journal of Physics D: Applied Physics 49(455102)

Sigalas M, Economou EN (1993) Band structure of elastic waves in two dimensional systems. Solid State Communications 86(3):141 – 143

Sigalas MM, Economou EN (1992) Elastic and acoustic wave band structure. Journal of Sound Vibration 158:377–382

Sigmund O (1994) Design of material structures using topology optimization. PhD thesis, Department of Solid Mechanics, Technical University of Denmark

Sigmund O (2001) A 99 line topology optimization code written in matlab. Structural and Multidisciplinary Optimization 21(2):120–127

Sigmund O, Jensen JS (2002) Topology optimization of phononic bandgap materials and structures. In: Fifth World Congress on Computational Mechanics

Sigmund O, Jensen JS (2003) Systematic design of phononic band-gap materials and structures by topology optimization. Philosophical Transactions of the Royal Society A: Mathematical, Physical and Engineering Sciences 361(1806):1001–1019

Soghrati S (2014) Hierarchical interface-enriched finite element method: An automated technique for mesh-independent simulations. Journal of Computational Physics 275:41 – 52

Soghrati S, Geubelle PH (2012) A 3d interface-enriched generalized finite element method for weakly discontinuous problems with complex internal geometries. Computer Methods in Applied Mechanics and Engineering 217-220:46 – 57

Soghrati S, Aragón AM, Armando Duarte C, Geubelle PH (2012a) An interface-enriched generalized FEM for problems with discontinuous gradient fields. Int J Numer Meth Eng 89:991 – 1008

Soghrati S, Thakre PR, White SR, Sottos NR, Geubelle PH (2012b) Computational modeling and design of actively-cooled microvascular materials. International Journal Of Heat And Mass Transfer 55:5309–5321

Soghrati S, Najafi AR, Lin JH, Hughes KM, White SR, Sottos NR, Geubelle PH (2013) Computational analysis of actively-cooled 3d woven microvascular composites using a stabilized interface-enriched generalized finite element method. International Journal Of Heat And Mass Transfer 65:153–164

Soghrati S, Duarte CA, Geubelle PH (2015) An adaptive interface-enriched generalized fem for the treatment of problems with curved interfaces. International Journal for Numerical Methods in Engineering 102(6):1352–1370

Soghrati S, Nagarajan A, Liang B (2017) Conforming to interface structured adaptive mesh refinement: New technique for the automated modeling of materials with complex microstructures. Finite Elements in Analysis and Design 125:24 – 40

Sridhar A, Kouznetsova VG, Geers MGD (2018) A general multiscale framework for the emergent effective elastodynamics of metamaterials. Journal of the Mechanics and Physics of Solids 111:414 – 433

Staten ML, Owen SJ, Shontz SM, Salinger AG, Coffey TS (2012) A comparison of mesh morphing methods for 3d shape optimization. In: Quadros WR (ed) Proceedings of the 20th International Meshing Roundtable, Springer Berlin Heidelberg, Berlin, Heidelberg, pp 293–311

Su XX, Li JB, Wang YS (2010) A postprocessing method based on high-resolution spectral estimation for {FDTD} calculation of phononic band structures. Physica B: Condensed Matter 405(10):2444 – 2449

Sukumar N, Pask JE (2009) Classical and enriched finite element formulations for bloch-periodic boundary conditions. International Journal for Numerical Methods in Engineering 77(8):1121–1138

Svanberg K (1987) The method of moving asymptotes—a new method for structural optimization. International Journal for Numerical Methods in Engineering 24(2):359–373

Svanberg K (2002) A class of globally convergent optimization methods based on conservative convex separable approximations. SIAM J on Optimization 12(2):555–573

Tan MHY, Geubelle PH (2017) 3d dimensionally reduced modeling and gradient-based optimization of microchannel cooling networks. Computer Methods in Applied Mechanics and Engineering 323:230–249

Tan MHY, Safdari M, Najafi AR, Geubelle PH (2015) A nurbs-based interface-enriched generalized finite element scheme for the thermal analysis and design of microvascular composites. Computer Methods in Applied Mechanics and Engineering 283:1382–1400

Tan MHY, Bunce D, Ghosh ARM, Geubelle PH (2018a) Computational design of microvascular radiative cooling pasonels for nanosatellites. Journal of Thermophysics and Heat Transfer 32(3):605–616

Tan MHY, Najafi AR, Pety SJ, White SR, Geubelle PH (2018b) Multi-objective design of microvascular panels for battery cooling applications. Applied Thermal Engineering 135:145 – 157

Tanaka Y, Tomoyasu Y, Tamura Si (2000) Band structure of acoustic waves in phononic lattices: Two-dimensional composites with large acoustic mismatch. Phys Rev B 62:7387–7392

Tol S, Degertekin FL, Erturk A (2019) 3d-printed phononic crystal lens for elastic wave focusing and energy harvesting. Additive manufacturing 29(100780)

Tur M, Albelda J, Nadal E, Ródenas JJ (2014) Imposing dirichlet boundary conditions in hierarchical cartesian meshes by means of stabilized lagrange multipliers. International Journal for Numerical Methods in Engineering 98(6):399–417

Van Miegroet L, Duysinx P (2007) Stress concentration minimization of 2d filets using x-fem and level set description. Structural and Multidisciplinary Optimization 33(4):425–438

Vasileiadis T, Varghese J, Babacic V, Gomis-Bresco J, Urrios DN, Graczykowski B (2021) Progress and perspectives on phononic crystals. Journal of Applied Physics 129(160901)

Vatanabe SL, Paulino GH, Silva ECN (2014) Maximizing phononic band gaps in piezocomposite materials by means of topology optimization. Journal of the Acoustical Society of America 136:494

Veres IA, Berer T, Matsuda O (2013) Complex band structures of two dimensional phononic crystals: Analysis by the finite element method. Journal of Applied Physics 114(083519)

Villanueva CH, Maute K (2014) Density and level set-xfem schemes for topology optimization of 3-d structures. Computational Mechanics 54(1):133–150

Villanueva CH, Maute K (2017) CutFEM topology optimization of 3D laminar incompressible flow problems. Comput Methods Appl Mech Eng 320:444–473

Wang L, Zheng H, Lu X, Shi L (2019) A petrov-galerkin finite element interface method for interface problems with bloch-periodic boundary conditions and its application in phononic crystals. Journal of Computational Physics 393:117 – 138

Wang S, Wang MY (2006) Radial basis functions and level set method for structural topology optimization. International Journal for Numerical Methods in Engineering 65(12):2060–2090

Wang YF, Wang YZ, Wu B, Chen W, Wang YS (2020) Tunable and active phononic crystals and metamaterials. Applied Mechanics Reviews 72:040,801

Wei C, Jing X (2017) A comprehensive review on vibration energy harvesting: Modelling and realization. Renewable and Sustainable Energy Reviews 74:1 – 18

Wei P, Li Z, Li X, Wang MY (2018) An 88-line matlab code for the parameterized level set method based topology optimization using radial basis functions. Structural and Multidisciplinary Optimization 58(2):831–849

Wendland H (1995) Piecewise polynomial, positive definite and compactly supported radial functions of minimal degree. Advances in Computational Mathematics 4(1):389–396

Witarto W, Wang SJ, Yang CY, Wang J, Mo YL, Chang KC, Tang Y (2019) Three-dimensional periodic materials as seismic base isolator for nuclear infrastructure. AIP Advances 9(4):045,014

Xie L, Xia B, Huang G, Lei J, Liu J (2017) Topology optimization of phononic crystals with uncertainties. Structural and Multidisciplinary Optimization 56:1319–1339

Xie L, Xie L, Liu J, Huang G, Zhu W, Xia B (2018) A polynomial-based method for topology optimization of phononic crystals with unknown-but-bounded parameters. International Journal for Numerical Methods in Engineering 114:777–800

Xu W, Ning J, Lin Z, Qi W, Liu H, Wang W (2020) Multi-objective topology optimization of two-dimensional multi-phase microstructure phononic crystals. Materials today communications 22:100,801

Yamasaki S, Yamanaka S, Fujita K (2017) Three-dimensional grayscale-free topology optimization using a level-set based r-refinement method. International Journal for Numerical Methods in Engineering 112(10):1402–1438

Yan Y, Cheng Z, Menq F, Mo YL, Tang Y, Shi Z (2015) Three dimensional periodic foundations for base seismic isolation. Smart Materials and Structures 24(7)

Yera R, Forzani L, Méndez CG, Huespe AE (2021) A topology optimization algorithm based on topological derivative and level-set function for designing phononic crystals. Engineering Computations 39:354–379

Yi G, Youn BD (2016) A comprehensive survey on topology optimization of phononic crystals. Structural and Multidisciplinary Optimization 54(5):1315–1344

Yuksel O, Yilmaz C (2020) Realization of an ultrawide stop band in a 2-d elastic metamaterial with topologically optimized inertial amplification mechanisms. International Journal of Solids and Structures 203:138–150

Zhang J, van den Boom SJ, van Keulen F, Aragón AM (2019a) A stable discontinuity-enriched finite element method for 3-d problems containing weak and strong discontinuities. Computer Methods in Applied Mechanics and Engineering 355:1097–1123

Zhang J, Zhebel E, van den Boom SJ, Liu D, Aragón AM (Submitted) An object-oriented geometric engine for the use in enriched finite element formulations and immersed domain methods

Zhang S, Norato JA (2018) Finding Better Local Optima in Topology Optimization via Tunneling. International Design Engineering Technical Conferences and Computers and Information in Engineering Conference, vol Volume 2B: 44th Design Automation Conference

Zhang X, Zhang X, He J, Takezawa A, Kang Z (2018) Robust topology optimization of phononic crystals with random field uncertainty. International Journal for Numerical Methods in Engineering 115:1154–1173

Zhang X, Brandyberry DR, Geubelle PH (2019b) Igfem-based shape sensitivity analysis of the transverse failure of a composite laminate. Computational Mechanics 64:1455–1472

Zhang X, Zhang X, Takezawa A, Kang Z (2019c) A phase-field based robust topology optimization method for phononic crystals design considering uncertain diffuse regions. Computational Materials Science 160:159–172

Zhang X, Xing J, Liu P, Luo Y, Kang Z (2021) Realization of full and directional band gap design by non-gradient topology optimization in acoustic metamaterials. Extreme Mechanics Letters 42:101,126

Zhao J, Li Y, Liu WK (2015) Predicting band structure of 3d mechanical metamaterials with complex geometry via xfem. Computational Mechanics 55(4):659–672

Zheng H, Zhang C, Wang Y, Sladek J, Sladek V (2016) A meshfree local rbf collocation method for anti-plane transverse elastic wave propagation analysis in 2d phononic crystals. Journal of Computational Physics 305:997 – 1014

Zhou M, Lian H, Sigmund O, Aage N (2018) Shape morphing and topology optimization of fluid channels by explicit boundary tracking. International Journal for Numerical Methods in Fluids 88(6):296–313

CURRICULUM VITÆ

Sanne Jolene VAN DEN BOOM



01-06-1989 Born in Bergen op Zoom, the Netherlands.

EDUCATION

2015-2022 PhD in Mechanical Engineering
Delft University of Technology, Delft
Thesis: A discontinuity-enriched finite element method for the computational design of phononic crystals
Promotor: Prof. dr. ir. A. van Keulen
Copromotor: Dr. A.M. Aragón

2012–2014 Master in Mechanical Engineering
Delft University of Technology, Delft
Internship: Topology optimization of metallic grids on photovoltaic cells, *internship at TNO*
Thesis: Topology optimization including buckling analysis *cum laude*

2007–2012 Bachelor in Industrial Design
Delft University of Technology, Delft
Minor: Mechanical engineering

2001–2007 VWO / Gymnasium
R.K. Gymnasium Juvenaat H. Hart, Bergen op Zoom

PROFESSIONAL

2019-present Research scientist at TNO
2009-2018 Teaching assistant

LIST OF PUBLICATIONS

JOURNAL PAPERS

8. **van den Boom, S.J.**, Abedi, R., van Keulen, F. and Aragón, A.M., *'On the importance of boundary smoothness in the computational design of phononic crystals', in preparation*

7. Zhang, J., Zhebel, E., **van den Boom, S.J.**, Liu, D.and Aragón, A.M. *'An Object Oriented Geometric Engine for the use in Enriched Finite Element Formulations and Immersed Domain Methods', submitted*

6. Liu, D., **van den Boom, S.J.**, Simone, A. and Aragón, A.M., *'An interface-enriched generalized finite element formulation for locking-free coupling of non-conforming discretizations and contact', accepted for publication*

5. **van den Boom, S.J.**, van Keulen, F. and Aragón, A.M., *'Fully decoupling geometry from discretization in the Bloch-Floquet finite element analysis of phononic crystals'*, Computer Methods in Applied Mechanics and Engineering. 2021 (382) 113848

4. De Lazzari, E., **van den Boom, S.J.**, Zhang, J., Aragón, A.M., *'A critical view on the use of NURBS to improve geometry representation in enriched finite element methods'*, International Journal for Numerical Methods in Engineering. 2021

3. **van den Boom, S.J.**, Zhang, J., van Keulen, F. and Aragón, A.M., *'An Interfaced-enriched Generalized Finite Element Method for level set based topology optimization'*, Structural and Multidisciplinary Optimization. 2021

2. **van den Boom, S.J.**, Zhang, J., van Keulen, F. and Aragón, A.M., *'A stable interface-enriched formulation for immersed domains with strong enforcement of essential boundary conditions'*, International Journal for Numerical Methods in Engineering. 2019 (120) 1163 – 1183

1. Zhang, J., **van den Boom, S.J.**, van Keulen, F. and Aragón, A.M.,*'A Stable Discontinuity-Enriched Finite Element Method for 3-D Problems containing Weak and Strong Discontinuities'*, Computer Methods in Applied Mechanics and Engineering. 2019 (355) 1097-1123

CONFERENCE PAPERS

1. **van den Boom, S.J.**, Aragón, A.M. and van Keulen, F., *'Mesh-independent design of phononic crystals using an advanced finite element formulation', Proceedings of the ASME 2016 IMECE.*

JOURNAL COVERS

1. **van den Boom, S.J.**, Aragón, A.M. and van Keulen, F., *'Cover Image'*, International Journal for Numerical Methods in Engineering. 2019 (120)

ACKNOWLEDGEMENTS

The fact that this dissertation only has one author should not be misinterpreted as that I could have done it alone. During the writing of this thesis, I have received support from many people, for which I am very grateful.

First, I would like to thank my supervisors: Fred van Keulen and Alejandro Aragón. Fred, thank you for giving me the opportunity to pursue a PhD, and for the insightful comments and questions during our meetings. Alejandro, thank you for the many discussions we have had over the years. It is safe to say we did not always agree but we always managed to find common ground eventually. I really enjoyed our pair programming sessions on the Hybrida framework, especially in the beginning of my PhD. There is no doubt in my mind that I could not have written this thesis without your help. Fred, Alejandro, I hope our paths will cross in the future.

I would also like to thank my fellow Hybrida team members and co-authors Jian Zhang, Dongyu Liu, Elena Zhebel, and Elena De Lazzari. Collaborating on the Geometric Engine was sometimes challenging because of the different requirements for the different research projects, but it certainly paid of. More importantly, this collaboration meant that there was always somebody around to discuss bugs and "features" with.

Somebody was also always around near the whiteboard at the coffee machine on the PME square. This quickly became one of my favourite spots in the building, because an interesting discussion was never far away. The topic for these discussions could be anything: a problem a colleague recently encountered, a topic from a recent Charles meeting, or great ideas for future research. For this I am grateful for everybody in the department of Precision and Microsystems engineering and in the Structural Optimization and Mechanics group. I particularly want to thank Roy, Emiel, and Jian, for sharing their experiences on the final stages of finalizing and defending a dissertation.

I should also mention all my colleagues in TNO, where I've worked for the past three years. Thank you for giving me the opportunity to continue to work on my thesis, and for keeping me motivated by allowing me to work on many interesting projects. Your slight teasing about the not-yet-finished-state of my thesis was certainly encouraging.

A sincere appreciation goes out to all of my (former-) colleagues that made sure that my time at the university was not only productive, but also a lot of fun. Over the years there were many colleagues in the SOM group and in PME, with whom I enjoyed lunch, coffee, and drinks. People who made me feel at home, and who offered much needed help, discussions, and distractions from the inevitable problems and setbacks I encountered in my research. At the very beginning when I just joined the department it were Evert, Michael, Maarten, and Cristina, who quickly included me in social activities. Over time, the group of people who joined for dinner and drinks in the city center changed, but what remained were the many fun nights, for which I need to thank Dirk, Stijn, Emiel, Floris, Arnoud, Max, and many others.

Besides the coffee and drinks in Delft, there were also opportunities to travel to conferences, and—most memorably—the wedding of Laura in Sicily. Rob, I will never forget our epic hike in the burning heat on mount Etna, after which spaghetti with (only!) canned tuna tasted like the best thing ever. Banafsheh, our adventures did not only take us to Italy, but even all the way to the USA, where you took me to San Diego to attend a Persian dinner party. I have made some very good friends during my years in the university, and I hope to stay in touch with all of you, not only on a professional level, but also for bouldering, dinners, and drinks.

I am lucky to also have good friends outside of work. Crystel, thank you for being my friend since the very beginning of our lives in Delft. While designing the cover of this thesis it became clear once again that we are a great design team. Thank you for being my paranymph! Has, thank you for the dinners with port. Mira, Wouter, and all of the other friends from the Koornbeurs, thank you for understanding when I missed events because I was working on my thesis. A thanks also goes to Marieke, who as my friend from "back home" gave me some welcomed non-Delft perspectives, to Ellen for the occasional but long tea drinking sessions, and to Ilona for the dinners while watching movies or the songfestival.

Of course I also want to thank my family for all their love and support. My parents, Jos and Conny, have never once doubted that I would finish this thesis, even when I was not so sure myself. Sofie, thank you for wanting to be my paranymph from the very beginning, sorry to have had you waiting for so long. Last but not least I want to thank my beloved Max. I am so glad I met you during the course of this research. Thank you for understanding the frustrations of doing research, for all the proof-reading, and for giving me much needed support. I cannot count the number of times that you have encouraged me to continue working on my thesis when I was ready to give up.